

UNIVERSITY OF OKLAHOMA

GRADUATE COLLEGE

LABORATORY AND FIELD ASSESSMENT OF CHEMICALLY-STABILIZED  
SUBGRADE MODULI UNDER COMPRESSIVE AND FLEXURAL LOADING

A DISSERTATION

SUBMITTED TO THE GRADUATE FACULTY

in partial fulfillment of the requirements for the

Degree of

DOCTOR OF PHILOSOPHY

By

MOEEN NAZARI  
Norman, Oklahoma  
2016

LABORATORY AND FIELD ASSESSMENT OF CHEMICALLY-STABILIZED  
SUBGRADE MODULI UNDER COMPRESSIVE AND FLEXURAL LOADING

A DISSERTATION APPROVED FOR THE  
SCHOOL OF CIVIL ENGINEERING AND ENVIRONMENTAL SCIENCE

BY

---

Dr. Musharraf Zaman, Chair

---

Dr. Sesh Commuri

---

Dr. Kianoosh Hatami

---

Dr. Gerald A. Miller

---

Dr. Dar Hao Chen



*To my parents, Farahnaz and Ali,  
and to Anahita*

## ACKNOWLEDGEMENTS

I would like to express my deepest gratitude to my advisor, Professor Musharraf Zaman for the continuous support of my Ph.D. study and related research, for his patience, motivation, and immense knowledge. His guidance helped me tremendously throughout this research and writing of this dissertation. I learned a lot from him, which I will be using for the rest of my professional career.

I solemnly submit my honest and humble thanks to Professor Sesh Commuri for his creative suggestions, motivation, encouragement, and exemplary guidance throughout the course of my doctoral research. I would like to thank him for providing funding during my stay at the University of Oklahoma (OU).

I wish to thank Dr. Kianoosh Hatami for serving on my doctoral committee. I have learned a lot from his “Earthquake Engineering” class. I am greatly thankful to him for sharing his knowledge and ideas during the class lecture. I am also gratefully thankful to Dr. Gerald A. Miller for serving on my doctoral committee. It was Dr. Miller’s “Unsaturated Soil Mechanics” class that I took first when I came to OU. I would like to thank him for sharing his wealth of knowledge and experience with me. I would also like to thank Dr. Dar Hao Chen from the Texas Department of Transportation (TxDOT) for accepting to serve on my doctoral committee and for providing valuable comments.

I would like to express my special thanks to Dr. Manik Barman. He is an excellent example of a good friend and a research colleague. I was privileged to be in Dr. Barman’s team, who led the day-to-day activities of the Intelligent Compaction of Stabilized Subgrade project under Dr. Zaman’s and Dr. Commuri’s supervision. I would like to thank him for his generosity in sharing his time, ideas and knowledge, and for his active

involvement and contribution in research. I would also like to extend my sincere thanks to Dr. Imran Asif. I had the opportunity to work with him in the Intelligent Compaction of Stabilized Subgrade project. I would like to acknowledge Dr. Rouzbeh Ghabchi, not only for guiding me in the laboratory work, but as a valuable colleague and friend. I also learned a lot from his knowledge and would like to thank him for sharing his experience with me. I am also grateful to Dr. Dharamveer Singh for being an excellent colleague, a sincere researcher and a fine person.

I would like to thank the Volvo Construction Equipment (VCE), Oklahoma Department of Transportation, Oklahoma Transportation Center (OkTC), and Southern Plains Transportation Center (SPTC) for providing financial and logistic support needed for this research. I also wish to thank the Nancy L. Mergler Dissertation Completion Fellowship selection committee for selecting me as the recipient of the fellowship, which helped me to complete my doctoral degree on the last year of my studies. I especially would like to thank Dr. Nancy Mergler as the senior vice president and provost of the University of Oklahoma, Norman Campus.

My thanks are also extended to Mr. Michael Schmitz for his technical support in the laboratory. I would like to acknowledge the faculty and staff of the School of Civil Engineering and Environmental Science, Ms. Molly Smith and Mrs. Susan Williams. I cannot forget to thank some of my friends, Mr. Koohyar Faizi, Mr. Mohamad Darayi, Dr. Moien Farmahini, Mr. Ali Taghichian, Dr. Amirhossein Khosrojerdi and Dr. Mani Razi for their encouragement and support during this study.

Finally, I would like to express my eternal love and gratitude to my father, Mr. Ali Nazari, and my mother, Mrs. Farahnaz Sadeghimoghaddam, for their unconditional

love, encouragement, sacrifice, patience and support. They selflessly have given me the best years of their lives to let me pursue my dreams. I express my heartiest gratitude for their love, without which this work would not have been completed. I also would like to use this opportunity to express my thanks and love to my dear brother, Dr. Morad Nazari, and my sister Mrs. Moones Nazari for being such a great source of kindness and positive energy during these years. I take this moment to express my never ending love and respect towards my wife, Mrs. Anahita Abdollahifar for her endless support, inspiration, and motivation during this journey. She has been my best friend and great companion, loved, supported, encouraged, entertained, and helped me get through this agonizing period in the most positive way.

## TABLE OF CONTENTS

ACKNOWLEDGEMENTS .....	IV
TABLE OF CONTENTS .....	VII
LIST OF TABLES .....	IV
LIST OF FIGURES .....	VII
ABSTRACT .....	XII
<b>CHAPTER 1: INTRODUCTION .....</b>	<b>1</b>
1.1 Background and Needs .....	1
1.1.1 Chemical Stabilization of Subgrade Soil .....	2
1.1.2 Compressive Performance of Stabilized Subgrade During Compaction.....	4
1.1.3 Flexural Performance of Chemically-Stabilized Subgrade .....	5
1.2 Objectives .....	7
1.3 Organization of the Dissertation.....	8
<b>CHAPTER 2: DEVELOPMENT OF REGRESSION MODELS FOR ESTIMATING RESILIENT MODULI .....</b>	<b>12</b>
2.1 Introduction .....	12
2.2 Background and Literature Review .....	13
2.3 Methodology.....	17
2.3.1 Site Selection for Case Studies and Material Collection .....	18
2.3.2 Specimen Preparation and Resilient Modulus Testing.....	19
2.3.3 Developing Regression Models for Mr .....	22
2.3.4 Developing 0-day to 7-day and 28-day Mr Conversion Models .....	23
2.3.5 Developing a Generic Model for 28-day Mr of CKD-stabilized Soil.....	24
2.4 Case Study 1 (CS1): 60 <sup>th</sup> Avenue Northwest Project.....	25
2.4.1 Site Location and Material Collection.....	25
2.4.2 Test Combinations and Resilient Modulus Testing.....	25
2.4.3 Developing Regression Models for Mr .....	27
2.4.4 Developing 0-day to 28-day Mr Conversion Model.....	28
2.5 Case Study 2 (CS2): Apple Valley Project.....	29
2.5.1 Site Location and Material Collection.....	29
2.5.2 Test Combinations and Resilient Modulus Testing.....	30
2.5.3 Developing Regression Models for Mr .....	31
2.5.4 Developing 0-day to 28-day Mr Conversion Model.....	32
2.6 Case Study 3 (CS3): Main Street-Interstate 35 Intersection Project .....	33
2.6.1 Site Location and Material Collection.....	33



2.6.2 Test Combinations and Resilient Modulus Testing.....	33
2.6.3 Developing Regression Models for Mr .....	36
2.6.4 Developing 0-day to 28-day Mr Conversion Model.....	37
2.7 Case Study 4 (CS4): Interstate 35 Service Road Project.....	37
2.7.1 Site Location and Material Collection.....	37
2.7.2 Test Combinations and Resilient Modulus Testing.....	39
2.7.3 Developing Regression Models for Mr .....	40
2.7.4 Developing 0-day to 7-day and 28-day Mr Conversion Models .....	41
2.8 Developing a Generic Model for 28-day Mr of CKD-stabilized Soil .....	42
2.8.1 Influence of Different Parameters on the Mr of the CKD-stabilized Soil .....	43
2.8.2 Development of 28-day Mr Generic Model of CKD-stabilized Soil.....	44
2.9 Conclusions .....	45
<b>CHAPTER 3: EVALUATION OF COMPRESSIVE MODULI OF STABILIZED SUBGRADE DURING COMPACTION USING THE ICA .....</b>	<b>78</b>
3.1 Introduction .....	78
3.2 Background of Intelligent Compaction Methods .....	79
3.3 The University of Oklahoma Intelligent Compaction Analyzer (ICA).....	81
3.4 Methodology.....	83
3.4.1 Organization of the Field Investigation Plan .....	84
3.4.2 The ICA Calibration .....	85
3.4.3 The ICA Measurements.....	86
3.4.4 Identification and Remediation of Under-compacted Zones .....	87
3.4.5 Complementary Field Measurements and Validation of the ICA-Estimated Moduli .....	87
3.5 Case Study 1 (CS1): 60 <sup>th</sup> Avenue Northwest Project.....	88
3.5.1 Construction Site Identification.....	88
3.5.2 ICA Measurements and Identification of Test Stations.....	89
3.5.3 Validation of the ICA-Estimated Moduli .....	89
3.5.3.1 Validation with Laboratory Developed Regression Models .....	89
3.5.3.2 Validation with FWD Back-calculated Moduli.....	90
3.6 Case Study 2 (CS2): Apple Valley Project.....	91
3.6.1 Construction Site Identification.....	91
3.6.2 ICA Measurements and Identification of Test Stations.....	92
3.6.3 Validation of the ICA-Estimated Moduli .....	92
3.7 Case Study 3 (CS3): Main Street-Interstate 35 Intersection Project .....	93

3.7.1 Construction Site Identification.....	93
3.7.2 ICA Measurements and Identification of Test Stations.....	94
3.7.3 Identification and Remediation of Under-compacted Zones .....	96
3.7.4 Validation of the ICA-Estimated Moduli .....	96
3.7.5 Moduli Improvement Due to Remedial Compaction .....	97
3.8 Case Study 4 (CS4): Interstate 35 Service Road Project.....	98
3.8.1 Construction Site Identification.....	98
3.8.2 ICA Measurements and Identification of Test Stations.....	99
3.8.3 Identification and Remediation of Under-compacted Zones .....	100
3.8.4 Validation of the ICA-Estimated Moduli .....	101
3.8.4.1 Validation with Laboratory Developed Regression Models .....	101
3.8.4.2 Validation with DCP Indices .....	101
3.8.4.3 Validation with FWD Back-calculated Moduli.....	102
3.8.5 Moduli Improvement Due to Remedial Compaction .....	102
3.9 Conclusions .....	104
<b>CHAPTER 4: LABORATORY EVALUATION OF FLEXURAL</b>	
<b>    PROPERTIES OF STABILIZED SUBGRADE.....</b>	<b>128</b>
4.1 Introduction .....	128
4.2 Literature Review .....	130
4.2.1 Euler-Bernoulli Beam Theory.....	135
4.2.2 Fatigue Life Prediction Models.....	136
4.3 Materials and Mixture Combinations .....	140
4.3.1 Materials.....	140
4.3.2 Mixture Combinations .....	140
4.4 Methodology.....	141
4.4.1 Specimen Preparation .....	141
4.4.2 Laboratory Tests.....	143
4.4.2.1 Mr and UCS Tests .....	143
4.4.2.2 MoR Tests.....	144
4.4.2.3 FPFf Tests.....	145
4.5 Results and Discussion .....	147
4.5.1 Mr and UCS Tests .....	147
4.5.2 MoR Tests .....	150
4.5.3 FPFf Tests .....	153
4.5.4 Fatigue Life Prediction Model.....	157
4.5.4.1 Model Based on Compressive Properties .....	157

4.5.4.2 Model Based on Flexural Properties .....	158
4.6 Conclusions .....	160
<b>CHAPTER 5: EVALUATING THE APPLICABILITY OF EULER- BERNOULLI BEAM THEORY IN DETERMINING FLEXURAL PROPERTIES OF CHEMICALLY- STABILIZED SOIL.....</b>	<b>190</b>
5.1 Introduction .....	190
5.2 Concrete Damaged Plasticity Model in Abaqus.....	191
5.3 Creating the Finite Element Models .....	193
5.3.1 FE Model of UCS Test.....	193
5.3.2 FE Model of MoR Test.....	194
5.3.3 FE Model of FPF Test.....	195
5.4 FE Analysis Results and Discussion .....	197
5.4.1 UCS Test.....	197
5.4.2 MoR Test.....	198
5.4.3 FPF Test.....	200
5.5 Conclusions .....	201
<b>CHAPTER 6: CONSIDERATION OF FLEXURAL PROPERTIES OF CHEMICALLY-STABILIZED SUBGRADE IN MECHANISTIC-EMPIRICAL DESIGN OF SEMI-RIGID PAVEMENTS .....</b>	<b>213</b>
6.1 Introduction .....	213
6.2 Background of M-EPDG .....	215
6.3 Determining the Minimum Required Thickness of HMA Layer .....	220
6.3.1 Finite Element Model of Semi-Rigid Pavement Structure .....	221
6.3.1.1 Geometry of the Model.....	221
6.3.1.2 Layer Thicknesses .....	222
6.3.1.3 Material Properties.....	222
6.3.1.4 The FE Mesh and Boundary Conditions.....	223
6.3.1.5 Model Verification .....	224
6.3.2 Traffic Induced Tensile Strain at the Bottom of CSS Layer.....	225
6.3.3 Minimum Required Thickness of HMA Layer.....	226
6.4 Design of Semi-Rigid Pavement Using AASHTOWare.....	229
6.4.1 Selecting the Design Parameters.....	229
6.4.1.1 General Information, and Performance Criteria Inputs.....	229
6.4.1.2 Traffic Input .....	229
6.4.1.3 Climate Input .....	230

6.4.1.4 Pavement Structural Configuration and Material Properties .....	230
6.4.2 Designed Thicknesses of HMA Layer .....	231
6.5 Conclusions .....	235
<b>CHAPTER 7: SUMMARY, CONCLUSIONS, AND RECOMMENDATIONS ...</b>	<b>250</b>
7.1 Summary.....	250
7.2 Conclusions .....	253
7.2.1 Regression Models for $M_r$ .....	253
7.2.2 Calibration and Validation of ICA .....	255
7.2.3 Flexural Properties of Chemically-Stabilized Soil .....	256
7.2.4 Finite Element Model of Laboratory Tests .....	257
7.2.5 M-EPDG Analysis of Semi-Rigid Pavement .....	258
7.3 Recommendations .....	259
<b>REFERENCES .....</b>	<b>262</b>

## LIST OF TABLES

Table 2.1 Material Properties of Different Case Studies.....	48
Table 2.2 Test Combinations and Specimens' Characteristics for all Case Studies .....	49
Table 2.3 Test Sequence Used for Resilient Modulus Tests .....	50
Table 2.4 Summary of $M_r$ Values of Case Study 1 at 0-day Curing Period.....	51
Table 2.5 Summary of $M_r$ Values of Case Study 1 at 28-day Curing Period .....	51
Table 2.6 Back-calculated $k_1$ , $k_2$ and $k_3$ values for 0-, 7- and 28-day Curing Period...	52
Table 2.7 Calculated a, b and c values for 0-, 7- and 28-day Curing Period.....	53
Table 2.8 Summary of $M_r$ Values of Case Study 2 at 0-day Curing Period .....	54
Table 2.9 Summary of $M_r$ Values of Case Study 2 at 28-day Curing Period .....	54
Table 2.10 Summary of $M_r$ Values of Case Study 3 at 0-day Curing Period .....	55
Table 2.11 Summary of $M_r$ Values of Case Study 3 at 28-day Curing Period .....	56
Table 2.12 Summary of $M_r$ Values of Case Study 4 at 0-day Curing Period .....	57
Table 2.13 Summary of $M_r$ Values of Case Study 4 at 7-day Curing Period .....	58
Table 2.14 Summary of $M_r$ Values of Case Study 4 at 28-day Curing Period .....	59
Table 2.15 Characteristics and 28-day Regression Coefficients of the Additional Compacted Specimens of Soil from Case Study 3 .....	60
Table 2.16 Summary of $M_r$ Values of Additional Compacted Specimens of Case Study 3 at 28-day Curing Period .....	60
Table 3.1 Comparison of VSDRs Used in This Study with the VSDR used by Mooney and Rinehart (2002).....	106
Table 3.2 Moisture and Compaction Levels and the ICA-Estimated Modulus Values at Selected Test Stations of Case Study 1 .....	106
Table 3.3 Back-calculated $k_1$ , $k_2$ and $k_3$ Coefficients and Estimated $M_{r-0}$ at Selected Test Stations of Case Study 1 .....	107
Table 3.4 Back-calculated $k_1$ , $k_2$ and $k_3$ Coefficients and Estimated $M_{r-28}$ at Selected Test Stations of Case Study 1 .....	107
Table 3.5 Comparison between $M_{FWD-28}$ and Converted $M_{FWD-0}$ , and $M_{ICA}$ Values at Selected Test Stations of Case Study 1 .....	108
Table 3.6 Moisture and Compaction Levels, and the ICA-Estimated Modulus Values at Selected Test Stations of Case Study 2 .....	108
Table 3.7 Back-calculated $k_1$ , $k_2$ and $k_3$ Coefficients and Estimated $M_{r-0}$ at Selected Test Stations of Case Study 2 .....	109
Table 3.8 Back-calculated $k_1$ , $k_2$ and $k_3$ Coefficients and Estimated $M_{r-28}$ at Selected Test Stations of Case Study 2 .....	109

Table 3.9 Comparison between 28-day $M_r$ and Converted $M_{r-0}$ , and $M_{ICA}$ Values at Selected Test Stations of Case Study 2 .....	110
Table 3.10 Moisture and Compaction Levels, and the ICA-Estimated Modulus Values at Calibration and Random Points of Case Study 3 .....	110
Table 3.11 Influence of Remedial Compaction on the Dry Unit Weight and Modulus Values of the Soft Points of Case Study 3 .....	111
Table 3.12 Back-calculated $k_1$ , $k_2$ and $k_3$ Coefficients and Estimated $M_{r-0}$ at all Test Stations of Case Study 3 .....	112
Table 3.13 Back-calculated $k_1$ , $k_2$ and $k_3$ Coefficients and Estimated $M_{r-28}$ at all Test Stations of Case Study 3 .....	113
Table 3.14 Moisture and Compaction Levels, and the ICA-Estimated Modulus Values at Calibration and Random Points of Case Study 4 .....	114
Table 3.15 Influence of Remedial Compaction on the Dry Unit Weight and Modulus Values at the Soft Points of Case Study 4 .....	114
Table 3.16 Back-calculated $k_1$ , $k_2$ and $k_3$ Coefficients and Estimated $M_{r-0}$ at all Test Stations of Case Study 4 .....	115
Table 3.17 Back-calculated $k_1$ , $k_2$ and $k_3$ Coefficients and Estimated $M_{r-28}$ at all Test Stations of Case Study 4 .....	116
Table 3.18 Summary of DCP Test Results for Case Study 4 .....	117
Table 3.19 Summary of FWD Test Results for Case Study 4 .....	117
Table 4.1 Summary of Fatigue Life Prediction Models from the Literature .....	162
Table 4.2 Chemical Components of the CKD and Lime Used in the Study .....	163
Table 4.3 Combinations and Compaction Properties of Soil-Additive Mixtures .....	163
Table 4.4 Moisture and Compaction Properties of the Prepared Specimens .....	164
Table 4.5 Summary of $M_r$ Test Results for CKD-Stabilized Soil .....	166
Table 4.6 Summary of $M_r$ Test Results for Lime-Stabilized Soil .....	166
Table 4.7 Summary of Compressive Tests Results .....	167
Table 4.8 Summary of MoR Test Results .....	167
Table 4.9 Summary of FPF Test Results .....	167
Table 4.10 Fatigue Life and Flexural Properties of the Materials Used for Validating the Fatigue Prediction Model .....	168
Table 4.11 Comparison of Predicted Fatigue Lives using Different Models .....	169
Table 5.1 Material Parameters for CDP Model in Compression .....	203
Table 5.2 Material Parameters for CDP Model in Tension .....	204
Table 6.1 The Selected Layers Thicknesses for the Parametric Analysis .....	238
Table 6.2 Material Properties of the Finite Element Model .....	238

Table 6.3 Comparison between $\varepsilon_{t-CSS}$ ( $\mu\text{mm/mm}$ ) Achieved from KENLAYER (Solanki, 2010) and FE Analysis (Current Study).....	238
Table 6.4 Maximum Allowed $\varepsilon_{t-CSS}$ after Considering Shift Factor and Shrinkage...	239
Table 6.5 Minimum Required HMA Layer Thickness to Avoid CSS Fatigue .....	239
Table 6.6 Selected Performance Criteria for Pavement Design .....	239
Table 6.7 Design Traffic Configuration .....	240
Table 6.8 CSS Material Properties and Thickness Layer for Different Design Sections.....	241
Table 6.9 HMA Material Properties for Pavement Design .....	242
Table 6.10 HMA Designed Thicknesses for Different Pavement Sections .....	243

## LIST OF FIGURES

Figure 2.1 Resilient Modulus Test Setup inside the MTS Frame .....	61
Figure 2.2 Particle Size Distribution of the Subgrade Soils for Four Case Studies .....	61
Figure 2.3 Moisture-Dry Unit Weight Curve of Different Soil-Additive Mixtures.....	62
Figure 2.4 $M_r$ versus Stress Level for Case Study 1 (a) CM1, and (b) CM2 .....	62
Figure 2.5 Comparison Between Estimated and Laboratory Measured $M_{r-0}$ for Case Study 1 .....	63
Figure 2.6 Comparison Between Estimated and Laboratory Measured $M_{r-28}$ for Case Study 1 .....	63
Figure 2.7 Comparison Between Estimated $M_{r-0}$ Using $r_{28}$ Ratio and Laboratory Measured $M_{r-0}$ for Case Study 1 .....	64
Figure 2.8 $M_r$ versus Stress Level for Case Study 2 (a) CM1, and (b) CM2.....	65
Figure 2.9 Comparison Between Estimated and Laboratory Measured 0-day $M_r$ - Case Study 2.....	65
Figure 2.10 Comparison Between Estimated and Laboratory Measured $M_{r-28}$ for Case Study 2.....	66
Figure 2.11 Comparison Between Estimated $M_{r-0}$ Using $r_{28}$ Ratio and Laboratory Measured $M_{r-0}$ for Case Study 2.....	66
Figure 2.12 Comparison of Field Measured $w$ and $\gamma_d$ Values with $w$ and $\gamma_d$ of the $M_r$ Test Combinations and Specimens for Case Study 3 .....	67
Figure 2.13 $M_r$ versus Stress Level for Case Study 3 (a) CM1, (b) CM2, (c) CM3, (d) CM4, and (e) CM5 .....	69
Figure 2.14 Comparison Between Estimated and Laboratory Measured $M_{r-0}$ for Case Study 3.....	69
Figure 2.15 Comparison Between Estimated and Laboratory Measured $M_{r-28}$ for Case Study 3.....	70
Figure 2.16 Comparison Between Estimated $M_{r-0}$ Using $r_{28}$ Ratio and Laboratory Measured $M_{r-0}$ for Case Study 3.....	70
Figure 2.17 Conditioning of Soil-Quick Lime Mixture in the Laboratory.....	71
Figure 2.18 Comparison of Field Measured $w$ and $\gamma_d$ Values with $w$ and $\gamma_d$ of the $M_r$ Test Combinations and Specimens for Case Study 4 .....	71
Figure 2.19 $M_r$ versus Stress Level for Case Study 4 (a) CM1, (b) CM2, (c) CM3, (d) CM4, and (e) CM5 .....	73
Figure 2.20 Comparison Between Estimated and Laboratory Measured $M_{r-0}$ for Case Study 4.....	73
Figure 2.21 Comparison Between Estimated and Laboratory Measured $M_{r-7}$ for Case Study 4.....	74



Figure 2.22 Comparison Between Estimated and Laboratory Measured $M_{r-28}$ for Case Study 4.....	74
Figure 2.23 Comparison Between Estimated $M_{r-0}$ Using $r_7$ Ratio and Laboratory Measured $M_{r-0}$ for Case Study 4.....	75
Figure 2.24 Comparison Between Estimated $M_{r-0}$ Using $r_{28}$ Ratio and Laboratory Measured $M_{r-0}$ for Case Study 4.....	75
Figure 2.25 Influence of CKD Amount on the $M_{r-28}$ (at $\sigma_d = 68.9$ kPa and $\sigma_3 = 41.34$ kPa) of Stabilized Soil from Case Study 3 .....	76
Figure 2.26 Relationship Between $M_{r-28}$ (at $\sigma_d = 68.9$ kPa and $\sigma_3 = 41.34$ kPa) and UCS of all Specimens .....	76
Figure 2.27 Comparison Between $M_{r-28}$ Calculated from the Generic Model and the Laboratory Measured $M_{r-28}$ .....	77
Figure 3.1 (a) The ICA Equipped VSDR during Subgrade Compaction, and (b) Functional Schematic of the ICA for Stiffness Measurement (Commuri and Zaman, 2008).....	118
Figure 3.2 Location Measurement and Marking of Test Stations .....	119
Figure 3.3 Complementary Field Measurements on Compacted Subgrade, (a) NDG Measurements, (b) DCP Test, and (c) FWD Test.....	119
Figure 3.4 Case Study 1 Field Project Sketch and Positions of the Calibration Stretch and Test Stations.....	120
Figure 3.5 Correlation between Converted 0-day $M_{FWD}$ and $M_{ICA}$ for Case Study 1 ..	120
Figure 3.6 Case Study 2 Field Project Sketch and Positions of the Calibration Stretch and Test Stations.....	121
Figure 3.7 Correlation between Converted $M_{r-0}$ and $M_{ICA}$ for Case Study 2 .....	121
Figure 3.8 Physical Location of Case Study 3 Construction Project .....	122
Figure 3.9 Case Study 3 Field Project Sketch and Positions of the Calibration Stretch and Test Stations.....	122
Figure 3.10 Summary of NDG Measurements ( $w$ - $\gamma_d$ Relationship ) at Test Stations of Case Study 3 .....	123
Figure 3.11 Correlation between 0-day $M_r$ and $M_{ICA}$ for Case Study 3 .....	123
Figure 3.12 Improvement of Subgrade Moduli Due to Remedial Compaction at Soft Points of Case Study 3 .....	124
Figure 3.13 Physical Location of Case Study 4 Construction Project .....	124
Figure 3.14 Case Study 4 Field Project Sketch and Positions of the Calibration Stretch and Test Stations.....	125
Figure 3.15 Summary of NDG Measurements ( $w$ - $\gamma_d$ Relationship) at Test Stations of Case Study 4 .....	126
Figure 3.16 Correlation between 0-day $M_r$ and $M_{ICA}$ for Case Study 4 .....	126

Figure 3.17 Correlation between Inverse of DCP Index and $M_{ICA}$ for Case Study 4 ..	127
Figure 3.18 Improvement of Subgrade Moduli Due to Remedial Compaction at Soft Points of Case Study 4.....	127
Figure 4.1 Dry Unit Weight-Moisture Content Relationship for (a) CKD- stabilized Soil, and (b) Lime-stabilized Soil.....	170
Figure 4.2 Shape and Dimensions of (a) $M_r$ and UCS Test, (b) MoR Test, and (c) FPFf Test Specimens .....	171
Figure 4.3 Linear Kneading Compactor during Compaction of a Beam Specimen.....	171
Figure 4.4 MoR Test Setup (a) Schematic Sketch, and (b) Photographic View .....	172
Figure 4.5 (a) FPFf Fixture, and (b) ATM-100 Test Setup .....	173
Figure 4.6 $M_r$ versus Stress Level for CKD-Stabilized Soil (a) CKD5, (b) CKD10, and (c) CKD15 Specimens.....	174
Figure 4.7 $M_r$ versus Stress Level for Lime-Stabilized Soil (a) LM3, (b) LM6, and (c) LM9 Specimens .....	175
Figure 4.8 Mean $M_r$ Values for Different Soil-Additive Mixtures .....	176
Figure 4.9 Stress-Strain Curves from UCS Test on (a) CKD-Stabilized, and (b) Lime-Stabilized Soil.....	177
Figure 4.10 Effect of Additive Content on the UCS and Axial Strain at Failure of (a) CKD-Stabilized, and (b) Lime-Stabilized Soil .....	178
Figure 4.11 Relationship between Resilient Modulus and UCS Values of All Soil-Additive Mixtures .....	179
Figure 4.12 The Cracked Beam at the End of the MoR Test .....	179
Figure 4.13 Tensile Stress versus Tensile Strain at the Bottom of the CKD- Stabilized Beams during MoR Test (a) CKD5, (b) CKD10, and (c) CKD15 Specimens .....	180
Figure 4.14 Tensile Stress versus Tensile Strain at the Bottom of the Lime- Stabilized Beams during MoR Test (a) LM3, (b) LM6, and (c) LM9 Specimens .....	181
Figure 4.15 Effect of Additive Content on the MoR and Tensile Strain at Failure of (a) CKD-Stabilized, and (b) Lime-Stabilized Soil .....	182
Figure 4.16 Relationship between MoR and UCS Values of All Soil-Additive Mixtures .....	182
Figure 4.17 Relationship between $\varepsilon_{tf}$ (from MoR Test) and $\varepsilon_{af}$ (from UCS Test) for All Soil-Additive Mixtures .....	183
Figure 4.18 Flexural Stiffness versus Number of Load Cycles for (a) CKD5, (b) CKD10, and (c) CKD15 Specimens.....	184
Figure 4.19 Flexural Stiffness versus Number of Load Cycles for (a) LM3, and (b) LM6 Specimens.....	185

Figure 4.20 Flexural Stiffness versus Number of Load Cycles for (a) LM3, and (b) LM6 Specimens.....	186
Figure 4.21 Fatigue Life of Different Mixtures versus (a) $\varepsilon_{tf}$ , and (b) $\varepsilon_{af}$ .....	186
Figure 4.22 Relationship between Flexural Modulus and Fatigue Life .....	187
Figure 4.23 Relationship between Fatigue Life and $\varepsilon_{af}/M_r$ of Tested Specimens .....	187
Figure 4.24 Comparison between Laboratory Measured and Predicted (using Equation 4.20) Fatigue Life of Different Soil-Additive Mixtures .....	188
Figure 4.25 Predictability of Fatigue Life Prediction Model (Equation 4.20) for Different Soil-Additive Mixtures Including Data from Solanki (2010) and Arnold et al. (2012) .....	188
Figure 4.26 Predicted versus Measured Fatigue Life using Models Proposed by (a) Freeme et al. (1982) (b) Jameson et al. (1992), and (c) Austroads (2004) .....	189
Figure 5.1 Stress-Strain Terms of CDP Model in (a) Compression, and (b) Tension (Simulia, 2013) .....	205
Figure 5.2 Geometry and Mesh Configuration of FE Model of UCS Test .....	206
Figure 5.3 Geometry and Mesh Configuration of FE Model of MoR Test.....	206
Figure 5.4 (a) FPFF Test Fixture, and (b) Detail of Specimen Clamping Mechanism in FPFF Test Fixture (Hartman and Gilchrist, 2004) .....	207
Figure 5.5 Geometry and Mesh Configuration of FE Model of UCS Test .....	207
Figure 5.6 Comparison between UCS Stress-Strain Curves of FE Models and Experimental Results for (a) CKD5, (b) CKD10, (c) CKD15, (d) LM3, (e) LM6, and (f) LM9.....	208
Figure 5.7 Stress Distribution and Maximum Tensile Stress at x-direction of the FE Model of MoR Test for CKD15 Material.....	209
Figure 5.8 Comparison between MoR Stress-Strain Curves of FE Models and Experimental Results for (a) CKD5, (b) CKD10, (c) CKD15, (d) LM3, (e) LM6, and (f) LM9.....	210
Figure 5.9 Comparison between $\varepsilon_{tb}-\Delta U$ Curves from FE Models and Experimental Results for (a) CKD5, (b) CKD10, (c) CKD15, (d) LM3, (e) LM6, and (f) LM9.....	211
Figure 5.10 Strain Distribution in x-direction of the FE Model of FPFF Test for CKD5 Material .....	212
Figure 5.11 Comparison between $\Delta U_{200}$ Values Achieved from FE Model and LVDT Measurement for Different Materials.....	212
Figure 6.1 Dimensions and Mesh of the 3-D Finite Element Model of Semi- Rigid Pavement Structure .....	244
Figure 6.2 Standard Axle Load Application and Configuration of the Tire Contact Area .....	244

Figure 6.3 Deformed Shape of the Pavement Structure and the CSS Layer .....	245
Figure 6.4 Variation of $\epsilon_{t-CSS}$ for Different Thicknesses for HMA and CSS Layers with (a) CKD5, (b) CKD10, (c) CKD15, (d) LM3, (e) LM6, and (f) LM9 Material for CSS .....	246
Figure 6.5 Fatigue Crack Propagation Shift Factor for CSS Layer (Theyse et al., 1996).....	247
Figure 6.6 Designed HMA Layer Thicknesses for Different Pavement Sections.....	248
Figure 6.7 Influence of Using $M_f$ on Reduction of the Designed HMA Layer Thickness .....	249

## ABSTRACT

Chemical stabilization of subgrade soils is widely used at national and local levels to improve their engineering properties, including compressive and tensile strengths and stiffness (modulus). During the construction of the pavement layers, the last occasion of increasing the chemically-stabilized subgrade (CSS) quality (specifically, the modulus) is roller compaction. In this study, the application of the Intelligent Compaction Analyzer (ICA), developed at the University of Oklahoma, in quality control and quality improvement of CSS layers supporting asphalt pavements is addressed. It consisted of four case studies associated with four different pavement construction projects in Oklahoma involving compaction of stabilized subgrades. The soils and additives, i.e. cement kiln dust (CKD) and lime, were collected from the construction sites, processed and specimens of soil-additive mixtures prepared for laboratory resilient modulus ( $M_r$ ) tests, at different curing periods. Using the test results regression models were developed to estimate  $M_r$  of each soil-additive mixture based on the moisture content and dry unit weight. At each construction site, the CSS was compacted using an ICA-equipped smooth drum roller, and the ICA-estimated moduli for the construction stretch were recorded. The accuracy of the ICA-estimated moduli was evaluated using the aforementioned regression models and/or in-situ tests such as Dynamic Cone Penetrometer (DCP) and Falling Weight Deflectometer (FWD). The results from these case studies show that the ICA was able to estimate the modulus of the CSS with an accuracy suitable for the control of compaction quality. The ICA could estimate the moduli of the subgrade with an error of less than  $\pm 25\%$ , compared to laboratory results. The case studies demonstrated that the ICA was helpful in identifying and remediating the under-compacted regions. It was also

found that the average subgrade modulus and the overall uniformity of compaction could be improved with the use of the ICA.

In the Mechanistic-Empirical Pavement Design Guide (M-EPDG), the response of subgrade soils is represented in terms of  $M_r$ . However, using chemical stabilizers such as cement kiln dust (CKD) and lime, makes the flexural behavior of subgrades more dominant, compared to untreated subgrades. Vehicular traffic loading of a pavement with a CSS layer may result in a premature fatigue failure of the CSS layer and reflective cracking in the asphalt layers. In the present study, the flexural properties of chemically-stabilized soil were evaluated. Specimens of a lean clay soil mixed with different types and amounts of additive, namely 5%, 10% and 15% CKD and 3%, 6% and 9% lime (by weight), were prepared. Unconfined compressive strength (UCS) and  $M_r$  tests on cylindrical specimens, and modulus of rupture (MoR), flexural modulus and four point flexural fatigue (FPFF) tests on beam specimens were conducted. For flexural tests, the Euler-Bernoulli beam theory was used to determine the stress-strain behavior of the beams. The tested mixtures found to have relatively higher flexural moduli than their corresponding resilient moduli. Increasing additive amounts had a negative effect on fatigue performance of the stabilized subgrade soil, in general. Lightly-stabilized specimens showed the highest fatigue life among different mixtures. The results of the MoR and FPFF tests were used to develop a fatigue life prediction model based on such properties as flexural modulus, tensile strain at failure, and induced tensile strain at the bottom of the chemically-stabilized beam. In addition, the applicability of the Euler-Bernoulli beam theory in estimating the flexural characteristics of the chemically-stabilized beams was evaluated by creating three-dimensional finite element models of

MoR and FPF tests. The Euler-Bernoulli beam theory was found to have an acceptable accuracy in estimating the tensile strains at the bottom of the beam during these two tests.

In the next segment of the present study, design of semi-rigid pavements with regard to flexural properties of the CSS layer was conducted using the M-EPDG method. Three-dimensional finite element models of different pavement sections under a standard single axle load of 80 kN were developed. The thicknesses of the hot mix asphalt (HMA) and CSS layers, and the material used for the CSS layer were varied for different sections. The minimum required thickness of the HMA layer to avoid fatigue failure of the CSS layer was determined for different sections using the finite element analyses and the developed fatigue life prediction model. The final thickness of the HMA layer was designed using the M-EPDG software, namely AASHTOWare Pavement M-E Design. For each section, the M-EPDG analyses were conducted using both resilient modulus and flexural modulus for the CSS layer. For the CSS materials with relatively low fatigue lives (e.g., soils with 10% CKD and 15% CKD), the fatigue cracking of the CSS layer was found to be the most critical distress one should consider in designing the pavement structure. Using these mixtures in the CSS layer led to a thicker HMA layer, which may not be economically feasible. Using flexural modulus in the M-EPDG instead of resilient modulus, the designed HMA thickness was reduced. Other factors such as durability (e.g., wet-dry and freeze-thaw cycles), soil types, additive types, and cracking of CSS layer should be examined before the potential benefits of flexural modulus in designing semi-rigid pavements could be realized.

# CHAPTER 1

## INTRODUCTION

### 1.1 Background and Needs

The long term and short term performance of an asphalt pavement depends on the quality of the supporting layers, among other factors. The importance of the supporting layer's quality increases when its stiffness and strength increases (Schaefer et al., 2008). For semi-rigid pavements, where the aggregate base is replaced by the chemically-stabilized subgrade (CSS)<sup>1</sup>, the design and quality of the CSS layer has a vital role on the overall performance of the asphalt pavement. A properly designed, and well and uniformly compacted CSS layer would have high strength and stiffness, and high fatigue life to support the hot mix asphalt (HMA) layer under vehicular traffic loads (Van Niekerk et al., 2002; Commuri et al., 2014). Uniform compaction of the CSS layer to the desired level can assure the amenability to design considerations (Ganju et al., 2015).

Often, untreated soils at a construction site do not meet the strength and stiffness requirements for the subgrade layer. In such cases, it is a common practice to use chemically-stabilized subgrade (CSS) to support roadway pavements. Stabilization of subgrade soil using chemical additives such as cement kiln dust (CKD), lime and fly ash is widely used at national and local levels, in order to improve the engineering characteristics of the subgrade and to decrease the required thickness of the pavement

---

<sup>1</sup> Both “chemically-stabilized base” and “chemically-stabilized subgrade” (CSS) terms have been used in the literature for the stabilized layer of a semi-rigid pavement (Mallela et al., 2004; Hanley et al., 2013; and Solanki and Zaman, 2016). However, since the CSS is usually prepared by stabilizing the available untreated subgrade soil at the construction site, the term “chemically-stabilized subgrade” (CSS) is used in this study.



layers (Petry and Little, 2002; Parsons et al., 2004). Although a great deal of investigations has been performed to identify engineering properties of stabilized subgrade soils, there is a lack of knowledge relating the stabilized subgrade properties to the performance of pavements they support (Mandal, 2013). To address this weakness, in recent years, the American Association of State Highway and Transportation Officials (AASHTO) has developed a methodology for designing and analyzing pavement layers. This approach, called Mechanistic-Empirical Pavement Design Guide (M-EPDG), is aimed to improve the 1993 AASHTO Guide for Design of Pavement Structures.

Out of two important distress modes for stabilized subgrade soils, i.e. compression mode and flexural mode, the M-EPDG primarily addresses the compression mode in term of resilient modulus. However, the flexural performance of stabilized subgrade is considered an important factor in the overall function of pavements, which is not comprehensively addressed in the M-EPDG.

#### ***1.1.1 Chemical Stabilization of Subgrade Soil***

The most widely used chemical additives, also known as cementitious additives<sup>2</sup>, for subgrade stabilization in the United States are hydrated lime, class C fly ash (CFA), Portland cement, and cement kiln dust (CKD). The soil stabilization by the above-mentioned chemical additives is performed by pozzolanic reactions and cation exchange (Little and Nair, 2009). The reactions between lime, water, soil silica, and alumina that result in the formation of calcium-silicate-hydrates and calcium-aluminate-hydrates are referred to as pozzolanic reactions. While the cation exchange takes place

---

<sup>2</sup> Both “chemical additive” and “cementitious additive” terms have been used the literature for additives such as cement kiln dust, lime, cement and fly ash (Parsons et al. 2004). In this study the “chemical stabilization” term is used.

instantaneously, the rate of pozzolanic reaction is affected by soil pH (Malella et al., 2004; Rodd et al. 2004). Hydrated lime and CKD are two most widely used chemical additives in Oklahoma (ODOT, 2009a; Miller and Martha, 2012). Currently, the suggested percentages of additives by Oklahoma Department of Transportation (ODOT) for CKD, Portland cement and fly ash are discussed in the OHD L-50 document (ODOT, 2009b). The percent additive depends on the soil type, pH of soil-additive mixture, unconfined compressive strength (UCS) and maximum dry unit weight ( $\gamma_{dmax}$ ) of the stabilized soil (ODOT, 2009b; ASTM, 2006; and ASTM, 2008).

CKD is a by-product of the Portland cement manufacturing industry. The lime (CaO) content directly affects the cementitious properties of CKD. The coarser particles of CKD contain a higher percentage of free lime (Naik et al., 2003). Depending on the chemical composition, CKD can reduce the plasticity index (PI) and improve the unconfined compressive strength (UCS) of clay soils. In some cases, the shrinkage limits may increase to higher values than their respective optimum moisture contents. The most recognized advantage of application of CKD is to improve the UCS and stiffness of the treated soil (Parsons et al., 2004). With increased percentage of CKD, the pH and optimum moisture content ( $w_{opt}$ ) increases and the  $\gamma_{dmax}$  decreases (Miller and Azad, 2000).

Hydrated lime is a manufactured product from limestone, which is widely used to stabilize and modify subgrade, subbase, and base materials. Lime stabilization r the following important engineering properties of soil: improved strength; reduction in plasticity; improved workability; improved resistance to fracture, fatigue and permanent deformation; improved resilient properties; reduced swelling; and resistance to the

damaging effects of moisture (Little et al., 2000). The best performance of stabilization with lime is achieved in medium, moderately fine and fine grained soils (generally, soils with higher amounts of passing #40 Sieve) (Little, 1995).

### ***1.1.2 Compressive Performance of Stabilized Subgrade During Compaction***

Implementation of the M-EPDG requires strength and deformation parameters for critical performance assessment of the stabilized subgrade layer (ARA Inc., 2004). One of the important measures of performance to be considered in the design is the stiffness of the subgrade. In the M-EPDG, this stiffness is specified in terms of resilient modulus ( $M_r$ ). Hence, measuring  $M_r$  of subgrade layer is important for evaluation of the layer stiffness, which is an indicator of load carrying capacity of pavements. In general,  $M_r$  of stabilized subgrade is determined in a laboratory according to the AASHTO T307 (2004) test procedure. This test is generally conducted under a cyclic load in a triaxial chamber. For in-situ evaluation, many researchers have correlated  $M_r$  with the test results obtained from non-destructive devices, such as density gauges, Dynamic Cone Penetrometer (DCP), Light Weight Deflectometer (LWD), and Falling Weight Deflectometer (FWD) (Burnham 1997; Russell and Hossain 2000; Siekmeier et al. 2000; Davisch et al. 2006; and Nazzal and Mohammad 2010). There have been various attempts to estimate  $M_r$  as a function of soil properties, additive properties, stress state and moisture content (Santha, 1994; Mohammad et al., 1999; Amber and Quintus, 2002; Solanki et al. 2010; and Hossain et al. 2011).

The  $M_r$  of the subgrade soil can be improved by uniform compaction at a properly selected moisture content (Seed et al., 1962; Thompson, 1989; and Nazarian et al., 1996). Lack of adequate tools to determine the quality of compaction of the entire pavement in

a non-destructive manner is a leading factor in the early deterioration of pavements (Von Quintus et al., 1997; Master, 2003; Commuri et al. 2014; and Lin et al., 2015). Tools that can estimate the quality in real-time can help avoid over/under-compaction during the construction process. Improved quality of roads through real-time monitoring of construction quality for the entire pavement can minimize pavement distresses such as rutting, cracking and other forms of pavement distress, and improve the long-term performance of the pavement (Petersen, 2005; Zambrano et al., 2006; Maupin, 2007; Chang, 2011; and Commuri et al., 2014). Intelligent Compaction (IC) techniques have been proposed for continuous monitoring of quality of compaction. Some of these techniques also attempt to alter the machine parameters to ensure uniform compaction (Camargo et al. 2006; Chang et al. 2011). In the present study, the Intelligent Compaction Analyzer (ICA), developed at the University of Oklahoma, was used to estimate the moduli of CSS layer in four different pavement construction projects. The ICA-estimated moduli were compared and validated by the moduli determined by laboratory tests and/or other in-situ tests.

### ***1.1.3 Flexural Performance of Chemically-Stabilized Subgrade***

As mentioned in the previous section, currently, resilient modulus test is the only major test recommended by the M-EPDG for both stabilized (called bound materials) and non-stabilized (called unbound materials) base and subgrade soils (AASHTO, 2008; Baus and Stires, 2010). Although resilient modulus (under cyclic compressive stress type loading) of stabilized and natural subgrades are widely used by the state Department of Transportation (DOT), there is a need to study the stiffness characteristics of such materials under flexure.

Chemical stabilization improves the strength and stiffness of subgrade soils. An unintended consequence of such stabilization is increased potential for reduced fatigue life under flexure, particularly when the amount of additives exceeds certain levels (Thompson, 1966; Little, 2000; and Zhang et al. 2010). Increased brittleness is believed to be a major factor in reduced fatigue life. Chemically-stabilized subgrade (CSS) layer can be viewed as a relatively thin and stiff slab of a comparatively brittle material that is supported by underlying untreated soil or natural subgrade, which is a much softer material. Depending upon the level and uniformity of compaction of the supporting natural subgrade, importance of the flexural mode in a stabilized subgrade can vary. The flexural mode becomes particularly important when loss of natural subgrade occurs due to erosion and/or pumping. Under repetitive traffic load, fatigue cracks can develop at the bottom of the stabilized subgrade and propagate upward causing a fatigue failure. Because fatigue cracks form at the bottom and propagate upward, they are particularly problematic. Consequently, a cylindrical specimen tested for resilient modulus (as recommended by the M-EPDG) under compressive loads may not capture such flexural behavior of the stabilized layer (Freeme et al., 1982). With increased accumulated loading cycles, the flexural fatigue and cumulative damage of the stabilized layer can play an important role in crack initiation and propagation, and the overall design of pavements with CSSs.

For the aforementioned reasons, there is a need to investigate the flexural behavior of CSS soils under repetitive loads similar to those imposed by vehicular traffic. A review of published works reveals the lack of a rich body of knowledge on this topic. Hence, the present research aims to evaluate the influence of selected types and amounts of chemical

additives, namely hydrated lime and CKD, mixed with a lean clay soil from Oklahoma and to study the flexural behavior of the soil-stabilizer mixtures. Specifically, the flexural moduli (under cyclic loading) of chemically-stabilized beams, representing a CSS layer, and the number of cycles to failure (fatigue life) were studied in the laboratory using a four-point flexural fatigue (FPFF) test. The same stabilized subgrade soil was also evaluated for resilient modulus under compressive loading. The modulus in flexure was compared with the resilient modulus under compressive or cyclic triaxial loading. The other important flexural property of the stabilized subgrade soils, which is flexural strength (modulus of rupture), was evaluated using the modulus of rupture (MoR) test (under an increasing static load) for different soil-additive mixtures. A finite element model was developed and used to establish the appropriate strain level for FPFF testing. Finally, the flexural properties, especially the fatigue life of the stabilized subgrade soil were considered for designing a semi-rigid pavement structure with regard to the M-EPDG method.

## **1.2 Objectives**

The main goal of this research is to increase the cost-effectiveness of semi-rigid pavements by improving the quality, i.e., stiffness and uniformity, of the CSS layer during compaction, and also, by considering the flexural modulus and fatigue life of the CSS layer in the M-E design of pavements. The specific objectives of this study are as follows:

- Develop regression models to correlate the soil-additive mixture properties (moisture content and dry unit weight) with the resilient modulus of the chemically-stabilized specimens.

- Develop a generic model to predict  $M_r$  based on basic physical properties of soil-CKD mixture, such as 28-day UCS, degree of compaction, moisture content, and CKD content of the mixture, and plasticity index and clay content of the soil.
- Compare and validate the Intelligent Compaction Analyzer- (ICA-) estimated moduli with the developed regression models based on the laboratory test data, and traditional in-situ test results (FWD and DCP measurements).
- Evaluate influence of additive type and amount on the flexural properties, such as modulus of rupture, flexural modulus and fatigue life of chemically-stabilized soil, and compare them with compressive properties of the mixture.
- Develop a strain-based model for predicting the fatigue life based on tensile strain at failure, flexural modulus and induced tensile strain at the bottom of chemically-stabilized soil beam.
- Develop finite element models of selected laboratory tests and evaluate the applicability of Euler-Bernoulli beam theory in estimating the induced tensile strain at bottom of the chemically-stabilized beam.
- Evaluate the influence of considering flexural properties of the CSS layer, namely flexural modulus and fatigue life, on the overall design of the semi-rigid pavements using M-EPDG method.

### 1.3 Organization of the Dissertation

Following the introduction presented in Chapter 1, Chapter 2 describes the procedure for developing regression models for estimating  $M_r$  of chemically-stabilized

soil. The investigation consisted of four case studies associated with four different construction projects involving compaction of stabilized subgrades. The soils and additives (CKD and/or lime) were collected from the construction sites and laboratory  $M_r$  tests at different curing periods were conducted on the soil-additive mixtures. Using 80% of test data regression models were developed to estimate the  $M_r$  of each soil-additive mixture based on moisture content and dry unit weight. Finally, the experimental results from all four projects were used to develop a generic model to predict the  $M_r$  of CKD-stabilized soil based on the basic physical properties of the mixture. The validity of all models was evaluated using the remaining 20% data.

In Chapter 3, the developed regression models for resilient modulus were used to calibrate and validate the Intelligent Compaction Analyzer- (ICA-) estimated modulus during compaction of the chemically-stabilized subgrade (CSS) in the field. For this reason, field investigations, such as Nuclear Density Gauge (NDG), Dynamic Cone Penetrometer (DCP) and Falling Weight Deflectometer (FWD) measurements, were conducted at four different pavement construction projects. Also, for each construction project, the stabilized subgrade was compacted using ICA-equipped smooth drum roller, and the ICA-estimated moduli through the construction stretch were recorded. The validity of the ICA-estimated moduli was evaluated using the laboratory developed regression models and/or other in-situ tests.

Chapter 4 of this dissertation focuses on evaluating the flexural properties of chemically-stabilized soil. Specimens of a lean clay soil mixed with different types (CKD and hydrated lime) and amounts of additive were prepared, and compressive and flexural tests were conducted on these specimens. Unconfined compressive strength (UCS) and



resilient modulus ( $M_r$ ) tests on cylindrical specimens, and modulus of rupture (MoR), flexural modulus and four point flexural fatigue (FPFF) tests on beam specimens were conducted. Specifically, the influence of the tensile strain at failure on the fatigue life of the specimens was studied. A fatigue life prediction model was developed based on flexural modulus, tensile strain at failure and induced tensile strain at the bottom of the chemically-stabilized beam. Using data available in the literature, the validity of the fatigue life model was evaluated.

Chapter 5 is devoted to creating three-dimensional finite element models of UCS, MoR and FPFF tests. The plastic stress-strain behavior of the materials was simulated using a material model, namely concrete-damaged plasticity. The results from the finite element analyses were compared with the experimental results. The vertical displacement of the middle-center of the beams determined by finite element analyses was compared with the ones from experimental results. Using this comparison, the applicability of the Euler-Bernoulli beam theory in estimating the flexural characteristics of the chemically-stabilized beams was evaluated

In Chapter 6, design of semi-rigid pavements with regard to flexural fatigue life of the CSS layer was conducted using M-EPDG method. Three-dimensional finite element models of different pavement sections under a standard 80 kN single axle load were developed. The thicknesses of HMA and CSS layers, and the material used for CSS layer were varied for different sections. The minimum required thickness of HMA layer to avoid fatigue failure of the CSS layer was determined for different sections using the finite element analyses and the fatigue life prediction model developed in the previous chapter. The final thickness of the HMA layer was designed using the M-EPDG software,

namely AASHTOWare Pavement M-E Design. For each section, the M-EPDG analyses were conducted using both resilient modulus and flexural modulus for the CSS layer. Finally, the influence of moduli type (resilient or flexural) on the design HMA layer thickness was evaluated.

Chapter 7 presents the summary and conclusions of this study, as well as recommendations for future studies.

## CHAPTER 2

### DEVELOPMENT OF REGRESSION MODELS FOR ESTIMATING RESILIENT MODULI

#### 2.1 Introduction

Asphalt pavements are subjected to long-term frequent stresses/strains during their service lives. These stresses/strains are generally caused by vehicular loads and environmental factors (Molenaar, 1993; Cebon, 1999; and Huang, 2004). Vehicular loads are imposed on the pavement surface through the footprints of tires. Depending on the structure of the pavement (number of layers, thicknesses and moduli), vehicular weight, axle configuration, speed and other factors, the stress levels are different at different depths within the pavement structure and the underlying subgrade. Due to the repetitive nature of traffic loads and relatively low range of stresses in layers beneath the hot mix asphalt (HMA) layer(s), plastic deformations of these layers can be neglected after a certain number of repetitions (Ping and Ling, 2007). The concept of resilient modulus used widely in designing pavements is based on this major assumption (Yoder and Witczak, 1975; Elliot and Thornton, 1988). Therefore, laboratory testing of stress-strain behavior of subgrade soils within the resilient strain limits are important to pavement design and maintenance.

In the mechanistic-empirical design of asphalt pavements, the response of subgrade soils is represented in terms of resilient modulus ( $M_r$ ). During construction, it is important to compact subgrade soils sufficiently so that the subgrade moduli meet or exceed the design  $M_r$ . Subgrade compaction quality for the entire pavement is essential to avoiding distresses such as rutting, fatigue, and potholes during the service life of the

pavement, particularly during the early years of service life. Implementation wise, an accurate estimation of the subgrade moduli during compaction in the field is an important element of the quality control process.

Usually, in a pavement construction project involving chemically-stabilized subgrade soils, the two important factors governing the compaction quality are moisture content and dry density or unit weight. Therefore, if the moduli of the chemically-stabilized subgrade layer could be formulated in terms of moisture content and dry unit weight, the  $M_r$  of the compacted layer can be estimated during construction at the site. In this chapter, the development of the regression models developed in this study for the estimation of  $M_r$  is discussed, along with four case studies used to examine the predictability of these models.

## 2.2 Background and Literature Review

Resilient modulus is defined as the ratio of the cyclic deviator stress to the resilient (recoverable) strain with the following expression:

$$M_r = \frac{\sigma_d}{\varepsilon_r} \quad (2.1)$$

where,  $\sigma_d$  = cyclic deviatoric stress, and  $\varepsilon_r$  = recoverable or resilient strain. Seed et al. (1964) conducted repeated load triaxial tests on subgrade soils to investigate resilient characteristics. In 1986, the AASHTO Guide for Design of Pavement Structures specified resilient modulus for determining the coefficients of base, subbase and subgrade layers as an input in designing flexible pavements. Also, AASHTO T274 was introduced as the standard test protocol for measuring resilient modulus (Pederson, 2007). As noted by Kim et al. (2001), resilient modulus of subgrade soils is an important property in the analysis

and design of flexible pavements. In fact, resilient modulus is also a key parameter in the newest Mechanistic-Empirical Pavement Design Guide (M-EPDG) (AASHTO, 2004), which is currently used by most states' Department of Transportation (DOTs) for designing flexible pavements. It provides a rational measure of stiffness of compacted subgrade soils under different conditions, namely moisture content, compaction level and stress level.

Influence of different parameters or factors on resilient modulus of pavement materials has been studied by many researchers (Seed et al., 1962; Tuncer and Basma, 1991; Drumm et al., 1997; Zhu et al., 1999; Witczak et al., 2000; Puppala et al., 2003; Khoury and Zaman, 2004; Khoury et al., 2009; Solanki, 2010; Khoury et al., 2013; Mandal, 2014; and Pinilla et al., 2016). The investigations on the influence of moisture content of fine grained subgrade soils show that increasing moisture content, beyond a certain level, reduces  $M_r$  (Drumm et al., 1997; Khoury and Zaman, 2004; and Khoury et al., 2009). Khoury et al. (2013) investigated the effect of increase in moisture content on the resilient modulus of CFA-stabilized soil. It was reported that an increase in compaction moisture content had a negative effect on resilient modulus, meaning it reduced the modulus. Witczak et al. (2000) also noted that compaction moisture content negatively affects the resilient modulus by increasing the pore water pressure and weakening the cementitious bonds between clay particles.

Previous studies have shown that a higher level of compaction leads to a higher  $M_r$ , when the moisture content is relatively low (Seed et al., 1962; Thompson, 1989; and Nazarian et al., 1996). Increasing compaction levels under high moisture contents, however, have an adverse effect on  $M_r$  (Seed et al., 1962; Butalia et al., 2003; and Titi et

al., 2006). This can be justified by the increase in degree of saturation of the specimen due to a reduction in void volume and consequently an increase in the ratio of the water volume to the void volume. Khoury and Zaman (2004) reported a reduction in subgrade resilient modulus due to an increase in compaction moisture content, beyond certain level.

The influence of curing time on modulus of chemically-stabilized soil has been studied by many researchers (Tuncer and Basma, 1991; Zhu et al., 1999; Puppala et al., 2003; Solanki, 2010; Mandal, 2014; and Pinilla et al., 2016). All of these and other studies have reported an increase in resilient modulus due to increased curing time.

Thompson (1966), Little et al. (1994), and Toohey et al. (2013) described linear relationships between unconfined compressive strength (UCS) and resilient modulus of stabilized soils. The relationship between  $M_r$  of subgrade soils with such parameters as particle size distribution (Solanki et al., 2009; Ebrahimi et al., 2012) and amount of stabilizing agent (Zhu et al., 1999; Solanki et al., 2009), and chemical properties of stabilizing agent (Solanki et al., 2009) were of interest to many of these researchers. For example, Solanki et al. (2009) studied the influence of different types, i.e., cement kiln dust (CKD), lime and class C fly ash (CFA), and percentages of additives on resilient modulus of four different types of soil. For all of these additives, an increase in the percentage of stabilizer resulted in an increase in  $M_r$ . The highest enhancement of  $M_r$  was achieved by adding 15% CKD.

Attempts have been made to directly estimate  $M_r$  of subgrade soils from physical and strength properties of soils, for a specific stress level (Thompson and Robnett, 1979; Carmichael and Stuart, 1985; Elliot and Thornton, 1988; Drumm et al., 1990; Farrar and Turner, 1991; and Rahim and George, 2004). However, these models do not consider the

stress dependency of  $M_r$  of subgrade soil (Ozel and Mohajerani, 2011). Several models have been suggested in the literature correlating resilient modulus of pavement materials with stress levels (Hicks and Monismith, 1971; Thompson and Robnett, 1979; Rada and Witczak, 1981; Shook et al., 1982; Witczak and Uzan, 1988; AASHTO, 1993; NCHRP, 1997; Witczak, 2000; AASHTO, 2002; AASHTO, 2004, Andrei et al., 2004; and Khoury and Zaman, 2007). The following log-log model was suggested in the AASHTO design guide (1993):

$$M_r = k_1 p_a \left( \frac{\theta}{p_a} \right)^{k_2} \left( \frac{\sigma_d}{p_a} \right)^{k_3} \quad (2.2)$$

where,  $p_a$  = atmospheric pressure (101.283 kPa),  $\sigma_d$  = cyclic deviatoric stress acting on the material,  $\theta$  = bulk stress (sum of three principal stresses), and  $k_1$ ,  $k_2$  and  $k_3$  = regression coefficients.

Another log-log model recommended by the NCHRP (1997) is given below:

$$M_r = k_1 p_a \left( \frac{\sigma_3}{p_a} \right)^{k_2} \left( \frac{\sigma_d}{p_a} \right)^{k_3} \quad (2.3)$$

where,  $\sigma_3$  = confining pressure.

A semi-log model was suggested by Andrei et al. (2004), with the following expression:

$$M_r = k_1 p_a k_2 \left( \frac{\sigma_3}{p_a} \right) k_3 \left( \frac{\sigma_d}{p_a} \right) \quad (2.4)$$

AASHTO (2004) has suggested the following log-log model, which is recommended by the new M-EPDG, for unbound materials:

$$M_r = k_1 p_a \left( \frac{\theta}{p_a} \right)^{k_2} \left( \frac{\tau_{oct}}{p_a} + 1 \right)^{k_3} \quad (2.5)$$

where,  $\tau_{oct}$  = octahedral shear stress acting on the material.

Different regression models have been suggested in the literature for determining the regression coefficients  $k_1$ ,  $k_2$  and  $k_3$  by using different material properties such as chemical and physical index properties (Santha, 1994; Mohammad et al., 1999; Amber and Quintus, 2002; Solanki et al., 2010; and Hussain et al., 2011). These models were developed using multiple linear regression analyses. Except for the study conducted by Solanki et al. (2010), no other studies could be found to correlate  $k_1$ ,  $k_2$  and  $k_3$  to soil and additive properties of chemically-stabilized soil together. In the present study, the resilient modulus of the stabilized subgrade is evaluated by conducting  $M_r$  tests on the materials collected from the field from a number of construction projects. These test data are used to develop regression models for predicting  $M_r$ , and these models were used to estimate field  $M_r$ , as a compaction quality control tool, as part of OU's development of the Intelligent Compaction Analyzer (ICA) technology.

### **2.3 Methodology**

The principal purpose of development of regression models for estimating  $M_r$  was to calibrate and validate the ability of the Intelligent Compaction Analyzer (ICA) to give a real-time estimate of stabilized subgrade moduli during compaction. The methodology presented in this chapter is a part of the methodology used for validation of the ICA. The procedure for application of the ICA during compaction of stabilized subgrades and validation of the ICA-measured moduli is explained in Chapter 3.



### ***2.3.1 Site Selection for Case Studies and Material Collection***

The project consisted of four case studies associated with four different construction projects involving compaction of stabilized subgrades. These case studies are listed as follows:

- Case Study 1 (CS1): 60<sup>th</sup> Avenue Northwest Project
- Case Study 2 (CS2): Apple Valley Project
- Case Study 3 (CS3): Main Street-Interstate 35 Intersection Project
- Case Study 4 (CS4): Interstate 35 Service Road Project

All of these sites are located in Oklahoma. In all of these projects, the subgrade soil was stabilized with CKD. Additional treatments were done in some projects. For the CS4 project, the subgrade was pre-treated with quick-lime 14 days prior to stabilization with CKD. Falling Weight Deflectometer (FWD) tests were conducted at the CS1 and CS4 sites seven days and 28 days after subgrade compaction. Also, Dynamic Cone Penetrometer (DCP) measurements were taken at the CS4 site on the day of compaction. The procedure of the field investigations, including the FWD and DCP testing, and the results obtained from these tests are discussed in Chapter 3.

For CS1 and CS2, conducting resilient modulus tests in the laboratory and developing the related regression models were done before the beginning of construction, while for CS3 and CS4, the resilient modulus tests and development of regression models were done after the field compaction due to changes in project schedules.

Materials were collected for laboratory testing from each of these sites. The materials collection included bulk subgrade soils and chemical additives. The collected materials were brought to OU Broce Laboratory for testing. The bulk soils were air dried,

broken into small pieces using a drum processor (Commuri et al., 2014), and then passed through a standard No. 4 Sieve and stored in sealed buckets. The chemical additives were placed in two layers of air sealed plastic bags and kept in sealed buckets. The particle size distribution (ASTM D422, 2007) and Atterberg limit (ASTM D4318, 2010) tests were performed on the collected soils to classify them based on the Unified Soil Classification System (USCS) (ASTM D2487, 2011) and AASHTO Soil Classification System (AASHTO M145, 2000). The particle size distribution was determined from the percentages of soils passing through the following US Standard sieves: 4, 10, 40, 60, 100 and 200. To determine the fractions of clay (percent finer than 0.002 mm) and silt percent (coarser than 0.002 mm and finer than 0.075 mm), hydrometer tests were conducted on soils according to ASTM D422 (2007). The specific gravity of each soil was determined using a pycnometer test (ASTM D845, 2014). Also, the standard Proctor test was carried out on the soil mixed with the same amount and type of chemical additive, as used in the field, according to ASTM D698 (2012). The properties of stabilized subgrade soil attributed to each case study are provided in Table 2.1.

### ***2.3.2 Specimen Preparation and Resilient Modulus Testing***

Cylindrical specimens of stabilized soil were prepared for conducting resilient modulus tests in the laboratory. The amount of chemical additive for each case study was selected in accordance with the subgrade soil-additive mixture design for the associated construction project. To cover the variations of moisture content ( $w$ ) and dry unit weight ( $\gamma_d$ ) of compacted subgrade soils in the field, different combinations of these two parameters were selected for each case study. The specimens were prepared with the

designated soil type, additive amount,  $w$  and  $\gamma_d$ . Table 2.2 shows different  $w$ - $\gamma_d$  combinations designated to each case study.

For all of the specimens, the virgin soil was mixed with a specific amount of additive. The amount of additive was added based on the dry weight of the soil. The additive and soil were mixed manually to attain uniformity. After the blending, half of the required water, based on the target moisture content, was added to the soil-additive mixture and mixed thoroughly. Then, the remaining water was added and mixed again until a uniform mixture was achieved. For preparing the specimens for resilient modulus test, the soil-additive mixture was compacted in a mold of 101.6 mm diameter and 203.2 mm height. Each specimen was compacted in five layers of equal mass and thickness (40.6 mm). Each layer was compacted using a standard Proctor hammer until the target  $\gamma_d$  was achieved. The number of blows per layer varied between 15 and 36, depending on the target  $w$  and  $\gamma_d$  of each specimen. After compaction of the last layer, the remaining mixture, as the representative of the compacted specimen, was oven-dried to estimate the  $w$  of the compacted specimen. For evaluating the accuracy of this estimation, extra specimens were compacted, as needed. Both the extra specimens and their representative mixtures were oven-dried. A comparison between  $w$  of the extra specimens and  $w$  of the representative mixtures showed less than 0.05% error in estimation of  $w$ . Hence, the measured  $w$  of the representative mixtures were reported as  $w$  of the specimens. The dry unit weight of each specimen was calculated according to the measured weight and dimensions, and the moisture content. The prepared specimens were named as  $CSi$ - $CMj$ - $\#k$ , where,  $CSi$  is the  $i^{\text{th}}$  case study,  $CMj$  is the  $j^{\text{th}}$  combination, and  $k$  is the number of specimen (see Table 2.2).

The resilient modulus tests were performed on compacted specimens in accordance with the AASHTO T307 (2004) test method using the Material Testing System (MTS) machine shown in Figure 2.1. Accordingly, a total of 15 stress sequences were applied to the compacted specimens using a cyclic haversine-shaped load pulse with a loading period of 0.1 second and a rest period of 0.9 second. The configuration of the test sequences is shown in Table 2.3. The required load was applied using a 22.3 kN internal load cell.

The vertical displacements were measured using two loose core linear variable differential transformers (LVDTs) attached by aluminum clamps to the specimens and placed inside the cell (Figure 2.1). The required confining pressure was applied using an air compressor via a brass port. The resilient modulus for each sequence was calculated from the average recoverable strain and average deviatoric stress from the last five cycles using Equation 2.1.

Resilient modulus tests were conducted for two different curing periods. The first set of tests were conducted immediately after the compaction. These test results were referred to as the resilient modulus at 0-day curing period, or simply 0-day  $M_r$  ( $M_{r-0}$ ). The  $M_{r-0}$  tests were aimed to simulate the subgrade compaction in the field. It should be noted that the changes in modulus of the compacted stabilized subgrade/ specimen is fast in the first few hours, after mixing with water and compaction. Accordingly, to simulate the field conditions, the time span between the specimen compaction and  $M_{r-0}$  test in the laboratory was selected approximately equal to the time span between water springing and final compaction in the field. The time span varied between 10 minutes to 45 minutes, depending on the construction project site. After the completion of the 0-day test,

specimens were cured at a temperature of  $23 \pm 2$  °C and a relative humidity of approximately 96% for 28 days and then tested for 28-day resilient modulus ( $M_{r-28}$ ). For CS4 (Interstate 35 Service Road Project) additional resilient modulus tests were performed at 7 days of curing period ( $M_{r-7}$ ). The  $M_{r-7}$  values were aimed at comparing the laboratory  $M_r$  with the FWD moduli measured in the field seven days after the compaction of subgrade.

### ***2.3.3 Developing Regression Models for $M_r$***

Estimating the subgrade moduli using the ICA requires regression models for each case study site. These models were developed separately for each study site. In the first step, 80% of laboratory test data were used to develop the models. For this reason, the measured  $M_r$  values of each specimen at all 15 sequences were considered. The empirical model suggested by AASHTO (1993) (Equation 2.2) was used to estimate the  $M_r$  values as a function of stress level:

$$M_r = k_1 p_a \left( \frac{\theta}{p_a} \right)^{k_2} \left( \frac{\sigma_d}{p_a} \right)^{k_3} \quad (2.2)$$

Using this model, the coefficients  $k_1$ ,  $k_2$ , and  $k_3$  were determined for each specimen. As stated previously, for a specific case study, the specimens were prepared using different moisture contents and dry unit weights, as listed in Table 2.2. Considering the calculated coefficients for all of the specimens, three regression equations were developed for calculating  $k_1$ ,  $k_2$ , and  $k_3$  values as a function of  $w$  and  $\gamma_d$ . As suggested by previous researchers (Santha, 1994; Mohammad et al., 1999; Amber and Quintus, 2002; Solanki et al., 2009; and Hussain et al., 2011), a multiple linear regression model was considered for evaluating  $k_1$ ,  $k_2$ , and  $k_3$  as follows:

$$k_n = a + b (w) + c (\gamma_d) \quad (2.6)$$

where,  $k_n$  can be  $k_1$ ,  $k_2$ , or  $k_3$ ; and  $a$ ,  $b$  and  $c$  are the regression constants for each  $n = 1, 2$  and  $3$ . It should be noted that other forms of model, such as polynomial regression model, were tried also for evaluating  $k_1$ ,  $k_2$ , and  $k_3$ . However, the multiple linear regression produced the best correlation. Having the constants  $a$ ,  $b$  and  $c$  evaluated for each  $k_n$ , the model was validated using the remaining 20% of the laboratory test data. Accordingly,  $w$  and  $\gamma_d$  values corresponding to each laboratory specimen were used in Equation 2.6 and regression coefficients  $k_1$ ,  $k_2$ , and  $k_3$  values were determined. The regression coefficients, thus, determined were used in Equation 2.2 to estimate the resilient modulus for a given combination of deviatoric stress and confining pressure. The estimated  $M_r$  values were compared with the laboratory  $M_r$  test results.

#### ***2.3.4 Developing 0-day to 7-day and 28-day $M_r$ Conversion Models***

Since the ICA measurements were taken on the day of compaction (0-day), to have a better prediction of the resilient modulus after 28 days of curing, conversion models were developed using the laboratory test data. In this regard, it may be noted that in the new M-EPDG,  $M_{r-28}$  of chemically-stabilized material is a required input parameter for the design of flexible pavements (AASHTO, 2004). A correlation between  $M_{r-28}$  and  $M_{r-0}$  can be used to verify if the ICA is able to predict  $M_{r-28}$  during the construction of the subgrade. For this reason, the relationship between  $M_{r-28}$  and  $M_{r-0}$  was modeled as a function of stress level, moisture content, dry unit weight and  $M_{r-0}$  using regression analysis. A similar method was deployed to find a relationship between  $M_{r-7}$  and  $M_{r-0}$  for CS4; FWD tests were conducted at this site seven days after the

compaction of subgrade. These models are aimed to formulate a ratio of the  $M_{r-28}$  to  $M_{r-0}$ , called  $r_{28}$  here, and the ratio of the  $M_{r-7}$  to  $M_{r-0}$ , called  $r_7$  in this study.

### ***2.3.5 Developing a Generic Model for 28-day $M_r$ of CKD-stabilized Soil***

The laboratory test data for soils collected from the case study sites were used to develop a model by which  $M_{r-28}$  of the soil-CKD mixture could be estimated. The general form of the equations and basic properties used for generating the model were selected according to the model suggested by Solanki et al. (2010). Since only one type of chemical additive (CKD) was used in the current study, the following properties were selected:

- Unconfined compressive strength of the specimen after 28 days of curing (UCS),
- Moisture content and dry unit weight of the specimen,
- Plasticity index and clay content of the soil, and
- CKD content of the mixture.

To study the influence of CKD amount on the resilient modulus,  $M_{r-28}$  tests were conducted on specimens for one type of soil (from CS3) mixed with three selected amounts (5%, 10% and 15% by soil weight) of CKD.

UCS tests were conducted on all specimens after completion of  $M_{r-28}$  test in accordance with the ASTM D2166 (2000) test method, having a loading rate of 0.02 mm/sec. The tests were terminated after failure of specimens. The resulting stress-strain curves were plotted to determine the UCS.

## **2.4 Case Study 1 (CS1): 60<sup>th</sup> Avenue Northwest Project**

### ***2.4.1 Site Location and Material Collection***

The first case study site was located on the 60<sup>th</sup> Avenue Northwest, Norman, OK, between Tecumseh Road and Franklin roads. The construction at this site was carried out between May 2012 and June 2012. The subgrade soil was stabilized by mixing 10% CKD to a depth of 202 mm. In this project FWD tests were conducted one month after construction of the stabilized subgrade layer.

Bulk subgrade soil and CKD samples were collected from the construction site, as indicated earlier. The gradation of the soil was determined and plotted (Figure 2.2) using sieve analysis and hydrometer test data. The percentage passing through No. 200 (75  $\mu$ m) sieve was 79.3. The liquid limit (LL), and plasticity index (PI) of the virgin soil were found to be 23%, and 4%, respectively. The soil was classified as CL-ML (silty lean clay) according to USCS and as A-4 as per AASHTO soil classification. The optimum moisture content ( $w_{opt}$ ) and maximum dry unit weight ( $\gamma_{dmax}$ ) of the soil with 10% CKD mixture were found as 14.6% and 17.3  $kN/m^3$ , respectively. The  $w$ - $\gamma_d$  curve of the soil-CKD mixture is plotted in Figure 2.3. According to the pycnometer test the specific gravity of the mixture was 2.71 (see Table 2.1).

### ***2.4.2 Test Combinations and Resilient Modulus Testing***

Similar to the soil-CKD mixture at the construction site, the laboratory specimens were prepared by adding 10% CKD by weight of the dried soil. Two  $w$ - $\gamma_d$  combinations were selected, namely CM1 and CM2. The target degree of compaction was 100% ( $\gamma_d = \gamma_{dmax}$ ) for both combinations. The target moisture content was  $w_{opt} - 2\%$  for the first



combination (CM1) and  $w_{opt}$  for the second combination (CM2). Three cylindrical specimens were compacted for each combination (moisture content). The characteristics of the prepared specimens are represented in Table 2.2. It can be seen that the moisture contents achieved for these specimens varied between  $w_{opt} - 2.5\%$  and  $w_{opt} - 0.2\%$ , and the degree of compaction had a range of 97% to 99%.

Resilient modulus tests were conducted on the prepared specimens at 0-day curing period followed by 28 days of curing in an environmental chamber (at a temperature of  $23 \pm 2$  °C and a relative humidity of 96% approximately) and resilient modulus testing. The  $M_r$  test results for all specimens at different test sequences are presented in Table 2.4 for 0-day and in Table 2.5 for 28-day curing periods. The results associated with one of the specimens (specimen CS1-CM2-#2 in Table 2.3) were not reported due to breakage of the specimen. The breakage, which was scarcely visible in the form of a crack in the middle of the specimen, could have occurred during placing the specimen on the platen. Since the breakage was detected few days before the actual subgrade compaction in the field, a substitute specimen could not be prepared. The mean  $M_r$  value for three specimens for each combination is plotted in Figure 2.4. The increase in resilient modulus value due to 28 days of curing is evident from Figure 2.4. Similar observations have been reported in previous studies (Mitchell and Shen, 1967; Achampong et al., 1997). As expected, the  $M_r$  values decreased with the increase in the deviatoric stress. It can also be seen that at higher confining pressures, specimens exhibited a higher  $M_{r-0}$ . For specimens compacted at  $w_{opt}$  (CM2), the influence of confining pressure is more than that of those which were compacted at  $w_{opt} - 2\%$  (CM1). The  $M_{r-28}$  of the specimens showed very small sensitivity towards changes in confining pressure.

### 2.4.3 Developing Regression Models for $M_r$

As noted earlier, regression models were developed based on the laboratory resilient modulus test results as a function of  $w$ ,  $\gamma_d$  and stress level. These models were developed using 80% of all test data. These data were selected randomly. Equation 2.2 was used for modeling the resilient modulus based on the stress level. Having the resilient modulus of all specimens at different stress levels, the regression coefficients  $k_1$ ,  $k_2$  and  $k_3$  in Equation 2.2 were back-calculated using the Minitab numerical analysis tool (Table 2.6). Then, the coefficients  $k_1$ ,  $k_2$  and  $k_3$  were formulated as a function of  $w$ ,  $\gamma_d$  (Equation 2.6) and constants  $a$ ,  $b$  and  $c$  were evaluated for each of  $k_1$ ,  $k_2$  and  $k_3$  using linear regression analysis (Table 2.7). The regression models for calculating  $k_1$ ,  $k_2$  and  $k_3$  values are given as follows:

For 0-day curing period:

$$k_1 = -53060.478 - 482.317(w) + 3790.046(\gamma_d) \quad (2.7)$$

$$k_2 = -0.467 + 0.034(w) + 0.008(\gamma_d) \quad (2.8)$$

$$k_3 = -2.553 - 0.052(w) + 0.175(\gamma_d) \quad (2.9)$$

For 28-day curing period:

$$k_1 = 203060.877 + 410.151(w) - 10565.166(\gamma_d) \quad (2.10)$$

$$k_2 = -2.547 - 0.006(w) + 0.151(\gamma_d) \quad (2.11)$$

$$k_3 = -0.402 - 0.0149(w) + 0.033(\gamma_d) \quad (2.12)$$

Using these equations, the regression coefficients  $k_1$ ,  $k_2$  and  $k_3$  at 0-day and 28-day curing periods could be estimated having  $w$  and  $\gamma_d$  of the specimen. Consequently, by using the estimated  $k_1$ ,  $k_2$  and  $k_3$  in Equation 2.2, resilient modulus of each specimen

could be estimated at a given stress level. Using this method, the resilient moduli were estimated for all specimens at different stress levels, including the remaining 20% of the data. Then, the estimated  $M_r$  values were compared with the laboratory measured  $M_r$  values.

Figures 2.5 and 2.6 show a comparison between estimated and laboratory measured  $M_r$  values for 0- and 28-day curing periods, respectively. All data points, including the data used for developing the model (80% of the data) and the data used for validating the model (20% of the data), are presented in Figures 2.5 and 2.6. It can be seen in Figure 2.5 that the predictability of model for 0-day curing period is quite good with a  $R^2 = 0.81$  (for the data used to validate the model) and an error within  $\pm 15\%$ . For 28-day curing period, although the  $R^2$  value was low (0.34), less than 15% error was observed in the estimation (Figure 2.6). This can be explained by the small range of  $M_{r-28}$  values (2,279 to 3,100 MPa). This small range of data resulted in a low value of coefficient of determination. However, the difference between the estimated and laboratory measured  $M_{r-28}$  remained less than 15%. Thus, the developed model could estimate the resilient modulus of the stabilized subgrade soil within a reasonable accuracy for a given moisture content and dry unit weight.

#### ***2.4.4 Developing 0-day to 28-day $M_r$ Conversion Model***

A relationship between the 0- and 28-day resilient moduli was developed using laboratory resilient modulus test data. The ratio of the  $M_{r-28}$  to  $M_{r-0}$ , called  $r_{28}$ , was correlated with the stress level and  $M_{r-0}$ . From the regression analysis it was found that, for the soil-CKD mixture used herein,  $w$  and  $\gamma_d$  have negligible effect on the  $r_{28}$  value. This could be due to relatively small variations in moisture contents used in the

experimental program. These two parameters ( $w$  and  $\gamma_d$ ) were not included in the equation. The regression model for determining the  $r_{28}$  value was configured as follows:

$$r_{28} = -0.0091(\sigma_3) + 0.0289(\sigma_d) + 0.0032(M_{r-0}) \quad (2.13)$$

This relationship could be used to predict the  $M_{r-28}$  from the knowledge of  $M_{r-0}$ , and vice versa. The predictability of the conversion model is shown in Figure 2.7. It can be seen that the  $M_{r-0}$  was predicted from the  $M_{r-28}$  with an error less than 12%.

## 2.5 Case Study 2 (CS2): Apple Valley Project

### 2.5.1 Site Location and Material Collection

The second case study site was located at Apple Valley, Edmond OK, on East Hefner Road. The construction at this site was carried out in September 2011. In this project the subgrade was stabilized by mixing 10% CKD to a depth of 304.8 mm.

As before, bulk samples of subgrade soil and CKD were collected from the field in air tight bags. Figure 2.2 shows the particle size distribution of the soil according to sieve analysis and hydrometer tests. About 24.9% of the particles were finer than No. 200 sieve. From the Atterberg limits test it was found that the subgrade soil was non-plastic (NP). This soil was classified as SM (silty sand) as per USCS and as A-2-4 according to AASHTO soil classification. By conducting standard Proctor test on the soil mixed with 10% CKD, the  $w_{opt}$  and  $\gamma_{dmax}$  values were obtained as 12.7% and  $18.29 \text{ kN/m}^3$ , respectively. The  $w$ - $\gamma_d$  curve of the soil-CKD mixture is plotted in Figure 2.3. The specific gravity of the mixture was determined as 2.66, according to pycnometer test. The physical properties of the soil-CKD mixture are summarized in Table 2.1.

### 2.5.2 Test Combinations and Resilient Modulus Testing

Similar to the field situation, all laboratory specimens in CS2 were prepared by mixing soil with 10% CKD (by dry weight of the soil). Two combinations of  $w$  and  $\gamma_d$  were selected. The target moisture content was equal to  $w_{opt} - 2\%$  and  $w_{opt}$  for the first (CM1) and second combination (CM2), respectively. The specimens for both combinations were aimed to reach 100% compaction ( $\gamma_d = \gamma_{dmax}$ ). The properties of the prepared specimens are listed in Table 2.2. The moisture content of the prepared specimens had a range of  $w_{opt} - 2.1\%$  to  $w_{opt} + 0.1\%$ , and the degree of compaction varied between 97% and 100%.

After preparation of the cylindrical specimens,  $M_r$  tests were performed. Following the test, the specimens were cured for 28 days at a temperature of  $23 \pm 2$  °C and a relative humidity of 96% approximately. After 28 days, another set of  $M_r$  tests were conducted on the same specimens. The 0-day  $M_r$  test results for two specimens (specimens CS2-CM2-#2 and CS2-CM2-#3 in Table 2.3) were discarded because they were considered outliers. The measured axial strains for these two specimens were excessively low. The problem in strain measurements could be attributed to a fault in positioning the LVDTs. The data for the  $M_r$  tests were analyzed few days before subgrade compaction. Hence, the remaining time was insufficient to prepare and test substitute specimens. The  $M_r$  test results at 0- and 28-day curing periods are shown in Tables 2.8 and 2.9, respectively. The effect of stress level on mean  $M_r$  value is demonstrated in Figure 2.8 for both combinations. It can be observed that the increase in deviatoric stress resulted in a reduction in  $M_{r-0}$  for all specimens. Also, changes in confining pressure considerably affected the resilient modulus of the specimens at 0-day curing period. As

expected, at a fixed deviatoric stress, the higher confining pressure resulted in higher  $M_r$  values. This is consistent with the findings of Achampong et al. (1997) and Ramakrishna (2002). The resilient modulus of specimens of both combinations improved significantly after 28 days of curing. It can be seen that the  $M_{r-28}$  values are relatively stress independent when compared to  $M_{r-0}$  values. This is consistent with the findings of Lotfi and Witczak (1982).

### **2.5.3 Developing Regression Models for $M_r$**

The 0-day and 28-day  $M_r$  results were used to develop regression models for estimating resilient modulus at given  $w$ ,  $\gamma_d$  and stress level. Similar to the procedure described for Case Study 1, the regression coefficients  $k_1$ ,  $k_2$  and  $k_3$  were back-calculated for all specimens (Table 2.6). Afterwards, constants  $a$ ,  $b$  and  $c$  in Equation 2.6 were determined by conducting linear regression analysis (Table 2.7). Equations 2.14 to 2.19 show the models for calculating coefficients  $k_1$ ,  $k_2$  and  $k_3$  for Case Study 2 at 0-day and 28-day curing periods.

0-day curing period:

$$k_1 = -116808.633 - 200.155(w) + 6676.181(\gamma_d) \quad (2.14)$$

$$k_2 = -11.509 - 0.109(w) + 0.722(\gamma_d) \quad (2.15)$$

$$k_3 = 2.867 + 0.223(w) - 0.321(\gamma_d) \quad (2.16)$$

28-day curing period:

$$k_1 = 127792.503 - 835.980(w) - 4183.115(\gamma_d) \quad (2.17)$$

$$k_2 = -0.880 + 0.035(w) + 0.028(\gamma_d) \quad (2.18)$$

$$k_3 = 3.662 + 0.055(w) - 0.238(\gamma_d) \quad (2.19)$$

The predictability of the developed regression models for 0-day and 28-day  $M_r$  are shown in Figures 2.9 and 2.10, respectively. The developed models were found to estimate the resilient modulus of the specimens with an error within  $\pm 20\%$  and  $\pm 15\%$  for 0-day and 28-day curing periods, respectively. Further, it can be observed from Figures 2.9 and 2.10 that the estimated modulus values had good correlations with the laboratory measured values ( $R^2 = 0.84$  for 0-day data and  $R^2 = 0.65$  for 28-day data).

#### ***2.5.4 Developing 0-day to 28-day $M_r$ Conversion Model***

A relationship between the 0-day and 28-day  $M_r$  values was established through a regression model. For this case study,  $r_{28}$  was expressed as a function of moisture content, dry unit weight, stress level and  $M_{r-0}$ . Contrary to CS1, it was found that  $w$  and  $\gamma_d$  considerably affected the  $r_{28}$  value for the stabilized subgrade soil in CS2. Equation 2.20 shows the regression model for determining the  $r_{28}$  value.

$$r_{28} = -11.4931 \left( \frac{w}{w_{opt}} \right) + 28.6638 \left( \frac{\gamma_d}{\gamma_{dmax}} \right) - 0.00313(\theta) - 0.0168(M_{r-0}) \quad (2.20)$$

Figure 2.11 shows a comparison between the estimated (using Equation 2.20) and laboratory measured 0-day  $M_r$  values. It can be seen that the model could estimate the 0-day  $M_r$  with an error less than 15%.

## **2.6 Case Study 3 (CS3): Main Street-Interstate 35 Intersection Project**

### ***2.6.1 Site Location and Material Collection***

The site of CS3 was located on the north-bound side of Interstate 35 near West Main Street, Norman, OK. The construction at this site was done between April 2013 and August 2013. The subgrade soil was stabilized with 12% CKD to a depth of 202 mm.

As before, bulk soil and CKD samples were collected from the construction site before the subgrade compaction. Figure 2.2 shows the particle size distribution of the collected soil. Percent passing No. 200 sieve was found to be 68.4. Atterberg limits test showed that the LL and PI of the subgrade soil were of 25% and 9%, respectively. The soil was classified as CL (clay of low plasticity) as per USCS and as a A-4 as per AASHTO soil classification system. The  $w$ - $\gamma_d$  relationship for the soil-CKD mixture (soil + 12% CKD), obtained by standard Proctor test, is plotted in Figure 2.3. The  $w_{opt}$  and  $\gamma_{dmax}$  of the stabilized soil were found as 14.8% and  $17.3 \text{ kN/m}^3$ , respectively. The specific gravity of the soil-CKD mixture was found as 2.67 according pycnometer test. The physical properties of the stabilized subgrade soil are presented in Table 2.1.

### ***2.6.2 Test Combinations and Resilient Modulus Testing***

The  $M_r$  tests related to CS3 were conducted after the subgrade compaction. Therefore, the laboratory test combinations could be selected in accordance with the measured  $w$  and  $\gamma_d$  values in the field. Similar to the field conditions, the CKD content for all combinations was kept at 12% (weight of the dried soil). The Nuclear Density Gauge (NDG) measurements at selected stations in the field showed a range of 15.2% to 16.4% for  $w$  (except one station with a  $w$  of 19.4%), and a range of 15.14 to  $17.20 \text{ kN/m}^3$



for  $\gamma_d$ . The details of the NDG measurements along with the other field investigations are presented in Chapter 3. To have a better selection of  $w$ - $\gamma_d$  combinations, the NDG measured data were plotted on a  $w$ - $\gamma_d$  plane (Figure 2.12). Also, the  $w$ - $\gamma_d$  curve from Proctor tests on the soil-CKD mixture was included in the plot. Accordingly, five combinations were selected for preparing the laboratory specimens, four of which had moisture contents and dry unit weights close to upper and lower limits of  $w$  and  $\gamma_d$  ranges in the field (CM1, CM2, CM4 and CM5). One combination (CM3) was selected in the middle of the other four combinations (Figure 2.12). The  $w$  and  $\gamma_d$  values for the five combinations are represented in Table 2.2. Table 2.2 also represents the  $w$  and  $\gamma_d$  values of the prepared specimens. Figure 2.12 gives a better demonstration of  $w$  and  $\gamma_d$  of the prepared specimens. The laboratory compacted specimens had a moisture content range of  $w_{opt} - 0.9\%$  to  $w_{opt} + 3.1\%$  and a degree of compaction range of 87.6% to 99.5%.

The resilient modulus tests were conducted on the specimens at 0-day and 28-day curing periods. A summary of the  $M_r$  test results is presented in Tables 2.10 and 2.11 for 0-day and 28-day cured specimens, respectively. The mean  $M_r$  value for each combination at 0-day is compared with the ones for the 28-day curing period at different stress levels in Figure 2.13. The  $M_{r-0}$  and  $M_{r-28}$  values showed similar trends due to changes in the deviatoric stress. The  $M_{r-0}$  values of the specimens increases with increase in confining pressure and with decreasing deviatoric stress. Also,  $M_{r-28}$  values increased by an increase in deviatoric stress. Changes in confining pressure had an insignificant effect on the  $M_{r-28}$  of the specimens. This is in agreement with the findings of previous studies (Achampong et al.,1997; Ramakrishna, 2002; and Solanki, 2010). The highest values of  $M_{r-0}$  and  $M_{r-28}$  were achieved for the specimens of CM1, with target  $w$  and

degree of compaction of  $w_{opt}$  and 100%, respectively. For example, at  $\sigma_d = 68.9$  kPa and  $\sigma_3 = 41.34$  kPa, the mean  $M_{r-0}$  was equal to 333 MPa and the  $M_{r-28}$  was equal to 1,992 MPa. This represents a 498% increase in resilient modulus after 28 days of curing. A significant increase in  $M_r$  values after 28 days of curing was observed for the specimens of CM5. For this combination, the mean  $M_{r-0}$  was very low (40 MPa); however, after 28 days of curing the mean  $M_r$  showed a 3,400% increase and reached to a value as high as 1,402 MPa (at  $\sigma_d = 68.9$  kPa and  $\sigma_3 = 41.34$  kPa). The low value of  $M_{r-0}$  for CM5 could be attributed to high degree of saturation (about 87%), which could result in a build-up of pore water pressure in the specimen during  $M_r$  testing. Such pore water pressure build-up leads to a reduction in effective stress during  $M_r$  testing and results in a lower stiffness and strength. This is consistent with the findings of previous studies (Witczak et al., 2000; and Khouri, 2016). After 28 days of curing, the resilient modulus values increased significantly. CKD being a slow reacting stabilizing agent, a longer curing time is needed to achieve full modulus.

Another reason for the significant increase in  $M_r$  of the specimens with high degree of saturation could be thixotropic effect (Nazarian et al., 1996). In soils with high degree of saturation, the strength and stiffness can increase significantly at a constant moisture content, if the specimen is allowed to rest after compaction or remolding (Mitchell, 1960; Seed et al., 1962). This phenomenon, called thixotropic hardening, occurs as a result of rearrangement of folliculated interparticles in the soil by attractive forces (Seng and Tanaka, 2012). It can be concluded that the specimens of CM5, which had the highest degree of saturation among other combinations, showed a significant increase in resilient modulus due to thixotropic hardening.

### 2.6.3 Developing Regression Models for $M_r$

$M_r$  regression models were developed using 0-day and 28-day  $M_r$  values using the procedure described in Section 2.3.3. Table 2.6 shows the back-calculated values for coefficients  $k_1$ ,  $k_2$ , and  $k_3$ , and Table 2.7 presents the constants  $a$ ,  $b$  and  $c$  calculated using linear regression analysis. The developed regression models are given in Equations 2.21 to 2.26.

0-day curing period:

$$k_1 = -4653.4 - 309(w) + 706.5(\gamma_d) \quad (2.21)$$

$$k_2 = -0.232 + 0.045(w) - 0.023(\gamma_d) \quad (2.22)$$

$$k_3 = -0.057 - 0.043(w) + 0.033(\gamma_d) \quad (2.23)$$

28-day curing period:

$$k_1 = -37893.561 - 1162.634(w) + 4311.167(\gamma_d) \quad (2.24)$$

$$k_2 = 0.0674 + 0.0004(w) - 0.0045(\gamma_d) \quad (2.25)$$

$$k_3 = -0.127 - 0.0005(w) + 0.0068(\gamma_d) \quad (2.26)$$

Figures 2.14 and 2.15 show the predictability of the developed regression models for 0-day and 28-day curing periods, respectively. It can be seen that the predictability of the models is very good with a  $R^2 = 0.91$  and  $0.90$  for 0-day and 28-day data, respectively (for the data used to validate the model). Also, the model could predict the resilient moduli within  $\pm 25\%$  and  $\pm 15\%$  error limit for 0-day and 28-day curing periods, respectively.

#### **2.6.4 Developing 0-day to 28-day $M_r$ Conversion Model**

A regression model was developed to correlate the 0-day and 28-day resilient modulus values. Using the procedure discussed in Section 2.3.4, the following relationship for calculating  $r_{28}$  was developed:

$$r_{28} = -2.4612 \left( \frac{w}{w_{opt}} \right) + 13.4185 \left( \frac{\gamma_d}{\gamma_{dmax}} \right) - 0.0152861(M_{r-0}) \quad (2.27)$$

The regression analysis showed that stress level had a negligible effect on the  $r_{28}$  value. This was because of the similar trends of  $M_{r-0}$  and  $M_{r-28}$  due to changes in stress levels. In other words, for CS3, both  $M_{r-0}$  and  $M_{r-28}$  values of the specimens were decreased by an increase in deviatoric stress, which resulted in insignificance of the stress level effect in the  $r_{28}$  value. Figure 2.16 shows the comparison between the estimated (using Equation 2.27) and laboratory measured  $M_{r-0}$ . The coefficient of determination,  $R^2$ , for the correlations was found to be 0.94. The estimation error was less than 20%.

### **2.7 Case Study 4 (CS4): Interstate 35 Service Road Project**

#### **2.7.1 Site Location and Material Collection**

The fourth case study site was located on Interstate 35 Service Road at the University Park area of Northwest Norman, Oklahoma. The construction at this site was carried out in August 2014. The subgrade was pre-treated by adding 3% quick lime. The average moisture content of the soil during the mixing of quick lime was 22%. This value was determined both by NDG measurements and oven drying the sealed samples collected from several stations in the field on the day of pre-treatment. The quick lime-treated soil was subsequently stabilized by mixing 12% CKD to a depth of 202 mm after

a 14-day curing period, under ambient conditions. As earlier mentioned in Section 2.3.1, FWD tests were conducted at this site, seven days after subgrade compaction.

As before, bulk samples of soil and lime were collected from the field on the pre-treatment day. Bulk CKD sample was collected from the plant of the construction company (Silver Star Construction Company, Moore, OK). Figure 2.2 shows the particle size distribution of the subgrade soil. About 78.9% of the particles were finer than No. 200 sieve size (75  $\mu$ m). The LL and PI of the soil were found as 40% and 21%, respectively. The soil was classified as CL (clay of low plasticity) according to the USCS classification system. According to the AASHTO classification, the subgrade soil was categorized as A-6 (see Table 2.1).

In order to simulate the field conditions, the natural subgrade soil was air dried, processed and passed through ASTM No. 4 sieve. Then, quick lime (3%) was added to the soil and mixed to attain uniformity under dry conditions. Afterwards, water (22% by weight of the dry mixture) was added to the soil-quick lime mixture. The prepared mixtures were kept in plastic bags (approximately 50 Kg per bag).

Since the soil-quick lime mixture in the field was exposed to ambient conditions, the plastic bags were kept untied as shown in Figure 2.17-a. The plastic bags allowed moisture exchange only from the top surface. To simulate the thickness of the loose soil-quick lime mixture in the field before compaction, the depth of the moist soil-quick lime mixture in each plastic bag was around 280 mm. Plastic bags containing the mixtures were placed inside an environmental chamber where the relative humidity and temperature were controlled (Figure 2.17-b). The average day and night temperature (29.5 °C and 23.1 °C, respectively), and average day and night humidity (61% and 97%,

respectively) of the project location for over a 14-day period were notated from the website of National Oceanic and Atmospheric Administration (NOAA). The environmental chamber was programmed in such a way that the daytime (29.5 °C temperature and 61% humidity) and nighttime ambient conditions (23.1 °C temperature and 97% humidity) lasted for 15 and 9 hours, respectively.

After 14 days, 12% CKD (by weight of the dry mixture) was mixed with the soil-quick lime mixture. The prepared soil-quick lime-CKD mixture was used for the standard Proctor and resilient modulus tests. Figure 2.3 shows the  $w-\gamma_d$  curve according to standard Proctor test. The optimum moisture content and maximum dry unit weight were obtained as 21.4% and  $15.4 \text{ kN/m}^3$ , respectively. The specific gravity of the mixture was measured 2.67 (see Table 2.1).

### ***2.7.2 Test Combinations and Resilient Modulus Testing***

Similar to Case Study 3, the laboratory tests were conducted after completion of the subgrade compaction. All of the specimens were prepared by adding 12% CKD (by dry weight of the soil-quick lime mixture) to the soil. With regard to the collected  $w$  and  $\gamma_d$  data from the field, five different combinations were selected for preparation of  $M_r$  test specimens. A graphical depiction of the range of moisture content and dry unit weight measured in the field is shown in Figure 2.18. Table 2.2 shows the target moisture content and degree of compaction for each of the combinations. These combinations were selected so that a reasonable range of field  $w$  and  $\gamma_d$  could be captured in the laboratory. Three specimens were prepared for each combination.

The resilient modulus tests were conducted immediately after the compaction of the specimen to simulate the field condition. Additionally, the specimens were tested after

7-day (to be compared with FWD test results) and 28-day curing periods. A summary of  $M_{r-0}$ ,  $M_{r-7}$  and  $M_{r-28}$  test results is presented in Tables 2.12, 2.13 and 2.14, respectively. Figure 2.19 demonstrates the changes of  $M_r$  due to changes in stress level for different curing periods. The  $M_{r-0}$ ,  $M_{r-7}$  and  $M_{r-28}$  values showed a similar increasing trends due to reduction of deviatoric stress. Also, the  $M_{r-0}$  and  $M_{r-7}$  values increased by an increase in confining pressure. The resilient modulus of all specimens showed improvement both after 7-day and 28-day curing periods (Achampong et al.,1997; Ramakrishna, 2002). The increase in resilient modulus was significant for specimens of CM1 and CM5, which had the highest degrees of saturation (more than 80%). For CM1, the mean  $M_r$  increased from 142 MPa at 0-day to 1,678 MPa at 7-day and to 3,500 MPa at 28-day curing period (at  $\sigma_d = 68.9$  kPa and  $\sigma_3 = 41.34$  kPa). For CM5, the 0-day, 7-day and 28-day the mean  $M_r$  was equal to 112, 1,300 and 2,860 MPa, respectively. The significant increase in  $M_r$  of CM1 and CM5 specimens, with had a relatively high degree of saturation (about 86% and 83%, respectively), in this case study could be attributed to the same reasons discussed for the CM5 specimens in CS3: Low initial (0-day)  $M_r$  due to creation of pore water pressure during resilient modulus test, and increase in the stiffness due to stabilization and thixotropic hardening of the material after curing.

### ***2.7.3 Developing Regression Models for $M_r$***

Regression models were developed for estimating 0-day, 7-day and 28-day resilient moduli. The same procedure used for the other three case studies was deployed to configure the regression equations for CS4. Back-calculated values of regression coefficients  $k_1$ ,  $k_2$ , and  $k_3$ , and constants  $a$ ,  $b$  and  $c$  are listed in Tables 2.6 and 2.7,

respectively. The developed models for estimating the resilient modulus of the mixture at different curing periods are as follows:

0-day curing period:

$$k_1 = -3121.68 - 108.733(w) + 432.5896(\gamma_d) \quad (2.28)$$

$$k_2 = 1.803884 + 0.030014(w) - 0.14429(\gamma_d) \quad (2.29)$$

$$k_3 = -0.84907 - 0.01073(w) + 0.050347(\gamma_d) \quad (2.30)$$

7-day curing period:

$$k_1 = -75106.387 - 425.864(w) + 6529.877(\gamma_d) \quad (2.31)$$

$$k_2 = 0.0599 - 0.0043(w) + 0.003570(\gamma_d) \quad (2.32)$$

$$k_3 = -0.11033 + 0.00027(w) + 0.00251(\gamma_d) \quad (2.33)$$

28-day curing period:

$$k_1 = -141595.156 + 237.445(w) + 10888.325(\gamma_d) \quad (2.34)$$

$$k_2 = 1.301 + 0.0116(w) - 0.1012(\gamma_d) \quad (2.35)$$

$$k_3 = -0.677 - 0.0178(w) + 0.0653(\gamma_d) \quad (2.36)$$

The predictability of 0-day, 7-day and 28-day models is shown in Figures 2.20, 2.21 and 2.22, respectively. It can be seen that the predictability of the models is very good with a  $R^2 = 0.95, 0.96$  and  $0.8$  for 0-day, 7-day and 28-day data points, respectively (considering the data used to validate the model). Also, the model was seen to predict the resilient moduli with an error less than 15% for all curing periods.

#### **2.7.4 Developing 0-day to 7-day and 28-day $M_r$ Conversion Models**

As stated in Section 2.3.4, since for this Case Study the FWD test was conducted seven days after compaction, a regression model was developed to correlated 7-day to 0-



day resilient modulus. It was found that the polynomial regression resulted in the lowest error values for estimating the  $M_{r-0}$  from  $M_{r-7}$ . Due to similar trends of  $M_{r-0}$  and  $M_{r-7}$  by changes in stress level (see Figure 2.19), the effect of stress level on increase in  $M_r$  after seven days was found to be negligible. The following equation was established to determine  $r_7$  value:

$$r_7 = -6.105 \left( \frac{w}{w_{opt}} \right) + 24.319 \left( \frac{\gamma_d}{\gamma_{dmax}} \right)^2 - 0.047(M_{r-0}) \quad (2.37)$$

Figure 2.23 shows a comparison between estimated (using Equation 2.37) and laboratory measured  $M_{r-0}$ . It can be seen that the predictability of the model has a coefficient of determination of 0.91. Also, the model was found to predict the resilient moduli with error within  $\pm 20\%$ .

Similarly, a conversion model was developed to predict the  $M_{r-28}$  from the knowledge of  $M_{r-0}$ , and vice versa. The equation for calculating the  $r_{28}$  value was established as follows:

$$r_{28} = 10.7876 \left( \frac{w}{w_{opt}} \right) + 25.5138 \left( \frac{\gamma_d}{\gamma_{dmax}} \right)^3 - 0.0954(M_{r-0}) \quad (2.38)$$

The model could predict the  $M_{r-0}$  from knowledge of  $M_{r-28}$  with a  $R^2$  of 0.9 and with an error within  $\pm 20\%$  (Figure 2.24).

## 2.8 Developing a Generic Model for 28-day $M_r$ of CKD-stabilized Soil

The laboratory data from four case studies were used to establish a generic model to predict  $M_{r-28}$  based on basic physical properties of the soil-CKD mixture. As previously mentioned in Section 2.3.5, such properties as UCS, degree of compaction,

moisture content, and CKD content of the mixture, and plasticity index and clay content of the soil were considered for developing the model.

### ***2.8.1 Influence of Different Parameters on the $M_r$ of the CKD-stabilized Soil***

To take into account the influence of CKD amount on resilient modulus, additional specimens were prepared with three different CKD amounts using the subgrade soil collected from the CS3 site. The properties of these specimens containing 5% (CS3-CKD5), 10% (CS3-CKD10) and 15% of CKD (CS3-CKD15) (by weight of the dried soil) are presented in Table 2.15. Three specimens for each amount of CKD was prepared. All of the additional specimens were compacted at optimum moisture content and maximum dry unit weight. The results of the  $M_{r-28}$  tests on these additional specimens are presented in Table 2.16. Figure 2.25 shows the influence of CKD content (5%, 10%, 12% and 15%) on the  $M_{r-28}$  at  $\sigma_d = 68.9$  kPa and  $\sigma_3 = 41.34$  kPa (mean value for three specimens,). The data for the soil mixed with 12% CKD were reported in Section 2.6.2. The resilient modulus increased almost linearly ( $R^2=0.98$ ) by increasing CKD amount (from 748 MPa for 5% CKD to 2610 MPa for 15% CKD).

The UCS tests were conducted on the specimens according to the procedure described in Section 2.3.5. Figure 2.26 shows a comparison between UCS and the  $M_{r-28}$  (at  $\sigma_d = 68.9$  kPa and  $\sigma_3 = 41.34$  kPa) for all of specimens (including the nine additional specimens of CS3-CKD5, CS3-CKD10 and CS3-CKD15). It can be seen that UCS values have a strong correlation with the  $M_r$  of the specimens. The following linear relationship was found between UCS and  $M_{r-28}$ :

$$M_{r-28} = 461.3 + 1.1049(UCS) \quad (2.39)$$

where  $M_{r-28}$  is the 28-day  $M_r$  in MPa; and UCS is the unconfined compressive strength

of the specimen in kPa. The  $R^2$  value associated with this correlation was equal to 0.82 which shows the significance of considering the UCS in developing the generic regression model.

### **2.8.2 Development of 28-day $M_r$ Generic Model of CKD-stabilized Soil**

The constitutive model suggested by AASHTO (1993) (Equation 2.2) was used for developing the generic model. For this reason, regression coefficients  $k_1$ ,  $k_2$ , and  $k_3$  of the additional specimens of CS3-CKD5, CS3-CKD10 and CS3-CKD15 were back-calculated using Equation 2.2 (see Table 2.15). The regression coefficients of the additional specimens along with the previously back-calculated coefficients for CS1 to CS4 (data for 28-day curing period in Table 2.6) were used in multiple linear regression analysis in Minitab numerical analysis tool. Approximately 80% of the data was used for developing the model. The data from nine specimens of the CS3 (specimens of CM2, CM3 and CM4) were used for validating the model. The following generic regression models for estimating  $k_1$ ,  $k_2$ , and  $k_3$  were developed:

$$\begin{aligned}
 \log k_1 = & 3.05553 + 0.474455 \log \left( \frac{UCS}{P_a} \right) \\
 & - 2.14289 \log \left( \frac{w}{w_{opt}} \right) \\
 & + 2.71456 \log \left( \frac{\gamma_d}{\gamma_{dmax}} \right) \\
 & + 0.71034 \log \left( \frac{AC}{100} \right)
 \end{aligned} \tag{2.40}$$

$$k_2 = 0.0840668 \log \left( \frac{UCS}{P_a} \right) - 0.0942818 \log c_c \\ + 0.00290806 \log PI - 0.134293 \log \left( \frac{AC}{100} \right) \quad (2.41)$$

$$k_3 = 0.0124595 \log \left( \frac{UCS}{P_a} \right) - 0.529607 \log \left( \frac{w}{w_{opt}} \right) \\ + 1.63155 \log \left( \frac{\gamma_d}{\gamma_{dmax}} \right) + 0.081046 \log c_c \\ + 0.0013958 \log PI - 0.0314137 \log \left( \frac{AC}{100} \right) \quad (2.42)$$

where  $P_a$  is the atmospheric air pressure (101.283 kPa);  $AC$  is the percent of CKD content in the mixture;  $c_c$  is the clay content of the soil; and  $PI$  is the plasticity index of the soil.

The predictability of the model is shown in Figure 2.27. It can be seen that majority of the estimated data points were within  $\pm 25\%$  error lines. A cluster of data points corresponding to Case Study 4 stands out of the 25% error which can be explained by the changes of the soil properties due to pre-treatment by quick lime. The model had a coefficient of determination of 0.72 for the validation data points.

## 2.9 Conclusions

Resilient modulus tests were performed on the chemically-stabilized subgrade soils from four different pavement construction sites. The results from  $M_r$  tests at different curing periods along with the physical properties of the specimens were used for developing models for estimating  $M_r$  of chemically-stabilized subgrade soil. The developed regression models were aimed to be used for validating the ICA-estimated moduli during compaction of the subgrade layer. The following conclusions were achieved:

1. The specimens with higher degree of saturation (higher than 83%), i.e., specimens with high moisture content and high degree of compaction, showed lower  $M_{r-0}$  compared to other specimens. This could be attributed to build-up of pore water pressure in the specimen testing and reduction in effective stress during  $M_{r-0}$ .
2. The increase in resilient modulus after 28 days of curing period was significant for the specimens with higher degree of saturation (higher than 83%). A  $r_{28}$  ratio of 38 was observed for the specimens with a degree of saturation of 87% for CS3. This could be attributed to the low  $M_{r-0}$  values due to creation of pore water pressure during  $M_{r-0}$  tests, and thixotropic effect during 28 days of curing.
3. The developed regression models for calibrating and/or validating ICA-estimated moduli could predict the  $M_{r-0}$  of the stabilized subgrade with an error ranged between  $\pm 15\%$  and  $\pm 25\%$  for different case studies. Also, the  $M_{r-28}$  values could be predicted within  $\pm 15\%$  of error range for all of the case studies. The developed regression models for resilient modulus were used to calibrate and validate the ICA-estimated modulus during compaction of the CSS in the field.
4. The  $M_{r-0}$  to  $M_{r-28}$  conversion relationships (using  $r_{28}$  ratio) could successfully convert  $M_{r-28}$  to  $M_{r-0}$  with an error ranged between  $\pm 12\%$ , and  $\pm 20\%$  for different case studies. Also, the conversion model for  $M_{r-7}$  to  $M_{r-0}$  predicted the  $M_{r-0}$  with and less than  $\pm 20\%$  error. These conversion relationships were aimed to be used for converting the ICA-estimated moduli to  $M_{r-28}$  and FWD moduli, and vice versa.

5. The resilient modulus of soil-CKD specimens using basic properties of the soil-CKD mixture could be predicted by developing a generic regression model. Majority of the estimated data points were within  $\pm 25\%$  error lines ( $R^2 = 0.72$ ). Using this model the resilient modulus of fine grained soil stabilized with different amounts of CKD could be predicted for different moisture contents and dry unit weights.

**Table 2.1 Material Properties of Different Case Studies**

<b>Parameter</b>	<b>Standard Test Method</b>	<b>Case Study 1</b>	<b>Case Study 2</b>	<b>Case Study 3</b>	<b>Case Study 4</b>
Project Location	-	60th Avenue Northwest, Norman, OK	East Hefner Road, Edmond OK	Interstate 35 near West Main Street, Norman, OK	Interstate 35 Service Road, Norman, OK
USCS Soil Classification	ASTM D2487	CL-ML	SM	CL	CL
USCS Name	ASTM D2487	Silty lean clay	Silty sand	Lean clay	Lean clay
AASHTO Soil Classification	AASHTO M 145	A-4	A-2-4	A-4	A-6
% Passing Sieve #200	ASTM D422	79.3	24.9	69.4	78.9
% Finer than 0.002 mm (clay content)	ASTM D422	26.1	18.2	26.5	37.2
Liquid Limit	ASTM D4318	23	NP	25	40
Plastic Limit	ASTM D4318	19	NP	14	19
Plasticity Index	ASTM D4318	4	NP	9	21
Subgrade Mixture	-	Soil + 10% CKD	Soil + 10% CKD	Soil + 12% CKD	Soil + 3% quick lime + 10% CKD
Specific Gravity	ASTM D854	2.71	2.66	2.67	2.67
Optimum Moisture Content (%)	ASTM D698	14.6	12.7	14.8	21.4
Maximum Dry Unit weight (kN/m <sup>3</sup> )	ASTM D698	17.3	18.3	17.3	15.4

**Table 2.2 Test Combinations and Specimens' Characteristics for all Case Studies**

Project	CM #	Specimen Code	Target $w$	$w$	Target $\gamma_d$	$\gamma_d$	Degree of Compaction	Degree of Saturation
			(%)	(%)	(kN/m <sup>3</sup> )	(kN/m <sup>3</sup> )	(% of $\gamma_{dmax}$ )	(%)
CS1	CM1	CS1-CM1-#1	12.6	12.1	17.3	17.3	97.7	60.7
		CS1-CM1-#2		12.4		17.1	96.9	60.8
		CS1-CM1-#3		12.1		17.2	97.4	60.1
	CM2	CS1-CM2-#1	14.6	14.7	17.3	17.4	98.7	75.9
		CS1-CM2-#2		14.6		17.5	99.1	76.4
		CS1-CM2-#3		14.8		17.6	99.4	78.1
CS2	CM1	CS2-CM1-#1	10.7	10.8	18.3	18.1	97.3	65.1
		CS2-CM1-#2		10.8		18.3	98.3	67.5
		CS2-CM1-#3		10.6		18.3	98.1	66.3
	CM2	CS2-CM2-#1	12.7	12.6	18.3	18.5	99.2	81.7
		CS2-CM2-#2		12.8		18.3	98.1	80.0
		CS2-CM2-#3		11.4		18.6	99.9	75.3
CS3	CM1	CS3-CM1-#1	14.8	13.9	17.3	17.1	98.8	69.7
		CS3-CM1-#2		14.4		17.2	99.5	73.9
		CS3-CM1-#3		14.4		17.0	98.0	70.7
	CM2	CS3-CM2-#1	14.8	14.7	15.2	15.3	100.6	55.3
		CS3-CM2-#2		15		15.2	99.6	55.1
		CS3-CM2-#3		14.9		15.5	101.9	57.8
	CM3	CS3-CM3-#1	16.2	15.9	16.3	16.3	100.5	70.5
		CS3-CM3-#2		16.1		16.3	100.0	70.5
		CS3-CM3-#3		15.9		16.2	99.5	68.6
	CM4	CS3-CM4-#1	17.8	17.8	15.2	15.4	101.1	67.8
		CS3-CM4-#2		17.8		15.2	99.6	65.3
		CS3-CM4-#3		17.9		15.3	100.5	67.1
	CM5	CS3-CM5-#1	17.8	17.9	17.3	16.9	97.6	86.8
		CS3-CM5-#2		17.8		16.9	97.9	87.1
		CS3-CM5-#3		17.8		17.0	98.0	87.3
CS4	CM1	CS4-CM1-#1	21.4	22.5	15.4	15.3	99.3	84.3
		CS4-CM1-#2		22.6		15.4	99.7	85.5
		CS4-CM1-#3		22.5		15.5	100.6	87.1
	CM2	CS4-CM2-#1	19.3	19.3	15.4	15.3	99.2	72.3
		CS4-CM2-#2		19.3		15.4	100.0	73.6
		CS4-CM2-#3		19.4		15.6	101.1	76.0
	CM3	CS4-CM3-#1	21.4	20.4	13.9	14.0	91.1	62.8
		CS4-CM3-#2		20.2		14.2	92.2	63.9
		CS4-CM3-#3		19.7		14.2	92.2	62.2
	CM4	CS4-CM4-#1	18.4	18.8	14.6	14.8	96.1	65.3
		CS4-CM4-#2		18.5		15.1	98.0	67.3
		CS4-CM4-#3		18.8		14.9	96.9	66.6
	CM5	CS4-CM5-#1	23.4	23.3	14.6	14.8	96.0	80.6
		CS4-CM5-#2		23.4		15.0	97.3	83.6
		CS4-CM5-#3		23.3		15.0	97.2	83.1



**Table 2.3 Test Sequence Used for Resilient Modulus Tests**

Sequence #	Confining Pressure (kPa)	Maximum Axial Stress (kPa)	Cyclic Deviatoric Stress (kPa)	Constant Stress (kPa)	Maximum Bulk Stress (kPa)	No of Load Application
0	41.4	27.6	24.8	2.8	151.8	500
1	41.4	13.8	12.4	1.4	138.0	100
2	41.4	27.6	24.8	2.8	151.8	100
3	41.4	41.4	37.3	4.1	165.6	100
4	41.4	55.2	49.7	5.5	179.4	100
5	41.4	68.9	62.0	6.9	193.1	100
6	27.6	13.8	12.4	1.4	96.5	100
7	27.6	27.6	24.8	2.8	110.2	100
8	27.6	41.4	37.3	4.1	124.1	100
9	27.6	55.2	49.7	5.5	137.9	100
10	27.6	68.9	62.0	6.9	151.6	100
11	13.8	13.8	12.4	1.4	55.2	100
12	13.8	27.6	24.8	2.8	69.0	100
13	13.8	41.4	37.3	4.1	82.8	100
14	13.8	55.2	49.7	5.5	96.6	100
15	13.8	68.9	62.0	6.9	110.3	100

**Table 2.4 Summary of  $M_r$  Values of Case Study 1 at 0-day Curing Period**

Sequence #	$\sigma_3$ (kPa)	$\sigma_d$ (kPa)	$M_r$ (MPa)					
			CS1- CM1- #1	CS1- CM1- #2	CS1- CM1- #3	CS1- CM2- #1	CS1- CM2- #2*	CS1- CM2- #3
1	41.4	13.8	1003	861	857	940	443	1023
2	41.4	27.6	914	823	808	929	407	933
3	41.4	41.4	850	756	741	850	368	880
4	41.4	55.2	787	695	687	795	334	807
5	41.4	68.9	745	653	644	732	313	765
6	27.6	13.8	882	854	808	994	405	1009
7	27.6	27.6	844	815	772	904	371	898
8	27.6	41.4	811	747	707	808	340	837
9	27.6	55.2	771	693	679	755	319	783
10	27.6	68.9	750	657	649	707	299	735
11	13.8	13.8	874	842	761	856	364	945
12	13.8	27.6	829	760	749	804	330	843
13	13.8	41.4	787	712	700	748	305	769
14	13.8	55.2	765	659	663	698	287	721
15	13.8	68.9	737	637	631	664	267	675

\* The specimen was damaged

**Table 2.5 Summary of  $M_r$  Values of Case Study 1 at 28-day Curing Period**

Sequence #	$\sigma_3$ (kPa)	$\sigma_d$ (kPa)	$M_r$ (MPa)				
			CS1- CM1-#1	CS1- CM1-#2	CS1- CM1-#3	CS1- CM2-#1	CS1- CM2-#3
1	41.4	13.8	2546	2751	3193	3273	2632
2	41.4	27.6	2403	2650	2960	2715	2934
3	41.4	41.4	2376	2772	3065	2629	2810
4	41.4	55.2	2486	2764	3030	2615	2751
5	41.4	68.9	2491	2781	2901	2581	2727
6	27.6	13.8	2546	3368	3033	3100	2955
7	27.6	27.6	2413	2770	2970	2488	2793
8	27.6	41.4	2402	2669	2997	2588	2819
9	27.6	55.2	2464	2730	2891	2597	2737
10	27.6	68.9	2375	2842	2968	2541	2678
11	13.8	13.8	2610	3032	3091	2565	2554
12	13.8	27.6	2536	2844	3024	2578	2772
13	13.8	41.4	2471	2843	2876	2575	2713
14	13.8	55.2	2451	2799	2809	2609	2723
15	13.8	68.9	2353	2876	2841	2514	2711

**Table 2.6 Back-calculated  $k_1$ ,  $k_2$  and  $k_3$  values for 0-, 7- and 28-day Curing Period**

Project	Specimen Code	0-day Curing Period			28-day Curing Period		
		$k_1$	$k_2$	$k_3$	$k_1$	$k_2$	$k_3$
CS1	CS1-CM1-#1	6757.17	0.105	-0.160	43609.10	-0.003	-0.033
	CS1-CM1-#2	6006.76	0.056	-0.182	43347.80	0.044	-0.074
	CS1-CM1-#3	5910.87	0.089	-0.167	39877.50	-0.029	-0.169
	CS1-CM2-#1	5841.44	0.224	-0.274	37817.50	0.045	-0.057
	CS1-CM2-#3	6409.30	0.132	-0.225	41754.00	0.100	0.014
CS2	CS2-CM1-#1	2092.46	0.404	-0.556	41798.90	0.051	-0.127
	CS2-CM1-#2	2847.57	0.468	-0.651	23652.10	-0.020	-0.029
	CS2-CM1-#3	3719.49	0.618	-0.605	28180.30	-0.070	0.010
	CS2-CM2-#1	4210.71	0.480	-0.261	27610.10	0.042	-0.054
	CS2-CM2-#2	#	#	#	22974.90	0.066	-0.125
	CS2-CM2-#3	#	#	#	25627.50	0.043	-0.067
CS3	CS3-CM1-#1	3139.04	0.006	-0.095	18441.60	0.018	0.005
	CS3-CM1-#2	3244.81	0.013	-0.114	20780.90	-0.017	-0.051
	CS3-CM1-#3	3209.92	0.036	-0.116	19300.00	0.003	-0.001
	CS3-CM2-#1	1528.43	0.071	-0.191	9921.47	0.015	-0.036
	CS3-CM2-#2	1533.36	0.076	-0.194	9876.34	-0.016	-0.035
	CS3-CM2-#3	1649.74	0.075	-0.185	11372.00	0.018	-0.026
	CS3-CM3-#1	1633.90	0.070	-0.191	12993.60	0.033	-0.040
	CS3-CM3-#2	1653.29	0.075	-0.204	15744.00	-0.067	-0.026
	CS3-CM3-#3	1503.13	0.082	-0.204	13593.60	-0.003	-0.026
	CS3-CM4-#1	760.86	0.232	-0.321	7441.06	0.018	-0.045
	CS3-CM4-#2	804.98	0.207	-0.324	7633.75	0.007	-0.025
	CS3-CM4-#3	736.26	0.223	-0.324	7576.62	0.012	-0.025
	CS3-CM5-#1	199.97	1.019	-0.458	12323.80	0.042	-0.036
	CS3-CM5-#2	218.02	0.933	-0.383	16474.60	-0.070	0.016
	CS3-CM5-#3	204.55	0.835	-0.407	12653.80	0.030	-0.039
CS4	CS4-CM1-#1	1091.12	0.221	-0.307	33651.30	-0.102	-0.082
	CS4-CM1-#2	1171.82	0.185	-0.282	30001.60	-0.054	-0.014
	CS4-CM1-#3	1094.20	0.235	-0.315	33990.60	0.063	-0.084
	CS4-CM2-#1	1223.03	0.230	-0.310	26250.90	-0.032	-0.064
	CS4-CM2-#2	1396.24	0.164	-0.283	29020.90	-0.044	-0.050
	CS4-CM2-#3	1579.46	0.151	-0.258	32938.60	-0.091	0.007
	CS4-CM3-#1	804.65	0.336	-0.342	16511.90	0.103	-0.142
	CS4-CM3-#2	825.58	0.357	-0.350	*	*	*
	CS4-CM3-#3	808.99	0.371	-0.350	16849.00	0.064	-0.096
	CS4-CM4-#1	1223.03	0.230	-0.310	25034.00	-0.009	-0.018
	CS4-CM4-#2	1482.65	0.159	-0.295	28221.70	0.100	-0.009
	CS4-CM4-#3	1322.75	0.226	-0.295	26609.70	0.025	-0.009
	CS4-CM5-#1	718.23	0.419	-0.360	*	*	*
	CS4-CM5-#2	785.69	0.382	-0.367	22647.30	0.185	-0.139
	CS4-CM5-#3	781.36	0.383	-0.364	28722.20	0.041	-0.106

\* Damaged specimens

# Error in LVDT measurements

**Table 2.6 Continued**

Project	Specimen Code	7-day Curing Period		
		$k_1$	$k_2$	$k_3$
CS4	CS4-CM1-#1	15669.50	0.018	-0.067
	CS4-CM1-#2	15724.20	-0.064	-0.073
	CS4-CM1-#3	15434.30	0.122	-0.126
	CS4-CM2-#1	16612.20	0.039	-0.078
	CS4-CM2-#2	18109.50	0.011	-0.033
	CS4-CM2-#3	17666.40	0.126	-0.085
	CS4-CM3-#1	8814.29	0.039	-0.080
	CS4-CM3-#2	7954.32	0.060	-0.079
	CS4-CM3-#3	8777.30	0.072	-0.079
	CS4-CM4-#1	13378.90	-0.026	-0.110
	CS4-CM4-#2	16284.40	0.000	-0.032
	CS4-CM4-#3	13857.00	-0.016	-0.032
	CS4-CM5-#1	*	*	*
	CS4-CM5-#2	12093.30	-0.005	-0.038
	CS4-CM5-#3	13748.30	-0.021	-0.027

\* Damaged specimens

# Error in LVDT measurements

**Table 2.7 Calculated  $a$ ,  $b$  and  $c$  values for 0-, 7- and 28-day Curing Period**

Project	Regression Coefficient	0-day Curing Period			28-day Curing Period		
		$a$	$b$	$c$	$a$	$b$	$c$
CS1	$k_1$	-53060.478	-482.317	3790.046	203060.877	410.151	-10565.166
	$k_2$	-0.46744	0.03421	0.00787	-2.54700	-0.00590	0.15141
	$k_3$	-2.55251	-0.05156	0.17514	-0.40150	-0.01495	0.03254
CS2	$k_1$	-116808.633	-200.155	6676.181	127792.503	-835.980	-4183.115
	$k_2$	-11.50942	-0.10905	0.72202	-0.87971	0.03526	0.02771
	$k_3$	2.86740	0.22267	-0.32104	3.66156	0.05532	-0.23809
CS3	$k_1$	-4653.358	-309.041	706.500	-37893.561	-1162.634	4311.167
	$k_2$	-0.23220	0.04463	-0.02330	0.06747	0.00041	-0.00449
	$k_3$	-0.05670	-0.04295	0.03297	-0.12701	-0.00053	0.00677
CS4	$k_1$	-3121.678	-108.733	432.590	-141595.156	237.446	10888.325
	$k_2$	1.80388	0.03001	-0.14429	1.30075	0.01158	-0.10119
	$k_3$	-0.84907	-0.01073	0.05035	-0.67740	-0.01775	0.06534
Project	Regression Coefficient	7-day Curing Period					
		$a$	$b$	$c$			
CS4	$k_1$	-75106.387	-425.864	6529.877			
	$k_2$	0.05991	-0.00428	0.00357			
	$k_3$	-0.11033	0.00027	0.00251			

**Table 2.8 Summary of  $M_r$  Values of Case Study 2 at 0-day Curing Period**

Sequence #	$\sigma_3$ (kPa)	$\sigma_d$ (kPa)	$M_r$ (MPa)					
			CS2- CM1- #1	CS2- CM1- #2	CS2- CM1- #3	CS2- CM2- #1	CS2- CM2- #2	CS2- CM2- #3
1	41.4	13.8	689	1169	2967	817	*	*
2	41.4	27.6	546	903	1093	757	*	*
3	41.4	41.4	449	661	872	707	*	*
4	41.4	55.2	388	563	767	672	*	*
5	41.4	68.9	351	517	703	641	*	*
6	27.6	13.8	667	1053	2381	672	*	*
7	27.6	27.6	427	665	827	629	*	*
8	27.6	41.4	353	550	686	598	*	*
9	27.6	55.2	326	480	648	581	*	*
10	27.6	68.9	315	444	619	570	*	*
11	13.8	13.8	519	837	2073	555	*	*
12	13.8	27.6	346	514	667	518	*	*
13	13.8	41.4	296	440	566	488	*	*
14	13.8	55.2	279	396	541	478	*	*
15	13.8	68.9	266	380	508	453	*	*

\* Error in LVDT measurements

**Table 2.9 Summary of  $M_r$  Values of Case Study 2 at 28-day Curing Period**

Sequence #	$\sigma_3$ (kPa)	$\sigma_d$ (kPa)	$M_r$ (MPa)					
			CS2- CM1-#1	CS2- CM1-#2	CS2- CM1-#3	CS2- CM2-#1	CS2- CM2-#2	CS2- CM2-#3
1	41.4	13.8	4582	*	5587	*	4288	4704
2	41.4	27.6	4653	4334	5007	4190	3651	5110
3	41.4	41.4	4518	4703	4696	4283	4173	4678
4	41.4	55.2	4267	4504	4730	3979	4429	4814
5	41.4	68.9	4524	4602	4368	3886	4129	4610
6	27.6	13.8	5524	6183	6603	4296	5048	5460
7	27.6	27.6	4631	4836	5317	3723	4668	5631
8	27.6	41.4	4204	4902	4432	3911	4456	4457
9	27.6	55.2	4419	4275	4057	3937	4307	4827
10	27.6	68.9	4616	4686	4195	4069	4499	4576
11	13.8	13.8	4858	*	5791	3410	3797	5349
12	13.8	27.6	4983	4690	5598	3447	3980	4855
13	13.8	41.4	4417	4706	4815	3868	4195	4538
14	13.8	55.2	4341	4543	4460	4130	4614	4614
15	13.8	68.9	4338	4424	4282	4387	4082	4504

\* Out of LVDTs' range

**Table 2.10 Summary of  $M_r$  Values of Case Study 3 at 0-day Curing Period**

Sequence #	$\sigma_3$ (kPa)	$\sigma_d$ (kPa)	$M_r$ (MPa)								
			CS3- CM1- #1	CS3- CM1- #2	CS3- CM1- #3	CS3- CM2- #1	CS3- CM2- #2	CS3- CM2- #3	CS3- CM3- #1	CS3- CM3- #2	CS3- CM3- #3
1	41.4	13.8	384	406	410	224	228	240	242	243	229
2	41.4	27.6	367	394	393	215	214	229	228	229	215
3	41.4	41.4	351	377	373	197	197	211	209	212	196
4	41.4	55.2	337	352	356	182	182	195	193	196	180
5	41.4	68.9	324	337	338	169	170	183	180	183	167
6	27.6	13.8	372	409	404	222	225	237	236	238	222
7	27.6	27.6	375	400	396	211	212	226	224	226	210
8	27.6	41.4	359	378	378	195	196	210	208	211	195
9	27.6	55.2	341	361	357	182	183	195	195	197	182
10	27.6	68.9	332	343	343	170	171	183	181	185	169
11	13.8	13.8	378	403	391	214	214	227	227	228	214
12	13.8	27.6	368	383	382	199	199	213	214	215	200
13	13.8	41.4	347	369	365	184	185	199	197	197	183
14	13.8	55.2	334	352	350	170	173	185	183	184	170
15	13.8	68.9	322	336	332	159	161	172	171	172	157

**Table 2.10 Continued**

Sequence #	$\sigma_3$ (kPa)	$\sigma_d$ (kPa)	$M_r$ (MPa)					
			CS3- CM4- #1	CS3- CM4- #2	CS3- CM4- #3	CS3- CM5- #1	CS3- CM5- #2	CS3- CM5- #3
1	41.4	13.8	153	155	148	78	71	69
2	41.4	27.6	139	141	134	66	60	58
3	41.4	41.4	120	124	117	47	48	42
4	41.4	55.2	105	109	102	40	41	36
5	41.4	68.9	97	100	93	41	42	37
6	27.6	13.8	140	143	137	34	*	33
7	27.6	27.6	125	130	122	32	*	31
8	27.6	41.4	114	118	110	35	*	32
9	27.6	55.2	104	108	100	39	*	35
10	27.6	68.9	95	98	91	41	*	37
11	13.8	13.8	126	130	122	*	*	27
12	13.8	27.6	111	116	109	*	*	26
13	13.8	41.4	100	105	98	*	*	28
14	13.8	55.2	91	96	89	*	*	32
15	13.8	68.9	83	86	80	*	*	35

\* Out of LVDTs' range

**Table 2.11 Summary of  $M_r$  Values of Case Study 3 at 28-day Curing Period**

Sequence #	$\sigma_3$ (kPa)	$\sigma_d$ (kPa)	$M_r$ (MPa)								
			CS3- CM1- #1	CS3- CM1- #2	CS3- CM1- #3	CS3- CM2- #1	CS3- CM2- #2	CS3- CM2- #3	CS3- CM3- #1	CS3- CM3- #2	CS3- CM3- #3
1	41.4	13.8	1861	2223	2117	1093	1071	1248	1466	1586	1413
2	41.4	27.6	1914	2145	1941	1052	1031	1245	1336	1627	1428
3	41.4	41.4	1893	2145	1939	1045	1042	1170	1405	1622	1423
4	41.4	55.2	1898	2120	1978	1032	1004	1160	1375	1580	1415
5	41.4	68.9	1892	2144	1939	1038	1009	1160	1356	1559	1402
6	27.6	13.8	1850	2607	1776	1085	1062	1188	1478	1776	1451
7	27.6	27.6	1746	2235	1967	1026	1048	1145	1355	1566	1468
8	27.6	41.4	1866	2118	1975	1030	1033	1168	1369	1601	1375
9	27.6	55.2	1870	2134	1943	1032	1038	1178	1371	1625	1382
10	27.6	68.9	1901	2188	1914	1031	1007	1173	1384	1567	1383
11	13.8	13.8	1819	2234	1913	1069	1101	1177	1366	1750	1473
12	13.8	27.6	1942	2288	2086	1058	1036	1226	1382	1715	1413
13	13.8	41.4	1826	2085	1969	1025	1042	1181	1365	1639	1376
14	13.8	55.2	1818	2162	1981	1018	1013	1175	1324	1614	1381
15	13.8	68.9	1853	2162	1943	1026	1014	1178	1371	1572	1380

**Table 2.11 Continued**

Sequence #	$\sigma_3$ (kPa)	$\sigma_d$ (kPa)	$M_r$ (MPa)					
			CS3- CM4- #1	CS3- CM4- #2	CS3- CM4- #3	CS3- CM5- #1	CS3- CM5- #2	CS3- CM5- #3
1	41.4	13.8	819	878	824	1387	1576	1376
2	41.4	27.6	828	865	808	1376	1646	1392
3	41.4	41.4	795	825	803	1287	1638	1336
4	41.4	55.2	788	809	789	1302	1584	1324
5	41.4	68.9	765	781	768	1284	1605	1319
6	27.6	13.8	831	871	779	1290	1582	1418
7	27.6	27.6	794	842	803	1305	1565	1352
8	27.6	41.4	789	803	781	1268	1676	1311
9	27.6	55.2	771	806	771	1279	1611	1312
10	27.6	68.9	762	790	774	1267	1622	1312
11	13.8	13.8	795	871	786	1286	1732	1334
12	13.8	27.6	816	841	811	1328	1676	1341
13	13.8	41.4	791	804	799	1288	1624	1301
14	13.8	55.2	776	804	789	1294	1661	1312
15	13.8	68.9	771	800	770	1273	1628	1322

**Table 2.12 Summary of  $M_r$  Values of Case Study 4 at 0-day Curing Period**

Sequence #	$\sigma_3$ (kPa)	$\sigma_d$ (kPa)	$M_r$ (MPa)								
			CS4- CM1- #1	CS4- CM1- #2	CS4- CM1- #3	CS4- CM2- #1	CS4- CM2- #2	CS4- CM2- #3	CS4- CM3- #1	CS4- CM3- #2	CS4- CM3- #3
1	41.4	13.8	214	214	218	244	258	275	175	184	181
2	41.4	27.6	192	193	193	219	229	249	157	162	160
3	41.4	41.4	169	173	169	191	205	224	135	140	140
4	41.4	55.2	150	157	153	169	183	203	119	125	124
5	41.4	68.9	140	145	142	156	170	189	112	117	117
6	27.6	13.8	196	204	203	217	241	261	154	160	156
7	27.6	27.6	173	181	175	194	214	235	133	137	135
8	27.6	41.4	158	165	161	177	194	215	121	125	124
9	27.6	55.2	146	153	148	163	180	199	114	118	116
10	27.6	68.9	135	142	137	152	168	187	106	110	108
11	13.8	13.8	179	185	181	202	224	241	133	136	135
12	13.8	27.6	154	163	154	173	197	217	113	116	113
13	13.8	41.4	140	149	140	158	178	198	104	106	104
14	13.8	55.2	129	137	131	147	165	185	98	101	99
15	13.8	68.9	120	127	121	136	154	172	91	95	92

**Table 2.12 Continued**

Sequence #	$\sigma_3$ (kPa)	$\sigma_d$ (kPa)	$M_r$ (MPa)					
			CS4- CM4- #1	CS4- CM4- #2	CS4- CM4- #3	CS4- CM5- #1	CS4- CM5- #2	CS4- CM5- #3
1	41.4	13.8	244	266	257	167	185	181
2	41.4	27.6	219	240	228	148	159	158
3	41.4	41.4	191	216	203	127	138	136
4	41.4	55.2	169	194	181	113	122	121
5	41.4	68.9	156	179	168	107	115	114
6	27.6	13.8	217	251	232	141	155	156
7	27.6	27.6	194	223	203	123	134	133
8	27.6	41.4	177	205	189	112	122	122
9	27.6	55.2	163	190	175	106	114	114
10	27.6	68.9	152	177	163	99	106	106
11	13.8	13.8	202	234	210	118	134	131
12	13.8	27.6	173	205	185	99	113	111
13	13.8	41.4	158	188	171	92	103	102
14	13.8	55.2	147	174	159	88	97	97
15	13.8	68.9	136	162	147	82	90	89



**Table 2.13 Summary of  $M_r$  Values of Case Study 4 at 7-day Curing Period**

Sequence #	$\sigma_3$	$\sigma_d$	Mr (MPa)								
	(kPa)	(kPa)	CS4- CM1- #1	CS4- CM1- #2	CS4- CM1- #3	CS4- CM2- #1	CS4- CM2- #2	CS4- CM2- #3	CS4- CM3- #1	CS4- CM3- #2	CS4- CM3- #3
1	41.4	13.8	1728	1809	2152	1959	2000	2483	1077	938	1034
2	41.4	27.6	1732	1681	1850	2023	1996	2073	987	963	1045
3	41.4	41.4	1653	1660	1776	1866	1900	1946	1005	918	1008
4	41.4	55.2	1673	1650	1741	1748	1855	1982	961	889	954
5	41.4	68.9	1663	1604	1766	1755	1848	1953	951	864	955
6	27.6	13.8	2092	1794	2123	1996	1831	1777	1033	973	1086
7	27.6	27.6	1587	1711	1725	1747	1924	1957	994	909	996
8	27.6	41.4	1657	1611	1742	1812	1904	1924	959	880	972
9	27.6	55.2	1639	1643	1759	1802	1848	1985	944	855	932
10	27.6	68.9	1646	1628	1777	1790	1920	1950	931	851	941
11	13.8	13.8	1636	2008	1782	1905	2011	2071	1019	921	950
12	13.8	27.6	1837	1768	1766	1862	1884	1862	985	897	981
13	13.8	41.4	1687	1659	1718	1697	1766	1897	953	855	964
14	13.8	55.2	1655	1593	1721	1785	1862	1933	936	827	940
15	13.8	68.9	1643	1625	1735	1734	1855	1943	925	835	930

**Table 2.13 Continued**

Sequence #	$\sigma_3$ (kPa)	$\sigma_d$ (kPa)	Mr (MPa)					
			CS4- CM4- #1	CS4- CM4- #2	CS4- CM4- #3	CS4- CM5- #1	CS4- CM5- #2	CS4- CM5- #3
1	41.4	13.8	1625	1719	1459	*	1285	1431
2	41.4	27.6	1452	1671	1466	*	1324	1492
3	41.4	41.4	1499	1746	1465	*	1301	1429
4	41.4	55.2	1451	1653	1416	*	1264	1388
5	41.4	68.9	1425	1669	1422	*	1228	1373
6	27.6	13.8	1875	1799	1521	*	1322	1491
7	27.6	27.6	1475	1691	1447	*	1296	1445
8	27.6	41.4	1447	1712	1411	*	1282	1425
9	27.6	55.2	1431	1704	1424	*	1243	1403
10	27.6	68.9	1412	1670	1431	*	1245	1364
11	13.8	13.8	1679	1712	1520	*	1307	1450
12	13.8	27.6	1563	1682	1475	*	1335	1482
13	13.8	41.4	1493	1707	1451	*	1294	1453
14	13.8	55.2	1429	1699	1427	*	1232	1430
15	13.8	68.9	1459	1655	1392	*	1219	1411

\* Damaged specimen

**Table 2.14 Summary of  $M_r$  Values of Case Study 4 at 28-day Curing Period**

Sequence #	$\sigma_3$ (kPa)	$\sigma_d$ (kPa)	Mr (MPa)								
			CS4- CM1- #1	CS4- CM1- #2	CS4- CM1- #3	CS4- CM2- #1	CS4- CM2- #2	CS4- CM2- #3	CS4- CM3- #1	CS4- CM3- #2	CS4- CM3- #3
1	41.4	13.8	3424	3045	3797	3056	3093	#	2397	*	2122
2	41.4	27.6	3583	3139	4008	2601	3286	3213	2095	*	1887
3	41.4	41.4	3553	3061	3913	2743	3182	3316	2180	*	1934
4	41.4	55.2	3610	3026	3798	2827	3032	3136	1909	*	1906
5	41.4	68.9	3563	3118	3820	2645	2921	3402	1915	*	1854
6	27.6	13.8	4460	2685	4713	3008	2968	3105	2118	*	2136
7	27.6	27.6	3578	3124	3472	2933	3271	3417	1961	*	1863
8	27.6	41.4	3208	3044	3416	2927	3238	3156	1918	*	1830
9	27.6	55.2	3490	3097	3692	2813	3010	3098	1820	*	1935
10	27.6	68.9	3439	3008	3568	2754	2937	3006	1833	*	1822
11	13.8	13.8	4448	3736	3883	3176	3720	3731	2081	*	1961
12	13.8	27.6	3844	2921	3586	2828	2874	3193	1993	*	1904
13	13.8	41.4	3510	2848	3616	2689	3026	3406	1868	*	1878
14	13.8	55.2	3406	2890	3639	2681	2957	3384	1847	*	1884
15	13.8	68.9	3292	2935	3702	2725	2967	3368	1818	*	1668

**Table 2.14 Continued**

Sequence #	$\sigma_3$ (kPa)	$\sigma_d$ (kPa)	Mr (MPa)					
			CS4- CM4- #1	CS4- CM4- #2	CS4- CM4- #3	CS4- CM5- #1	CS4- CM5- #2	CS4- CM5- #3
1	41.4	13.8	2567	3195	#	*	3184	3696
2	41.4	27.6	2603	3164	2647	*	2776	3190
3	41.4	41.4	2602	3031	2753	*	2879	2926
4	41.4	55.2	2660	3022	2852	*	2693	3139
5	41.4	68.9	2524	3084	2645	*	2740	2980
6	27.6	13.8	2667	2877	2809	*	3405	3624
7	27.6	27.6	2517	3014	2813	*	2649	3524
8	27.6	41.4	2479	3081	2867	*	2597	3205
9	27.6	55.2	2558	2997	2764	*	2686	3298
10	27.6	68.9	2533	3040	2722	*	2655	3184
11	13.8	13.8	#	2850	2626	*	2471	3447
12	13.8	27.6	2673	2937	2700	*	2605	3206
13	13.8	41.4	2628	2881	2655	*	2752	3298
14	13.8	55.2	2544	2922	2762	*	2492	3078
15	13.8	68.9	2495	2857	2671	*	2571	3031

\* Damaged specimen

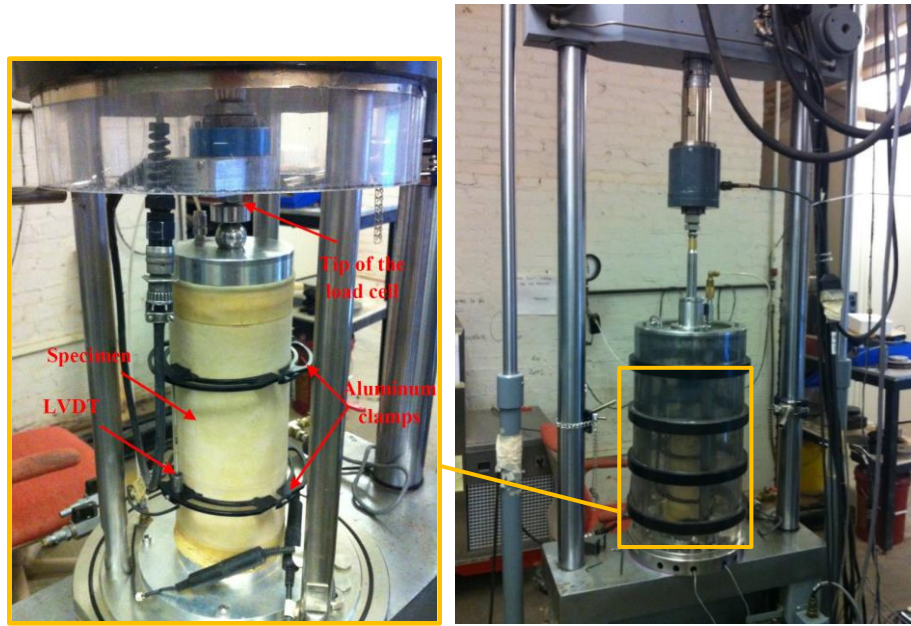
# Out of LVDTs' range

**Table 2.15 Characteristics and 28-day Regression Coefficients of the Additional Compacted Specimens of Soil from Case Study 3**

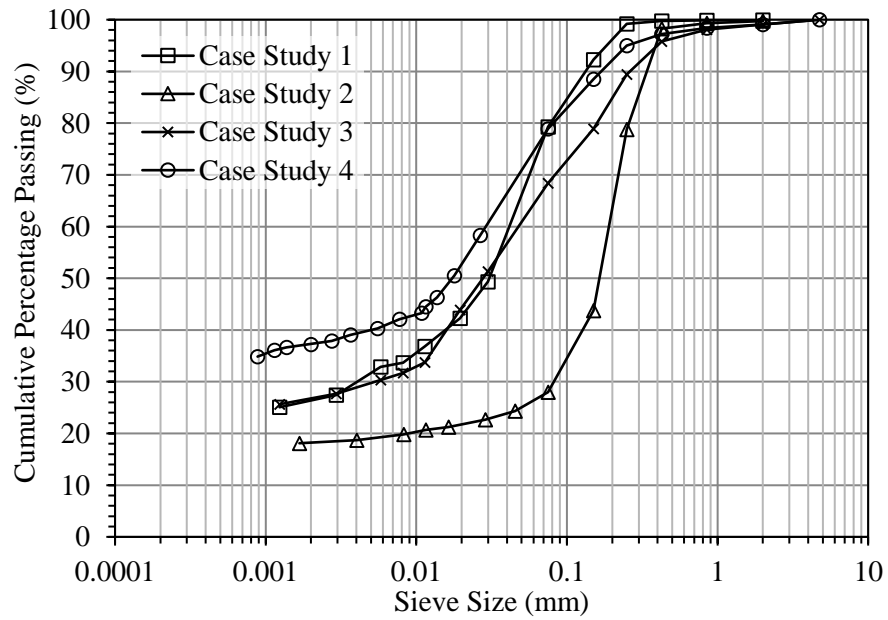
CM#	Specimen Code	% CKD (%)	w (%)	$\gamma_d$ (kN/m <sup>3</sup> )	Degree of Compaction % of $\gamma_{dmax}$	k <sub>1</sub>	k <sub>2</sub>	k <sub>3</sub>
1	CS3-CKD5-#1	5	13.6	17.9	100.6	7380.19	0.03506	-0.08322
	CS3-CKD5-#2		13.5	17.6	98.9	7149.48	0.03064	-0.08281
	CS3-CKD5-#3		13.8	17.8	100.1	6705.57	0.05545	-0.05981
2	CS3-CKD10-#1	10	14.4	17.5	100.1	19084	-0.03136	0.01391
	CS3-CKD10-#2		14.6	17.7	101.3	17494.2	0.00079	-0.02364
	CS3-CKD10-#3		14.4	17.3	99.0	17711.1	0.06659	-0.06771
3	CS3-CKD15-#1	15	15.1	17.1	99.1	26176.1	-0.07031	-0.04833
	CS3-CKD15-#2		15	17.2	99.7	21618.3	-0.11718	-0.17949
	CS3-CKD15-#3		14.9	17.4	100.9	26096.4	0.01106	-0.03536

**Table 2.16 Summary of  $M_r$  Values of Additional Compacted Specimens of Case Study 3 at 28-day Curing Period**

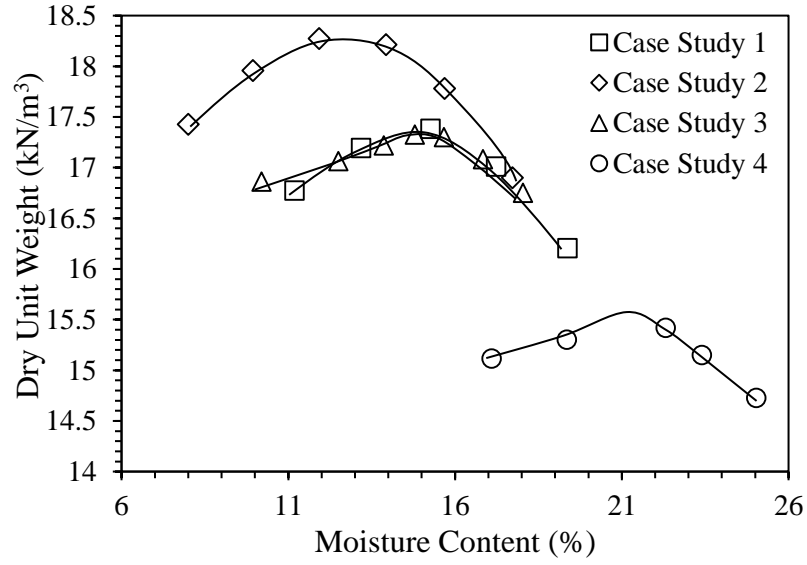
Sequence #	$\sigma_3$ (kPa)	$\sigma_d$ (kPa)	$M_r$ (MPa)								
			CS3- CKD5- #1	CS3- CKD5- #2	CS3- CKD5- #3	CS3- CKD10- #1	CS3- CKD10- #2	CS3- CKD10- #3	CS3- CKD15- #1	CS3- CKD15- #2	CS3- CKD15- #3
			#1	#2	#3	#1	#2	#3	#1	#2	#3
1	41.4	13.8	905	845	765	1938	1811	1993	2805	2137	2811
2	41.4	27.6	842	824	795	1917	1837	2088	2884	2614	2945
3	41.4	41.4	830	816	759	1879	1816	2077	2549	2696	2853
4	41.4	55.2	809	783	735	1815	1828	1946	2733	2430	2714
5	41.4	68.9	782	753	708	1855	1823	1908	2785	2412	2631
6	27.6	13.8	868	862	718	1778	1908	2125	2857	4117	2585
7	27.6	27.6	819	798	744	1986	1813	1931	2516	2638	2820
8	27.6	41.4	812	786	727	1902	1737	1868	2663	2288	2760
9	27.6	55.2	786	763	705	1894	1784	1864	2724	2329	2703
10	27.6	68.9	784	748	697	1881	1799	1865	2653	2343	2675
11	13.8	13.8	868	833	755	1773	1876	1928	3388	3544	2997
12	13.8	27.6	818	807	736	2081	1847	2001	2706	2606	2661
13	13.8	41.4	819	783	710	1967	1773	1857	2827	2216	2745
14	13.8	55.2	784	754	689	1916	1791	1847	2682	2369	2645
15	13.8	68.9	772	743	688	1866	1802	1868	2654	2493	2657



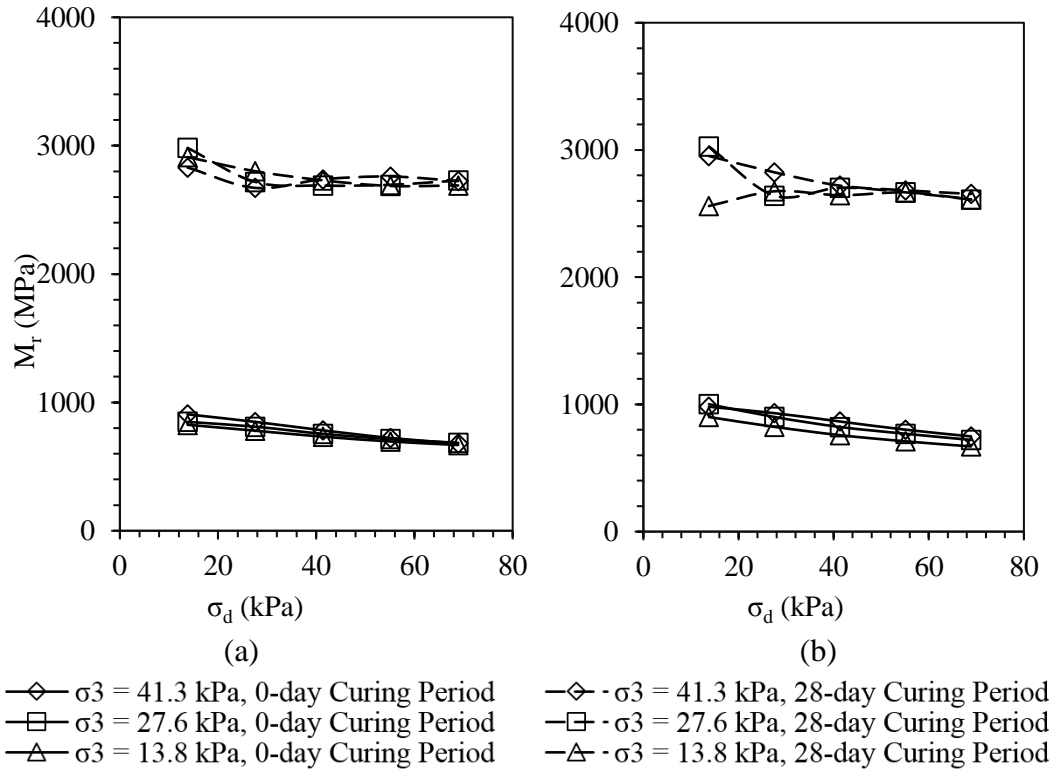
**Figure 2.1 Resilient Modulus Test Setup inside the MTS Frame**



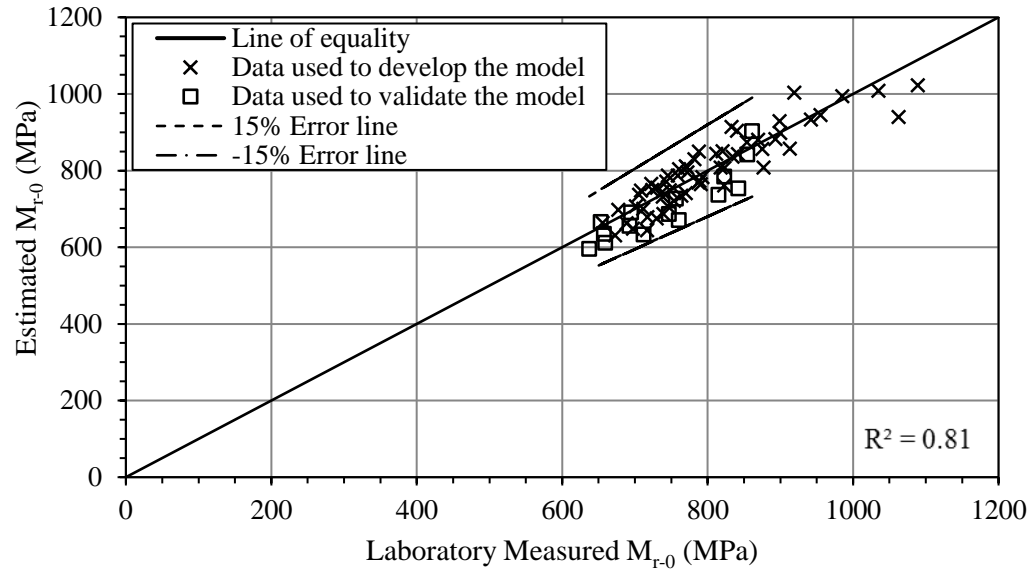
**Figure 2.2 Particle Size Distribution of the Subgrade Soils for Four Case Studies**



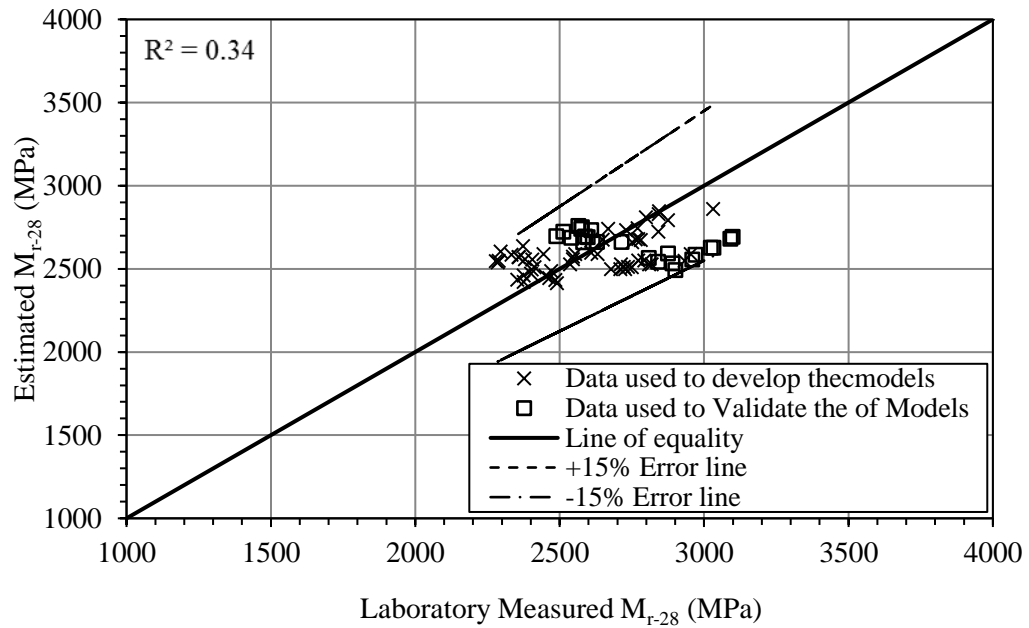
**Figure 2.3 Moisture-Dry Unit Weight Curve of Different Soil-Additive Mixtures**



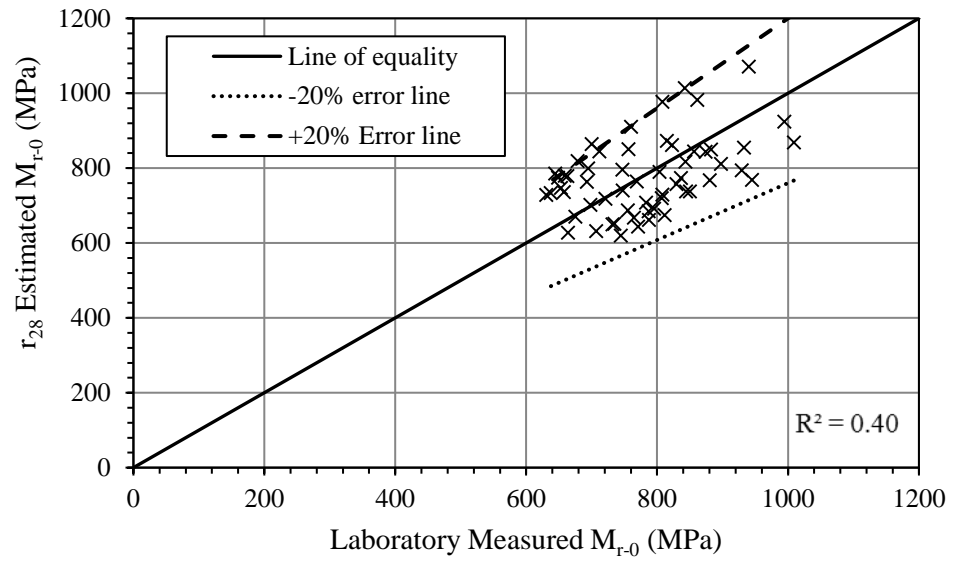
**Figure 2.4  $M_r$  versus Stress Level for Case Study 1 (a) CM1, and (b) CM2**



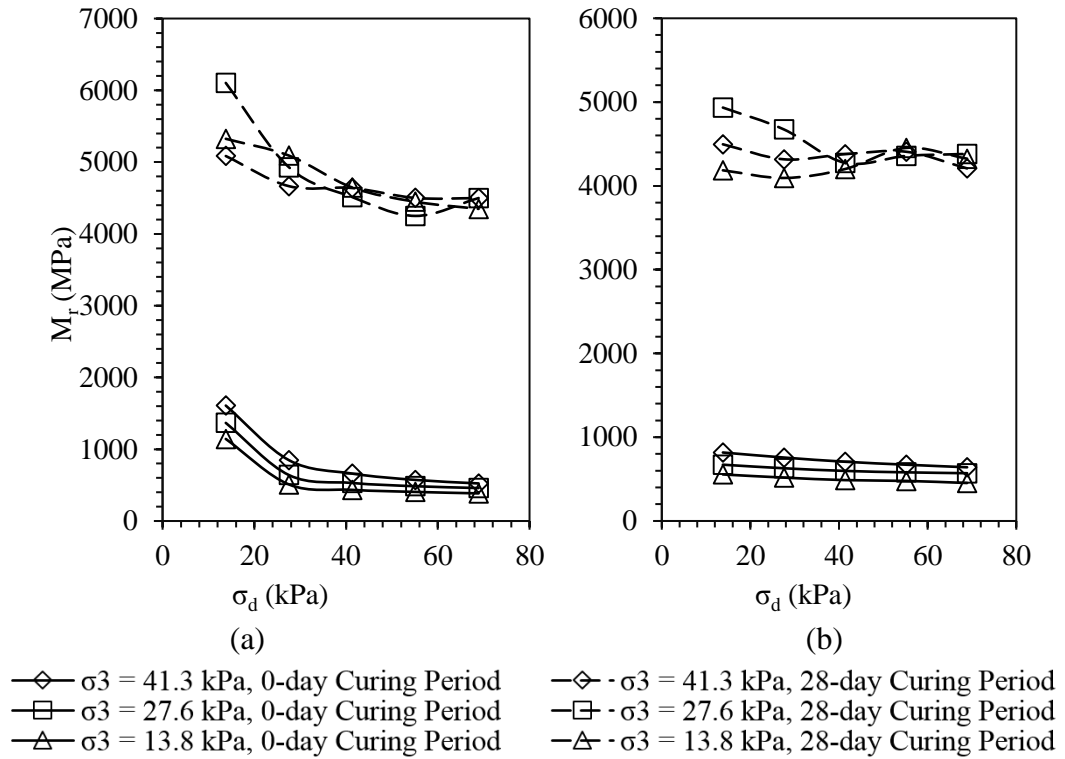
**Figure 2.5 Comparison Between Estimated and Laboratory Measured  $M_{r-0}$  for Case Study 1**



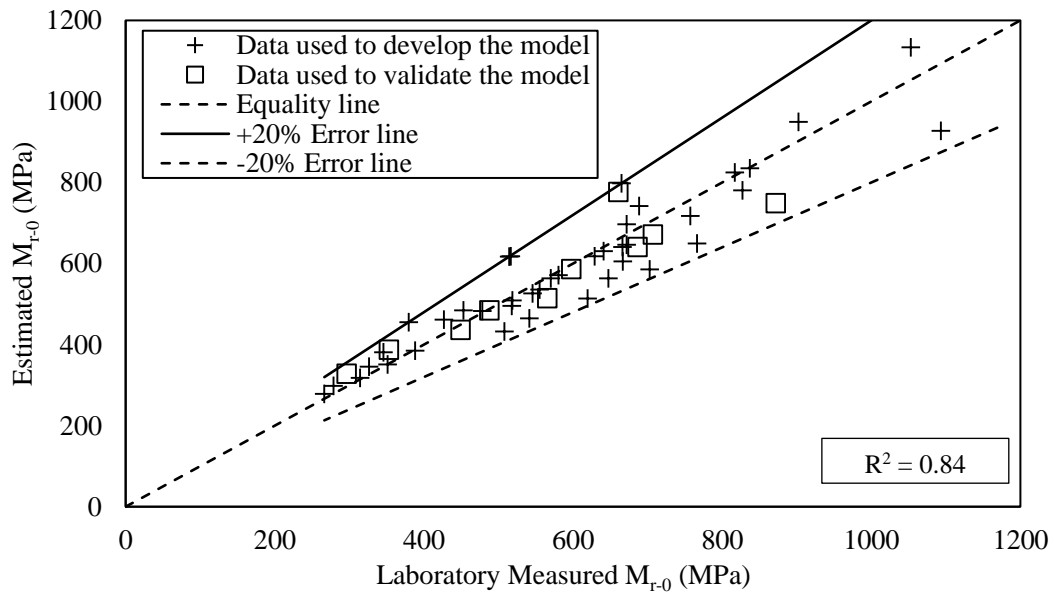
**Figure 2.6 Comparison Between Estimated and Laboratory Measured  $M_{r-28}$  for Case Study 1**



**Figure 2.7 Comparison Between Estimated  $M_{r-0}$  Using  $r_{28}$  Ratio and Laboratory Measured  $M_{r-0}$  for Case Study 1**

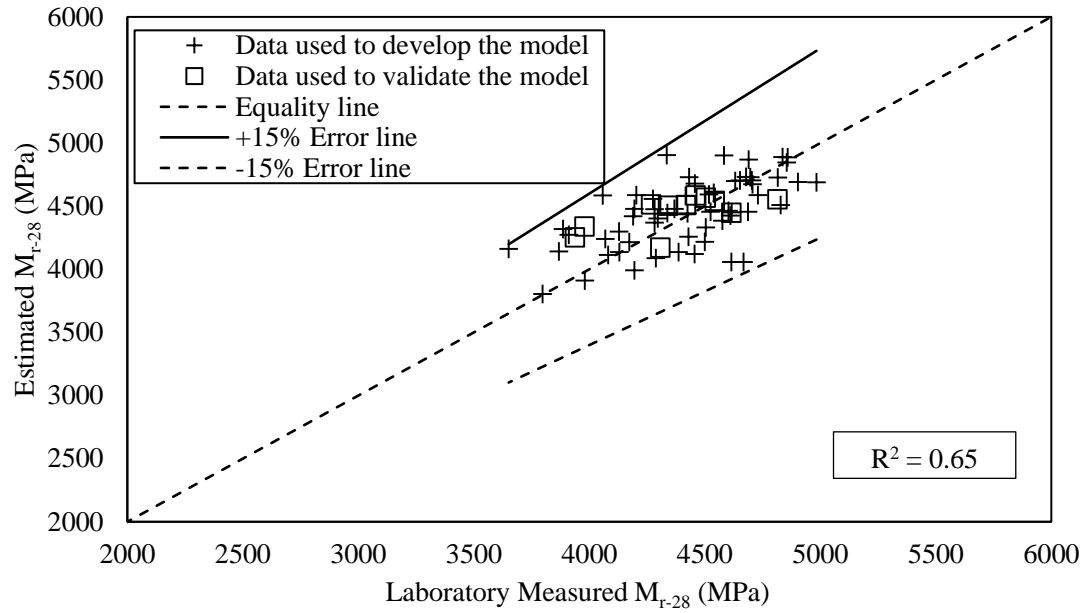


**Figure 2.8  $M_r$  versus Stress Level for Case Study 2 (a) CM1, and (b) CM2**

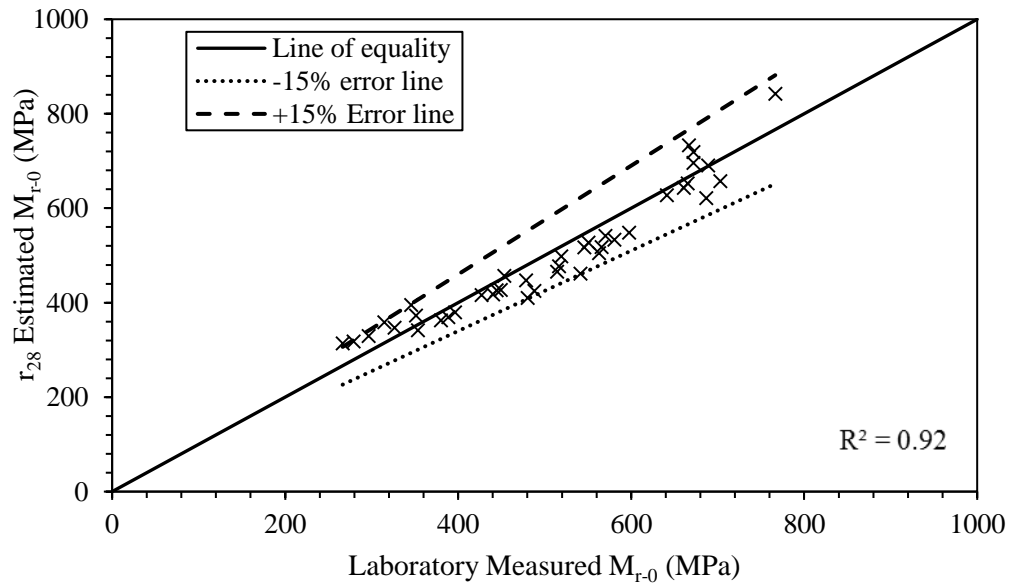


**Figure 2.9 Comparison Between Estimated and Laboratory Measured 0-day  $M_r$ -  
Case Study 2**

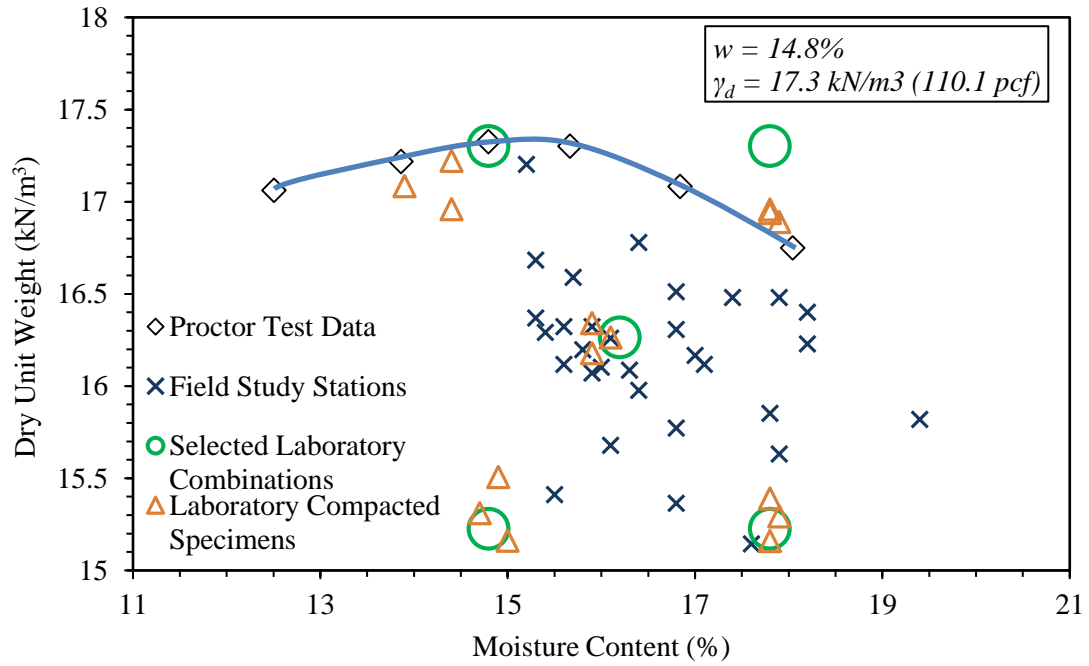




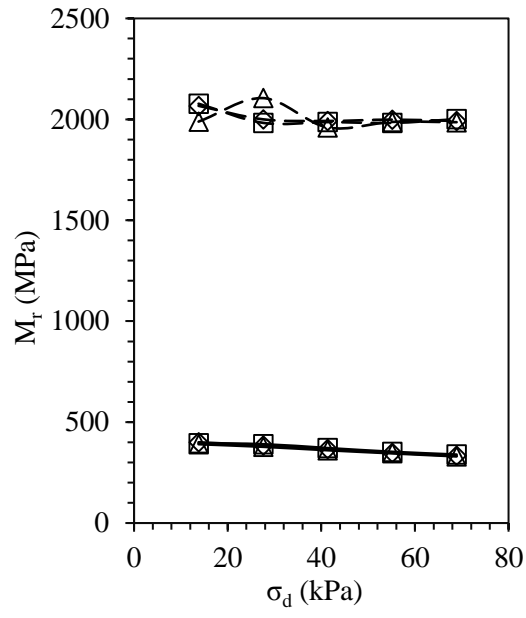
**Figure 2.10 Comparison Between Estimated and Laboratory Measured  $M_{r-28}$  for Case Study 2**



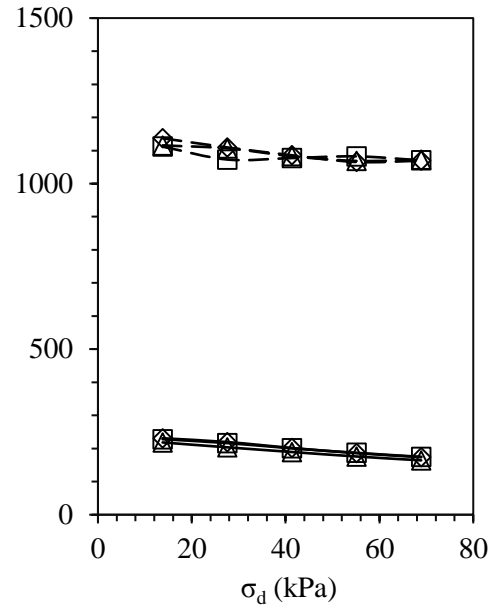
**Figure 2.11 Comparison Between Estimated  $M_{r-0}$  Using  $r_{28}$  Ratio and Laboratory Measured  $M_{r-0}$  for Case Study 2**



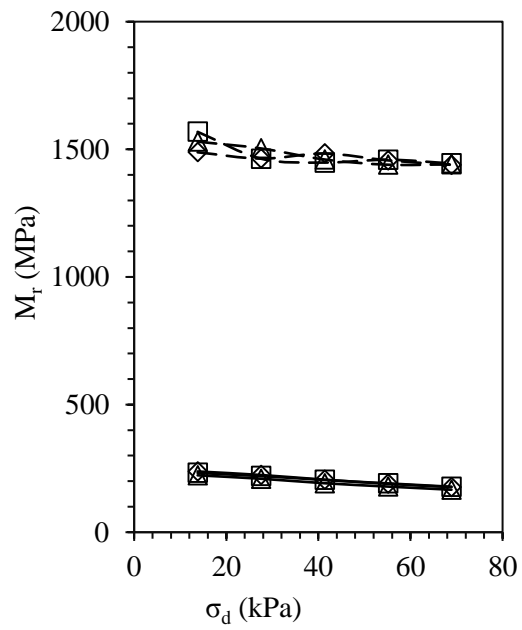
**Figure 2.12 Comparison of Field Measured  $w$  and  $\gamma_d$  Values with  $w$  and  $\gamma_d$  of the  $M_r$  Test Combinations and Specimens for Case Study 3**



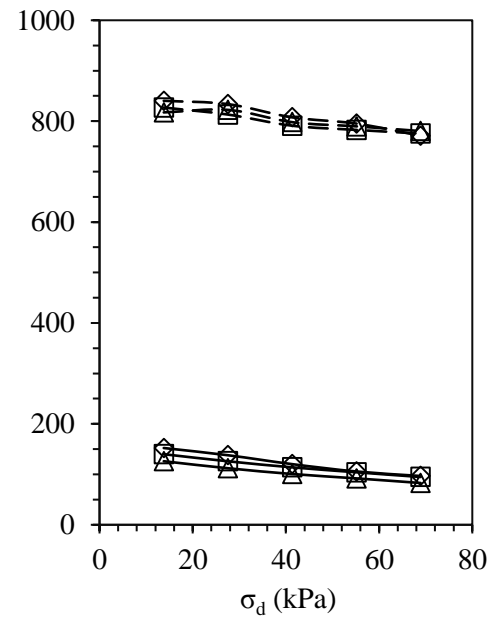
(a)



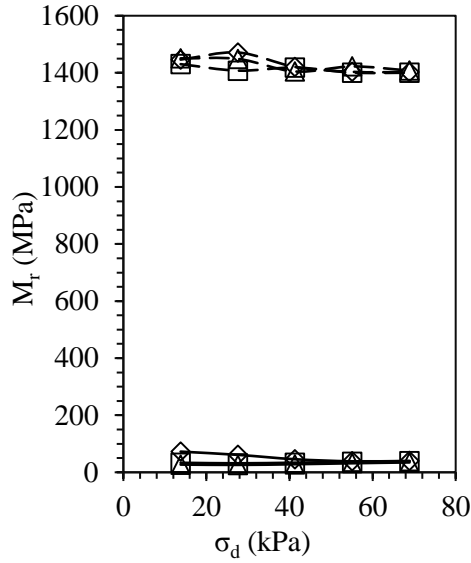
(b)



(c)



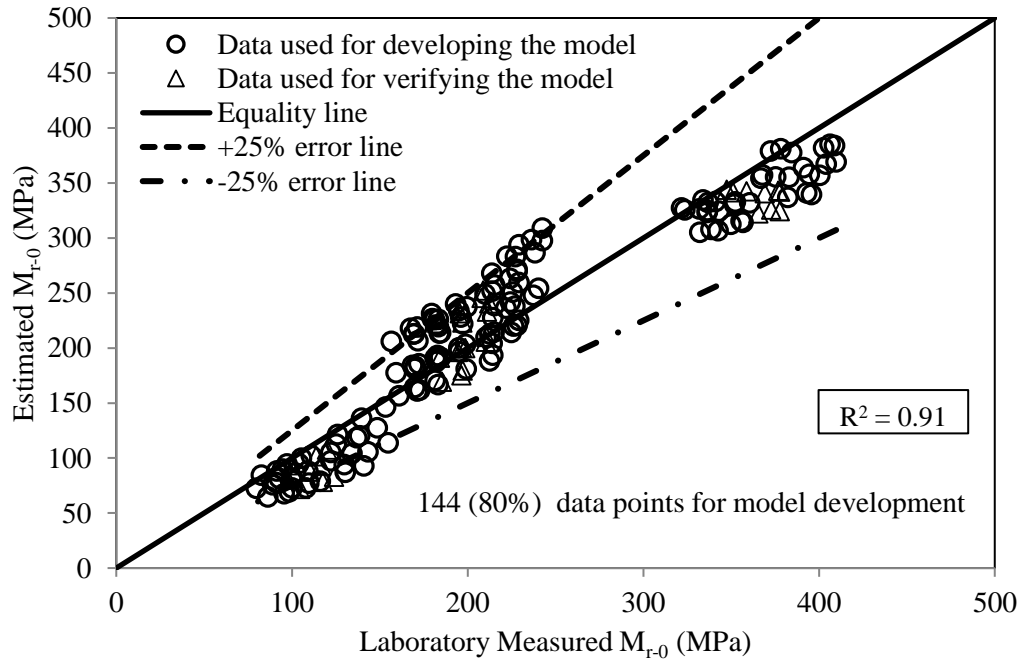
(d)



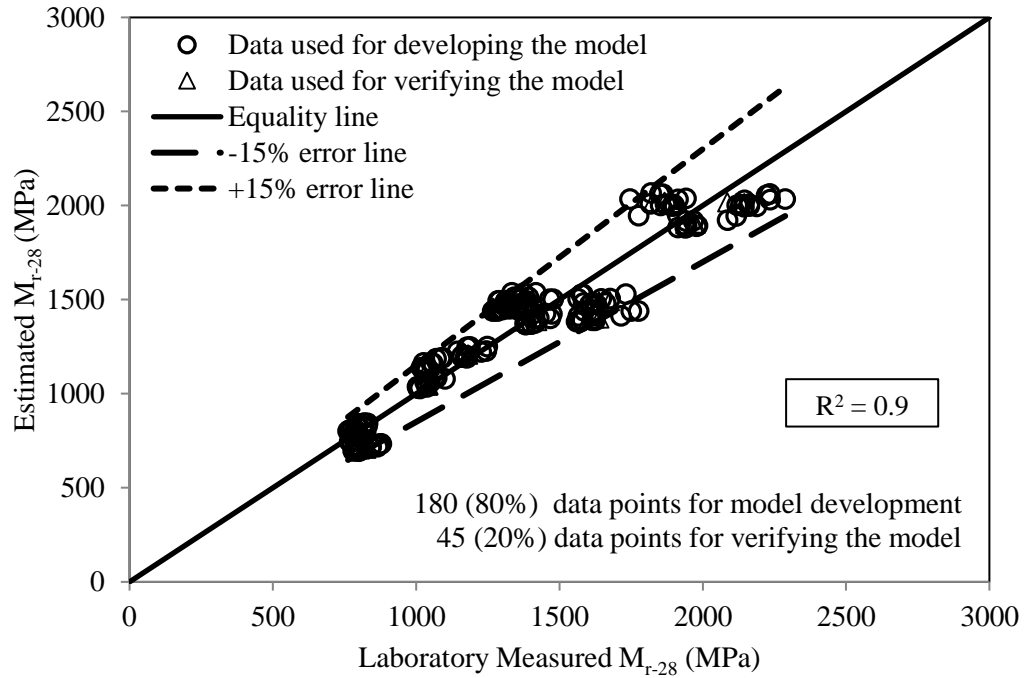
(e)

- |  |   |
|--|---|
| —◇— $\sigma_3 = 41.3$ kPa, 0-day Curing Period | —◇— $\sigma_3 = 41.3$ kPa, 28-day Curing Period |
| —□— $\sigma_3 = 27.6$ kPa, 0-day Curing Period | —□— $\sigma_3 = 27.6$ kPa, 28-day Curing Period |
| —△— $\sigma_3 = 13.8$ kPa, 0-day Curing Period | —△— $\sigma_3 = 13.8$ kPa, 28-day Curing Period |

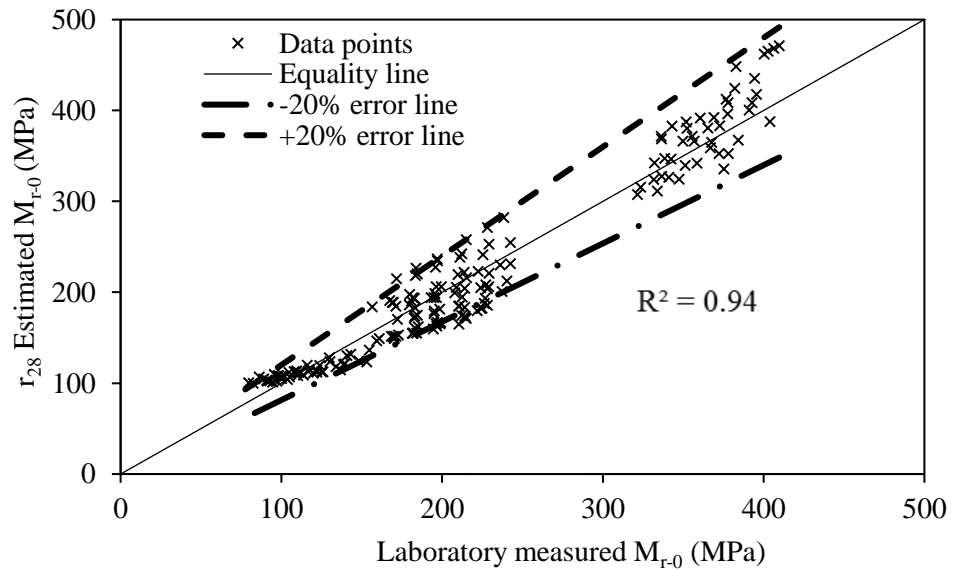
**Figure 2.13  $M_r$  versus Stress Level for Case Study 3 (a) CM1, (b) CM2, (c) CM3, (d) CM4, and (e) CM5**



**Figure 2.14 Comparison Between Estimated and Laboratory Measured  $M_{r-0}$  for Case Study 3**



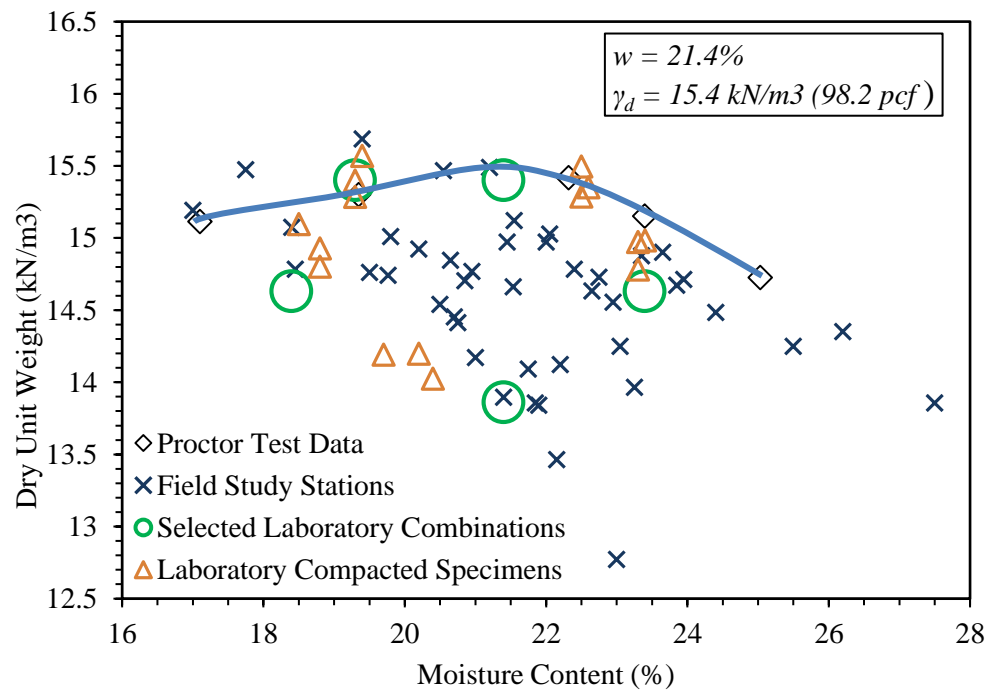
**Figure 2.15 Comparison Between Estimated and Laboratory Measured  $M_{r-28}$  for Case Study 3**



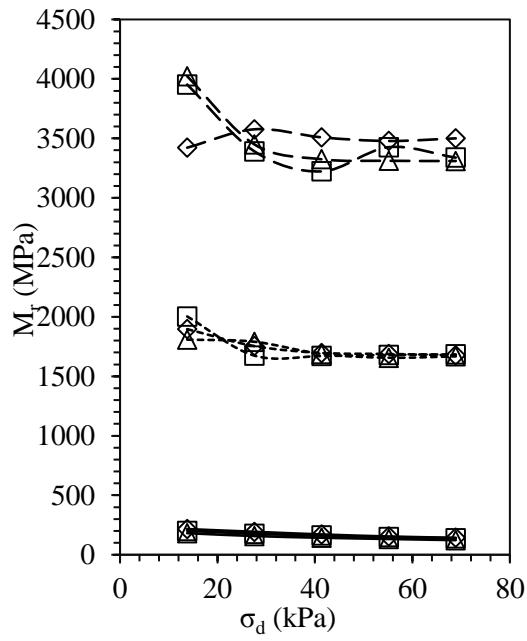
**Figure 2.16 Comparison Between Estimated  $M_{r-0}$  Using  $r_{28}$  Ratio and Laboratory Measured  $M_{r-0}$  for Case Study 3**



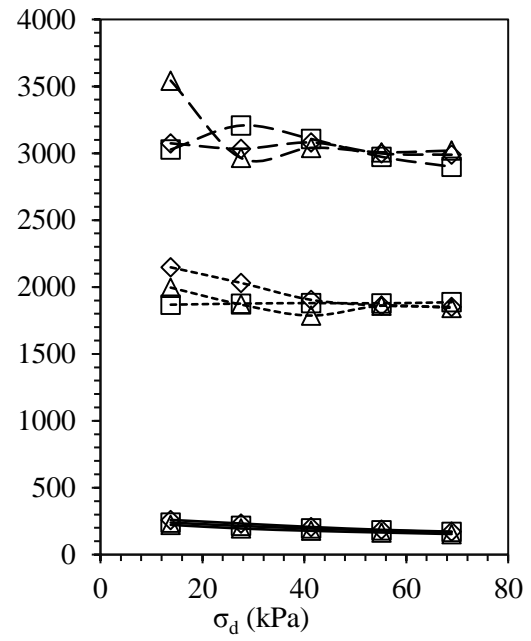
**Figure 2.17 Conditioning of Soil-Quick Lime Mixture in the Laboratory**



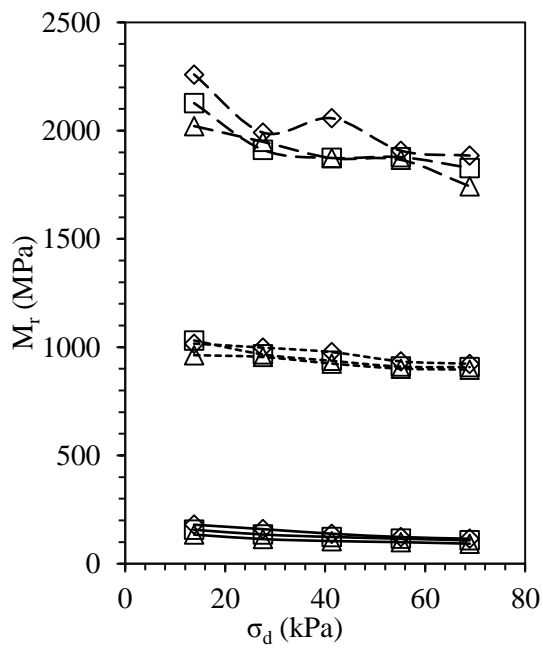
**Figure 2.18 Comparison of Field Measured  $w$  and  $\gamma_d$  Values with  $w$  and  $\gamma_d$  of the  $M_r$  Test Combinations and Specimens for Case Study 4**



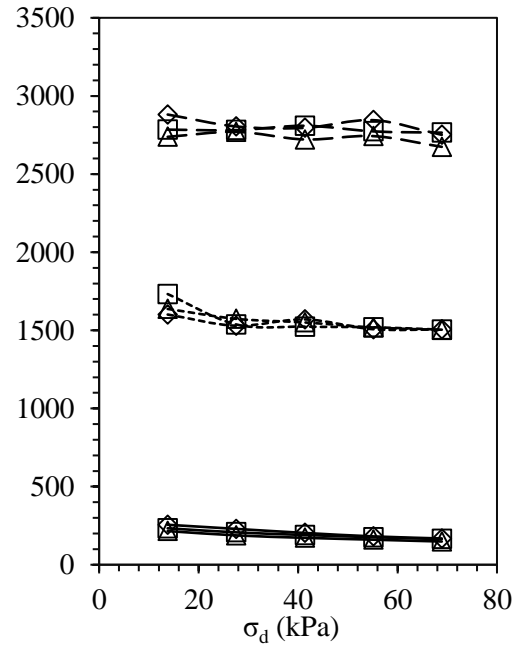
(a)



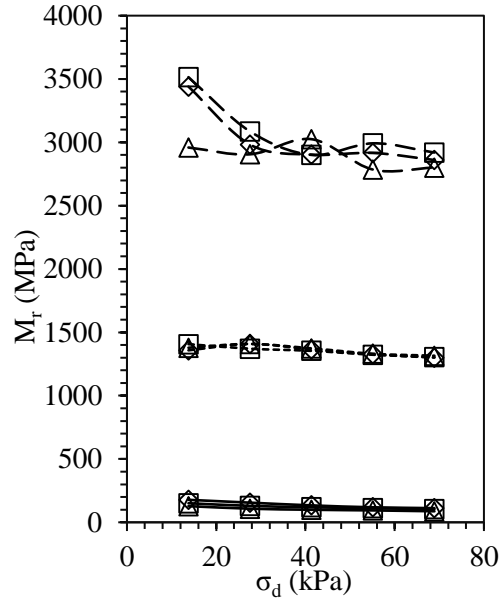
(b)



(c)



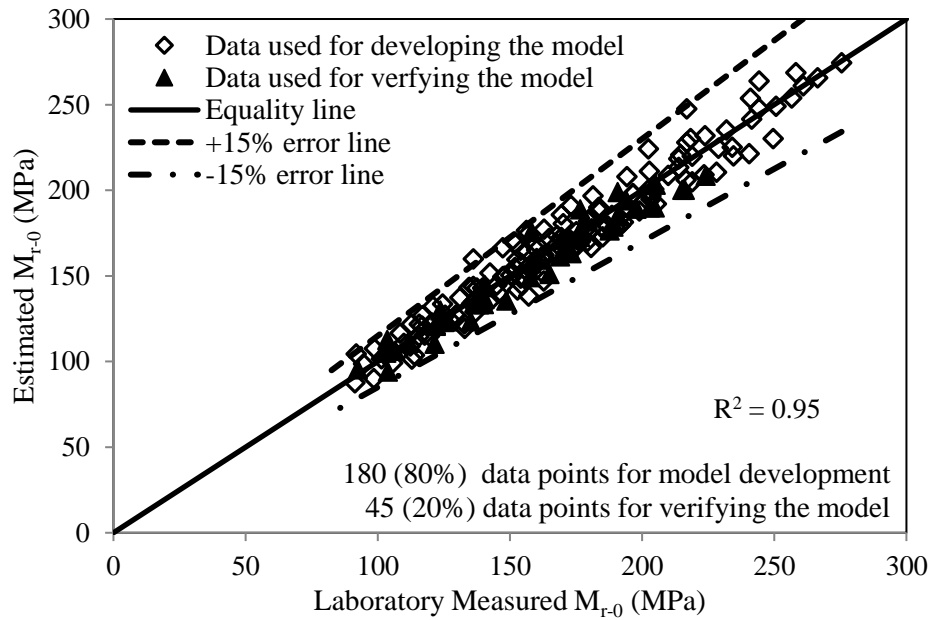
(d)



(e)

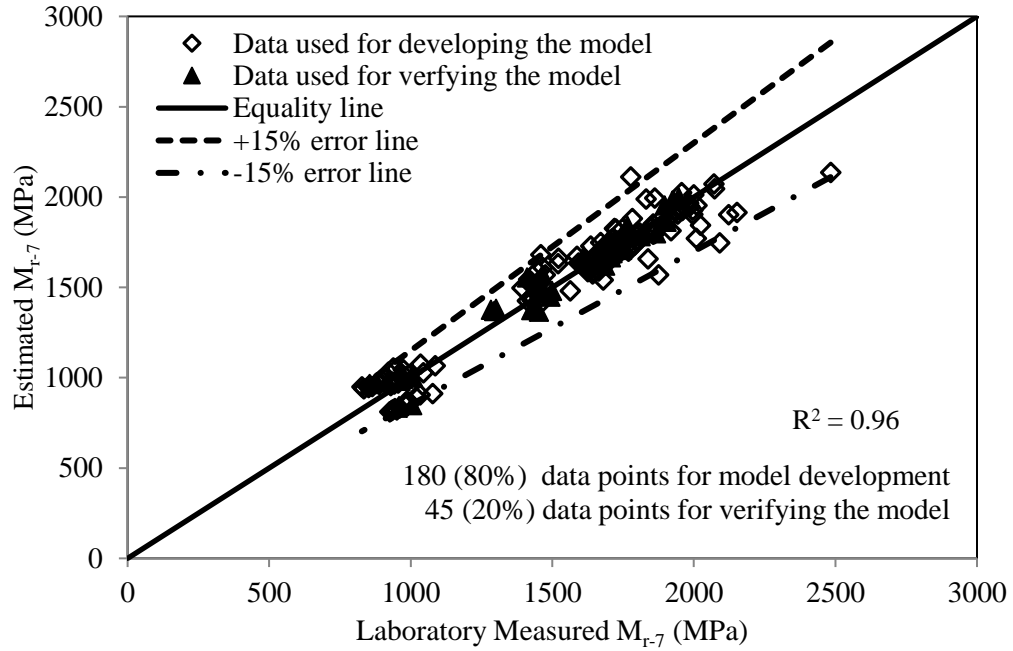
- $\diamond$   $\sigma_3 = 41.3$  kPa, 0-day Curing Period       $\diamond$   $\sigma_3 = 41.3$  kPa, 28-day Curing Period  
 $\square$   $\sigma_3 = 27.6$  kPa, 0-day Curing Period       $\square$   $\sigma_3 = 27.6$  kPa, 28-day Curing Period  
 $\triangle$   $\sigma_3 = 13.8$  kPa, 0-day Curing Period       $\triangle$   $\sigma_3 = 13.8$  kPa, 28-day Curing Period

**Figure 2.19  $M_r$  versus Stress Level for Case Study 4 (a) CM1, (b) CM2, (c) CM3, (d) CM4, and (e) CM5**

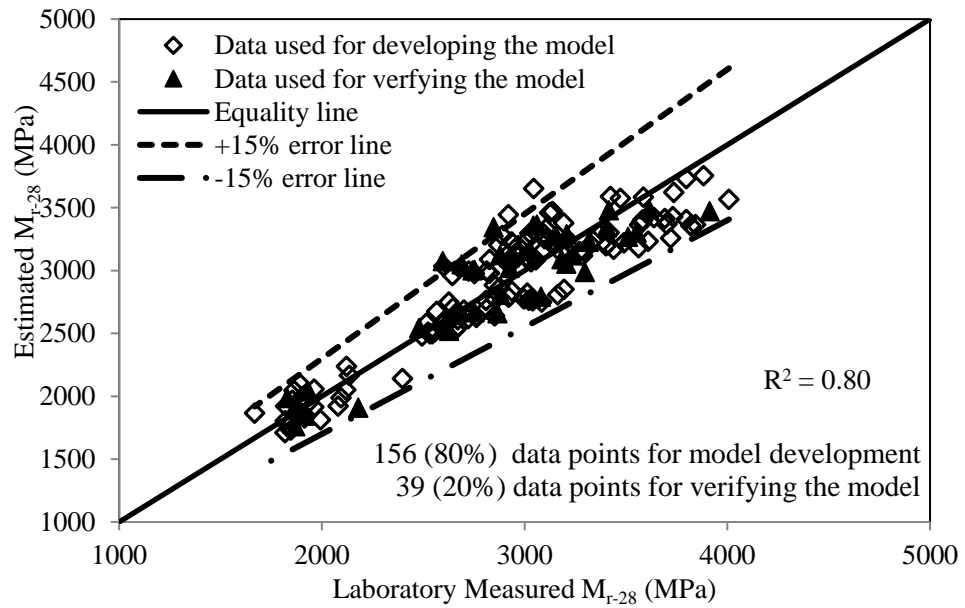


**Figure 2.20 Comparison Between Estimated and Laboratory Measured  $M_{r-0}$  for Case Study 4**

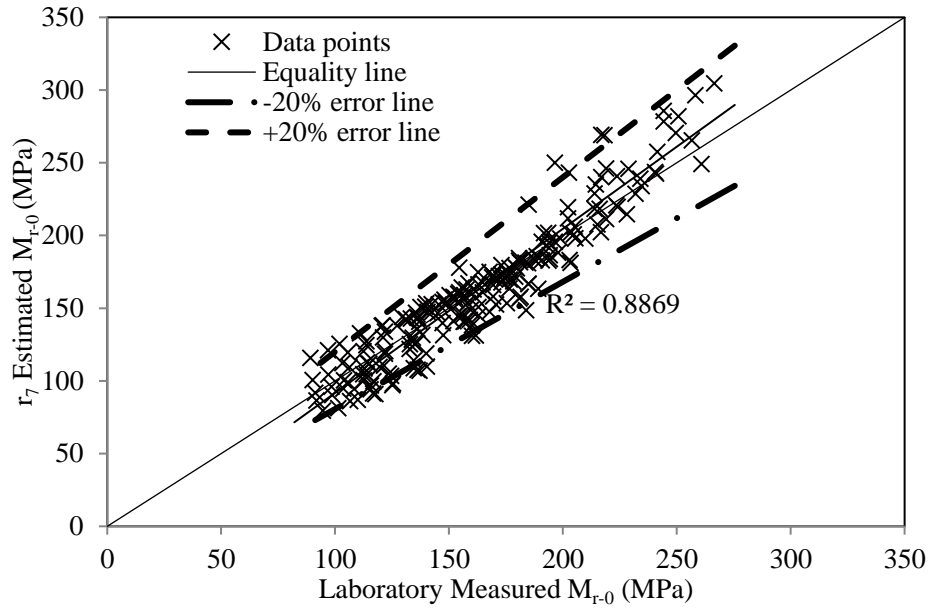




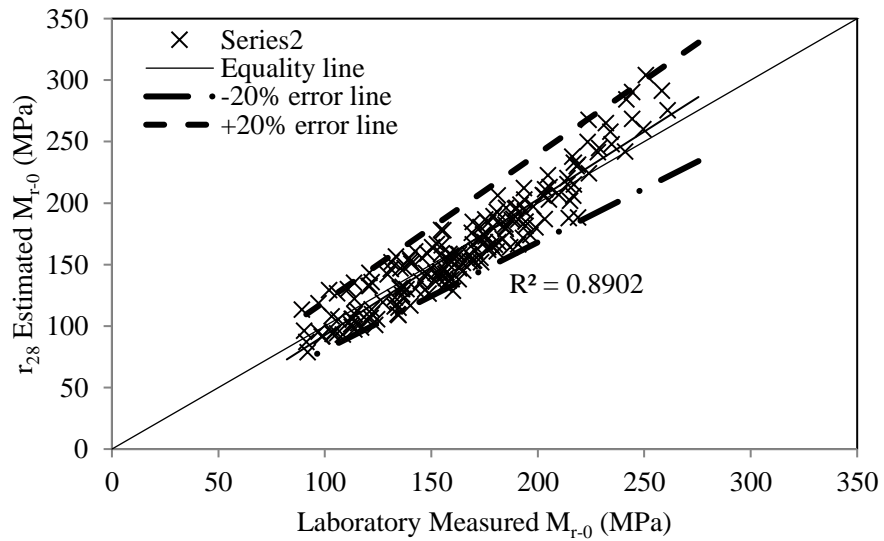
**Figure 2.21 Comparison Between Estimated and Laboratory Measured  $M_{r-7}$  for Case Study 4**



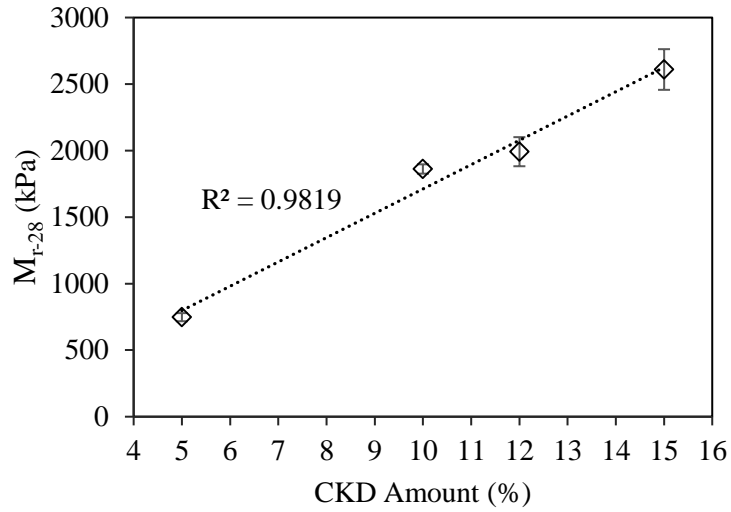
**Figure 2.22 Comparison Between Estimated and Laboratory Measured  $M_{r-28}$  for Case Study 4**



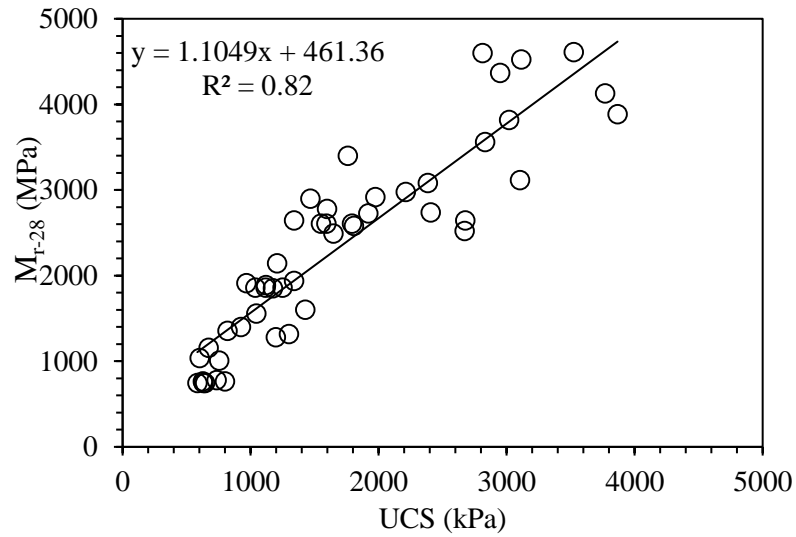
**Figure 2.23 Comparison Between Estimated  $M_{r-0}$  Using  $r_7$  Ratio and Laboratory Measured  $M_{r-0}$  for Case Study 4**



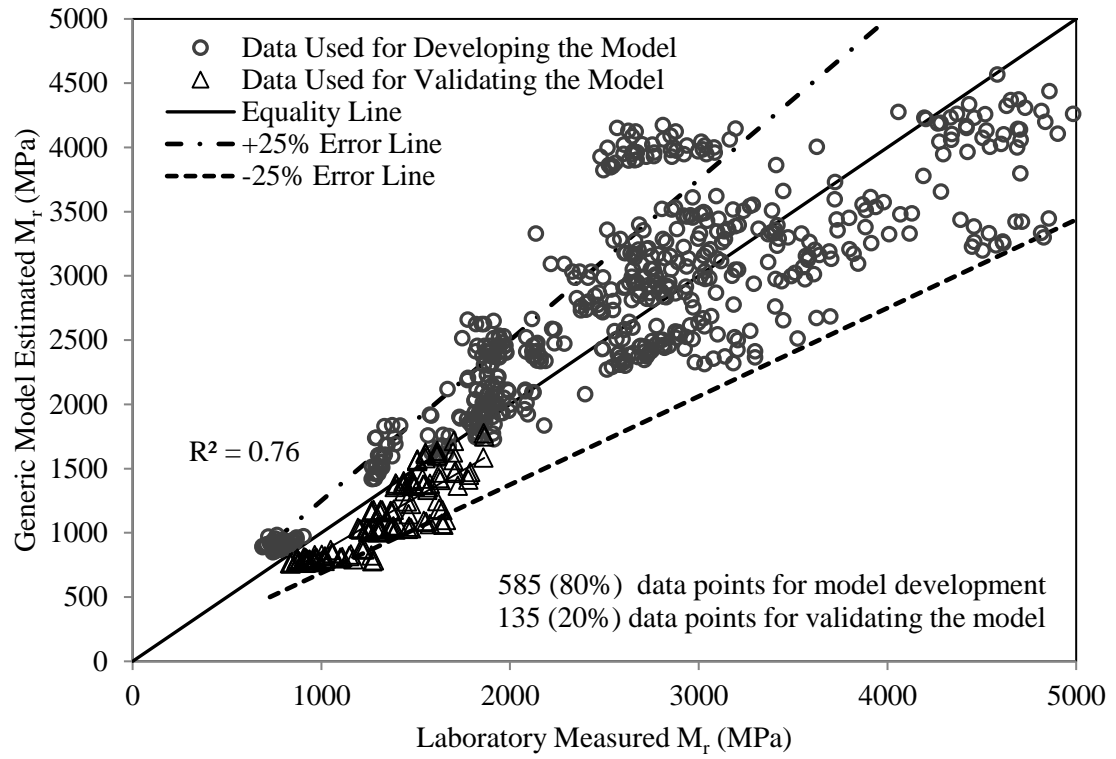
**Figure 2.24 Comparison Between Estimated  $M_{r-0}$  Using  $r_{28}$  Ratio and Laboratory Measured  $M_{r-0}$  for Case Study 4**



**Figure 2.25 Influence of CKD Amount on the  $M_{r-28}$  (at  $\sigma_d = 68.9$  kPa and  $\sigma_3 = 41.34$  kPa) of Stabilized Soil from Case Study 3**



**Figure 2.26 Relationship Between  $M_{r-28}$  (at  $\sigma_d = 68.9$  kPa and  $\sigma_3 = 41.34$  kPa) and UCS of all Specimens**



**Figure 2.27 Comparison Between  $M_{r-28}$  Calculated from the Generic Model and the Laboratory Measured  $M_{r-28}$**

## CHAPTER 3

### EVALUATION OF COMPRESSIVE MODULI OF STABILIZED SUBGRADE DURING COMPACTION USING THE ICA

#### 3.1 Introduction

Stiffness of chemically-stabilized subgrade layers is important to the durability and performance of pavements. Uniform and well compacted subgrade can reduce early deterioration of pavements. In the field, the last occasion of increasing the subgrade quality (stiffness and compaction level) is roller compaction, which is generally achieved through the passes of pad-foot roller followed by vibratory smooth drum roller (VSDR) (Proctor, 1933; Huang, 2004). The application of vibratory energy results in an increase in the density and modulus of the subgrade. Compaction also reduces the potential for changes in moisture, which significantly alter the strength of the subgrade (Lambe and Whitman, 1969; Das, 2008).

A major cause of pavement deterioration is insufficient quality control (QC) of pavement layers during construction (Schaefer et al., 2008). Traditionally, quality control of the subgrade is conducted after the completion of the VSDR proof rolling, and as such it is usually impossible to remediate the under-compacted areas. The current quality control tools and methods such as Dynamic Cone Penetrometer (DCP), Nuclear Density Gauge (NDG), Falling Weight Deflectometer (FWD) and Light Weight Deflectometer (LWD) measurements do not generally give a good assessment of the modulus (Little, 1996; Siekmeier et al., 2000; Lenke et al., 2001; Nazarian et al., 2003; Hoffman et al., 2004; Camargo et al., 2006; and Mooney and Rinehart, 2007). The other major

shortcoming of these equipment is that they are spot-testing devices that typically assess less than 1% of the constructed subgrade (Mooney and Rinehart, 2007).

The importance of developing an in-situ test that can measure strength and stiffness of stabilized subgrade layer was highlighted by Petry and Little (2002) and in the Transportation Research Board Research Needs Statement (TRB, 2009). The ability to assess the modulus of subgrade during compaction for the entire subgrade enables the identification and remediation of under-compacted zones prior to the construction of the other layers such as aggregate base and asphalt. In the present study, the development of intelligent compaction techniques to estimate the moduli of chemically-stabilized subgrades during compaction was investigated in four case studies (i.e., CS1, CS2, CS3, and CS4, discussed in Chapter 2).

### **3.2 Background of Intelligent Compaction Methods**

A review of previous studies reveals that no widely accepted field procedure is available to evaluate the moduli of the chemically-stabilized subgrade during compaction (Little, 1996; Siekmeier et al., 2000; Lenke et al., 2001; Nazarian et al., 2003; Hoffman et al., 2004; Camargo et al., 2006; and Mooney and Rinehart, 2007). DCP, Soil Stiffness Gauge, Plate Loading Test, Clegg Impact Hammer, California Bearing Ratio (CBR), FWD and LWD tests were conducted in these studies to evaluate the quality of compaction in stabilized subgrade layers. As stated previously, these methods have major limitations and cannot properly evaluate the quality of compaction for the entire stretch of the construction.

Intelligent Compaction (IC) of subgrade layers has been proposed in recent years to address the shortcomings of conventional quality control (Camargo et al., 2006; Chang et al., 2011). The IC techniques use accelerometers mounted on the frame of the roller to collect and analyze the vibrations of the roller during compaction. These vibration data are then processed using modern signal processing techniques to estimate the stiffness of the material being compacted. Global positioning system (GPS) receivers are used to record the location of the roller at each instant (pass) and these readings are used to provide as-built maps showing process information such as number of roller passes, roller path, and subgrade stiffness in real-time to the operator. Access to compaction quality data in real-time enables the roller operator to detect and correct any under-compacted zones on the subgrade and thereby improve the quality of construction. The IC techniques can help improve the productivity of the crew by reducing the amount of rework, improving the overall compaction quality of the subgrade, and leading to lower maintenance costs of the pavement (Chang et al., 2011).

Currently, there are several manufacturers offering the IC technology in the market notably, Compaction Information System (Sakai, 2013), Bomag Variocontrol (Bomag, 2013), Ammann Compaction Expert (Case, 2013), AccuGrade (Young and Oetken, 2013), and Dynapac Compaction Analyzer (Dynapac, 2013). These devices are mounted on the roller, and can collect and analyze the roller vibrations to estimate the level of compaction. A broader use of these devices in the quality control of subgrade compaction is still under investigation (Chang et al., 2014; Hu et al., 2016; and Kumar et al., 2016). The existing IC technology provides a measure of stiffness in terms of a Roller Measurement Value (RMV). Research is still underway (Mooney et al., 2011; Heersink

et al., 2013; and Kumar et al, 2016) to establish good correlations between RMV and the stiffness estimated by the conventionally available measurements such as FWD, DCP and laboratory resilient modulus.

### **3.3 The University of Oklahoma Intelligent Compaction Analyzer (ICA)**

The Intelligent Compaction Analyzer (ICA) is a roller mountable device that can capture the vibrations of the roller during compaction of a pavement layer. Using the knowledge (properties discussed in Chapter 2) of stabilized subgrade, the ICA can estimate the level of compaction/modulus of the layer. The ICA technology was developed at the University of Oklahoma during 2003-2009 under the name of the IACA (Intelligent Asphalt Compaction Analyzer), with support from the Oklahoma Center for the Advancement of Science and Technology (OCAST) (Commuri and Zaman, 2008). The IACA was aimed to give a continuous estimate of the asphalt pavements' density with an accuracy comparable to spot density measurement tools ( $\pm 1.5\%$  of the actual density). The IACA was later advanced to estimate the dynamic modulus of asphalt pavements on a continuous stretch during compaction (Singh et al., 2011). Subsequently, the IACA was modified to enable assessment of compaction quality of chemically-stabilized subgrades during construction.

The ICA is based on the hypothesis that the vibratory roller and the underlying pavement layer form a mechanically coupled system. The response of the roller is determined by the frequency of the vibratory motors and the natural vibratory modes of the coupled system. The vibration of the roller varies with the stiffness of the underlying subgrade layer being compacted. The analysis of the vibration spectra of the roller can,



therefore, be used to estimate the stiffness of the pavement layer(s). A GPS-based documentation system is installed for continuous recording of the spatial position of the roller. A user interface is incorporated to display the real time operational parameters like compaction level, roller pass, roller direction, GPS location of the roller, and a color coded map of compaction level at each location (Figure 3.1-a).

The functional modules of the ICA are shown in Figure 3.1-b (Commuri and Zaman, 2008). The sensor module (SM) in the ICA consists of an accelerometer for measuring the vibrations of the compactor during compaction. A user interface for specifying the amplitude and frequency of the vibration motors and for recording the soil type is also a part of the SM. The feature extraction (FE) module computes the Fast Fourier Transform of the input signal and extracts the features corresponding to vibrations at different salient frequencies. An Artificial Neural Network (ANN) classifier is a multi-layer Neural Network that is trained to classify the extracted features so that each class represents a vibration pattern specific to a pre-specified level of compaction. The Compaction Analyzer (CA) then post-processes the output of the ANN and estimates the stiffness in real time.

In order to extend the ICA to estimate the stiffness of chemically-stabilized subgrade, the ICA has to be first trained to extract salient features of the vibration spectra of the roller during compaction. Further, the neural network has to be trained to classify the observed features into predetermined groups. Finally, the compaction analyzer should be designed such that it can estimate the modulus value representing the under-compaction subgrade stiffness (Imran, 2016). These features could be achieved by correlating the laboratory results of resilient modulus tests to the vibration records during

compaction in the field. This chapter focuses on the procedure that was developed to calibrate and validate the ICA measured moduli using laboratory developed regression models.

### 3.4 Methodology

The evaluation of the ICA's ability to estimate the moduli of chemically-stabilized subgrades was achieved through combining a set of field investigations, laboratory tests and regression analyses. The overall study included four case studies involving four different pavement construction projects in Oklahoma. The following steps were used in the calibration and validation of the ICA for each case study:

- Identification of construction site and material collection;
- Laboratory resilient modulus tests;
- Development of regression models to estimate  $M_r$ ;
- Organization of field investigation plan;
- Calibration of the ICA and vibratory data collection,
- Field measurements (NDG, DCP and FWD) measurements; and
- Validation of the ICA results using developed regression models and field measurements.

The first three steps, including the development of regressions models to estimate  $M_r$ , based on laboratory test data, were discussed in Chapter 2. In this chapter, the procedure for using the developed regression models in calibration and validation of the ICA is explained.

### ***3.4.1 Organization of the Field Investigation Plan***

As mentioned in Section 2.3.1, four pavement construction projects were identified prior to commencement of subgrade compaction. For each project, on the day of the subgrade compaction, the construction plan and the vibratory smooth drum roller's (VSDR) paths were identified in collaboration with the construction personnel and the roller operator. For each case study, the following order was used in the construction:

- Preparation of the subgrade surface (conducted days before the compaction);
- Spread of the chemical additive (CKD) by spreader trucks (according to the soil-CKD mixture design);
- Spraying of water and mixing the CKD with the soil by a rotary mixer (with a target moisture content of  $w_{opt}$ );
- Initial pad-foot roller compaction followed by leveling by a motor grader;
- Proof rolling by VSDR passes; and
- Frequent water spraying of the compacted subgrade to account for the moisture loss due to evaporation.

The ICA measurements were taken during the VSDR compaction. Hence, the time interval before the proof rolling was used to install the ICA on the VSDR and to establish and finalize the field investigation plan. Also, the important dimensions of the VSDR, such as drum's width, distance between the GPS device and the drum's axle, and the manufacturer and model of the roller were recorded. This information was used in the calibration of the ICA (Imran, 2016).

A layout of the field investigation plan was prepared according to the VSDR's perceived path, and the length and width of the strip under construction. Before and

during compaction, the stations for complementary field measurements were marked by aerosol paint on the surface and labeled poles on the road side (Figure 3.2). The test stations were divided into three categories:

- Calibration points– Three test stations within a 10-meter-long stretch. These points were intended for the calibration of the ICA.
- Random points– The stations selected throughout the construction strip. These points were intended to represent the variation of the subgrade modulus along the strip.
- Soft points– The stations on zones with relatively low moduli, identified by the ICA during VSDR compaction.

The calibration points and the random points were marked before the beginning of proof rolling. While, the soft points were detected during the proof rolling, according to the ICA-estimated moduli.

### ***3.4.2 The ICA Calibration***

The calibration of the ICA was performed by compacting a 10-meter-long strip (including the three calibration points), known as the calibration strip, through multiple passes of the ICA-equipped VSDR. A preliminary calibration was performed using the vibration measurements and the initial and target  $M_r$  values. After each pass of the roller,  $w$  and  $\gamma_d$  measurements were taken at the three calibration points using a NDG device (Humboldt HS-5001EZ122). Once no considerable improvement in the density was observed, the compaction of the calibration stretch was stopped.

The NDG measured values of  $w$  and  $\gamma_d$  were used in the corresponding regression models (Equation 2.6) to calculate regression coefficients  $k_1$ ,  $k_2$ , and  $k_3$ . Subsequently,

the resilient modulus of the subgrade was estimated using Equation 2.2. According to Mooney and Rinehart (2009), for a clayey soil, the average induced vertical stress ( $\sigma_1$ ) beneath the drum at the peak drum deflection is 100 kPa. Also, the corresponding induced horizontal stress at the direction of the drum's axle ( $\sigma_3$ ) is about 40 kPa. Table 3.1 compares the important characteristics of the VSDR used in Mooney and Rinehart's (2009) study with the VSDRs used in the current study. It can be seen that the specifications of all three roller types are comparable. Hence, it was concluded that the  $\sigma_1$  and  $\sigma_3$  values determined by Mooney and Rinehart (2009) were applicable for estimating the stress level beneath the VSDR in all four case studies pursued herein. Accordingly, the deviatoric stress ( $\sigma_d = \sigma_1 - \sigma_3$ ) and confining pressure ( $\sigma_3$ ) were approximated as 60 kPa and 40 kPa, respectively. According to Table 2.1, Sequence #5 has the closest stress levels to these values ( $\sigma_d = 68.9$  kPa and  $\sigma_3 = 41.4$  kPa). The collected vibration data along with the estimated resilient modulus according to the NDG readings at the three calibration points were used for the final calibration of the ICA (Commuri et al., 2009).

### ***3.4.3 The ICA Measurements***

After calibrating the ICA, the VSDR was allowed to conduct regular compaction throughout the entire stretch of construction. At this stage, the VSDR's operator was asked to follow the conventional proof rolling practice. During compaction, the recorded vibration data were used to estimate the moduli of subgrade underneath the drum in real time. Other operational settings of the VSDR such as the speed was recorded during the compaction. Using the onboard GPS, connected to the ICA, geographic coordinates (longitude and latitude) were assigned to each modulus value. Using the geographic

coordinates system, the modulus values could be mapped on the  $x - y$  plane and used to produce the as-built map of the subgrade moduli.

#### ***3.4.4 Identification and Remediation of Under-compacted Zones***

For CS3 and CS4, the ability of the ICA in the identification and remediation of the under-compacted zones of the subgrade was evaluated. During the conventional compaction, the zones at which the ICA readings showed significantly lower modulus values, were identified and marked as soft points by labeled poles.

After completion of the conventional proof rolling, the operator was asked to conduct additional passes (with vibration) over the under-compacted zones. The ICA-estimated moduli ( $M_{ICA}$ ) was monitored during the remedial compaction. The compaction procedure was finished when no significant changes in the  $M_{ICA}$  were observed in the under-compacted zones (usually after 3 to 4 additional passes).

#### ***3.4.5 Complementary Field Measurements and Validation of the ICA-Estimated Moduli***

After completion of the compaction process, NDG measurements were taken at all of the marked stations, including the random points and the soft points (Figure 3.3-a). For this reason, two measurements were taken at each test station. The source rod of the NDG was adjusted at mid-depth of the chemically-stabilized subgrade layer (usually 102 or 152 mm). After each measurement, the values of moisture content and dry unit weight were recorded. Two measurements were taken at each station and the average was recorded as  $w$  and  $\gamma_d$  for that station. As previously stated in Sections 3.4.2 and 3.4.4, additional NDG measurements were taken at the calibration points before the conventional compaction and at the under-compacted zones before the remedial

compaction. The NDG measured  $w$  and  $\gamma_d$  were used to estimate the  $M_r$  of test stations using the regression models discussed in Chapter 2.

To compare the ICA-estimated moduli with conventional quality control methods, FWD and DCP tests were conducted at random points at the site when feasible (Figures 3.3-b and 3.3-c). For CS4, the DCP measurements were taken on the day of compaction. Also, FWD tests were conducted for CS1 and CS4, 28 days and 7 days after the compaction, respectively.

The ICA-estimated modulus values were compared with the estimated  $M_r$  values obtained from the regression models. In addition, the stabilized subgrade moduli obtained from the ICA ( $M_{ICA}$ ) were compared with the back-calculated FWD moduli and DCP index values obtained from the FWD and DCP tests.

### **3.5 Case Study 1 (CS1): 60<sup>th</sup> Avenue Northwest Project**

#### ***3.5.1 Construction Site Identification***

As mentioned in Section 2.4.1, the first case study (CS1) was performed at the 3.4 kilometers-long full-depth asphalt pavement construction site located at 60<sup>th</sup> Avenue Northwest, Norman, OK. This stretch was located between Tecumseh Road and Franklin Road in Northwest Norman. The subgrade soil was stabilized by mixing 10% CKD to a depth of 202 mm (8 inches). A summary of the subgrade properties was presented in Table 2.2. An Ingersoll-Rand SD-105DX VSDR was used for proof rolling of the subgrade. This roller is a single smooth drum roller. The specifications of the VSDR are presented in Table 3.1. The base layer over the subgrade consisted of two asphalt layers, the thickness of each layer being 90 mm (3.5 inch). The surface course was a 51-mm (2-

inch) thick layer, comprising of a S4 mix containing a PG 76-28 OK binder. In this project FWD measurements were taken one month after construction of the stabilized subgrade.

### ***3.5.2 ICA Measurements and Identification of Test Stations***

The ICA was calibrated and vibration data were collected on a 1 kilometer-long stretch of the construction project. Twelve test stations were marked on the compacted stretch. The first three stations, marked on a 10-meter-long strip, were taken as the calibration points. The locations of the test stations are shown in Figure 3.4.

NDG measurements were taken at all 12 test stations. A summary of the  $w$ - $\gamma_d$  measurements is presented in Table 3.2. The degree of compaction at each test location was determined using the laboratory determined  $\gamma_{dmax}$  for the CKD-stabilized soil from Table 2.2 ( $\gamma_{dmax} = 17.3 \text{ kN/m}^3$ ). It can be seen that the degree of compaction of all 12 test stations varied between 96% and 101.7%. Consequently no under-compacted zones were detected in this case by the ICA. According to the ICA produced as-built stiffness map, the corresponding  $M_{ICA}$  of the test stations were estimated from the regression models. The  $M_{ICA}$  values of the test stations are listed in Table 3.2. A relatively high range of NDG measured degree of compaction (96% to 101.7%) of the test stations complies with the ICA readings.

### ***3.5.3 Validation of the ICA-Estimated Moduli***

#### ***3.5.3.1 Validation with Laboratory Developed Regression Models***

The NDG measured  $w$  and  $\gamma_d$  values from the 12 test stations were used in Equations 2.7 to 2.9 and Equations 2.10 to 2.12 to determine the regression coefficients  $k_1$ ,  $k_2$ , and  $k_3$  for 0-day and 28-day curing periods, respectively. Subsequently,  $M_{r-0}$  and



$M_{r-28}$  of the chemically-stabilized subgrade for all 12 stations were evaluated at  $\sigma_d = 68.9$  kPa and  $\sigma_3 = 41.4$  kPa using Equation 2.2. The regression coefficients and the estimated resilient moduli, thus obtained, are presented in Tables 3.3 and 3.4 for 0-day and 28-day curing periods, respectively. The ICA-estimated moduli could not be validated with the estimated  $M_r$  values from the laboratory developed regression models due to poor relationship between the modulus values obtained from the two methods. This could be due to the unaccurate NDG measured moisture contents due to excessive spraying of water on the compacted stretch after the ICA measurements and before the NDG readings. Besides, the range of the field moisture content (12.3% to 17.1%) was beyond the achieved limit in the laboratory condition (12.1% to 14.8%). Five test stations (out of 12) possessed moisture contents higher than laboratory compacted specimens. Since, the regression models were developed based on the ranges achieved in the laboratory, extrapolation was needed to estimate the  $M_r$  values at these five test stations. This led to a low accuracy of estimation.

#### 3.5.3.2 Validation with FWD Back-calculated Moduli

For this case study,  $M_{ICA}$  values were validated by comparing them with the back-calculated modulus ( $M_{FWD}$ ) values from the FWD tests. FWD tests were performed at each of the 12 test stations 28 days after the compaction of the subgrade layer. The FWD tests were conducted on the top of the asphalt surface layer. The FWD deflection values and the thicknesses (measured from the asphalt cores) of different layers were used to back-calculate the asphalt layer moduli and subgrade resilient moduli at these locations. Outliers reflecting unreasonably low/high moduli were observed at test locations 2, 4, and 8, and were excluded from the analysis. To make the FWD moduli (taken 28 days after

compaction) compatible with the  $M_{ICA}$  values (taken on the compaction day) the  $M_{FWD}$  values were converted to an equivalent 0-day  $M_{FWD}$  ( $M_{FWD-0}$ ). The 28-day  $M_{FWD}$  ( $M_{FWD-28}$ ) was divided by the  $r_{28}$  ratio from Equation 2.13 to be converted  $M_{FWD-0}$ . Table 3.5 presents the  $M_{FWD-28}$  and  $M_{FWD-0}$  values at the nine test stations. A comparison between the  $M_{FWD-0}$  and  $M_{ICA}$  is shown in Figure 3.5. A reasonably good correlation ( $R^2 = 0.63$ ) between  $M_{FWD-0}$  and  $M_{ICA}$  can be seen. It is evident that the ICA can estimate the subgrade resilient modulus with a reasonable accuracy.

### **3.6 Case Study 2 (CS2): Apple Valley Project**

#### ***3.6.1 Construction Site Identification***

This construction project at Apple Valley, Edmond, OK consisted of two lanes of a 1.13 kilometers-long stretch of East Hefner Road. The road was constructed with a full-depth asphalt pavement. The subgrade was stabilized by mixing 10% CKD to a depth of 304.8 mm (12 inches). The important properties of the chemically-stabilized subgrade are summarized in Table 2.2. Similar to CS1, the final stage of compaction of the stabilized subgrade was conducted by an Ingersoll-Rand SD-105DX VSDR. In this case study, the base layer consisted of two asphalt layers. Each layer was 76.5 mm (3 inches) thick and consisted of a S3 mix prepared with a PG 70-28 OK binder. The surface course was a 50.8 mm (2 inches) thick asphalt layer consisting of a S4 mix, prepared with a PG70-28 OK binder.

### ***3.6.2 ICA Measurements and Identification of Test Stations***

The calibration procedure for the ICA for this project was similar to the procedure used in CS1. Three calibration points were selected on a 10-meter-long stretch on the west bound section of the project. As before, seven random points were marked on both sides of the stretch and the ICA measurements were taken at these points after calibration. The NDG measurements were taken at each of the test stations, and  $w$  and  $\gamma_d$  values were recorded. The position of the 10 marked points, including the three calibration points and the seven random points, are shown in Figure 3.6. The measured values of  $w$  and  $\gamma_d$  and the ICA-estimated moduli of the subgrade are shown in Table 3.6. Due to high degree of compaction of the subgrade after regular VSDR compaction (98% to 106%) no under-compacted zones could be recognized in CS2.

### ***3.6.3 Validation of the ICA-Estimated Moduli***

The measured  $w$  and  $\gamma_d$  values of the 10 test stations were used in Equations 2.14 to 2.19 to determine 0-day and 28-day regression coefficients  $k_1$ ,  $k_2$ , and  $k_3$ . Subsequently, resilient modulus at the test stations were calculated for  $\sigma_d = 68.9$  kPa and  $\sigma_3 = 41.4$  kPa using Equation 2.2 at 0-day and 28-day curing periods.

The coefficients  $k_1$ ,  $k_2$ , and  $k_3$  and estimated  $M_r$  at 10 test stations are listed in Tables 3.7 and 3.8 for 0-day and 28-day curing periods, respectively. It can be seen in Table 3.7 that the regression models yielded a very high 0-day  $M_r$  values. It may be noted that the degree of compaction measured in the field ranged between 98% to 106%. This range was out of the degree of compaction range of laboratory compacted specimens used in the development of regression models (97.3% to 99.9%). This led to an extrapolation of the regression models to estimate  $M_r$  values for the field stations. Consequently, the

developed model for 0-day  $M_r$  could not predict the  $M_r$  at the 10 test stations with a reasonable accuracy. It should also be mentioned that the model for  $M_{r-28}$  was not too sensitive to dry unit weight, and a reasonable estimate could be made by using the developed 28-day model. Therefore, the 0-day resilient moduli for the 10 stations were converted by using the  $r_{28}$  ratio (Equation 2.20). The converted  $M_{r-0}$  values are presented in Table 3.9.

A validation of the ICA measurements was performed by comparing the  $M_{ICA}$  values at the test stations with the  $r_{28}$  ratio converted  $M_{r-0}$  of the test stations. Figure 3.7 shows the relationship between the  $M_{ICA}$  and  $M_{r-0}$ . It can be seen that the  $M_{ICA}$  values (except for one data point) fall within 0 to -25% error, compared with the laboratory estimated  $M_r$ . It is observed that the ICA-estimated moduli were conservative compared to laboratory estimated resilient modulus. Also, the achieved correlation with  $R^2 = 0.59$  showed that the ICA could be calibrated with the  $M_r$  values predicted by the laboratory regression models.

### **3.7 Case Study 3 (CS3): Main Street-Interstate 35 Intersection Project**

#### ***3.7.1 Construction Site Identification***

The CS3 project consisted of a 800-meter-long pavement section constructed on the north-bound side of Interstate 35, near Main Street, Norman, OK (Figure 3.8). Two lanes and an access ramp were reconstructed as a part of this project. The subgrade soil was stabilized by mixing 12% CKD (by soil dry weight) to a depth of 202 mm (8 inches). Some of the properties of the subgrade soil are presented in Table 2.2. After compaction of the subgrade with a pad-foot roller, the proof rolling was performed by an ICA-

equipped Ingersoll-Rand SD-100/105 VSDR roller. Due to modifications in construction project, completion of laboratory resilient modulus tests prior to the field compaction was not possible. Also, the construction site was not accessible to the FWD trailer. Consequently, FWD tests could not be conducted, as previously planned.

### ***3.7.2 ICA Measurements and Identification of Test Stations***

The subgrade compaction was performed on two separate 396-meter-long sections adjacent to each other. These sections were referred to as Test Section 1 (TS1) and Test Section 2 (TS2), as shown in Figure 3.9. The TS1 was compacted using a conventional compaction procedure. In this section, the ICA measurements were recorded during conventional compaction, however, under-compacted zones were neither identified nor remedied. On TS2, the ICA compaction procedure was followed. For this section, the ICA measurements were recorded and monitored throughout the compaction process, and under-compacted zones were identified and marked. Under-compacted regions were then compacted using additional roller passes.

A preliminary calibration of the ICA was performed on a 10-meter-long stretch in TS1. The NDG measured  $w$  and  $\gamma_d$  values were recorded at three calibration points (CP1 to CP3 in Figure 3.9) before and after VSDR compaction. Since the subgrade compaction was performed before laboratory  $M_r$  tests, the initial and target modulus values were estimated using previously developed regression models for CS3 and the NDG readings ( $w$  and  $\gamma_d$ ). The modulus values were then used to perform raw calibration of the ICA (according to Commuri et al., 2014). The calibration parameters were adjusted subsequently after the completion of the resilient modulus tests and development of regression models for this site.

After preliminary calibration was performed, ICA measurements were taken during compaction. A total of 13 random points were marked on both test sections (TS1-R1 to TS1-R6 on TS1 and TS2-R1 to TS2-R7 on TS2) (see Figure 3.9) and the NDG measurements were taken after the compaction. Table 3.10 shows the measured  $w$  and  $\gamma_d$  values at all the calibration and random points. Additionally, two under-compacted zones were identified on TS2. Three test stations were marked (1-meter apart) on each under-compacted zone as SP1-A, SP1-B and SP1-C on first zone (SP1), and SP2-A, SP2-B and SP2-C on the second zone (SP2), as shown in Figure 3.9. Figure 3.10 shows a  $w$ - $\gamma_d$  plot of all field NDG measured points in contrast with the laboratory compacted specimens and Proctor test results of the same soil-CKD mixture (from Section 2.6). The NDG measurements at selected stations in the field showed a range of 15.2% to 16.4% for  $w$  (except one station with a  $w$  of 19.4%), and a range of 15.14 to 17.20  $kN/m^3$  for  $\gamma_d$  (between 87.5% and 99.4% degree of compaction). It is evident from Figure 3.10 that  $w$  and  $\gamma_d$  values at all field test stations are within the ranges of  $w$  and  $\gamma_d$  values achieved in the laboratory. Hence, the developed regression models based on laboratory tests could give a good estimation of the field moduli. It can be seen in Figure 3.10 that all of the field compacted points are located below the  $w$ - $\gamma_d$  curve from Proctor test. It can be concluded that the VSDR compaction energy is relatively lower than compaction energy of standard Proctor test (600  $kN\cdot m/m^3$ ) (ASTM D698, 2012). A majority of field data points are located on the wet side of the  $w$ - $\gamma_d$  curve. Also, it can be observed that the  $\gamma_d$  of the soft points have slightly improved due to remedial compaction.

Table 3.10 also presents the measured  $M_{ICA}$  values at the calibration and random points. Due to loss of satellite connection in the GPS unit of the ICA system, the

geographic coordinates of random point TS1-R4 and consequently the ICA measurements of this point could not be recorded. Hence, the  $M_{ICA}$  could not be determined at this test location.

### ***3.7.3 Identification and Remediation of Under-compacted Zones***

In TS2, an emphasis was given to identifying and remediating the under-compacted zones by additional VSDR passes. Similar to TS1, conventional compaction was conducted at this section. As mentioned in the previous section, during the conventional compaction two under-compacted zones (SP1 and SP2) were identified and six soft points were marked (SP1-A, SP1-B and SP1-C on SP1, and SP2-A, SP2-B and SP2-C on SP2).

Following the final pass of VSDR during conventional compaction, the NDG readings were taken at the six soft points. Then, the VSDR's operator was asked to perform additional passes on the identified under-compacted zones in order to improve the level of compaction. The NDG measurements were conducted again at the six soft points after the remedial passes. The results of the NDG readings at the soft points before and after the remedial compaction are presented in Table 3.11. Additionally, a plot of  $\gamma_d$ - $w$  measured values at the soft points before and after the remedial compaction are presented in Figure 3.10.

### ***3.7.4 Validation of the ICA-Estimated Moduli***

Similar to CS1 and CS2, the field measured  $w$  and  $\gamma_d$  values were applied in laboratory developed regression models (Equations 2.21 to 2.26) and subsequently, the resilient moduli at a stress level of  $\sigma_d = 68.9$  kPa and  $\sigma_3 = 41.4$  kPa were estimated. Tables 3.12 and 3.13 list the calculated  $k_1$ ,  $k_2$ , and  $k_3$  and resulting  $M_r$  values at all test

stations of this project (including the soft points before and after the remedial compaction) for 0-day and 28-day curing periods, respectively.

Figure 3.11 shows a relationship between the  $M_{ICA}$  and  $M_{r-0}$ . It can be seen that the ICA could estimate the modulus of the subgrade with an error between +10% and -25% compared to the laboratory estimated resilient modulus. Similar to CS2, the  $M_{ICA}$  values were relatively lower than the laboratory resilient modulus values. Also, the ICA-estimated moduli correlated well with the  $M_r$  estimated values with a  $R^2$  of 0.67.

### ***3.7.5 Moduli Improvement Due to Remedial Compaction***

The vibration data and the NDG readings taken before and after the remedial passes were compared in order to determine the improvement in compaction level and modulus. Table 3.11 presents a comparison of the NDG measured  $w$  and  $\gamma_d$  values as well as the ICA-estimated moduli taken before and after the remedial compaction. It can be seen that the compaction level of the under-compacted zones increased after the additional VSDR passes (from 93% before the remedial compaction to 93.8% after the remedial compaction), as expected. Additionally, the coefficient of variation of the degree of compaction decreased slightly (from 1.5% before the remedial compaction to 0.9% after the remedial compaction), indicating a more uniform compaction. Also, the average  $M_{ICA}$  was improved from 163 to 180 MPa and, more importantly, the coefficient of variation reduced from 7.4% to 4.6% due to remedial compaction.

It may be mentioned that a good level of compaction was already achieved through the entire length in TS2 during the conventional compaction process (with an average degree of compaction of 93%). The under-compacted zones identified by the ICA



were not significantly below the target compaction level. Therefore, while the average  $\gamma_d$  values for regions SP1 and SP2 increased, the improvement was not as significant.

Figure 3.12 shows the measured  $M_{ICA}$  values before and after the remedial passes at six soft points on the two under-compacted regions. Except for SP2-B, the improvement of moduli is observable for all soft points. The subgrade had a higher initial modulus at SP2-B compared to other test stations. The modulus levels after the ICA compaction were significantly higher and more uniform than that achieved through traditional compaction.

### **3.8 Case Study 4 (CS4): Interstate 35 Service Road Project**

#### ***3.8.1 Construction Site Identification***

For CS4, the ICA technology was used during the construction of the stabilized subgrade of a 300-meter-long construction stretch on the Interstate 35 Service Road. The site was located at the University Park area of Northwest Norman, Oklahoma. The location of the site is shown in Figure 3.13. As noted in Section 2.7.1, the subgrade soil was pre-treated with 3% quick lime 14 days before the compaction. On the compaction day, the quick lime-treated soil was stabilized by mixing 12% CKD to a depth of 202 mm (8 inches). Table 2.2 lists the characteristics of the material used as the subgrade layer in this project.

The project consisted of one east-west stretch and one north-south stretch. Construction of the stabilized subgrade layer was conducted on two separate days. On day-one, the east-west stretch was compacted, and on day-two, the north-south stretch was compacted. Similar to CS3, an Ingersoll-Rand SD-100/105 VSDR was used for proof

rolling (after pad-foot roller compaction). In this case study, DCP tests were conducted on the day of compaction, and FWD tests were conducted seven days after the compaction.

### ***3.8.2 ICA Measurements and Identification of Test Stations***

The project stretch was divided into four separate test sections of TS1, TS2, TS3, and TS4, as shown in Figure 3.14. TS1 and TS2 were located on the east-west stretch (compacted on day-one), and Test Sections TS3 and TS4 were on the north-south stretch (compacted on day-two) of the project. The ICA was calibrated on a 10-meter-long stretch prior to proof rolling. Three points (CP1, CP2 and CP3) spaced at three meter-intervals were marked on the calibration stretch. The calibration points were located on TS1 (Figure 3.14). Afterwards, the ICA measurements were taken during the proof rolling. Ten random points were selected and marked on TS1 and TS3. On TS2 and TS4, on which continuous low  $M_{ICA}$  values were observed during conventional compaction, a total of 13 soft points were marked (SP1 to SP6 on TS2, and SP7 to SP13 on TS4). Table 3.14 lists the  $w$  and  $\gamma_d$  values resulted from the NDG measurements as well as the ICA-estimated moduli at calibration points and random points. It can be seen that the degree of compaction varies between 95.5% and 101.3% in TS1, and between 91.0% and 97.7% for TS3 of the project. The results of NDG readings at all of the test stations (calibration and random points, and soft points before and after remediation) are summarized in Figure 3.15 in contrast with laboratory prepared specimens. The measured moisture content in the field ranged between 17% ( $w_{opt}-4.4\%$ ) and 26.2% ( $w_{opt}+4.8\%$ ). This shows 9.2% difference between the maximum and minimum  $w$  in the field. This can be attributed to the width of the stretch (three lanes) which caused an inconsistent sprinkle

of water on the spots with different distances from the pavement edges. Similar to CS3, a majority of the field compacted points are located below the  $w-\gamma_d$  curve from Proctor test, i.e., lower compaction energy of VSDR compared to standard Proctor test (ASTM D698, 2012).

### ***3.8.3 Identification and Remediation of Under-compacted Zones***

After performing the conventional compaction on all four test sections, remedial compaction was performed on TS2 and TS4 which were identified as under-compacted zones. The NDG measurements were taken before and after the remedial compaction process. The results of the NDG measurements were consistent with the ICA estimation and the marked points showed low values of compaction level. Table 3.15 demonstrates the moisture content and compaction level of the 13 soft points. The NDG measurements before the remedial compaction on TS2 (SP1 to SP6) showed relatively low degree of compaction values (92% to 96.7%). The pre-remediation degree of compaction of test stations on TS4 (SP7 to SP13) showed very low values (between 82.5% and 93.4%). Such severely under-compacted points, if not remediated, could result in localized distresses and lead to premature failure of the pavement structure.

For TS2 (SP1 to SP6), the remedial compaction was performed by two additional VSDR passes. For TS4 (SP7 to SP13), four additional VSDR passes were performed as the remediation procedure. A plot of the  $w$  and  $\gamma_d$  values of the soft points before and after these remedial passes are presented in Figure 3.15.

### **3.8.4 Validation of the ICA-Estimated Moduli**

#### **3.8.4.1 Validation with Laboratory Developed Regression Models**

The ICA modulus values were validated by the  $M_r$  values estimated using the regression models developed in Chapter 2 (Equations 2.28 to 2.30 and Equations 2.34 to 2.36). First, the resilient modulus values were determined using the dry unit weight and moisture content information from the 26 test points on TS1 to TS4 (calibration points CP1 to CP3, random points RP1 to RP10, and soft points SP1 to SP13). The ICA calibration parameters were then adjusted using the modulus values predicted at locations CP1 to CP3. The ICA modulus was then estimated for the remaining 23 test locations. Table 3.16 and 3.17 presents the calculated  $k_1$ ,  $k_2$ , and  $k_3$  coefficients and estimated  $M_r$  values for all 26 test points at 0-day and 28-day curing periods, respectively.

Figure 3.16 shows a relationship between the  $M_{r-0}$  and  $M_{ICA}$  values. It may be noted that densities and moisture contents measured at some points were outside the range of the densities and moisture contents considered in laboratory testing and regression model development. Hence, those points were not considered in the correlation, as shown in Figure 3.16. It can be observed that a majority of the ICA-estimated modulus values were within  $\pm 25\%$  error when compared with laboratory estimated  $M_r$ . A reasonably good correlation was, thus, found between 0-day  $M_r$  and  $M_{ICA}$ , with  $R^2 = 0.55$ .

#### **3.8.4.2 Validation with DCP Indices**

In order to validate the ICA-estimated moduli with respect to DCP indices (DPI), DCP tests were conducted at 15 randomly selected points (out of 26) after the completion of the ICA compaction. The DPI values were calculated using the penetration vs number of blows relationships obtained at each point in accordance with ASTM D6951 (2009).

These values are listed in Table 3.18. Figure 3.17 presents the correlation between the inverse of DCP index ( $1/DPI$ ) and the ICA-estimated modulus. A reasonably good correlation ( $R^2 = 0.63$ ) was observed between the DPI and  $M_{ICA}$  values. Thus, it could be concluded that the  $M_{ICA}$  values could be validated with the DCP test results.

#### *3.8.4.3 Validation with FWD Back-calculated Moduli*

In order to validate the ICA-estimated moduli with the FWD moduli, FWD tests were conducted at several test locations on the compacted subgrade. The FWD tests were conducted seven days after the compaction. It should be noted that when the research team visited the site after seven days of compaction, several previously marked test points (RP1, RP4, RP6 and RP8, and SP1, SP2, SP6 and SP8-SP13) were found to be considerably wet and the remaining points were found to be very dry. FWD tests could not be performed at many wet points. The exact reasons for the source of this water were not known. Construction work related to water pipes was a possible reason. A localized rainfall at the site could be another reason. Relatively smooth surface texture of the subgrade and the piles of dirt on the side of the subgrade suggested water run-off during the 7-day curing period were also a possible reason for localized wet spots.

Table 3.19 presents a summary of FWD test results. No correlation was found between  $M_{ICA}$  and 7-day  $M_{FWD}$  ( $M_{FWD-7}$ ) values. The FWD modulus was found to be varying significantly. Because of this poor correlation, further analysis was not conducted on the FWD test results.

#### *3.8.5 Moduli Improvement Due to Remedial Compaction*

As mentioned earlier, a total of 13 test points (SP1 to SP13) were identified as under-compacted zones in TS2 and TS4. The ICA moduli were estimated at these

locations before and after remedial compaction. A comparison between the degree of compaction and the estimated ICA moduli before and after remedial compaction is presented in Table 3.15.

According to Table 3.15, in TS2, a small improvement in the degree of compaction was observed (degree of compaction increased from 92%-96.7% to 92.7%-97.1%). While the ICA could accurately estimate low/inadequate compaction, the degree of compaction could not be improved with two additional roller passes. A possible reason for this could be the high level of moisture in the subgrade during compaction and probably two passes were not sufficient.

It can be seen in Table 3.15 that on TS4 the average degree of compaction increased by 1.5% after four remedial VSDR passes were performed. The range of degree of compaction in Section D was significantly improved from 82.5%-93.1% to 87.0%-98.1%.

A comparison between the ICA-estimated moduli before and after the remedial compaction at the soft points SP1 to SP13 is given in Table 3.15. It can be seen that the average  $M_{ICA}$  was increased from 108.2 to 129.1 MPa due to remediation. A slight reduction in the coefficient of variation (from 21.8% to 20.4%) was observed in of the moduli after remedial compaction.

An important finding of this study is that the ICA was found to be able to identify under-compacted zones with relatively low average modulus. Figure 3.18 shows the improvement in moduli after remedial compaction. Significant improvements in the mean modulus were observed in a majority of the test points. The improvement was significant

at locations where the moduli were very low and where the remedial compaction was performed for a longer period of time (4 passes in TS4 vs to 2 passes in TS2).

### 3.9 Conclusions

The ability of the ICA to estimate the moduli of chemically-stabilized subgrade during compaction was studied by conducting four case studies at different construction sites. For each case study, the ICA was calibrated according to the laboratory resilient modulus tests. Then the ICA measurements were taken during the compaction of the subgrade layer. The ICA-estimated moduli at selected test stations were validated with the  $M_r$  values estimated using the laboratory developed regression models. Also, the ICA was validated selectively using DCP and FWD test results. The following conclusions could be drawn from the results presented in this chapter:

1. The ICA could detect changes in stiffness in real-time, during the compaction of the chemically-stabilized subgrade. Also, the variations in the degree of compaction between different test stations captured by ICA and NDG were in agreement in most of the test stations.
2. ICA was able to estimate the modulus of the stabilized subgrade with an accuracy suitable for the control of compaction quality. The ICA could estimate the moduli of the subgrade with an error less than  $\pm 25\%$  compared to laboratory results, and with a coefficient of determination ranged between 0.55 and 0.67 for different case studies.
3. The ICA could be validated with the DCP and FWD measurements. It was observed that for CS1, the ICA-estimated subgrade modulus and FWD modulus

have a good correlation ( $R^2 = 0.63$ ). Also, for CS4, the linear correlation between  $M_{ICA}$  and inverse of DPI had a  $R^2$  of 0.63.

4. The ICA could be used to identify and remedy under-compacted regions during the construction of pavements. In CS3 and CS4, it was shown that the average modulus of the entire subgrade could be improved. The level of compaction in the entire project stretch was also more uniform when the ICA compaction procedure was followed. For CS3 the coefficient of variation in modulus reduced from 7.4% to 4.6% due to remedial compaction.
5. For the regions at which more remedial VSDR passes were conducted the improvement in ICA-estimated moduli was more significant. For the sections where four additional VSDR passes were conducted the range of degree of compaction was significantly improved from 82.5%-93.1% to 87.0%-98.1%.



**Table 3.1 Comparison of VSDRs Used in This Study with the VSDR used by Mooney and Rinehart (2002)**

Study	Mooney and Rinehart (2002)	Case Studies 1 and 2	Case Studies 3 and 4
Drum Model	Ammann	Ingersoll-Rand SD-105DX	Ingersoll-Rand SD-100/105
Drum Length (mm)	2200	2134	2134
Drum Radius (mm)	750	1500	1500
Static Mass (kg)	11,500	10750	10325
Static Linear Load under drum (kN/m)	31.5	28.3	27.6
Maximum Operating Frequency (Hz)	34	33.8	30
amplitude of Vertical Component of Eccentric Excitation Force (kN)	277	258	248

**Table 3.2 Moisture and Compaction Levels and the ICA-Estimated Modulus Values at Selected Test Stations of Case Study 1**

Test Station Type	Test Station Number	$w$ (%)	$\gamma_d$ (kN/m <sup>3</sup> )	Degree of compaction (%)	$M_{ICA}$ (MPa)
Calibration Points	1	14.2	16.6	96	429
	2	13.2	16.8	97.1	453
	3	12.3	17.6	101.7	408
Random Points	4	13.2	17.2	99.4	344
	5	13.9	16.9	97.7	312
	6	13.8	16.7	96.5	228
	7	15.1	17.3	100	314
	8	13.7	17	98.3	420
	9	16	17.1	98.8	380
	10	16.7	16.9	97.7	374
	11	17.1	16.6	96	334
	12	15.1	17.1	98.8	363

**Table 3.3 Back-calculated  $k_1$ ,  $k_2$  and  $k_3$  Coefficients and Estimated  $M_{r-0}$  at Selected Test Stations of Case Study 1 ( $\sigma_d = 68.9$  kPa and  $\sigma_3 = 41.4$  kPa)**

Test Station	$w$	$\gamma_d$	$k_1$	$k_2$	$k_3$	$M_{r-0}$
	(%)	(kN/m <sup>3</sup> )				(MPa)
1	14.2	16.6	2954.206	0.149	-0.38	381
2	13.2	16.8	4373.786	0.117	-0.285	533
3	12.3	17.6	7753.555	0.092	-0.102	867
4	13.2	17.2	5578.839	0.119	-0.229	666
5	13.9	16.9	4237.006	0.141	-0.312	530
6	13.8	16.7	3749.659	0.136	-0.331	471
7	15.1	17.3	5264.963	0.185	-0.299	674
8	13.7	17	4935.996	0.135	-0.274	606
9	16	17.1	4027.51	0.214	-0.383	543
10	16.7	16.9	2886.519	0.237	-0.456	406
11	17.1	16.6	1555.487	0.248	-0.529	227
12	15.1	17.1	4595.489	0.184	-0.33	595

**Table 3.4 Back-calculated  $k_1$ ,  $k_2$  and  $k_3$  Coefficients and Estimated  $M_{r-28}$  at Selected Test Stations of Case Study 1 ( $\sigma_d = 68.9$  kPa and  $\sigma_3 = 41.4$  kPa)**

Test Station	$w$	$\gamma_d$	$k_1$	$k_2$	$k_3$	$M_{r-28}$
	(%)	(kN/m <sup>3</sup> )				(MPa)
1	14.2	16.6	33645.92	-0.119	-0.074	3247
2	13.2	16.8	30623.05	-0.076	-0.051	3012
3	12.3	17.6	22042.5	0.047	-0.012	2312
4	13.2	17.2	27263.83	-0.028	-0.041	2755
5	13.9	16.9	30350.29	-0.072	-0.06	3002
6	13.8	16.7	31802.26	-0.093	-0.063	3108
7	15.1	17.3	26363.51	-0.015	-0.064	2710
8	13.7	17	28588.65	-0.047	-0.052	2866
9	16	17.1	28972.12	-0.053	-0.084	2930
10	16.7	16.9	31498.71	-0.089	-0.102	3133
11	17.1	16.6	34835.36	-0.137	-0.117	3380
12	15.1	17.1	28229.74	-0.042	-0.07	2859

**Table 3.5 Comparison between  $M_{FWD-28}$  and Converted  $M_{FWD-0}$ , and  $M_{ICA}$  Values at Selected Test Stations of Case Study 1**

Test Station	$M_{FWD-28}$	$r_{28}$	$M_{FWD-0}$	$M_{ICA}$
	(MPa)		(MPa)	(MPa)
1	1384	3.07	451	429
3	1707	3.29	519	408
5	993	2.77	358	312
6	380	2.18	174	228
7	894	2.69	333	314
9	1125	2.88	391	380
10	1012	2.79	363	374
11	586	2.40	244	334
12	593	2.41	246	363

**Table 3.6 Moisture and Compaction Levels, and the ICA-Estimated Modulus Values at Selected Test Stations of Case Study 2**

Test Station Type	Test Station Number	$w$	$\gamma_d$	Degree of compaction	$M_{ICA}$
		(%)	(kN/m <sup>3</sup> )	(%)	(MPa)
Calibration1		11.7	19.2	103	528
Points	2	12.6	18.6	100	546
	3	12.8	19.0	102	553
Random	4	12.4	19.0	102	599
Points	5	9.7	19.4	104	798
	6	10.6	19.0	102	765
	7	10	19.8	106	740
	8	10.7	19.2	103	770
	9	9.9	18.3	98	790
	10	9.3	18.5	99	786

**Table 3.7 Back-calculated  $k_1$ ,  $k_2$  and  $k_3$  Coefficients and Estimated  $M_{r-0}$  at Selected Test Stations of Case Study 2 ( $\sigma_d = 68.9$  kPa and  $\sigma_3 = 41.4$  kPa)**

Test Station	$w$ (%)	$\gamma_d$ (kN/m <sup>3</sup> )	$k_1$	$k_2$	$k_3$	$M_{r-0}$ (MPa)
1	11.7	19.2	9061.276	1.081	-0.693	2405
2	12.6	18.6	5146.814	0.579	-0.313	854
3	12.8	19.0	7596.331	0.826	-0.388	1521
4	12.4	19.0	7676.393	0.870	-0.477	1636
5	9.7	19.4	10706.36	1.433	-1.198	4333
6	10.6	19.0	8036.673	1.066	-0.878	2269
7	10	19.8	13135.86	1.670	-1.251	6318
8	10.7	19.2	9261.431	1.190	-0.915	2873
9	9.9	18.3	3197.685	0.604	-0.794	649
10	9.3	18.5	4562.552	0.804	-0.988	1135

**Table 3.8 Back-calculated  $k_1$ ,  $k_2$  and  $k_3$  Coefficients and Estimated  $M_{r-28}$  at Selected Test Stations of Case Study 2 ( $\sigma_d = 68.9$  kPa and  $\sigma_3 = 41.4$  kPa)**

Test Station	$w$ (%)	$\gamma_d$ (kN/m <sup>3</sup> )	$k_1$	$k_2$	$k_3$	$M_{r-28}$ (MPa)
1	11.7	19.2	37677.53	0.065	-0.264	4405
2	12.6	18.6	39264.98	0.081	-0.081	4323
3	12.8	19.0	37537.9	0.099	-0.158	4306
4	12.4	19.0	37872.29	0.085	-0.180	4342
5	9.7	19.4	38569.55	0.000	-0.419	4589
6	10.6	19.0	39377.05	0.021	-0.280	4503
7	10	19.8	36758.87	0.021	-0.491	4558
8	10.7	19.2	38513.51	0.030	-0.319	4496
9	9.9	18.3	43082.01	-0.024	-0.141	4536
10	9.3	18.5	42803.65	-0.040	-0.219	4596

**Table 3.9 Comparison between 28-day  $M_r$  and Converted  $M_{r-0}$ , and  $M_{ICA}$  Values at Selected Test Stations of Case Study 2**

Test Station	$M_{r-28}$ (MPa)	$r_{28}$	$M_{r-0}$ (MPa)	$M_{ICA}$ (MPa)
1	4405	5.55	794	528
2	4323	7.45	580	546
3	4306	6.54	658	553
4	4342	6.20	700	599
5	4589	4.75	967	798
6	4503	5.29	851	765
7	4558	4.58	995	740
8	4496	5.16	871	770
9	4536	5.71	795	790
10	4596	5.29	869	786

**Table 3.10 Moisture and Compaction Levels, and the ICA-Estimated Modulus Values at Calibration and Random Points of Case Study 3**

Test Station Type	Test Station Number	$w$ (%)	$\gamma_d$ (kN/m <sup>3</sup> )	Degree of compaction (%)	$M_{ICA}$ (MPa)
Calibration Points	CP1	17.9	16.5	95.2	191
	CP2	18.2	16.4	94.8	163
	CP3	18.2	16.2	93.8	151
Random Points	TS1-R1	16.8	15.4	88.8	127
	TS1-R2	16.1	15.7	90.6	163
	TS1-R3	16.3	16.1	93.0	150
	TS1-R4	17.6	15.1	87.5	*
	TS1-R5	17.8	15.9	91.6	186
	TS1-R6	16.8	16.3	94.2	161
	TS2-R1	15.5	15.4	89.1	211
	TS2-R2	15.3	16.4	94.6	270
	TS2-R3	16.4	16.8	97.0	250
	TS2-R4	15.2	17.2	99.4	263
	TS2-R5	15.7	16.6	95.9	249
	TS2-R6	16.8	15.8	91.2	250
	TS2-R7	15.7	16.6	95.9	199

\* Satellite connection lost

**Table 3.11 Influence of Remedial Compaction on the Dry Unit Weight and Modulus Values of the Soft Points of Case Study 3**

Test Station Number	Before Remediation			After Remediation		
	$w$	Degree of Compaction	$M_{ICA}$	$w$	Degree of Compaction	$M_{ICA}$
	(%)	(%)	(MPa)	(%)	(%)	(MPa)
SP1-A	16.4	92.4	170	15.9	92.9	189
SP1-B	15.6	93.2	164	17	93.4	188
SP1-C	17.9	90.4	166	15.8	93.6	182
SP2-A	15.4	94.2	142	17.4	95.3	164
SP2-B	15.9	94.4	181	16	93.1	178
SP3-C	16.1	94.0	156	15.6	94.4	178
Average	---	93.1	163.2	---	93.8	179.8
STDV	---	1.4	12.1	---	0.8	8.3
CoV (%)	---	1.5	7.4	---	0.9	4.6

STDV: Standard deviation

CoV: Coefficient of variation

**Table 3.12 Back-calculated  $k_1$ ,  $k_2$  and  $k_3$  Coefficients and Estimated  $M_{r-0}$  at all Test Stations of Case Study 3 ( $\sigma_d = 68.9$  kPa and  $\sigma_3 = 41.4$  kPa)**

Compaction Method	Test Station	$w$ (%)	$\gamma_d$ (kN/m <sup>3</sup> )	$k_1$	$k_2$	$k_3$	$M_{r-0}$ (MPa)
Conventional	CP1	17.9	16.5	1457.721	0.183	-0.282	185
Compaction	CP2	18.2	16.4	1309.513	0.198	-0.298	169
	CP3	18.2	16.2	1187.424	0.202	-0.303	154
	TS1-R1	16.8	15.4	1009.633	0.160	-0.272	126
	TS1-R2	16.1	15.7	1447.943	0.121	-0.231	173
	TS1-R3	16.3	16.1	1674.710	0.121	-0.226	200
	TS1-R4	17.6	15.1	607.013	0.201	-0.313	79
	TS1-R5	17.8	15.9	1044.663	0.193	-0.299	134
	TS1-R6	16.8	16.3	1675.577	0.138	-0.241	203
	TS2-R1	15.5	15.4	1444.684	0.101	-0.214	170
	TS2-R2	15.3	16.4	2183.535	0.069	-0.174	247
	TS2-R3	16.4	16.8	2132.165	0.109	-0.208	251
	TS2-R4	15.2	17.2	2802.689	0.045	-0.142	309
	TS2-R5	15.7	16.6	2215.305	0.082	-0.184	254
	TS2-R6	16.8	15.8	1298.209	0.150	-0.258	160
	TS2-R7	15.7	16.6	2215.305	0.082	-0.184	254
Before Remedial	SP1-A	16.4	16.0	1566.113	0.128	-0.234	188
Compaction	SP1-B	15.6	16.1	1913.237	0.089	-0.195	221
	SP1-C	17.9	15.6	858.372	0.203	-0.310	112
	SP2-A	15.4	16.3	2097.135	0.076	-0.181	239
	SP2-B	15.9	16.3	1964.813	0.097	-0.202	229
	SP3-C	16.1	16.3	1858.608	0.108	-0.212	219
After Remedial	SP1-A	15.9	16.1	1787.228	0.103	-0.210	210
Compaction	SP1-B	17.0	16.2	1513.877	0.150	-0.254	186
	SP1-C	15.8	16.2	1906.924	0.096	-0.201	222
	SP2-A	17.4	16.5	1612.242	0.160	-0.261	200
	SP2-B	16.0	16.1	1778.522	0.107	-0.213	209
	SP3-C	15.6	16.3	2057.525	0.084	-0.189	237

**Table 3.13 Back-calculated  $k_1$ ,  $k_2$  and  $k_3$  Coefficients and Estimated  $M_{r-28}$  at all Test Stations of Case Study 3 ( $\sigma_d = 68.9$  kPa and  $\sigma_3 = 41.4$  kPa)**

Compaction Method	Test Station	$w$ (%)	$\gamma_d$ (kN/m <sup>3</sup> )	$k_1$	$k_2$	$k_3$	$M_{r-28}$ (MPa)
Conventional	CP1	17.9	16.5	12342.111	0.001	-0.025	1263
Compaction	CP2	18.2	16.4	11654.680	0.001	-0.026	1193
	CP3	18.2	16.2	10909.670	0.002	-0.027	1118
	TS1-R1	16.8	15.4	8812.310	0.005	-0.032	907
	TS1-R2	16.1	15.7	10980.717	0.004	-0.029	1128
	TS1-R3	16.3	16.1	12509.121	0.002	-0.027	1282
	TS1-R4	17.6	15.1	6934.009	0.007	-0.034	715
	TS1-R5	17.8	15.9	9749.248	0.004	-0.029	1001
	TS1-R6	16.8	16.3	12875.998	0.001	-0.026	1318
	TS2-R1	15.5	15.4	10526.919	0.005	-0.031	1082
	TS2-R2	15.3	16.4	14890.862	0.000	-0.024	1523
	TS2-R3	16.4	16.8	15372.896	-0.001	-0.022	1569
	TS2-R4	15.2	17.2	18596.717	-0.004	-0.019	1893
	TS2-R5	15.7	16.6	9219.785	0.006	-0.032	949
	TS2-R6	16.8	15.8	16245.425	-0.001	-0.022	1658
	TS2-R7	15.7	16.6	10573.242	0.004	-0.029	1085
Before	SP1-A	16.4	16.0	11918.761	0.002	-0.028	1222
Remedial	SP1-B	15.6	16.1	13458.421	0.002	-0.026	1378
Compaction	SP1-C	17.9	15.6	8684.791	0.005	-0.031	893
	SP2-A	15.4	16.3	14435.958	0.001	-0.025	1477
	SP2-B	15.9	16.3	13990.097	0.001	-0.025	1431
	SP3-C	16.1	16.3	13486.658	0.001	-0.025	1380
After	SP1-A	15.9	16.1	12906.447	0.002	-0.027	1322
Remedial	SP1-B	17.0	16.2	12033.918	0.002	-0.027	1233
Compaction	SP1-C	15.8	16.2	13564.535	0.001	-0.026	1389
	SP2-A	17.4	16.5	12923.428	0.001	-0.025	1322
	SP2-B	16.0	16.1	12925.640	0.002	-0.026	1324
	SP3-C	15.6	16.3	14338.887	0.001	-0.025	1467



**Table 3.14 Moisture and Compaction Levels, and the ICA-Estimated Modulus Values at Calibration and Random Points of Case Study 4**

Test Section	Test Station Number	$w$ (%)	$\gamma_d$ (kN/m <sup>3</sup> )	Degree of Compaction (%)	$M_{ICA}$ (MPa)
Section A	CP1	19.4	15.6	101.3	147
	CP2	20.6	15.4	99.9	150
	CP3	22.4	14.7	95.5	93
	RP1	21.2	15.4	100.1	131
	RP2	20.2	14.9	96.4	133
	RP3	18.4	15.0	97.4	179
Section C	RP4	20.7	14.8	95.9	111
	RP5	21.8	14.0	91.0	72
	RP6	23	14.5	94.0	110
	RP7	21.5	14.6	94.7	115
	RP8	21.6	15.1	97.7	119
	RP9	19.8	15.0	97.0	172
	RP10	21	14.1	91.5	106

**Table 3.15 Influence of Remedial Compaction on the Dry Unit Weight and Modulus Values at the Soft Points of Case Study 4**

Test Section	Test Station Number	Before Remediation			After Remediation		
		$w$ (%)	Degree of Compaction (%)	$M_{ICA}$ (MPa)	$w$ (%)	Degree of Compaction (%)	$M_{ICA}$ (MPa)
Section B	SP1	23.4	95.0	76	24	96.1	118
	SP2	26.2	92.0	75	25.5	92.7	120
	SP3	22.1	96.7	150	21.5	97.1	117
	SP4	20.5	95.4	143	21	93.9	115
	SP5	22.5	96.3	130	23.7	96.2	85
	SP6	24.4	94.8	110	23.9	93.6	95
Section D	SP7	22.2	93.4	130	20.7	87.0	157
	SP8	20.7	89.5	86	21.9	93.4	150
	SP9	21.4	92.0	95	23.1	89.8	115
	SP10	21.9	93.1	107	20.8	89.5	144
	SP11	21.9	89.8	110	21.4	89.4	178
	SP12	20.8	82.5	85	23	93.1	120
	SP13	17	89.4	110	21.9	98.1	164
Average		---	92.3	108.2	---	93.1	129.1
STDV		---	3.7	23.6	---	3.2	26.3
CoV (%)		---	4.0	21.8	---	3.5	20.4

STDV: Standard deviation

CoV: Coefficient of variation

**Table 3.16 Back-calculated  $k_1$ ,  $k_2$  and  $k_3$  Coefficients and Estimated  $M_{r-0}$  at all Test Stations of Case Study 4 ( $\sigma_d = 68.9$  kPa and  $\sigma_3 = 41.4$  kPa)**

Compaction Method	Test Station	$w$ (%)	$\gamma_d$ (kN/m <sup>3</sup> )	$k_1$	$k_2$	$k_3$	$M_{r-0}$ (MPa)
Conventional	CP1	19.4	15.6	1519.595	0.134	-0.272	186
Compaction	CP2	20.6	15.4	1299.901	0.201	-0.295	168
	CP3	22.4	14.7	804.649	0.354	-0.349	117
	RP1	21.2	15.4	1239.366	0.217	-0.301	162
	RP2	20.2	14.9	1104.708	0.268	-0.318	150
	RP3	18.4	15.0	1364.656	0.192	-0.292	175
	RP4	20.7	14.8	1021.974	0.293	-0.327	142
	RP5	21.8	14.0	577.848	0.434	-0.377	89
	RP6	23.0	14.5	646.813	0.403	-0.366	98
	RP7	21.5	14.6	847.051	0.345	-0.346	122
	RP8	21.6	15.1	1042.429	0.280	-0.323	143
	RP9	19.8	15.0	1185.386	0.243	-0.310	158
	RP10	21.0	14.1	693.202	0.400	-0.365	105
Before	SP1	23.4	14.7	741.917	0.369	-0.354	109
Remedial	SP2	26.2	14.2	205.541	0.530	-0.411	34
Compaction	SP3	22.1	14.9	947.498	0.309	-0.333	133
	SP4	20.5	14.7	906.448	0.332	-0.341	130
	SP5	22.5	14.9	841.101	0.341	-0.345	121
	SP6	24.4	14.6	458.727	0.457	-0.385	72
	SP7	22.2	14.4	263.922	0.536	-0.412	44
	SP8	20.7	13.8	847.517	0.351	-0.347	123
	SP9	21.4	14.2	531.394	0.452	-0.383	83
	SP10	21.9	14.4	465.563	0.471	-0.390	74
	SP11	21.9	13.9	453.365	0.474	-0.391	72
	SP12	20.8	12.7	825.178	0.358	-0.350	120
	SP13	17.0	13.8	1567.588	0.133	-0.271	192
After	SP1	24.0	14.8	605.689	0.411	-0.369	92
Remedial	SP2	25.5	14.3	237.708	0.524	-0.409	40
Compaction	SP3	21.5	15.0	989.075	0.299	-0.329	138
	SP4	21.0	14.5	955.550	0.313	-0.334	135
	SP5	23.7	14.8	719.439	0.375	-0.357	106
	SP6	23.9	14.4	599.660	0.414	-0.370	91
	SP7	20.7	13.4	847.517	0.351	-0.347	123
	SP8	21.9	14.4	465.563	0.471	-0.390	74
	SP9	23.1	13.9	504.104	0.450	-0.383	79
	SP10	20.8	13.8	825.178	0.358	-0.350	120
	SP11	21.4	13.8	531.394	0.452	-0.383	83
	SP12	23.0	14.4	504.104	0.450	-0.383	79
	SP13	21.9	15.1	453.365	0.474	-0.391	72

**Table 3.17 Back-calculated  $k_1$ ,  $k_2$  and  $k_3$  Coefficients and Estimated  $M_{r-28}$  at all Test Stations of Case Study 4 ( $\sigma_d = 68.9$  kPa and  $\sigma_3 = 41.4$  kPa)**

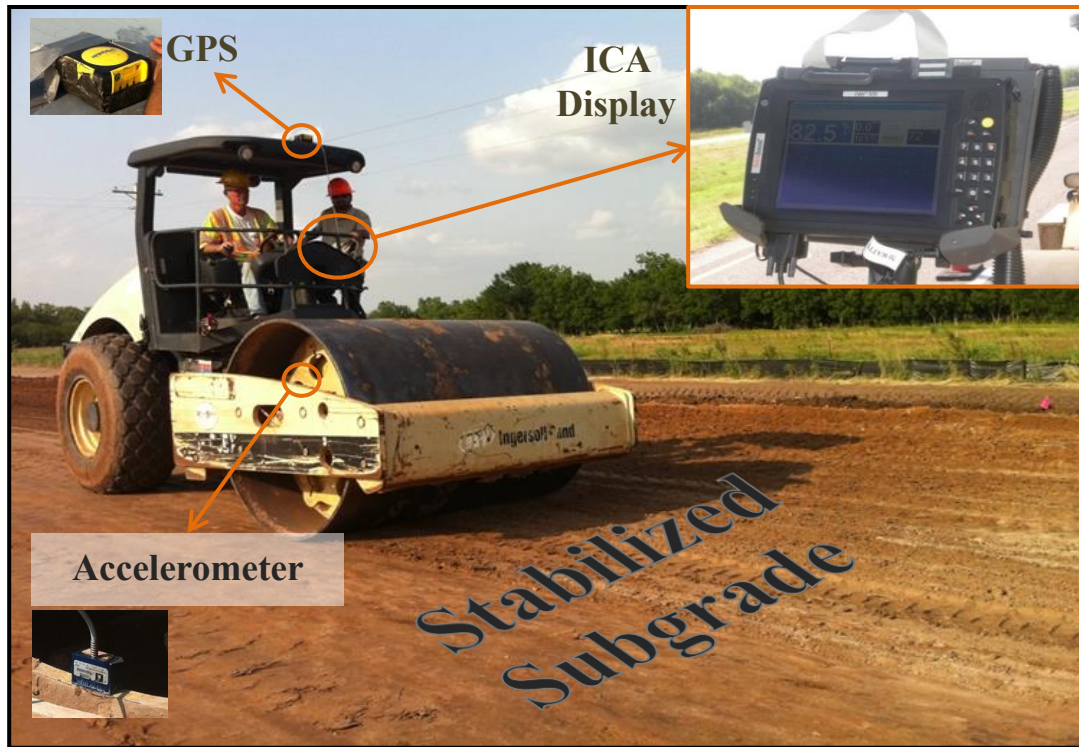
Compaction Method	Test Station	$w$ (%)	$\gamma_d$ (kN/m <sup>3</sup> )	$k_1$	$k_2$	$k_3$	$M_{r-28}$ (MPa)
Conventional	CP1	19.4	15.6	18532.532	0.033	-0.066	1966
Compaction	CP2	20.6	15.4	16614.035	0.027	-0.066	1756
	CP3	22.4	14.7	11386.847	0.017	-0.067	1196
	RP1	21.2	15.4	16490.304	0.024	-0.066	1740
	RP2	20.2	14.9	13242.233	0.026	-0.068	1400
	RP3	18.4	15.0	14978.299	0.035	-0.068	1592
	RP4	20.7	14.8	12540.325	0.024	-0.068	1324
	RP5	21.8	14.0	7173.293	0.017	-0.069	754
	RP6	23.0	14.5	9672.842	0.013	-0.068	1014
	RP7	21.5	14.6	10973.518	0.020	-0.068	1156
	RP8	21.6	15.1	13942.988	0.021	-0.067	1469
	RP9	19.8	15.0	13973.874	0.029	-0.067	1479
	RP10	21.0	14.1	8002.961	0.020	-0.069	843
Before	SP1	23.4	14.7	11594.599	0.013	-0.067	1215
Remedial	SP2	26.2	14.2	6962.084	-0.001	-0.067	723
Compaction	SP3	22.1	14.9	13117.733	0.019	-0.067	1380
	SP4	20.5	14.7	10614.156	0.024	-0.068	1121
	SP5	22.5	14.9	12058.637	0.017	-0.067	1267
	SP6	24.4	14.6	8596.097	0.007	-0.067	898
	SP7	22.2	14.4	2920.797	0.013	-0.071	307
	SP8	20.7	13.8	9967.688	0.023	-0.069	1052
	SP9	21.4	14.2	6046.674	0.018	-0.070	636
	SP10	21.9	14.4	5599.901	0.016	-0.070	589
	SP11	21.9	13.9	5476.554	0.015	-0.070	575
	SP12	20.8	12.7	9691.260	0.022	-0.069	1022
	SP13	17.0	13.8	16339.913	0.041	-0.068	1744
After	SP1	24.0	14.8	10267.516	0.010	-0.067	1074
Remedial	SP2	25.5	14.3	6596.840	0.001	-0.068	686
Compaction	SP3	21.5	15.0	13016.064	0.021	-0.067	1372
	SP4	21.0	14.5	11902.297	0.023	-0.068	1256
	SP5	23.7	14.8	11619.920	0.012	-0.067	1217
	SP6	23.9	14.4	10054.968	0.010	-0.067	1052
	SP7	20.7	13.4	9967.688	0.023	-0.069	1052
	SP8	21.9	14.4	5599.901	0.016	-0.070	589
	SP9	23.1	13.9	7640.208	0.012	-0.068	801
	SP10	20.8	13.8	9691.260	0.022	-0.069	1022
	SP11	21.4	13.8	6046.674	0.018	-0.070	636
	SP12	23.0	14.4	6962.084	-0.001	-0.067	723
	SP13	21.9	15.1	5476.554	0.015	-0.070	575

**Table 3.18 Summary of DCP Test Results for Case Study 4**

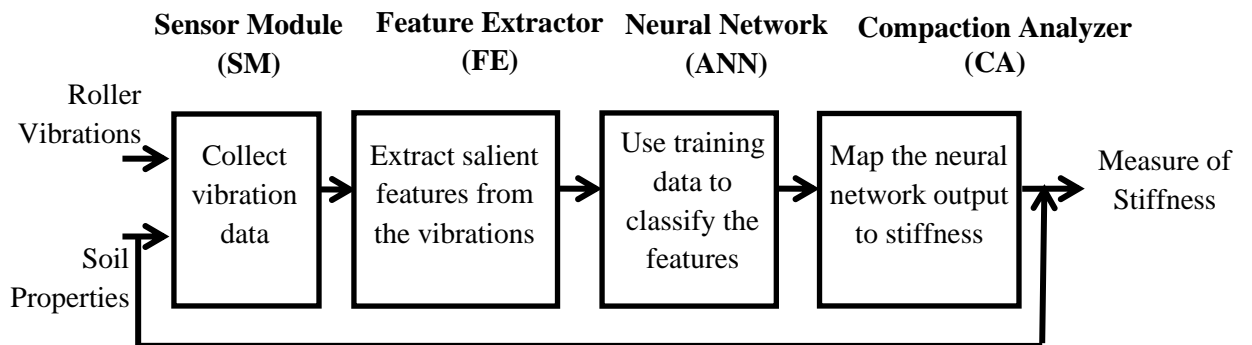
Test Station Number	$DPI$	$1/DPI$	$M_{ICA}$
	$mm/blow$	$blows/mm$	(MPa)
CP1	1.11	0.90	147
CP2	1.41	0.71	150
RP2	1.29	0.78	133
RP4	1.69	0.59	111
RP5	2.72	0.37	72
RP6	1.69	0.59	110
RP7	1.59	0.63	115
RP8	2.47	0.40	119
RP9	1.43	0.70	172
RP10	1.85	0.54	106
SP1	2.69	0.37	76
SP3	1.49	0.61	117
SP4	2.20	0.45	115
SP9	1.94	0.52	115
SP10	1.06	0.94	144
SP13	1.64	0.61	164

**Table 3.19 Summary of FWD Test Results for Case Study 4**

Test Station Number	$M_{FWD-7}$	$M_{ICA}$
	(MPa)	(MPa)
RP2	935.86	190
RP3	455.86	193
RP5	700.69	162
RP7	528.28	181
RP9	353.79	205
RP10	255.86	165
SP3	545.52	206
SP4	281.38	183
SP5	175.17	160
SP7	1262.76	166
SP13	771.03	163



(a)



(b)

**Figure 3.1 (a) The ICA Equipped VSDR during Subgrade Compaction, and (b) Functional Schematic of the ICA for Stiffness Measurement (Commuri and Zaman, 2008).**



**Figure 3.2 Location Measurement and Marking of Test Stations**



(a)

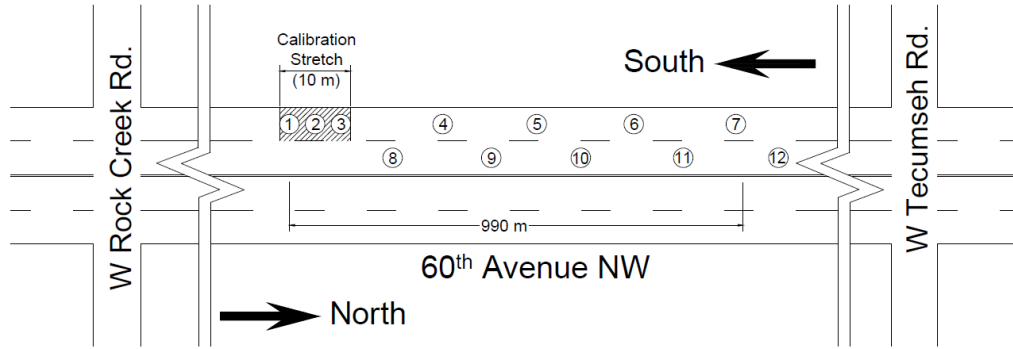


(b)

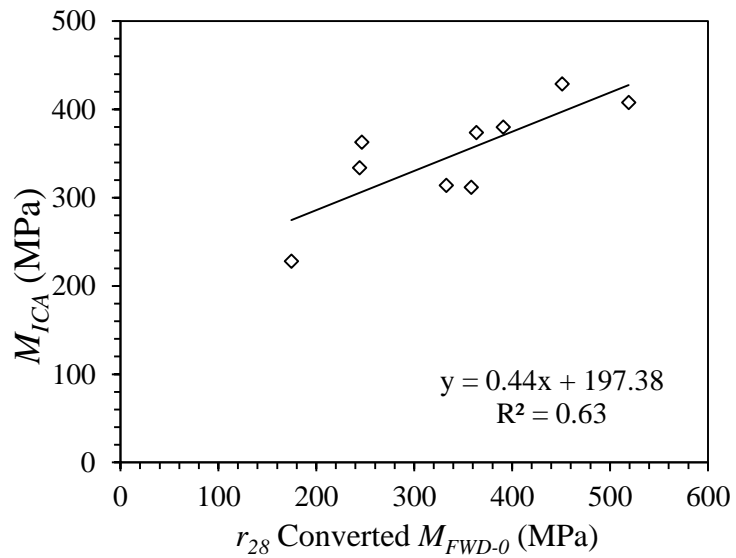


(c)

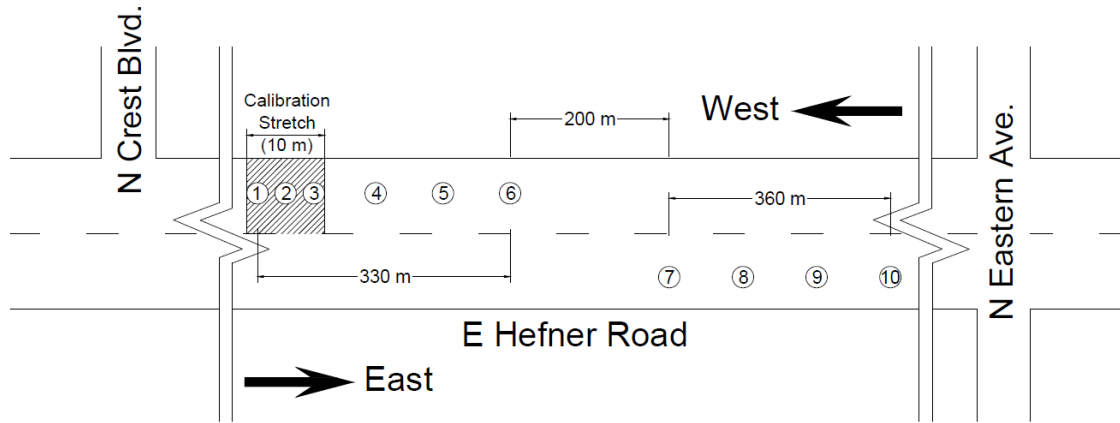
**Figure 3.3 Complementary Field Measurements on Compacted Subgrade, (a) NDG Measurements, (b) DCP Test, and (c) FWD Test**



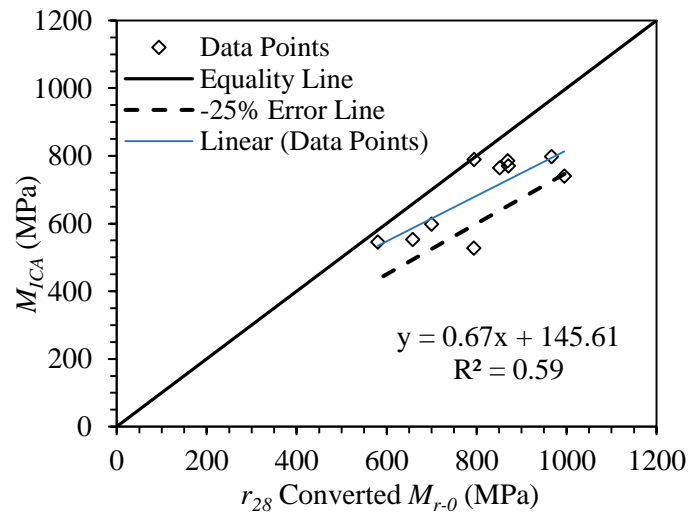
**Figure 3.4 Case Study 1 Field Project Sketch and Positions of the Calibration Stretch and Test Stations**



**Figure 3.5 Correlation between Converted 0-day  $M_{FWD}$  and  $M_{ICA}$  for Case Study 1**

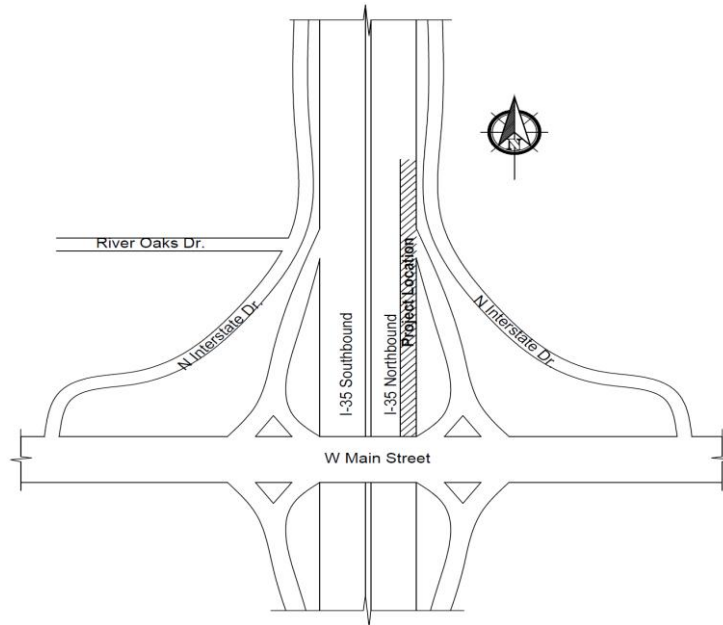


**Figure 3.6 Case Study 2 Field Project Sketch and Positions of the Calibration Stretch and Test Stations**

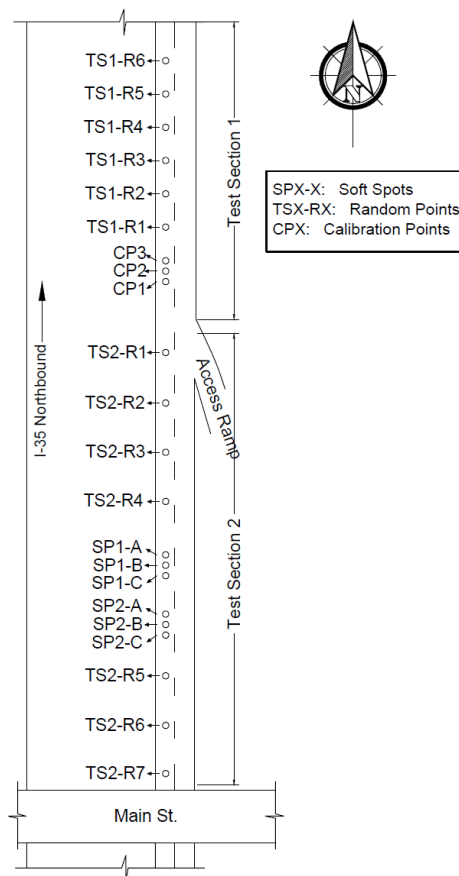


**Figure 3.7 Correlation between Converted  $M_{r-0}$  and  $M_{ICA}$  for Case Study 2**

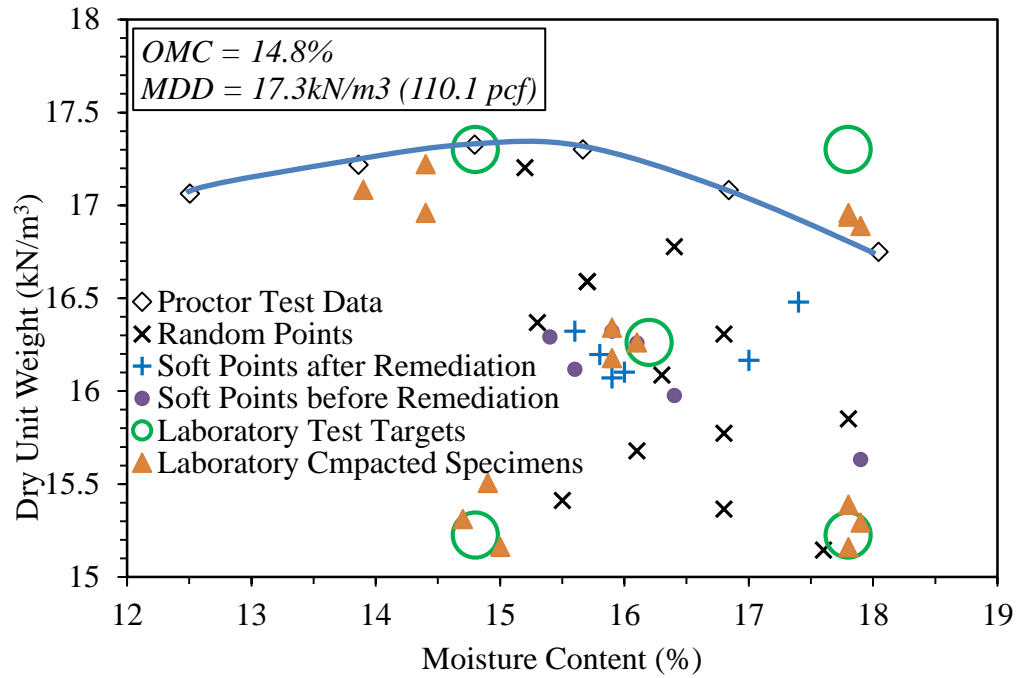




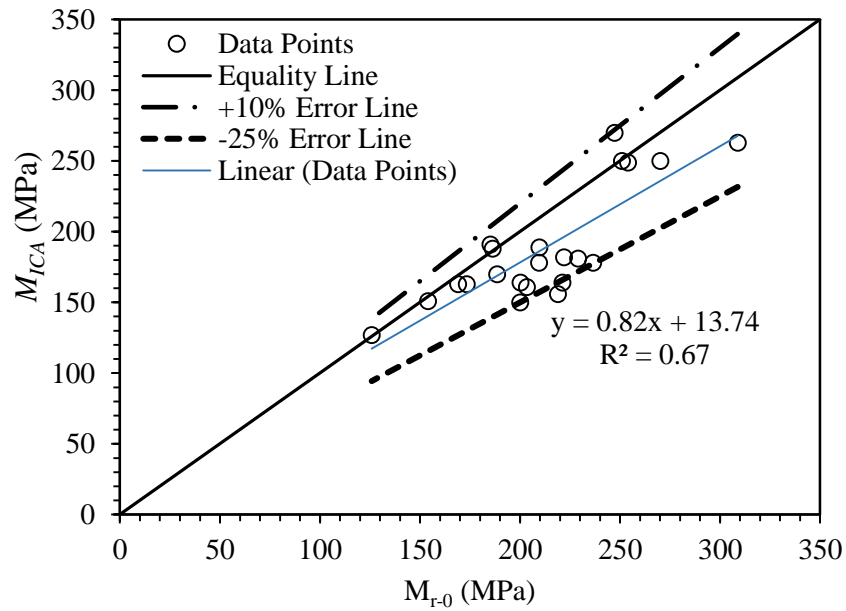
**Figure 3.8 Physical Location of Case Study 3 Construction Project**



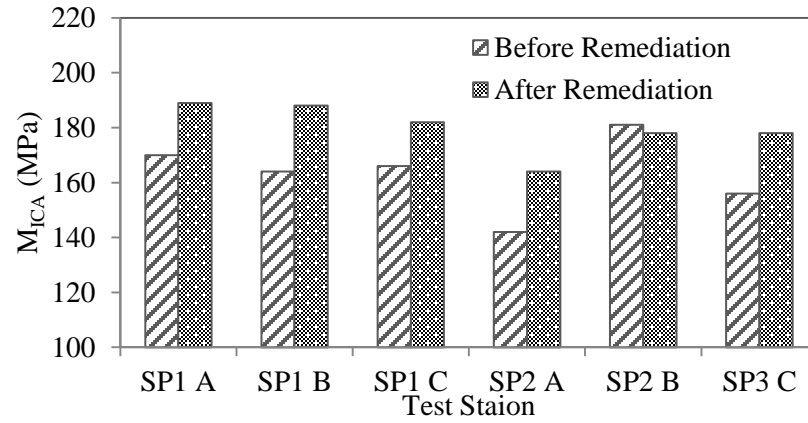
**Figure 3.9 Case Study 3 Field Project Sketch and Positions of the Calibration Stretch and Test Stations**



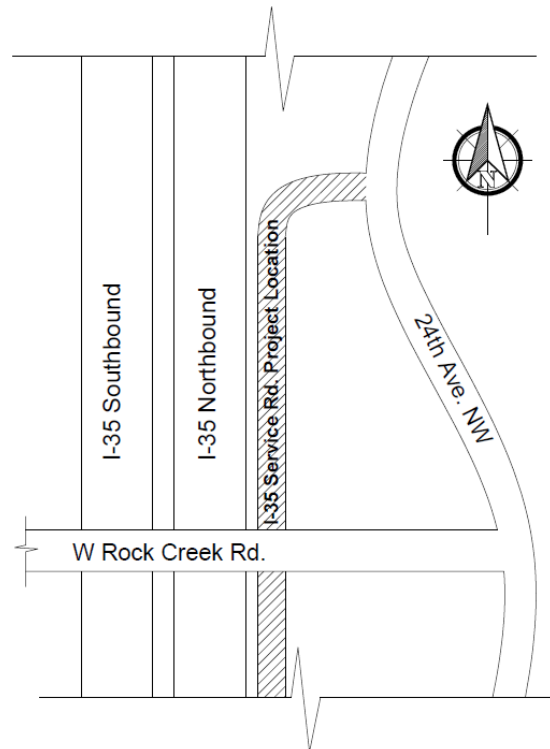
**Figure 3.10 Summary of NDG Measurements ( $w$ - $\gamma_d$  Relationship) at Test Stations of Case Study 3**



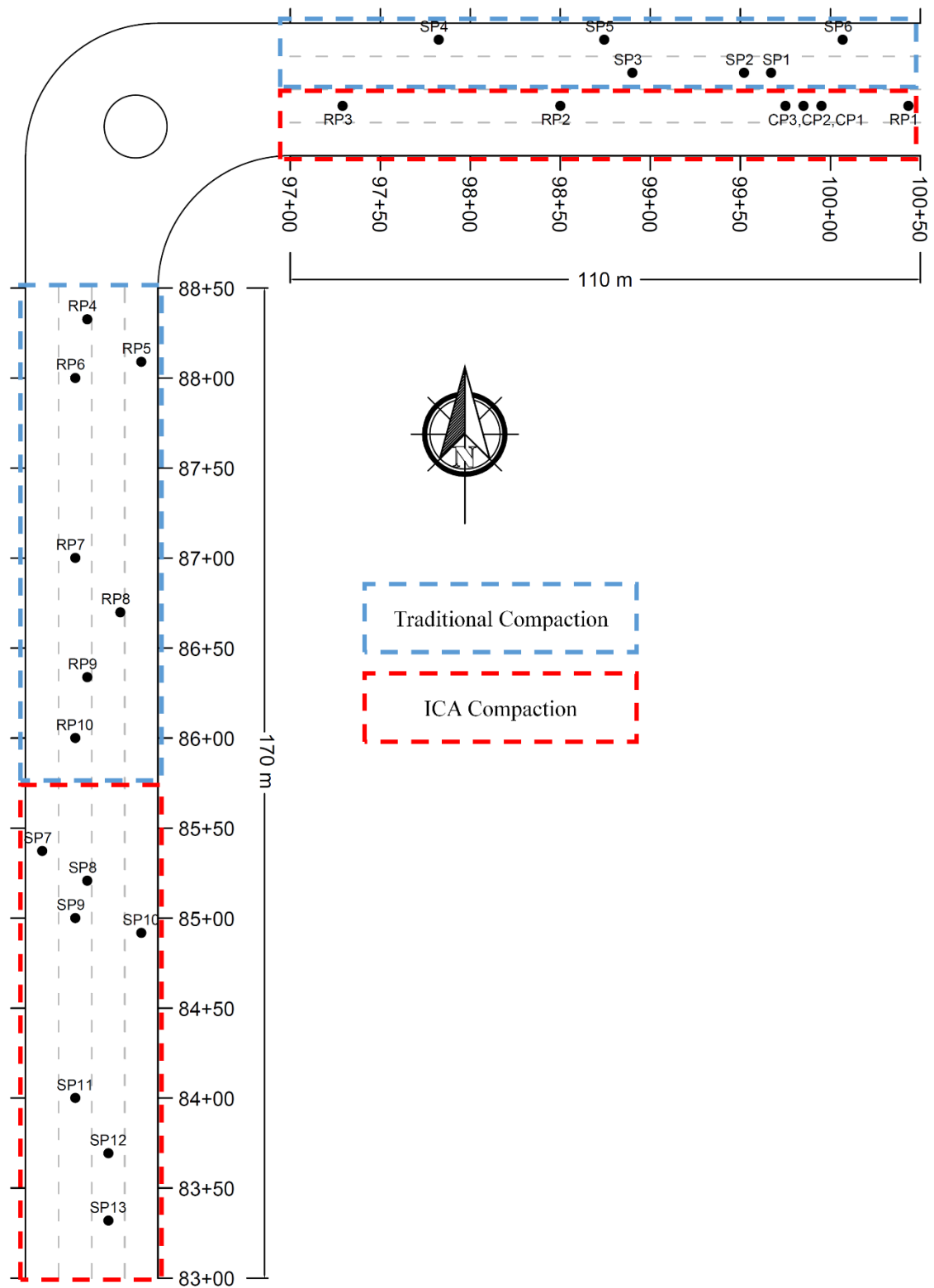
**Figure 3.11 Correlation between 0-day  $M_r$  and  $M_{ICA}$  for Case Study 3**



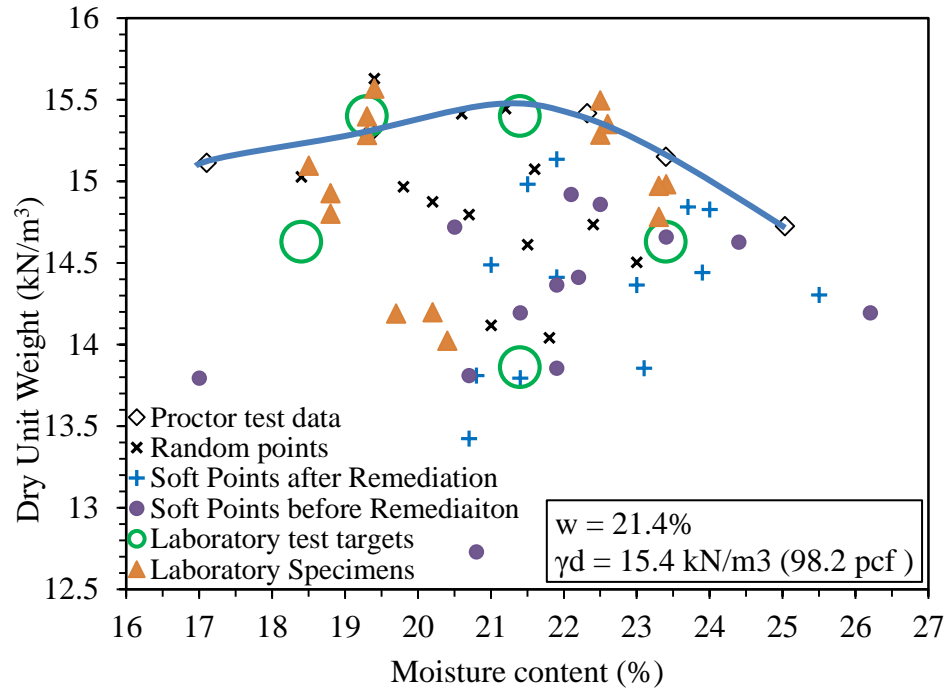
**Figure 3.12 Improvement of Subgrade Moduli Due to Remedial Compaction at Soft Points of Case Study 3**



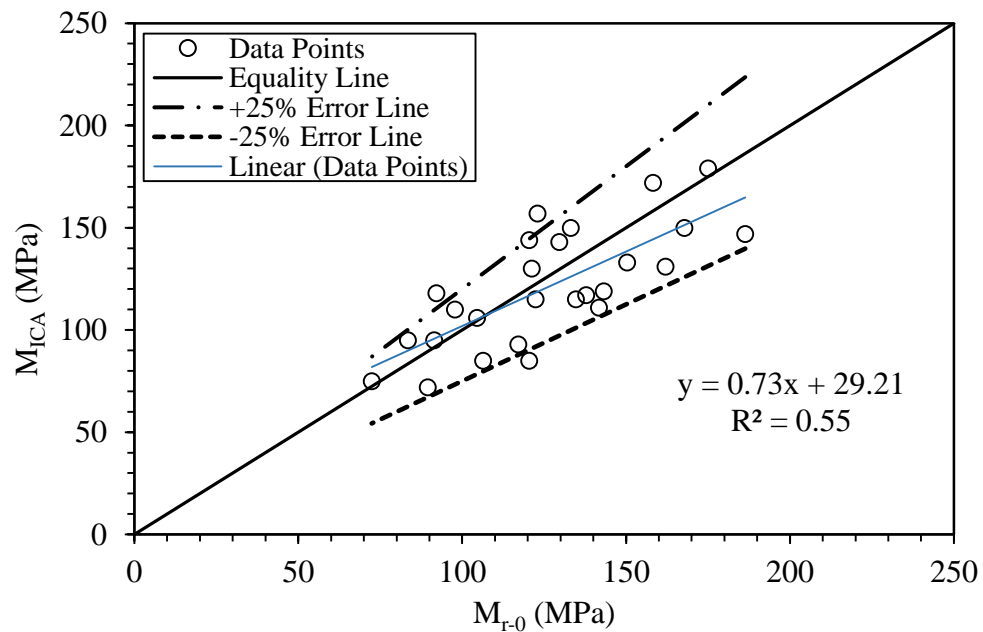
**Figure 3.13 Physical Location of Case Study 4 Construction Project**



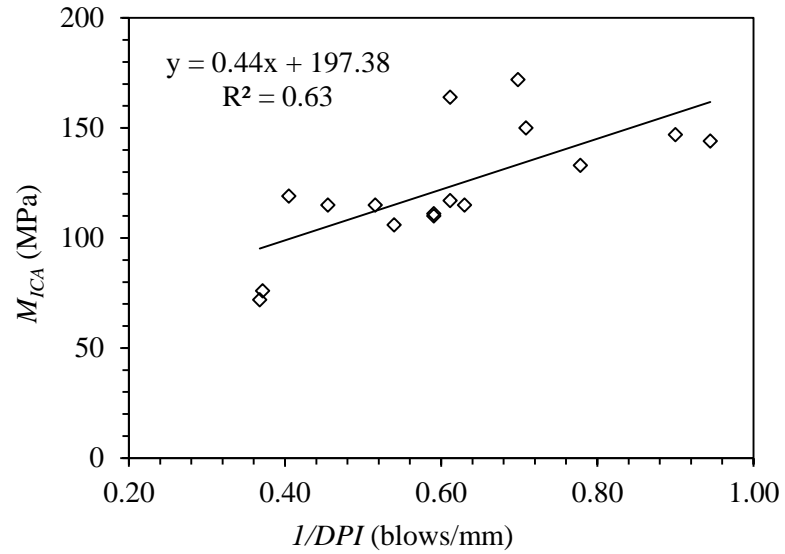
**Figure 3.14 Case Study 4 Field Project Sketch and Positions of the Calibration Stretch and Test Stations**



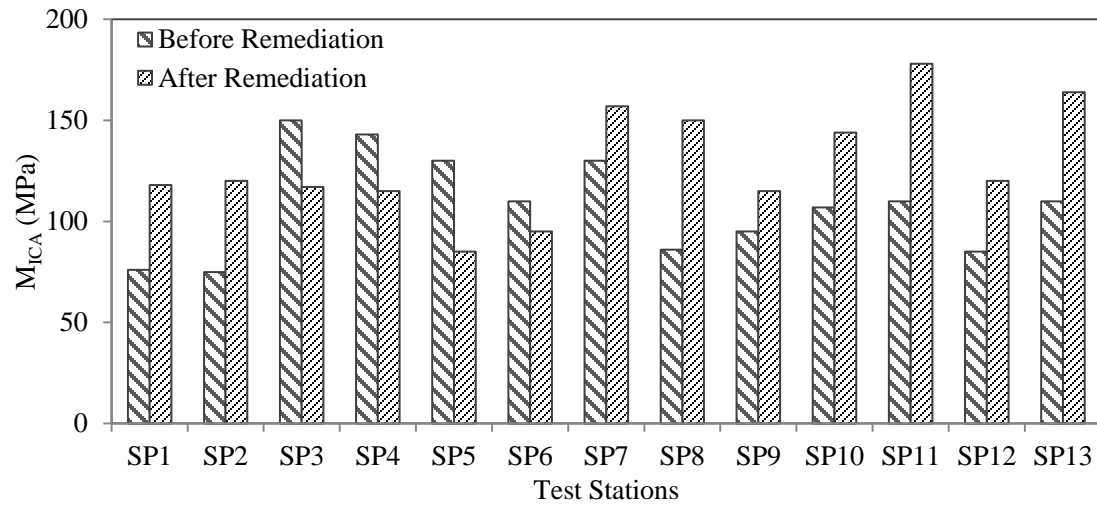
**Figure 3.15 Summary of NDG Measurements ( $w$ - $\gamma_d$  Relationship) at Test Stations of Case Study 4**



**Figure 3.16 Correlation between 0-day  $M_r$  and  $M_{ICA}$  for Case Study 4**



**Figure 3.17 Correlation between Inverse of DCP Index and  $M_{ICA}$  for Case Study 4**



**Figure 3.18 Improvement of Subgrade Moduli Due to Remedial Compaction at Soft Points of Case Study 4**

## **CHAPTER 4**

### **LABORATORY EVALUATION OF FLEXURAL PROPERTIES OF STABILIZED SUBGRADE**

#### **4.1 Introduction**

Chemical stabilization of subgrade soils is widely used at national and local levels to improve their engineering properties, including tensile strength and stiffness (modulus). Chemically-stabilized soils benefit the pavement design by reducing the required thicknesses of the pavement layers above (Little, 2000; TMR, 2012).

Despite the aforementioned advantages of chemical stabilization, it can negatively affect the long-term performance of the pavement, in an overall sense. Without a good understanding of the behavior of chemically-stabilized subgrade under vehicular traffic loading, it may result in a premature failure of the subgrade layer and reflective cracking in the asphalt layers (Thompson, 1966; Arellano and Thompson, 1998; Little, 2000; and Zhang et al. 2010). Reflective cracking in the asphalt layers caused by base or subgrade failures cannot be delayed significantly, in some instances, by such methods as geosynthetic reinforcement (Barksdale, 1991; Cleveland et al., 2002). Using right type and amount of stabilizing agents is important to preventing premature failure of the stabilized layers and enhancing pavement performance.

Using chemical additives for stabilizing subgrade soils generally leads to a subgrade which is brittle in nature. Brittle materials experience high tensile stress with a small increase in tensile strain, which may negatively affect its fatigue life (Molenaar 1984; Ahnberg, 2006; and Zhang et al., 2010). The tensile stress in a pavement is generally induced due to construction equipment and vehicular traffic loading on the

pavement. These loads lead to bending of a stabilized layer and development of compressive stresses at the top and tensile stresses under the neutral plane of the layer (McKenzie et al., 2002). Therefore, using chemical stabilizers such as CKD, lime, cement and fly-ash, makes the flexural behavior of subgrades more dominant, compared to untreated subgrades (Zhang et al., 2010). Consequently, it is important to consider the flexural behavior of a chemically-stabilized subgrade layer in pavement design.

Flexure-induced tensile stresses and strains at the bottom of a stabilized layer become more important under repetitive traffic loading, leading to fatigue (Theyse, 1996). Due to increased brittleness, a stabilized layer is more prone to fatigue cracks compared to untreated geo-materials (Pu, 2007). After initiation at the bottom, fatigue cracks propagate upward through the stabilized layer and develop discontinuities in the layer (Sobhan and Mashnad, 2000). These discontinuities are a leading cause of reflective cracks at the surface of the pavement (Francken et al., 1996; Shalaby and Fréchet, 2000). From a comprehensive review of literature, only a limited number of studies could be found on the effect of the fatigue failure of chemically-stabilized subgrade layers on the overall performance of the pavement. Most of these studies show the negative effects of fatigue failure of the chemically-stabilized subgrade layer on the overall performance of a pavement (Theyse et al., 1996; Jameson and Sharp, 2004; Molenaar and Pu, 2008).

Limited data are available on the tensile and flexural characteristics of chemically-stabilized subgrades. A number of variables affecting the determination of stabilized soil properties and considerable effect of curing time on soil-additive mixture properties are some of the factors that make the study of the fatigue properties of stabilized subgrade particularly challenging (Arellano and Thompson, 1998). The flexural behavior of



chemically-stabilized soil under monotonic and repetitive loading is described in this chapter. Specifically, the effect of different amounts of two chemical additives (CKD and lime) on the compressive and flexural strength, strain at failure, resilient and flexural modulus, and fatigue life of a chemically-stabilized clayey soil was investigated. In addition, the flexural properties of the soil-additive mixtures were compared with the compressive properties determined by UCS and  $M_r$  tests. Further, a fatigue life prediction model was suggested for the chemically-stabilized subgrade soil using flexural test results.

## **4.2 Literature Review**

To the author's knowledge, two widely accepted specifications are available for evaluation of flexural strength of chemically-stabilized soils, namely ASTM D1635 and Austroads AP-T101/08. The ASTM D1635 (2000) standard describes a method for measuring the flexural strength of simple beams of stabilized soil. A newer edition of this standard was published in 2012 (ASTM D1635, 2012). Yeo (2008) suggested a similar method for cemented materials, which was based on the Australian standards for concrete testing, published in the Austroads AP-T101/08 report. In both of these specifications, the span to depth ratio of the beam is three and the beam is subjected to third point loading. In both of these standards, the failure tensile stress at the bottom of the beam is taken as the flexural strength of the beam. These standards do not suggest a method for measuring the deformations and specifically the tensile strain at the bottom of the beam.

One of the earliest studies on flexural properties of chemically-stabilized soil was conducted by Walker (1976). Using laboratory test results, Walker (1976) suggested the

following relationship between flexural strength, also known as modulus of rupture (MoR), and unconfined compressive strength (UCS) of a chemically-stabilized soil:

$$MoR = 0.51 UCS^{0.88} \quad (4.1)$$

where UCS and MoR are in units of kPa.

Flexural performance of shale and aggregates stabilized with different types of additives (quick-lime, fly ash, cement, and CKD) was studied under monotonic loading by Laguros and Keshawarz (1987) and by Zhu (1998). A limited investigation was conducted by Raad (1985) to determine the influence of cement stabilization on the MoR of silty clay. Ansary et al. (2007) studied the MoR of stabilized soils collected from two sites of Chittagong coastal region in Bangladesh. The soils were stabilized using 3% lime and different percentages of fly ash (0, 6%, 12% and 18%). It was found that the stabilization results in 3 to 4.6 times increase in MoR, compared to the corresponding untreated soils. These studies focused on the stress at failure and did not determine the induced tensile strain at the bottom of the beam at the point of failure (tensile strain at failure).

When fatigue performance of brittle materials is of concern, the initiation of crack is more dependent on strain rather than stress (Kaplan, 1963). Otte (1972, 1978) reported that for chemically-stabilized materials engineers should have a good understanding of strain. For chemically-stabilized materials, considering strain values rather than stress values gives more consistent results (Otte, 1972; Otte, 1978; and Jitsangiam et al., 2016). Jitsangiam et al. (2016) showed that the strain-controlled testing was the preferred method for evaluating the fatigue endurance of cement-stabilized crushed rock compared to stress-controlled tests.

A comprehensive review of literature conducted in this study shows that only a limited number of studies have been pursued previously on the reflective cracking in asphalt layers due to fatigue failure of stabilized subgrade layers. Casmer (2011) used a large-scale experiment to study the fatigue cracking in cementitious pavement layers. The tested section was a stabilized base layer with a thickness of 0.2 m and was supported by uniformly-graded sand having a depth of 2.5 m. Four different types of soil (namely, gravel, sand, silt and clay) and three different types of chemical additives (namely, Portland cement, lime and fly-ash) were used to prepare the mixtures for the base layer. The applied load was increased gradually by increasing the number of loading cycles. The results could not be validated with the fatigue model available in the Mechanistic-Empirical Pavement Design Guide (M-EPDG) (Wen et al., 2011), due to the specimens' variability. It was concluded that due to the heterogeneity of the cementitious layers, cracks may form at local weak points and not necessarily at the maximum stress zone.

No widely-accepted standard methods could be found in the literature for evaluating flexural modulus and fatigue life of chemically-stabilized subgrades. Siripun et al. (2012), Arnold et al. (2012), Mandal (2013), Solanki and Zaman (2014), Jitsangiam et al. (2016) investigated the flexural modulus and flexural fatigue of chemically-stabilized specimens.

Siripun et al. (2012) and Mandal (2013) investigated the effect of additive amount on the fatigue life of selected cementitious materials. It was found that the fatigue life of cementitious crushed rocks decreases after the additive amount exceeds certain level. The fatigue behavior and modulus growth of chemically-stabilized pavement layers were studied by Mandal (2013). Four types of soil (gravel, sand, silt, and clay) and three types

of additive (cement, class C fly ash, and lime-class F fly ash), and nine different soil-additive mixtures were tested. Beam specimens were compacted using a rammer into a prismatic mold (400 mm  $\times$  102 mm  $\times$  102 mm). Beams were subjected to four-point cyclic loading during the flexural modulus test. The flexural modulus of the beams was measured at different load levels (20%, 30% and 40% of MoR of the mix). The measured fatigue lives of the beams were compared with the existing models for concrete, asphalt pavement and cement-stabilized aggregates. It was found that an increase in the additive amount may not necessarily increase the fatigue life of the mixture in a stress-controlled test. A comparison between flexural modulus and resilient modulus values reported by Mandal (2013) showed that two out of three mixtures (clay + 6% lime, and gravel + 13% fly ash) had higher flexural moduli than the corresponding resilient modulus values. One mixture (silt + 4% lime + 12% fly ash) showed a lower flexural modulus than the corresponding resilient modulus.

Arnold et al. (2012) conducted MoR tests as well as flexural fatigue tests on different New Zealand aggregates, including alluvial gravel, crushed limestone, and crushed basalt, stabilized with cement and/or foam bitumen. Both mold compacted and saw-cut beams were tested. Using monotonic flexural loading, tensile strain at failure and MoR of the beam specimens were evaluated. Also, flexural modulus and fatigue life of different specimens were determined using cyclic flexural loading. The fatigue life of the beams were found to be higher than the predicted values using the criteria suggested by Austroads (2004). However, the fatigue life from the flexural fatigue test was lower (conservative) compared to the fatigue life achieved from tests by an accelerated pavement testing facility.

Solanki and Zaman (2014) studied the flexural stiffness and fatigue life of chemically-stabilized beams. Different soil-additive mixtures were prepared by adding 6% lime and 10% CKD to two types of soil (silty clay and lean clay). The fatigue life of each beam specimen was determined using four-point bending test by applying a constant strain of 500  $\mu\text{mm/mm}$  (micro-strain). It was observed that the mean fatigue life of beams compacted using a silty clay, stabilized with 6% lime was greater than two million cycles. Beam specimens of the same silty clay, stabilized with 10% CKD, although had higher modulus than lime-stabilized specimens, failed at a relatively low number of cycles, approximately 50 cycles. The 6% lime- and 10% CKD-stabilized beams of lean clay exhibited mean fatigue lives of 1,430,000 and 965,000 cycles, respectively. A comparison between the reported flexural modulus values (Solanki and Zaman, 2014) and the resilient modulus values of the same mixtures, previously reported by Solanki (2010), showed higher flexural modulus for the mixture of lean clay stabilized by lime. The other three mixtures showed relatively lower flexural modulus values rather than resilient moduli.

Jitsangiam et al. (2016) conducted a series of flexural fatigue tests on mixtures prepared by blending a standard crushed rock base with different percentages (3% to 10%) of cement. The tests were conducted on 28-day cured specimens in both strain-controlled and stress-controlled conditions. Different strain levels (50 to 200  $\mu\text{mm/mm}$ ) were used for strain-controlled tests. It was found that the strain-controlled testing was preferable due to more consistent results compared to stress-controlled condition. Further, it was found that the adapted beam-fatigue test protocol of asphalt concrete was suitable for determining fatigue life of the chemically-stabilized material.

#### 4.2.1 Euler-Bernoulli Beam Theory

For majority of studies on chemically-stabilized soil, when tensile strain at the bottom of the beam/layer could not be directly measured using strain gauges, the Euler-Bernoulli beam theory was applied. The Euler-Bernoulli beam theory uses the following assumptions for calculating the developed stresses and deformations in the beam:

- The cross-section of the beam is infinitely rigid in its own plane;
- The cross-section of the beam remains plane after bending; and
- The cross-section of the beam remains perpendicular to the longitudinal plane of the beam.

Although, these assumptions are not satisfied by real-life structures exactly, the theory approximates the structure's behavior accurate enough (Superkar, 2007). Based on this theory the tensile stress and tensile strain at the bottom of the beam, and modulus in flexure as a result of third-point loading test can be expressed by Equations 4.2, 4.3 and 4.4:

$$\sigma_t = \frac{PL}{bh^2} \quad (4.2)$$

$$\varepsilon_t = \frac{12\delta h}{(3L^2 - 4a^2)} \quad (4.3)$$

$$M_f = \frac{\sigma_t}{\varepsilon_t} = \frac{aP(3L^2 - 4a^2)}{4b\delta h^3} \quad (4.4)$$

where,  $\sigma_t$  = tensile stress at the bottom of the beam,  $\varepsilon_t$  = tensile strain at the bottom of the beam,  $M_f$  = flexural modulus,  $P$  = applied load,  $L$  = length of the beam between the bearings (span),  $b$  = average width of the beam specimen,  $h$  = average height of the beam specimen,  $a$  = distance between the loading points, and  $\delta$  = vertical displacement at the mid-height and mid-span of the beam. The accuracy of Euler-Bernoulli beam theory in

determining the load-deformation properties of the chemically-stabilized beams will be examined in Chapter 5.

#### **4.2.2 Fatigue Life Prediction Models**

Due to importance of fatigue characterization of chemically-stabilized materials and factors affecting the fatigue performance, a majority of the fatigue investigations has led to development of relationships between fatigue life and induced tensile stresses/strains in the material (De Beer, 1986). A simple cumulative damage model was defined by Miner (1945) and is widely used for modeling fatigue failures. Miner's Law states that damage fraction ( $C$ ) can be calculated using the following equation:

$$C = \sum_{i=1}^k \frac{n_i}{N_i} \quad (4.5)$$

where,  $k$  = number of different stress levels,  $N_i$  = average number of cycles to failure at  $i^{\text{th}}$  stress level ( $S_i$ ), and  $n_i$  = number of cycles accumulated at stress  $S_i$ . Damage fraction  $C$  is the fraction of life consumed by exposure to the cycles at the different stress levels. In general, when the damage fraction reaches 1, failure occurs (ReliaSoft Corporation, 2007).

The models for fatigue life are generally defined as a function of the tensile stress or tensile strain, or a ratio to the breaking stress/ strain of the material. Both stress-based and strain-based models have been reported in the literature. The general relationship is usually defined as follows:

$$\text{Log} (N_f) = f_n \left[ \frac{\sigma_t}{\sigma_{tf}} \text{ or } \frac{\varepsilon_t}{\varepsilon_{tf}} \right] \quad (4.6)$$

where,  $N_f$  = fatigue life of the material,  $\sigma_t$  = induced tensile stress,  $\varepsilon_t$  = applied tensile strain,  $\sigma_{tf}$  = peak tensile stress, and  $\varepsilon_{tf}$  = tensile strain at failure of the material. The terms  $\frac{\sigma_t}{\sigma_{tf}}$  and  $\frac{\varepsilon_t}{\varepsilon_{tf}}$  are known as stress ratio and strain ratio, respectively. For fatigue life analysis,  $\sigma_t$  and  $\varepsilon_t$  are usually determined during the cyclic flexural loading. The values of  $\sigma_{tf}$  and  $\varepsilon_{tf}$  are usually determined during monotonic flexural loading which is typically conducted by means of third-point loading test (MoR test) in the laboratory.

Thompson (1994) developed a stress-based model for stabilized base for design purposes which was later adopted by the Illinois Department of Transportation. The relationship which showed the stress ratio (SR) as a function of the number of loading cycles to failure ( $N_f$ ) was represented by the following equation:

$$\text{Log } (N_f) = (0.9722 - SR)/0.0825 \quad (4.7)$$

Sobhan and Mashnad (2003) conducted third-point cyclic loading on beams of recycled aggregates mixed with CFA and reinforced with waste plastic strips. The stress ratio (SR) versus fatigue life ( $\log(N_f)$ ) for different specimens was plotted, and the following equation was reported as the best fit equation:

$$SR = - 0.038 \log(N_f) + 1.047 \quad (4.8)$$

AASHTO (2004) released the Mechanical-Empirical Pavement Design Guide (M-EPDG), which was developed based on the NCHRP 1-37A project in 1996. According to this guide, the fatigue model could be estimated from the following equation:

$$\text{Log } (N_f) = \left( \frac{k_1 \beta_{c1} - \left( \frac{\sigma_t}{\text{MoR}} \right)}{k_2 \beta_{c2}} \right) \quad (4.9)$$



where, MoR = modulus of rupture after 28 days of curing,  $k_1$  and  $k_2$  = regression coefficients, and  $\beta_{c1}$  and  $\beta_{c2}$  = field calibration factors. Due to the complexity of carrying out required field investigations, the fatigue cracking model was not field calibrated and the M-EPDG recommended the field calibration factors,  $\beta_{c1}$  and  $\beta_{c2}$ , to be defined as unity (ARA Inc., 2004).

A strain-based model was developed by Freeme et al. (1982) using the Heavy Truck Simulator (HVS) tests on pavements with different cemented base materials from South Africa. The base material mostly consisted of gravel and crushed stone stabilized with cement. The tensile strain at the bottom of the cemented base layer was measured using deflection gauges. The model was described by the following equation:

$$\log(N_f) = 9.1 \left( 1 - \frac{\varepsilon_t}{\varepsilon_{tf}} \right) \quad (4.10)$$

Jameson et al. (1992) developed the following fatigue life prediction model for cement-treated crushed rock using an Accelerated Loading Facility (ALF).

$$\log(N_f) = 8 \log \left( \frac{35000}{\mu\varepsilon_t E^{0.45}} \right) \quad (4.11)$$

where  $\mu\varepsilon_t$  = maximum value of the initial tensile strain in  $\mu\text{mm/mm}$ , and  $E$  = modulus of the cemented material. The modulus of the cemented material was determined by back-calculating the FWD test results. The model suggested by Jameson et al. (1992) was later developed by Austroads (2004) using additional ALF tests. The final model was published in 2004 Austroads Pavement Design Guide (Austroads, 2004) as follows:

$$\log(N_f) = 12 \log \left( \frac{\frac{113000}{E^{0.804}} + 191}{\mu\varepsilon_t} \right) \quad (4.12)$$

The ALF was also used by Lav et al. (2006) to evaluate fatigue performance of stabilized base materials. CFA was mixed with 2, 4, 8 and 10% of cement to create the base layer in the ALF. The test results showed that the failure mechanism of stabilized fly ash was fatigue cracking at the bottom and crushing at the top of the layer. The following relationship was established to model the fatigue performance:

$$N_f = \left( a / \mu \varepsilon_t \right)^b \quad (4.13)$$

where,  $a$  and  $b$  = regression coefficients.

Solanki (2010) developed a strain-based model (or transfer function) for chemically-stabilized soils using limited data points. A plot of  $\log(N_f)$  versus strain ratio was plotted and the best fit curve was reported as follows:

$$\log(N_f) = -0.68 \left( \varepsilon_t / \varepsilon_{tf} \right) + 6.55 \quad (4.14)$$

A summary of the suggested models for evaluation of fatigue life of chemically-stabilized materials is presented in Table 4.1. In this study, the results from MoR and four-point flexural fatigue (FPFF) tests on different soil-additive mixtures were employed to develop a strain-based model. Further, the accuracy of the model was examined using flexural laboratory test results from previous studies. The measured fatigue life values was also compared with the predicted fatigue lives assessed by suggested models in the literature.

### **4.3 Materials and Mixture Combinations**

#### ***4.3.1 Materials***

The soil used in this study was collected from a construction project site located at the intersection of Interstate 35 and Main Street in Norman, OK. This was the same soil used for CS3 in Chapter 2. Bulk soil samples collected from the site were used to conduct the following tests and analyses: Sieve analysis and hydrometer test (ASTM D422, 2007), Atterberg limits (ASTM D4318, 2010), specific gravity (ASTM D854, 2010), and soil classification (ASTM D2487, 2011). A summary of the test results is presented in Table 2.2 (same soil as in CS3). As stated previously in Section 2.6.1, the soil was classified as CL (clay of low plasticity), according to the Unified Soil Classification System (USCS).

Two types of chemical additives were used in this study, namely CKD and hydrated lime (hereinafter called lime). The CKD, provided by Holcim (US) Inc., was the same CKD used for stabilization of the subgrade layer in the Interstate 35 project. The lime was delivered by United States Lime and Minerals, Inc. The chemical components of the two chemical additives, provided by the suppliers, are presented in Table 4.2.

#### ***4.3.2 Mixture Combinations***

According to the literature, pH of the mixture is an important parameter in determining the amount of additives to be used for stabilization (Prusinski and Bhattacharja, 1999; Little, 2000; Miller and Azad, 2000; Qubain et al., 2000; Mallela et al., 2004; Parsons et al., 2004; Gomez, 2009; and Solanki, 2010). A survey of these studies showed that for majority of soils, pH of the mixtures had an asymptotic trend after adding more than 15% CKD and 8% lime. Application of less than 5% CKD and 3% lime

is usually not practical because of low improvement in soil properties. Based on the aforementioned observations, 5%, 10% and 15% CKD, and 3%, 6% and 9% lime were selected for further study. The specimens prepared with these amounts of chemical additives were called CKD5, CKD10, CKD15, LM3, LM6, and LM9, respectively

For all of the soil-additive mixtures, the corresponding  $w_{opt}$  and  $\gamma_{dmax}$  were determined according to ASTM D698 (2012). Figure 4.1 shows the  $w$ - $\gamma_d$  relationships for different soil-additive mixtures used in this study. All of the specimens were compacted at their respective  $w_{opt}$  and  $\gamma_{dmax}$ . The soil-additive mixtures used for the investigation along with their corresponding  $w_{opt}$  and  $\gamma_{dmax}$  are presented in Table 4.3. For both CKD- and lime-stabilized soils the  $w_{opt}$  increased and  $\gamma_{dmax}$  decreased by increasing the additive content.

## 4.4 Methodology

### 4.4.1 Specimen Preparation

Specimens were prepared for UCS,  $M_r$ , MoR and FPFF tests. Since the applied stress in  $M_r$  test is usually insignificant compared to the specimen's compressive strength, the  $M_r$  test could be assumed to be a non-destructive test (Rana, 2004). Hence, the specimens prepared for  $M_r$  tests could also be used for UCS tests. Accordingly, one set of cylindrical specimens were prepared for both  $M_r$  and UCS tests. Additionally, two distinct sets of cuboid (beam) specimens were prepared for MoR and FPFF tests.

The cylindrical specimens of  $M_r$  and UCS tests were compacted according to the procedure described in Section 2.3.2. After mixing the soil with the specific amount of chemical additive (CKD or lime) and adding water to reach  $w_{opt}$ , the specimens were

compacted in five layers so as to reach the corresponding  $\gamma_{dmax}$  in a mold, 101.6 mm in diameter and 203.2 mm in height (Figure 4.2-a). Afterwards, the specimens were stored at a temperature of  $23 \pm 1$  °C and a relative humidity of 96% for 28 days.

The beam specimens for the MoR tests were 381 mm in length, 93.1 mm in height, and 63.5 mm in width (Figure 4.2-b). A different set of beam specimens was prepared for the FPF tests. These specimens were 381 mm in length, 50.8 mm in height, and 63.5 mm in width (Figure 4.2-c). The beam specimens were compacted using a linear kneading compactor (Figure 4.3). A split compaction mold assembly, designed and fabricated in OU Broce Laboratory, was used for this purpose. The compaction procedure is explained by Solanki and Zaman (2014). To avoid any material loss and to facilitate the extraction of specimen after the compaction, the mold sides in contact with the specimen were covered with plastic sheets. After assembling the mold, the prepared soil-additive mixture was weighted and placed in the mold. According to the significance of applied pressure (ranging from 3,400 to more than 4,800 kPa) and the high number of kneading passes (more than 100 passes), each specimen was compacted in a single lift. The weight of the soil-additive mixture for each specimen was determined according to the maximum dry unit weight of each mixture. The compaction was achieved by a downward pressure applied by a rolling wheel on the top of the mold. After completion of the compaction process, the beam was gently removed from the mold and wrapped in a thin plastic sheet, in order to protect it against any changes in moisture content. The prepared specimens were cured for 28 days in a relative humidity of around 96% and a temperature of  $23 \pm 1$  °C, before testing.

Table 4.4 shows the characteristics of all of the specimens prepared for the study. For UCS,  $M_r$  and MoR tests, three specimens were compacted for each soil-additive mixture. For FPF tests, four specimens were compacted for each soil-additive mixture.

#### **4.4.2 Laboratory Tests**

##### **4.4.2.1 $M_r$ and UCS Tests**

After 28 days of curing, resilient modulus tests were conducted on the cured specimens, as discussed in Section 2.3.2 (in accordance with AASHTO T307, 2004). The resilient moduli for all 15 stress sequences were calculated from the average recoverable strain and average stress of the last five cycles of each test sequence. Among different levels of deviatoric stress and confining pressure, the  $M_r$  values at  $\sigma_d = 68.9$  kPa and  $\sigma_3 = 13.8$  kPa were considered for comparing with other laboratory test results. This stress condition was selected in accordance with the traffic induced vertical and horizontal stresses in the subgrade layer obtained in previous studies (Holewinski et al., 2003; Kim et al., 2009). Also, this loading condition in resilient modulus testing provides the closest strain rates to the strain rate used in the FPF tests.

Following the  $M_r$  tests, the UCS tests were conducted on the specimens in accordance with the ASTM D2166 (2000) standard. The load was applied on the top of the cylindrical specimen, through a platen, by downward movement of the load cell at a rate of 0.02 mm/sec. The tests were terminated after breakage of specimens and the stress-strain curves were plotted according to the recorded load-displacement data.

#### 4.4.2.2 MoR Tests

The MoR tests were conducted on the beam specimens to determine the flexural strength (MoR) and the tensile strain at failure ( $\varepsilon_{tf}$ ) at the bottom of the specimen (in accordance with ASTM D1635, 2012). Schematic and photographic views of the MoR test setup are shown in Figure 4.4-a and Figure 4.4-b, respectively. As seen in Figure 4.4-a, the beam was supported at both ends using two rollers, placed 279.3 mm apart, to achieve a span to height ratio of three. Two LVDTs were set on two aluminum studs. These studs were carefully glued on two sides of the beam at mid-height to measure the vertical displacements. The beam specimens were tested using a universal loading frame manufactured by the Material Testing System (MTS). A 2.22 kN load cell was used to measure the applied load. The load was applied on the middle-third portion of the beam span, as shown in Figure 4.4-a. The loading rate was set at 0.02 mm/sec. Using the Euler-Bernoulli beam theory and according to Equations 4.2 and 4.3, MoR and  $\varepsilon_{tf}$  were determined using the following equations:

$$MoR = \frac{P_{max}L}{bh^2} \quad (4.15)$$

$$\varepsilon_{tf} = \frac{12\delta_f h}{(3L^2 - 4a^2)} \quad (4.16)$$

where,  $P_{max}$  = maximum axial load reached during the test, and  $\delta_f$  = vertical displacement at the mid-height of the beam at failure. The value of  $\delta_f$  was determined by averaging displacements recorded by the two LVDTs. For each soil-additive mixture, the mean value of MoR and  $\varepsilon_{tf}$  for three specimens was considered as the flexural strength and tensile strain at failure, respectively.

#### 4.4.2.3 FPF F Tests

Compared to MoR test at which the beam is loaded monotonically, the FPF F test provides a method to evaluate the beam's flexural behavior under repetitive loading. The FPF F test was conducted to simulate vehicular traffic loading using a laboratory-scale test. This test was also used to determine the fatigue life and flexural modulus of the chemically-stabilized soil specimens. Due to lack of a widely-accepted standard test method for determining the fatigue characteristics of the stabilized soils, the standard for determining fatigue life of compacted hot mix asphalt (AASHTO T321, 2003) was adopted herein. Figure 4.5-a shows the FPF F fixture used for this purpose. The fixture consisted of two inner reaction clamps and two outer support clamps. The clamps were connected to the main frame of the fixture by a set of rollers and linear bearings to allow free longitudinal translation and rotation of the beam on the supports. A 0.89 kN load cell was connected to the reaction clamps to measure the load during the test. The FPF F fixture was placed in a loading frame and connected to a data acquisition system (GCTS ATM-100). Figure 4.5-b shows a photographic view of the test setup.

The vertical deflection of the beam was measured at the center of the beam's neutral axis using a LVDT. The LVDT tip was placed on an aluminum stud attached to the mid-height at the mid-span of the beam. The LVDT and load cell were connected to a SCON-1500 digital controller. The controller was connected to a computer equipped with the GCTS CATS 1.8 software providing a user interface to control the test parameters and record the data. The LVDT, controller, and the load cell formed a closed loop circuit in which the vertical displacement was translated to tensile strain at the



bottom of the beam. The stress, strain and stiffness of the specimen were calculated using Equations 4.2, 4.3 and 4.4, respectively.

The fatigue tests were conducted in the strain-controlled mode due to a better reproducibility (Kaplan, 1963; Otte, 1972; Otte, 1978; and Jitsangiam et al., 2016). The loading frequency was selected according to the traffic-induced stress pulse, and the time span of the pulse, underneath the pavement surface (Barksdale, 1971; McLean and Monismith, 1974; Huang 1993; and Loulizi et al., 2002). Previous studies have shown that the stress pulse time usually ranges between 0.01 seconds, for a vehicle speed of 97 km/h at a depth of 10 mm (McLean and Monismith, 1974), to 1 second, for a vehicle speed of 10 km/h at a depth of 597 mm (Loulizi et al., 2002). Accordingly, a constant loading frequency of 5 Hz (with a stress pulse time of 0.2 second) was selected for the fatigue test. The applied load had a cyclic sinusoidal shape with a minimum value of zero.

The maximum strain level at the bottom of the specimen was kept constant for all cycles. A parametric finite element model of the full-scale pavement structure under equivalent single axle load (ESAL), which is discussed in Chapter 6, showed that the tensile strain at the bottom of a typical chemically-stabilized subgrade layer ranged between 53 and 375  $\mu\text{mm/mm}$  (micro-strain). Hence, the cyclic strain at the bottom of the beam ( $\epsilon_t$ ) was maintained at 200  $\mu\text{mm/mm}$  (micro-strain). Also, this was consistent with the strain level used in the previous studies on evaluating the tensile strain at the bottom of the stabilized subgrades (Arnold et al., 2012; Solanki and Zaman, 2014; Jitsangiam et al., 2016).

The first 50 load cycles were considered as pre-conditioning step. The calculated stiffness at 50<sup>th</sup> load cycle was considered as the flexural modulus ( $M_f$ ) of the specimen

(AASHTO T321, 2003). For the specimens cracked before 50 load cycles, the last stiffness before failure was considered as the flexural modulus. The fatigue life ( $N_f$ ) was defined as the total number of load cycles until the stiffness of the specimen was reduced to 50 percent of the  $M_f$  (AASHTO T321, 2003). If the stiffness of the beam did not decrease 50 percent within 24 hours the test was terminated manually (at approximately 400,000 cycles) and a fatigue life of more than 400,000 cycles ( $N_f > 400,000$  cycles) was reported for that specimen.

## 4.5 Results and Discussion

### 4.5.1 $M_r$ and UCS Tests

The  $M_r$  tests were conducted on 18 cylindrical specimens (three specimens for each soil-additive mixture) after 28 days of curing. Tables 4.5 and 4.6 summarize the  $M_r$  test results for CKD- and lime-stabilized specimens, respectively. The changes in mean (of three specimens) resilient modulus with deviatoric stress ( $\sigma_d$ ) and confining pressure ( $\sigma_3$ ) are plotted in Figures 4.6 and 4.7 for CKD- and lime-stabilized mixtures, respectively. The  $M_r$  values decreased due to an increase in  $\sigma_d$ . It can be seen from Figure 4.5 that the changes of  $\sigma_3$  did not considerably affect the  $M_r$  of CKD-stabilized soil. On the other hand, as it can be seen in Figure 4.7, the lime-stabilized specimens showed more sensitivity to changes in confining pressure, especially for the specimens with 3% and 6% lime. This observation is consistent with the findings reported by other researchers (Achampong et al., 1997; Ramakrishna, 2002; and Solanki, 2010).

Figure 4.8 summarizes the  $M_r$  test results of different soil-additive mixtures. All of the reported  $M_r$  values in Figure 4.8 were calculated at  $\sigma_d = 68.9$  kPa and  $\sigma_3 = 13.8$

kPa. It can be observed that the CKD-stabilized soil showed much higher resilient moduli when compared with the lime-stabilized soil. The mean  $M_r$  values measured for CKD5, CKD10 and CKD15 specimens were 734, 1,845 and 2,602 MPa, respectively. It was observed that changes in lime content did not significantly affect the resilient modulus of the mixture. The  $M_r$  values of the soil-lime mixture were found to slightly reduce (from 624 MPa to 615 MPa) due to addition of lime. However, increasing the amount of lime to 9% increased the  $M_r$  value to 701 MPa. The error bars can scarcely be seen in Figure 4.8 because of low standard deviation, which indicates the repeatability of the  $M_r$  test for different mixtures. The mean, standard deviation and coefficient of variation of  $M_r$  values for three specimens are listed in Table 4.7 for different mixtures.

After completion of the  $M_r$  tests, UCS tests were conducted on all specimens. Figures 4.9-a and 4.9-b show the stress-strain curve for all specimens stabilized with CKD and lime, respectively. As it can be seen in Figure 4.9-a, there was a gap between the stress-strain curves of different amounts of CKD (CKD5, CKD10 and CKD15), especially at higher strain levels. This was because of the considerable improvement in UCS of the CKD-stabilized soil due to increase in the CKD amount from 5% to 10% and to 15%. This was not the case for lime-stabilized soil, especially for LM3 and LM6 mixtures which showed similar ranges of UCS values. Figures 4.10-a and 4.10-b provide a better demonstration of changes in UCS values due to the amount of CKD and lime, respectively. It was observed that an increase in the amount of CKD resulted in increased UCS in a linear fashion. The mean value of UCS for three specimens was equal to 1644 kPa at a CKD amount of 15%. This shows 165.1% and 44.9% increase compared to CKD5 and CKD10 specimens, respectively. On the other hand, by increasing the CKD

amount from 5% to 10%, the value of axial strain at the peak stress ( $\varepsilon_{af}$ ) decreases from  $13.1 \times 10^{-3}$  to  $8.9 \times 10^{-3}$ . By increasing the amount of CKD, the  $\varepsilon_{af}$  slightly increases to  $9.1 \times 10^{-3}$  for the CKD15 specimens (Figure 4.10-a).

The specimens stabilized with lime showed lower UCS values compared to the CKD-stabilized specimens. As presented in Figure 4.10-b, the UCS did not improve significantly by increasing the amount of lime from 3% to 6% (464 kPa to 515 kPa; i.e., 11% increment). However, the mean UCS value reached as high as 892 kPa for the LM9 specimens (73% increment). A gradual reduction of  $\varepsilon_{af}$  was the other consequence of increase in lime amount (Figure 4.10-b). Table 4.7 shows the mean, standard deviation and coefficient of variation of UCS and  $\varepsilon_{af}$  for the studied soil-additive mixtures. The maximum variations were observed for LM9 specimens with a coefficient of variation of 12.3% and 17.1% for UCS and  $\varepsilon_{af}$ , respectively.

The UCS values of all soil-additive mixtures were compared with the respective  $M_r$  values (Figure 4.11). A linear regression relationship was found between the UCS and  $M_r$  values, as shown by Equation 4.17. The coefficient of determination ( $R^2$ ) of the relationship was equal to 0.9.

$$M_r = 1.76 UCS - 362.08 \quad (4.17)$$

where the unit of  $M_r$  is MPa; and UCS is measured in kPa. In Figure 4.11, this relationship is compared with the plotted equation line between UCS and  $M_r$  for different CKD-stabilized specimens from Chapter 2 (Equation 2.39). Also, the suggested relationship for lime-stabilized soils by Thompson (1966) is plotted in Figure 4.11 for comparison. It was observed that, for majority of the mixtures, Equation 2.39 could give a reasonable estimation of  $M_r$  based on the UCS values of CKD-stabilized mixtures.

However, for lime-stabilized mixtures, Equation 2.39 estimated higher  $M_r$  values compared to the laboratory results (for example +107% error for LM9 specimens). The suggested relationship by Thompson (1966) was found to be conservative for the tested mixtures as that relationship gives lower values of  $M_r$  than the laboratory measured values (-74% to -90% error for the tested mixtures).

#### **4.5.2 MoR Tests**

It was observed that the specimens subjected to third point loading experienced a quick upward growth of crack, followed by a sudden failure. The measurements of crack path location after the test showed that for all of the tested specimens, the crack path was limited to mid-third of the beam, length-wise (Figure 4.12).

The load and beam mid-span deflection was recorded during the MoR test and the corresponding tensile stress ( $\sigma_{tb}$ ) and tensile strain ( $\epsilon_{tb}$ ) values at the bottom of the beam were calculated using Equations (4.2) and (4.3), respectively. Figures 4.13 and 4.14 show the tensile stress-strain curves at the bottom of the beams prepared with different amounts of CKD and lime, respectively. The MoR test data attributed to one of LM3 specimens (specimen FS-LM3-#3 in Table 4.4) is not presented due to the specimen's failure before the beginning of the test. From Figures 4.13-a, 4.14-a and 4.14-b, it was observed that the variation of stress with strain for CKD5, LM3, and LM6 mixtures followed a non-linear trend and the slope of the curve decreased as the strain increased. On the other hand, the beams prepared with the CKD10, CKD15, and LM9 mixtures showed a linear stress-strain behavior followed by a sudden failure. These results show a low resistance of the material against deflections, when subjected to flexural bending. This brittle behavior was

found to be consistent with the findings of Muhunthan and Sariosseiri (2008) and Arnold et al. (2012).

Figures 4.15-a and 4.15-b show the variations in mean MoR and  $\varepsilon_{tf}$  values with changes in CKD and lime contents, respectively. Among the CKD-stabilized mixtures, the maximum coefficients of variation of three specimens were observed for the CKD10 mixture (10.2% for MoR and 8.3% for  $\varepsilon_{tf}$ ). Similar to the UCS, the flexural strength of the beam increased significantly by an increase in the CKD content from 5% to 10% (94% increment) and from 10% to 15% (46% increment). The mean MoR value of lime-stabilized specimens generally improved by an increase in the lime content of the mixture. The increase in the MoR value was smaller for adding lime from 3% to 6% (18% increment) compared to increase in the MoR due to increasing the amount of lime from 6% to 9% (76% increment). These increments are comparable to the ones for the UCS test results, where the UCS improved by 11% and 73% by increasing the amount of lime from 3% to 6%, and from 6% to 9%, respectively.

For the CKD-stabilized soil (Figure 4.15-a), the highest  $\varepsilon_{tf}$  was observed for the CKD5 specimens (mean value for two specimens was found to be 746.9  $\mu\text{mm/mm}$ ). Similar to the UCS test results, specimens with 10% CKD exhibited the lowest  $\varepsilon_{tf}$  among the CKD-stabilized specimens (the mean value for three specimens was found to be 482.9  $\mu\text{mm/mm}$ ). This indicates that the mixtures containing 5% CKD endure the highest tensile strain before failure. On the other hand, the specimens with 10% CKD had the lowest resistance against deformation-induced strains. Although, increased flexural strength was expected as a result of using a higher amount of chemical additive, the strain level at failure did not follow any specific trend in many cases. This observation is

consistent with those reported in the literature (Muhunthan and Sariosseiri, 2008; Rodriguez, 2008; Ansary and Hasan, 2011; and Sarkar et al., 2012). Strain level is directly proportional to the stress and inversely proportional to the stiffness. It was evident that due to an increase in the amount of CKD from 5% to 10%, the flexural strength of the beam increased significantly. It was observed that an increase in stiffness resulted in a reduction in strain at which the maximum stress occurred. However, no significant increase in stiffness was observed due to increasing the CKD amount from 10% to 15%.

For the lime-stabilized specimens (Figure 4.15-b), the  $\varepsilon_{tf}$  decreased almost linearly by increasing the lime content from 3% to 9%. The  $\varepsilon_{tf}$  had a value of 360, 314, and 269  $\mu\text{mm/mm}$  for LM3, LM6, and LM9 specimens, respectively. It indicated that the specimens with 9% lime had the lowest resistance against the induced strains among lime-stabilized specimens.

Figure 4.16 shows a plot of MoR versus UCS for different mixtures. A linear relationship with a  $R^2 = 0.95$  was found between MoR and UCS of the studied mixtures as follows:

$$MoR = 0.3286 UCS - 73.992 \quad (4.18)$$

Also, the laboratory measured values can be seen in contrast with the equation proposed by Walker (1976) (Equation 4.1) in Figure 4.16. It can be seen that the equation proposed by Walker (1976) can provide a fair estimation of MoR for specimens with lower UCS.

Changes in the  $\varepsilon_{tf}$  of CKD- and lime-stabilized specimens due to changes in the additive amount showed a similar trend to those of  $\varepsilon_{af}$  from UCS test results. Figure 4.17 presents a comparison between mean  $\varepsilon_{tf}$  and  $\varepsilon_{af}$  for all soil-additive mixtures. The

tensile strain at failure (from MoR tests) and axial strain at peak (from UCS tests) was found to have a linear relationship with a  $R^2$  of 0.71. A summary of the MoR test results is presented in Table 4.8. The maximum values of coefficient of variation in  $\varepsilon_{tf}$  were observed for LM9 (12%) and CKD10 (8%) mixtures, which possessed the lowest  $\varepsilon_{tf}$  among the lime- and CKD-stabilized mixtures, respectively.

#### 4.5.3 FPF Tests

To determine the fatigue life ( $N_f$ ) of the chemically-stabilized subgrade soil, stiffness versus loading cycle was plotted on a semi-logarithmic scale ( $S - \log(N)$ ), for each tested specimen. Figures 4.18 and 4.19 show the  $S - \log(N)$  diagram for different soil-additive specimens of CKD and lime-stabilized soil, respectively. In general, all of the specimens of each mixture showed a similar behavior under cyclic flexural loading.

According to Figure 4.18, none of the CKD5 beams failed due to fatigue loading even after more than 400,000 loading cycles. All of the CKD10 beams failed at the first loading cycle. In this case, the stiffness at the first cycle was recorded as the flexural modulus of the specimen and the fatigue life of the specimens was considered not to exceed one cycle. By increasing the additive content to 15%, a higher fatigue life was achieved, when compared with that of the CKD10 mixture. For beams with 10% and 15% CKD, failure occurred in the form of a sudden drop in the  $S - \log(N)$  curve due to initiation and instantaneous propagation of crack.

As it can be seen in Figure 4.19, significant variations in stiffness of lime-stabilized specimens were observed in the form of fluctuations in the  $S - \log(N)$  diagram, especially at the loading cycles close to the failure. One of the LM6 specimens (specimen FF-LM6-#4 in Table 4.4) broke during installation in the FPF fixture, and



could not be tested. All of the LM9 specimens failed at the initiation of the test before the deflection reached the peak value of the first cycle. Hence, the FPF results of this set of specimens is not presented in Figure 4.19.

A summary of the FPF test results including the mean value, standard deviation and coefficient of variation of  $M_f$  (for three or four specimens) for different soil-additive mixtures is presented in Table 4.9. The CKD15 specimens possessed the highest  $M_f$  (3146 MPa) among all of the mixtures. The lime-stabilized mixtures showed lower flexural moduli compared to the CKD-stabilized mixtures. Also, the lime-stabilized mixtures showed higher values of coefficient of variation in  $M_f$  compared to CKD-stabilized specimens. The maximum coefficient of variation of flexural moduli was observed for LM6 specimens to be 15.3%. This indicates the consistency of test results and repeatability of the test procedure used for testing each mixture.

Figure 4.20 shows the changes in mean  $M_f$  and a comparison between  $M_f$  and  $M_r$  (at  $\sigma_d = 68.9$  kPa and  $\sigma_3 = 13.8$  kPa) for different soil-additive mixtures. All of the mixtures showed higher mean flexural modulus values than resilient modulus values. As mentioned before, similar observations have been reported by Solanki (2010) and Mandal (2013) for clay-lime mixtures. However, the reported flexural modulus of clay-CKD mixture was lower than its corresponding resilient modulus (Solanki, 2010). Similar to resilient modulus, it was found that the flexural modulus of the CKD-stabilized mixtures increased by an increase in CKD content. The mean  $M_f$  values were found to be 1,214, 2,662, and 3,146 MPa for CKD5, CKD10, and CKD15 mixtures, respectively. These values are 65.3%, 44.3%, and 20.9% higher than  $M_r$  of CKD5, CKD10, and CKD15 mixtures, respectively. In Chapter 6, the determined flexural modulus values are used as

a substitute for resilient modulus of chemically-stabilized subgrade (CSS) layer in designing of semi-rigid pavement using the M-EPDG method.

It can be seen in Figure 4.20 that the improvement of the mean  $M_f$  due to increase in lime content from 3% to 6% was not significant (from 728 to 797 MPa). However, these values were 16.7% and 21.6% higher than the resilient modulus of the same mixtures, respectively.

The fatigue lives of all soil-additive mixtures are listed in Table 4.9 and plotted in Figure 4.21. Specimens with 5% CKD were found to have the highest fatigue lives among other soil-additive mixtures and did not crack even after 400,000 loading cycles. It can be observed from Figure 4.21 that the flexural fatigue life of the stabilized subgrade was generally reduced due to an increase in the additive amount, from 5% to 15% for the CKD-stabilized specimens and from 3% to 9% for the lime-stabilized specimens. The CKD5, LM3 and LM6 specimens showed higher fatigue lives with mean values of more than 400,000, 69,662 and 22,384 cycles, respectively, when compared with other specimens. The LM9 specimens did not show any fatigue resistance at the 200  $\mu\text{mm/mm}$  strain level. CKD10 specimens also failed during the first load cycle. This behavior was attributed to the fact that CKD10 and LM9 specimens possess the lowest tensile strain at failure among other mixtures for the same additive type (483 and 269  $\mu\text{mm/mm}$ , respectively). The mean  $\varepsilon_{tf}$  values of the mixtures are included in Figure 4.21-a. It can be observed that fatigue life of the beams follows the same trend as that of  $\varepsilon_{tf}$ . Also, similar trends were observed for changes in fatigue life and  $\varepsilon_{af}$  (see Figure 4.21-b).

Considering the specimens stabilized with CKD, the maximum fatigue life was observed for the specimens with highest value of strain at failure (CKD5 specimens with

a  $\varepsilon_{af}$  of  $13.13 \times 10^{-3}$  mm/mm, and a  $\varepsilon_{tf}$  of 747  $\mu\text{mm/mm}$ ) (see Figure 4.21). The fatigue life decreased to 105 cycles by reduction of  $\varepsilon_{tf}$  to 578  $\mu\text{mm/mm}$  for CKD15 specimens and to 1 cycle for the CKD10 specimens with a  $\varepsilon_{tf}$  of 483  $\mu\text{mm/mm}$  ( $\varepsilon_{af} = 8.88 \times 10^{-3}$  mm/mm). Similarly, the fatigue life of specimens stabilized with lime was decreased along with the decrease in strain at failure. The fatigue life changed from 69,662 cycles with a  $\varepsilon_{tf}$  of 360 (LM3 specimens) to no fatigue resistance at a  $\varepsilon_{tf}$  of 269 (LM9 specimens). As stated earlier, this behavior was attributed to the fact that the specimens with 10% CKD and 9% lime possessed the lowest tensile strain at failure among other mixtures for the same additive type according to MoR results. Hence, at a fixed strain level ( $\varepsilon_t$ ) of 200  $\mu\text{mm/mm}$ , the beam experienced a higher cyclic strain ratio ( $\varepsilon_t/\varepsilon_{tf}$ ) when compared to the other mixtures. The values of the strain ratio for CKD10 and LM9 mixtures were 0.41 and 0.74, respectively. An increase in the strain ratio led to a reduction of the fatigue life of the chemically-stabilized subgrade soil (Freeme et al., 1982; Solanki and Zaman, 2014). The CKD5 and LM3 specimens, which had the lowest strain ratio among mixtures with the same additive type (mean value of 0.27 and 0.56, respectively), showed the highest fatigue lives. Therefore, in a strain-controlled fatigue test and a specific type of additive, the tensile strain at which the beam failed ( $\varepsilon_{tf}$ ) was found to play a more important role, compared to the flexural strength. This shows the importance of material's ductility/brittleness in the long-term performance of a chemically-stabilized subgrade layer. Therefore, the ability of a chemically-stabilized soil to resist higher flexural strains can lead to a higher number of load cycles which the subgrade layer can undergo before failure.

#### ***4.5.4 Fatigue Life Prediction Model***

Some of the strain-based models, such as the model proposed by Freeme et al. (1982) (Equation 4.10), consider the strain ratio as the main parameter for predicting the fatigue life of chemically-stabilized soils. Additionally, it was observed that generally, the fatigue life of the specimens had a reverse relationship with the modulus of the specimens (see Figure 4.22). For example, although LM3 and LM6 specimens had lower  $\varepsilon_{tf}$  compared to CKD10 and CKD15 specimens, they exhibited higher fatigue lives. This can be attributed to the fact that due to considerably lower moduli of LM3 and LM6, the induced tensile stresses at the bottom of beams of these two mixtures were lower than the ones at the bottom of CKD10 and CKD15 beams at a fixed strain level. A few strain-based fatigue life models, such as models proposed by Jameson et al. (1992) (Equation 4.11) and Austroads (2004) (Equation 4.12), have the modulus of the chemically-stabilized soil as an input. However, these models do not consider the tensile strain at failure of the material. In this study the strain ratio as well as the mixture's modulus was considered for developing the fatigue life prediction model.

##### ***4.5.4.1 Model Based on Compressive Properties***

A clear correlation between fatigue life and UCS of the chemically-stabilized soil was not found to exist. Therefore, according to the similar trends of fatigue life and  $\varepsilon_{af}$  in Figure 4.21-b, it could be concluded that the strain at failure plays a more important role in determining the long-term performance of the specimens rather than UCS. To develop a fatigue life prediction model based on the compressive properties, fatigue life versus  $\varepsilon_{af}/M_r$  for different mixtures was plotted in a semi-logarithmic scale (Figure 4.23). As fatigue life of CKD5 mixture could not be determined precisely ( $N_f > 400,000$ )

and LM9 mixture showed zero fatigue resistance, these two mixtures were not considered for developing the model. Figure 4.23 showed that an exponential relationship could be developed for fatigue life prediction as follows:

$$N_f = 0.6893 e^{7.436 \times 10^5 \frac{\varepsilon_{af}}{M_r}} \quad (4.19)$$

The equation had a  $R^2$  of 0.76. Using this equation, the fatigue life of the CKD5 mixture was predicted to be equal to 410,259 cycles. This value is marked with \* symbol in Figure 4.23. Although, the  $R^2$  value associated with Equation 4.19 is relatively high, it could not be validated with results of other studies. As no studies were found that assessed  $\varepsilon_{af}$  (from UCS tests),  $M_r$  and fatigue life of a chemically-stabilized mixture, all together. Hence, Equation 4.19 was not considered for further analysis.

#### 4.5.4.2 Model Based on Flexural Properties

The initial form of the fatigue model based on flexural properties was selected in accordance with strain-based model proposed by Austroads (2004) (Equation 4.11). However, the final form of the model was achieved by making some changes to the initial model. As mentioned in previous section, data points attributed to CKD5 and LM9 mixtures were not considered for developing the model. The fatigue life of the chemically-stabilized soil could be predicted using the following equation:

$$\log N_f = \frac{4127.44}{M_f^{1.145} \frac{\varepsilon_t}{\varepsilon_{tf}}} + 1.47 \quad (4.20)$$

Figure 4.24 shows the comparison between estimated and actual  $N_f$  of different mixtures of this study. The corresponding  $R^2$  was equal to 0.84. It can be observed that except for CKD10 mixture that had very low fatigue life ( $N_f = 1$ ), the model could predict

the fatigue life of other models with a reasonably high accuracy. Using Equation 4.20, the fatigue life of CKD5 mixture was predicted as 1,013,490 cycles which is marked with \* symbol in Figure 4.24.

To the author's knowledge, among several studies conducted previously on the fatigue life of chemically-stabilized subgrade soils, only two studies (Solanki, 2010; Arnold et al., 2012) have assessed all of the required parameters in Equation 4.20 (i.e.,  $M_f$ ,  $\varepsilon_t$ ,  $\varepsilon_{tf}$ , and  $N_f$ ). Hence, the laboratory test results of these two studies were used to assess the predictability of the developed model. The data attributed to the materials used in the two studies are presented in Table 4.10. These materials consist of four types of soils, namely CL, CL-ML, alluvial gravel (passed through sieve no. 40) and crushed limestone, and three types of additives, namely cement, CKD and lime. The mixtures with high variations in flexural fatigue test results were not considered (i.e., data attributed to Australian basalt + 3% cement, and Flat-top GAP25 + 3% cement, from Arnold et al., 2012). Figure 4.25 shows a comparison between predicted and actual (laboratory measured) fatigue life of all mixtures from Solanki (2010), Arnold et al. (2012) and the current study. As it can be seen, Equation 4.20 could predict the fatigue life of different mixtures with a  $R^2$  of 0.60. Although the prediction model was produced using limited data (4 data points), aggregation of the data points around the equality line shows the ability of the model in predicting the fatigue life of other chemically-stabilized subgrade soils. In Chapter 6, the developed model (Equation 4.20) is used for designing the semi-rigid pavement with consideration of fatigue life of the CSS layer.

Table 4.11 presents the predicted fatigue lives of different soil-additive mixtures using the models proposed by Freeme et al. (1982), Jameson et al. (1992) and Austroads

(2004), and the suggested model in this study (Equation 4.20). Figures 4.26-a, 4.26-b and 4.26-c shows the predictability of these three models for fatigue life of the studied mixtures, respectively. A poor relationship was observed for all of the models from previous studies. The highest coefficient of determination (0.15) among these three models was found for the Austroads (2004) model. The model proposed by Jameson et al. (1992) provided higher predicted fatigue lives than the actual values.

#### **4.6 Conclusions**

The flexural properties of chemically-stabilized subgrade soil were studied in laboratory using different types and amounts of chemical additives. Also, the flexural properties of the prepared mixtures were compared with their corresponding compressive properties. Further, a fatigue life prediction model was suggested using flexural test results and was applied for predicting fatigue life of materials from previous investigations in the literature. The following conclusions were drawn from this study:

1. The flexural strength and flexural modulus of the chemically-stabilized soil increased due to an increase in the amount of additive. The increase was more significant for CKD-stabilized soil compared to lime-stabilized soil. The increase in flexural strength was around 94% by increasing the CKD content from 5% to 10%.
2. Generally, the strain at failure reduced by adding more additives with an exception for specimens stabilized with 10% CKD, which had the lowest strain at failure among the CKD-stabilized mixtures. The CKD5 specimens showed the highest tensile strain at failure among CKD-stabilized specimens. For the lime-

stabilized specimens the tensile strain at failure decreased almost linearly by increasing the lime content from 3% to 9%.

3. All soil-additive mixtures found to have relatively higher flexural moduli (at a strain level of 200  $\mu\text{mm/mm}$ ) than their corresponding resilient moduli (at  $\sigma_d = 68.9 \text{ kPa}$  and  $\sigma_3 = 13.8 \text{ kPa}$ ). The flexural modulus values were aimed to be used as a substitute for resilient modulus of CSS layer in a semi-rigid pavement for designing using the M-EPDG method.
4. Increasing additive amounts had a negative effect on fatigue performance of the stabilized subgrade soil, in general. Lightly-stabilized specimens (CKD5, LM3 and LM6) showed the highest fatigue life among different mixtures.
5. Strain in failure played a key role in the fatigue performance of the stabilized soil. For a specific additive type, mixtures with the highest strain at failure (CKD5 and LM3) possess the highest fatigue life. On the other hand, specimens with the lowest strain at failure in UCS and MoR tests (CKD10 and LM9 mixtures) failed at the beginning of the FPF test, due to increased brittleness.
6. The developed fatigue life prediction model could predict the fatigue life of the mixtures reported in the literature with a good accuracy ( $R^2 = 0.60$ ), compared to the proposed models in the previous studies. The developed model can be used for considering the fatigue life of CSS layer in designing a semi-rigid pavement using the M-EPDG method.



**Table 4.1 Summary of Fatigue Life Prediction Models from the Literature**

Reference	Material	Model Type	Equation
Freeme et al. (1982)	Cement-stabilized base (pavement data base)	Strain-based	$\log(N_f) = 9.1 \left(1 - \frac{\varepsilon_t}{\varepsilon_{tf}}\right)$
Jameson et al. (1992)	Cement-stabilized base: Cement-gravel and cement-crushed stone (pavement data base)	Strain-based	$\log(N_f) = 8 \log \left( \frac{35000}{\mu \varepsilon_t E^{0.45}} \right)$
Thompson (1994)	High-strength stabilized-base: Cement-aggregate mixtures and pozzolanic-stabilized substances	Stress-based	$\text{Log} (N_f) = (0.9722 - SR)/0.0825$
Sobhan and Mashnad (2003)	CFA-recycled aggregates reinforced with plastic strips	Stress-based	$SR = -0.038 \log(N_f) + 1.047$
Austrad (2004)	Cement-stabilized base ALF data base)	Strain-based	$\log(N_f) = 12 \log \left( \frac{\frac{113000}{E^{0.804}} + 191}{\mu \varepsilon_t} \right)$
Lav et al. (2006)	CFA mixed with cement	Strain-based	$N_f = (a/\mu \varepsilon_t)^b$
Solanki (2010)	Clay mixed with lime and CKD	Strain-based	$\log(N_f) = -0.68 \left( \varepsilon_t / \varepsilon_{tf} \right) + 6.55$

**Table 4.2 Chemical Components of the CKD and Lime Used in the Study**


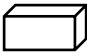
Chemical Compound/ Property	Percentage by Weight	
	CKD	Lime
SiO <sub>2</sub>	20.22	0.59
Al <sub>2</sub> O <sub>3</sub>	5.79	0.24
Fe <sub>2</sub> O <sub>3</sub>	2.77	0.21
CaO	56.39	70.43
MgO	0.99	0.61
SO <sub>3</sub>	8.28	---
Na <sub>2</sub> O	0.25	---
K <sub>2</sub> O	5.31	---
CO <sub>2</sub>	---	1.1
Other	---	2.62
Ca(OH) <sub>2</sub>	---	94.63
LOI*	19.34	24.2

\* Loss on ignition

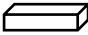
**Table 4.3 Combinations and Compaction Properties of Soil-Additive Mixtures**

Combination	Additive Type	Additive Amount	W <sub>opt</sub>	γ <sub>d</sub>
		(%)	(%)	(kN/m <sup>3</sup> )
CKD5	CKD	5	13.7	17.79
CKD10	CKD	10	14.6	17.48
CKD15	CKD	15	15.3	17.25
LM3	Hydrated Lime	3	13	17.52
LM6	Hydrated Lime	6	13.7	17.17
LM9	Hydrated Lime	9	15.1	16.72

**Table 4.4 Moisture and Compaction Properties of the Prepared Specimens**

Test Type	Additive Type	Additive Amount (%)	Specimen Code	Target $w$ ( $w_{opt}$ ) (%)	$w$ (%)	Target $\gamma_d$ ( $\gamma_{dmax}$ ) (kN/m <sup>3</sup> )	$\gamma_d$ (kN/m <sup>3</sup> )	Degree of Compaction (%)
UCS and $M_r$ 	CKD	5	RM-CKD5-#1	13.7	13.6	17.8	17.9	100.6
			RM-CKD5-#2		13.5		17.6	98.9
			RM-CKD5-#3		13.8		17.8	100.1
		10	RM-CKD10-#1	14.6	14.4	17.5	17.5	100.1
			RM-CKD10-#2		14.6		17.7	101.3
			RM-CKD10-#3		14.4		17.3	99.0
		15	RM-CKD15-#1	15.3	15.1	17.3	17.1	99.1
			RM-CKD15-#2		15		17.2	99.7
			RM-CKD15-#3		14.9		17.4	100.9
	Lime	3	RM-LM3-#1	13	12.8	17.5	17.6	100.6
			RM-LM3-#2		12.9		17.5	100.0
			RM-LM3-#3		12.8		17.6	100.6
		6	RM-LM6-#1	13.7	13.3	17.2	16.8	97.7
			RM-LM6-#2		13.7		17.0	98.8
			RM-LM6-#3		13.6		16.7	97.1
		9	RM-LM9-#1	15.1	15.3	16.7	16.3	97.6
			RM-LM9-#2		15.1		16.6	99.4
			RM-LM9-#3		15.1		16.4	98.2
MoR 	CKD	5	FS-CKD5-#1	13.7	14.4	17.8	17.4	97.8
			FS-CKD5-#2		14		17.4	97.8
			FS-CKD5-#3		14.1		17.6	98.9
		10	FS-CKD10-#1	14.6	14.4	17.5	17.2	98.4
			FS-CKD10-#2		14.8		17.2	98.4
			FS-CKD10-#3		14.9		17.4	99.5
		15	FS-CKD15-#1	15.3	15	17.3	17.3	100.3
			FS-CKD15-#2		15.3		17.0	98.6
			FS-CKD15-#3		15.4		17.1	99.1
	Lime	3	FS-LM3-#1	13	13	17.5	17.4	99.4
			FS-LM3-#2		12.6		17.6	100.6
			FS-LM3-#3		13.1		17.5	100.0
		6	FS-LM6-#1	13.7	14	17.2	17.0	98.8
			FS-LM6-#2		13.2		16.8	97.7
			FS-LM6-#3		13.4		17.2	100.0
		9	FS-LM9-#1	15.1	14.7	16.7	16.8	100.6
			FS-LM9-#2		15.5		16.6	99.4
			FS-LM9-#3		15.8		16.6	99.4

**Table 4.4 Continued**

Test Type	Additive Type	Additive Amount (%)	Specimen Code	Target $w$ ( $w_{opt}$ ) (%)	$w$ (%)	Target $\gamma_d$ ( $\gamma_{dmax}$ ) (kN/m <sup>3</sup> )	$\gamma_d$ (kN/m <sup>3</sup> )	Degree of Compaction (%)
FPFF 	CKD	5	FF-CKD5-#1	13.7	13.4	17.8	17.4	97.8
			FF-CKD5-#2		13.7		17.6	98.9
			FF-CKD5-#3		13.6		17.6	98.9
			FF-CKD5-#4		14.1		17.5	98.4
		10	FF-CKD10-#1	14.6	14.4	17.5	17.1	97.8
			FF-CKD10-#2		14.6		17.4	99.5
			FF-CKD10-#3		14.8		17.3	99.0
			FF-CKD10-#4		14.5		17.3	99.0
		15	FF-CKD15-#1	15.3	14.8	17.3	17.2	99.7
			FF-CKD15-#2		15.1		17.1	99.1
			FF-CKD15-#3		15.1		17.4	100.9
			FF-CKD15-#4		15.2		17.4	100.9
	Lime	3	FF-LM3-#1	13	13.4	17.5	17.6	100.6
			FF-LM3-#2		12.7		17.4	99.4
			FF-LM3-#3		12.9		17.3	98.9
			FF-LM3-#4		13.1		17.4	99.4
		6	FF-LM6-#1	13.7	13.5	17.2	17.1	99.4
			FF-LM6-#2		13.3		17.0	98.8
			FF-LM6-#3		13.7		16.8	97.7
			FF-LM6-#4		13.2		16.9	98.3
		9	FF-LM9-#1	15.1	15.3	16.7	16.4	98.2
			FF-LM9-#2		14.9		16.6	99.4
			FF-LM9-#3		15.2		16.6	99.4
			FF-LM9-#4		15		16.7	100.0

**Table 4.5 Summary of  $M_r$  Test Results for CKD-Stabilized Soil**

Sequenc e #	$\sigma_3$ (kPa)	$\sigma_d$ (kPa)	$M_r$ (MPa)								
			RM- CKD5- #1	RM- CKD5- #2	RM- CKD5- #3	RM- CKD10 -#1	RM- CKD10 -#2	RM- CKD10 -#3	RM- CKD15 -#1	RM- CKD15 -#2	RM- CKD15 -#3
1	41.4	13.8	905	845	765	1938	1811	1993	2805	2137	2811
2	41.4	27.6	842	824	795	1917	1837	2088	2884	2614	2945
3	41.4	41.4	830	816	759	1879	1816	2077	2549	2696	2853
4	41.4	55.2	809	783	735	1815	1828	1946	2733	2430	2714
5	41.4	68.9	782	753	708	1855	1823	1908	2785	2412	2631
6	27.6	13.8	868	862	718	1778	1908	2125	2857	4117	2585
7	27.6	27.6	819	798	744	1986	1813	1931	2516	2638	2820
8	27.6	41.4	812	786	727	1902	1737	1868	2663	2288	2760
9	27.6	55.2	786	763	705	1894	1784	1864	2724	2329	2703
10	27.6	68.9	784	748	697	1881	1799	1865	2653	2343	2675
11	13.8	13.8	868	833	755	1773	1876	1928	3388	3544	2997
12	13.8	27.6	818	807	736	2081	1847	2001	2706	2606	2661
13	13.8	41.4	819	783	710	1967	1773	1857	2827	2216	2745
14	13.8	55.2	784	754	689	1916	1791	1847	2682	2369	2645
15	13.8	68.9	772	743	688	1866	1802	1868	2654	2493	2657

**Table 4.6 Summary of  $M_r$  Test Results for Lime-Stabilized Soil**

Sequenc e #	$\sigma_3$ (kPa)	$\sigma_d$ (kPa)	$M_r$ (MPa)								
			RM- LM3- #1	RM- LM3- #2	RM- LM3- #3	RM- LM6- #1	RM- LM6- #2	RM- LM6- #3	RM- LM9- #1	RM- LM9- #2	RM- LM9- #3
1	41.4	13.8	797	772	808	734	724	697	786	809	811
2	41.4	27.6	741	766	735	713	709	700	771	778	794
3	41.4	41.4	730	723	697	699	681	693	732	744	768
4	41.4	55.2	712	699	657	695	659	677	710	732	757
5	41.4	68.9	688	661	642	678	641	680	697	718	732
6	27.6	13.8	756	762	736	740	705	706	759	791	806
7	27.6	27.6	713	722	694	687	675	671	735	760	779
8	27.6	41.4	708	688	667	672	653	659	727	743	760
9	27.6	55.2	685	666	633	668	634	661	703	728	742
10	27.6	68.9	683	647	623	664	631	664	692	716	730
11	13.8	13.8	719	761	715	693	670	665	751	773	776
12	13.8	27.6	677	696	672	667	652	645	721	745	761
13	13.8	41.4	678	660	644	641	621	635	716	726	741
14	13.8	55.2	649	645	624	649	602	624	694	703	728
15	13.8	68.9	639	623	610	630	607	609	683	701	720

**Table 4.7 Summary of Compressive Tests Results**

Mixture	$M_r$			UCS			$\epsilon_{cf}$		
	Mean	Stdv	CoV	Mean	Stdv	CoV	Mean	Stdv	CoV
	(MPa)	(MPa)	(%)	(kPa)	(kPa)	(%)	(10 <sup>-3</sup> mm/mm)	(10 <sup>-3</sup> mm/mm)	(%)
CKD5	734	34	4.6	620	26	4.2	13.13	0.72	5.5
CKD10	1845	31	1.7	1135	87	7.7	8.88	0.59	6.7
CKD15	2602	77	3.0	1644	106	6.4	9.10	0.33	3.6
LM3	624	12	1.9	464	43	9.3	10.17	0.95	9.3
LM6	615	11	1.8	515	46	8.9	7.45	0.75	10.0
LM9	701	15	2.1	892	110	12.3	6.83	1.17	17.1

Stdv: Standard deviation

CoV: Coefficient of variation

**Table 4.8 Summary of MoR Test Results**

Mixture	MoR			$\epsilon_{tf}$		
	Mean	Stdv	CoV	Mean	Stdv	CoV
	(kPa )	(kPa )	(%)	( $\mu$ mm/mm)	( $\mu$ mm/mm)	(%)
CKD5	166	8	4.7	747	28	3.8
CKD10	321	33	10.2	483	40	8.3
CKD15	470	23	4.9	578	20	3.5
LM3	78	13	16.3	360	24	6.7
LM6	92	4	4.1	314	26	8.1
LM9	160	6	4.0	269	32	11.9

Stdv: Standard deviation

CoV: Coefficient of variation

**Table 4.9 Summary of FPFF Test Results**

Mixture	$M_f$			$N_f$		
	Mean	Stdv	CoV	Mean	Stdv	CoV
	(MPa )	(MPa )	(%)	(Cycles)	(Cycles)	(%)
CKD5	1214	83	6.8	>400000	---	---
CKD10	2662	123	4.6	1	0	0.0
CKD15	3146	126	4.0	105	63	60.0
LM3	728	69	9.5	69662	69936	100.4
LM6	797	122	15.3	22384	7339	32.8
LM9	---	---	---	---	---	---

Stdv: Standard deviation

CoV: Coefficient of variation

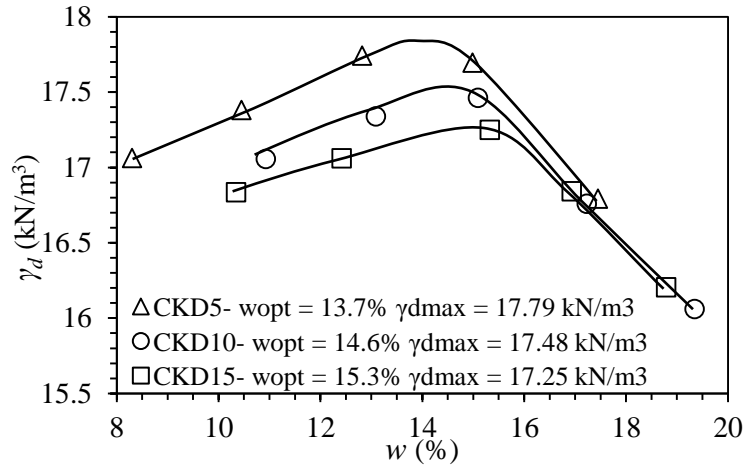
**Table 4.10 Fatigue Life and Flexural Properties of the Materials Used for  
Validating the Fatigue Prediction Model**

Study	Material	$\epsilon_{ff}$ ( $\mu\text{mm/mm}$ )	$\epsilon$ ( $\mu\text{mm/mm}$ )	$M_f$ (MPa)	$N_f$ (cycles)
Arnold et al., 2012	CAPTIF + 1% cement	257	140	1549	4,441
		257	83	1518	977
	CAPTIF + 2% cemen	467	174	1675	548,830
		467	197	1980	2,801
		467	181	2155	23,901
	CAPTIF + 4% cement	630	530	864	7,491
		630	563	635	661
		630	310	761	1,911,196
		630	409	875	111,201
		630	537	770	324
		630	347	747	44,062
		630	305	850	3,790,042
		630	378	2948	199
		550	296	3756	133
	Australian limestone + 3% cement-7days curing	610	343	1637	39
		610	247	1933	27,581
		610	194	1986	798
	Australian limestone + 3% cement-28days	1050	261	2260	9,262
		1050	196	1954	1,500,649
	Whitford GAP40 + 3% bitumen+ 1.3% cement	945	159	1897	293,351
		945	139	1861	949,241
		945	169	1927	113,601
Solanki, 2010	P-Soil + 10% CKD	620	500	1381	51
	V-Soil + 6% Lime	864	500	801	1,430,001
	V-Soil + 10% CKD	602	500	990	965,001

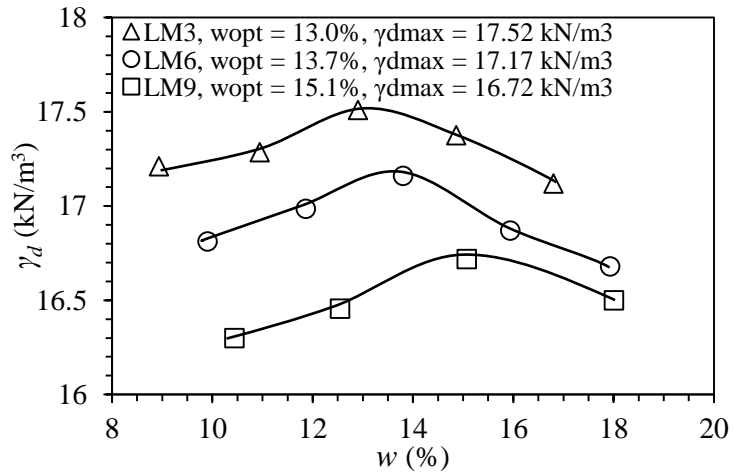
**Table 4.11 Comparison of Predicted Fatigue Lives using Different Models**

Study	Material	Fatigue Life (Cycles)				
		Laboratory Measured	Equation 4.19	Freeme et al. (1982)	Jameson et al. (1992)	Austroroads (2004)
Current Study	CKD5	> 400,000	1,013,490	4,605,130	6,936,128	260,708
	CKD10	1	462	214,512	410,729	3,038
	CKD15	105	448	891,891	225,099	1,371
	LM3	69,662	247,687	10,989	43,715,095	8,487,756
	LM6	22,384	36,305	2,031	31,554,001	4,445,153
	LM9	0	10,385	215	27,987,650	3,514,693
Arnold et al., 2012	CAPTIF + 1% cement	4,441	1,439	13,893	50,042,035	4,184,502
		977	24,122	1,449,070	3,526,478,482	2,504,242,639
	CAPTIF + 2% cemen	548,830	5,319	512,179	6,632,802	194,459
		2,801	1,305	182,491	1,345,302	17,028
		23,901	1,246	374,127	1,953,015	29,750
		7,491	4,001	28	9,703	21
	CAPTIF + 4% cement	661	21,138	9	18,134	93
		1,911,196	482,730	41,901	1,118,577	32,109
		111,201	15,583	1,557	73,710	432
		324	7,426	22	13,225	40
		44,062	206,755	12,240	485,238	9,478
		3,790,042	175,202	49,482	855,534	17,873
		199	160	4,365	1,747	1
		133	123	15,942	5,167	6
	Australian limestone + 3% cement-7days curing	39	1,012	9,619	31,595	65
		27,581	1,707	260,163	240,178	1,288
		798	4,412	1,606,577	1,504,545	20,134
	Australian limestone + 3% cement-28days curing	9,262	7,403	6,886,523	88,030	286
		1,500,649	175,092	25,196,101	1,469,492	19,467
	Whitford GAP40 + 3% bitumen+ 1.3% cement	293,351	631,323	37,058,590	8,716,155	282,448
		949,241	3,410,858	57,740,625	27,374,047	1,577,879
		113,601	296,226	29,688,796	5,056,809	124,500
Solanki, 2010	P-Soil + 10% CKD	51	590	58	2,858	2
	V-Soil + 6% Lime	1,430,001	70,649	6,820	20,310	72
	V-Soil + 10% CKD	965,001	2,080	35	9,473	17



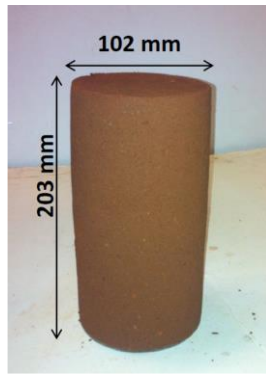


(a)

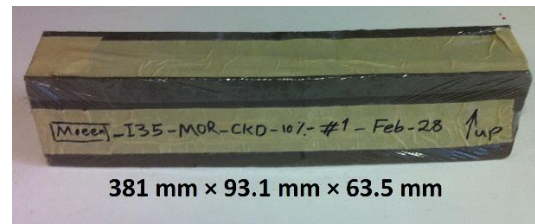


(b)

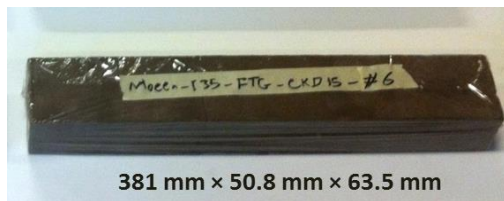
**Figure 4.1 Dry Unit Weight-Moisture Content Relationship for (a) CKD-stabilized Soil, and (b) Lime-stabilized Soil**



(a)



(b)

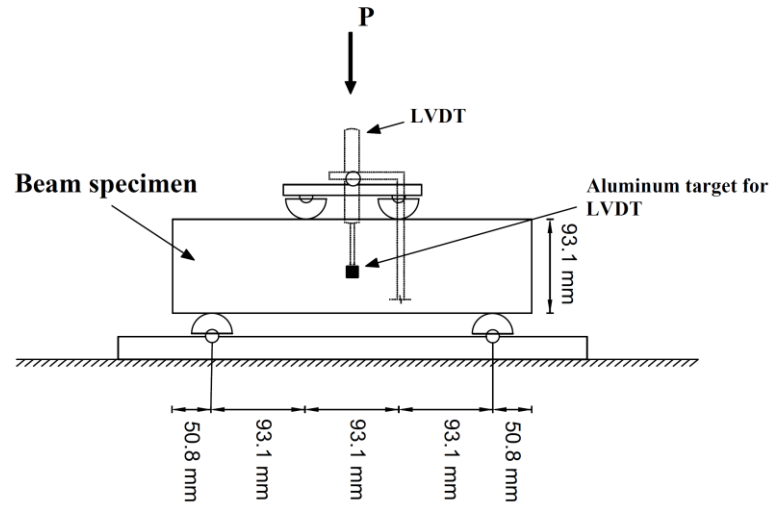


(c)

**Figure 4.2 Shape and Dimensions of (a)  $M_r$  and UCS Test, (b) MoR Test, and (c) FPF Test Specimens**



**Figure 4.3 Linear Kneading Compactor during Compaction of a Beam Specimen**

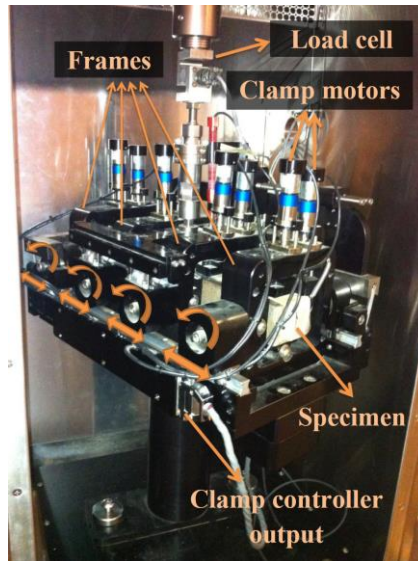


(a)

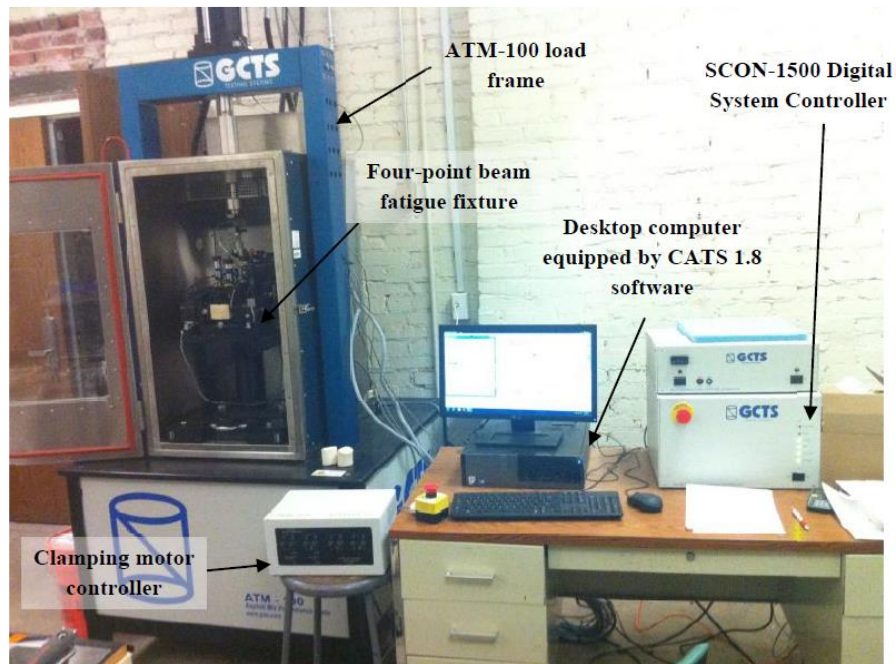


(b)

**Figure 4.4 MoR Test Setup (a) Schematic Sketch, and (b) Photographic View**

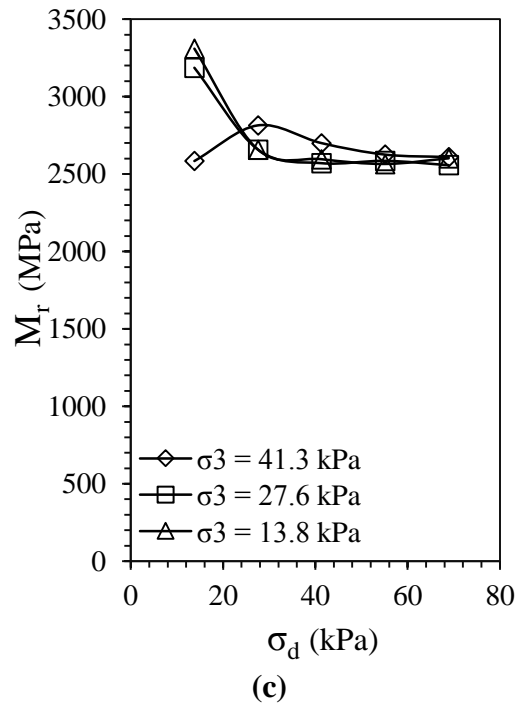
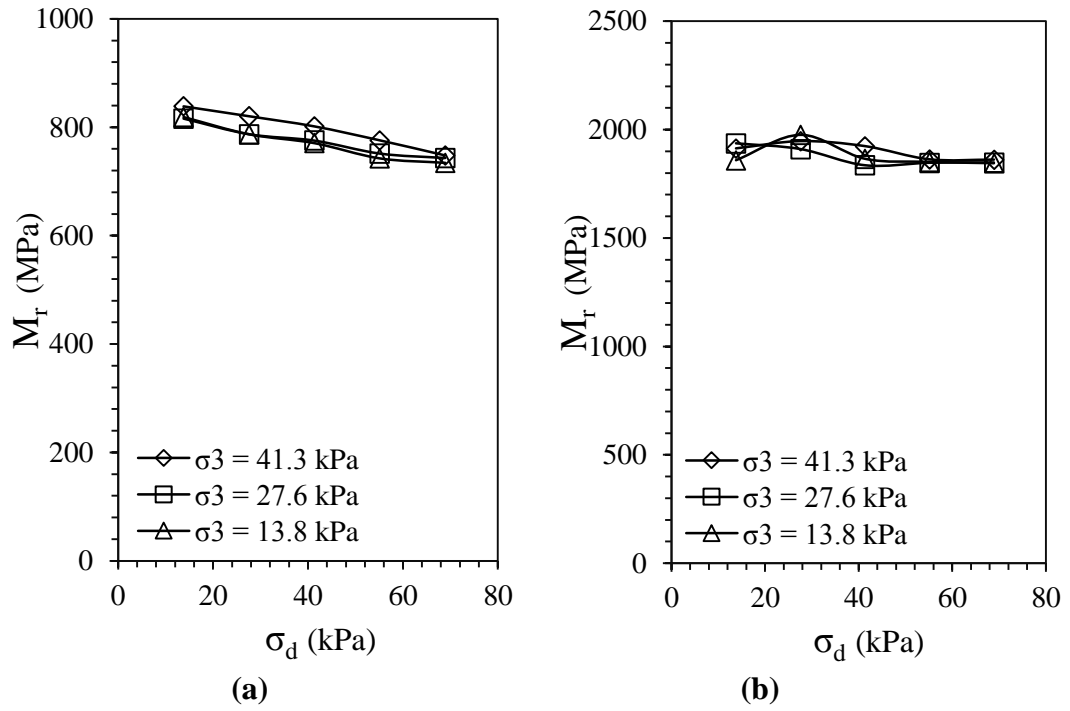


(a)

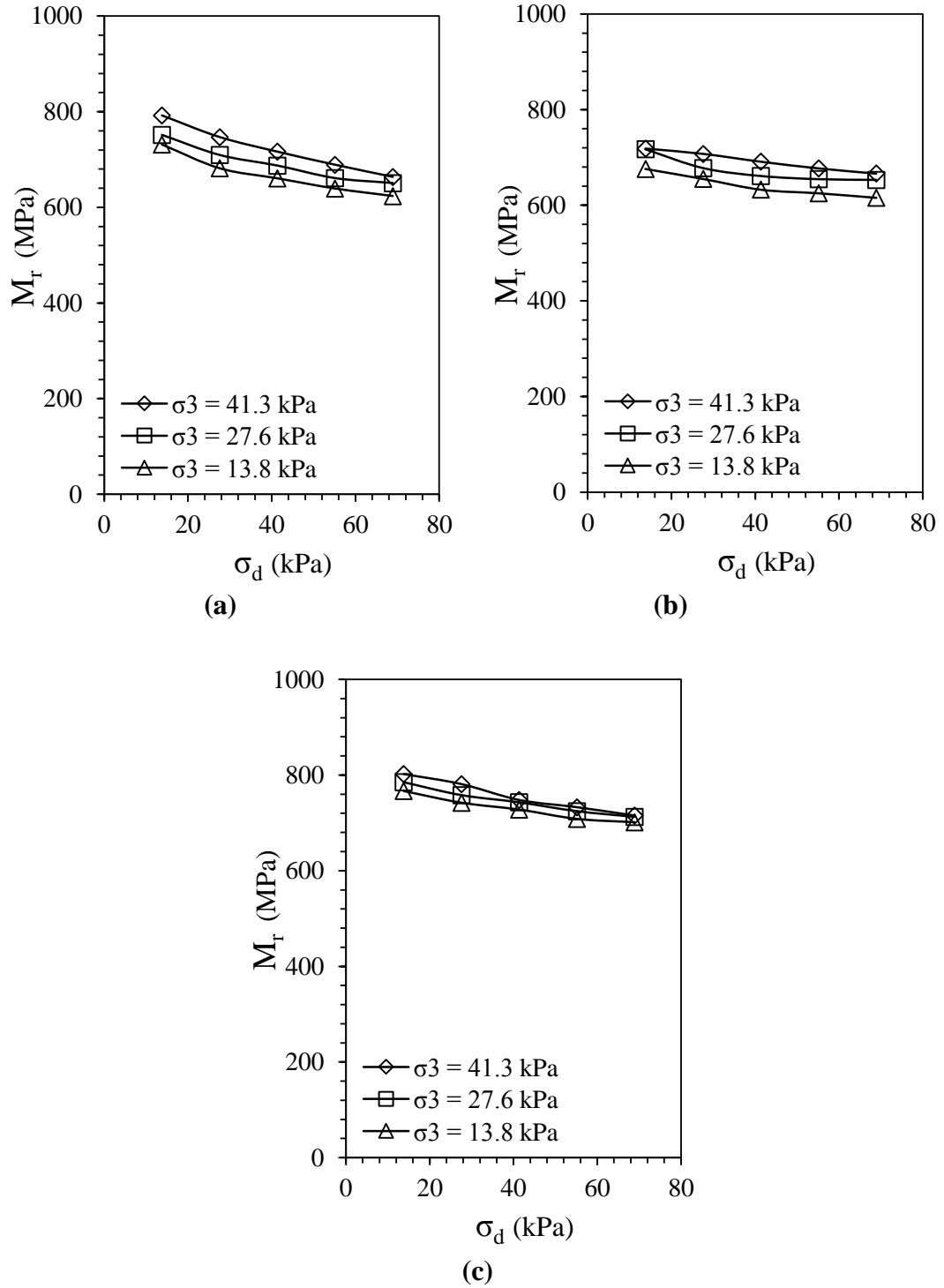


(b)

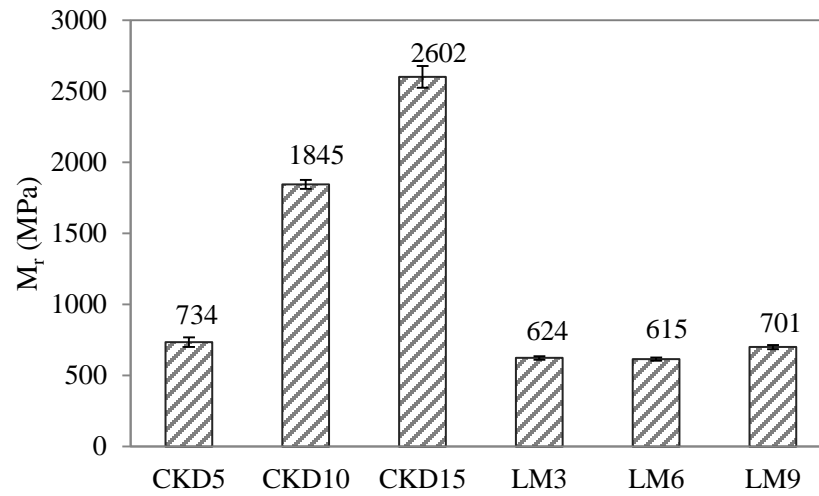
**Figure 4.5 (a) FPFF Fixture, and (b) ATM-100 Test Setup**



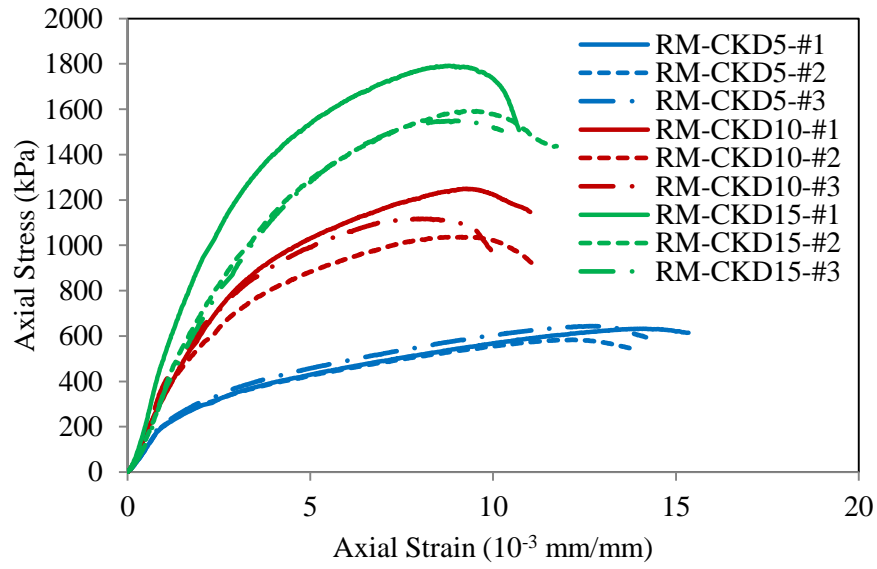
**Figure 4.6  $M_r$  versus Stress Level for CKD-Stabilized Soil (a) CKD5, (b) CKD10, and (c) CKD15 Specimens**



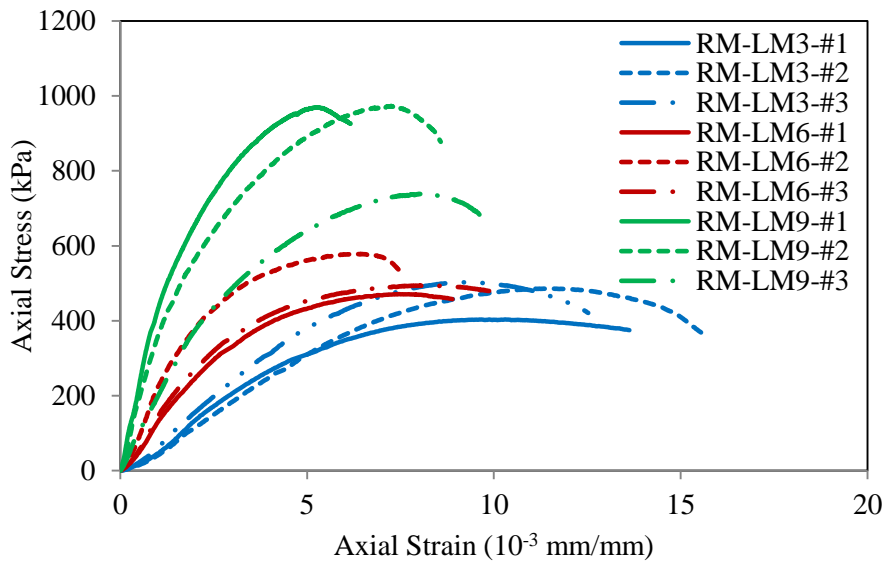
**Figure 4.7  $M_r$  versus Stress Level for Lime-Stabilized Soil (a) LM3, (b) LM6, and (c) LM9 Specimens**



**Figure 4.8 Mean  $M_r$  Values for Different Soil-Additive Mixtures**



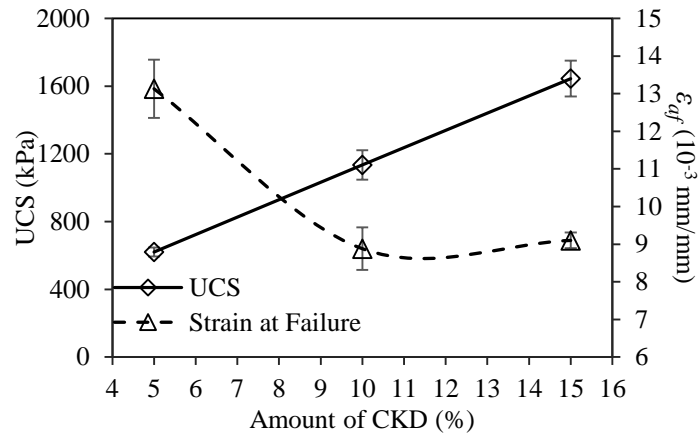
(a)



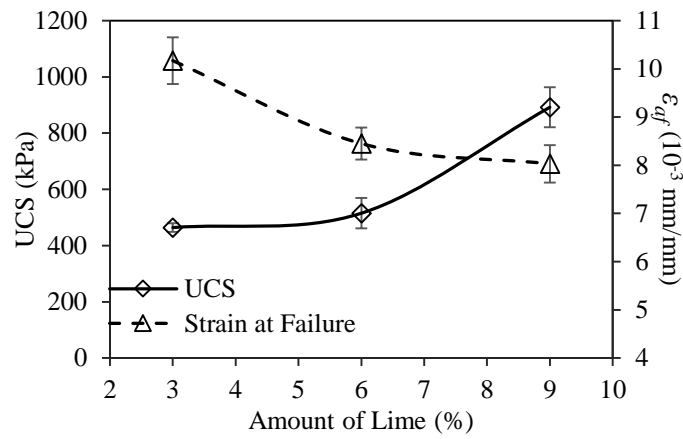
(b)

**Figure 4.9 Stress-Strain Curves from UCS Test on (a) CKD-Stabilized, and (b) Lime-Stabilized Soil**



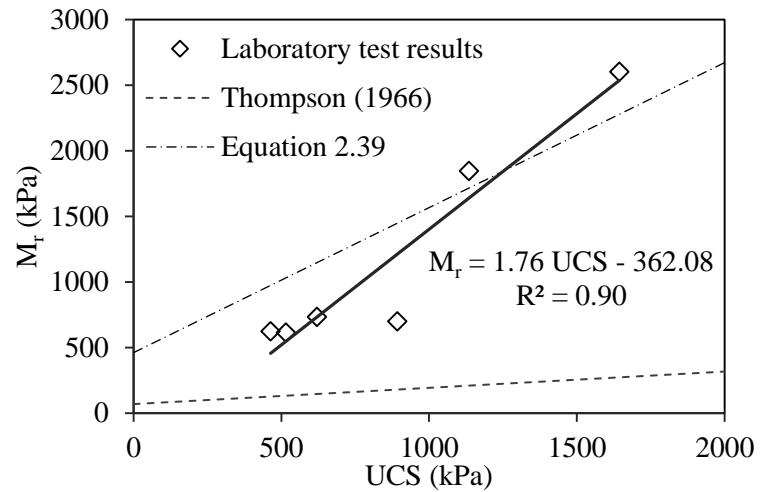


(a)

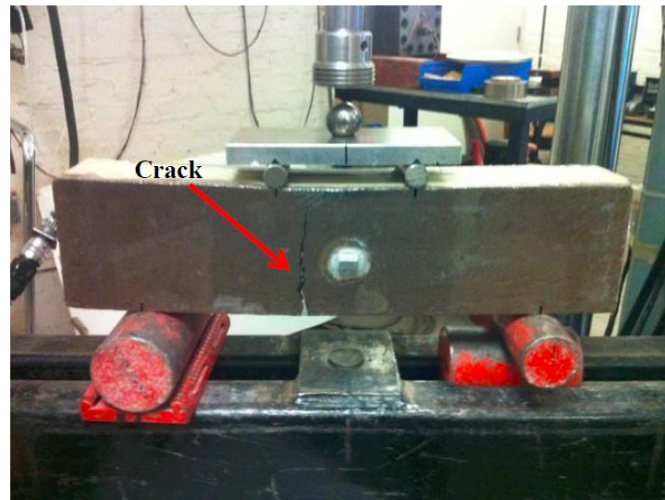


(b)

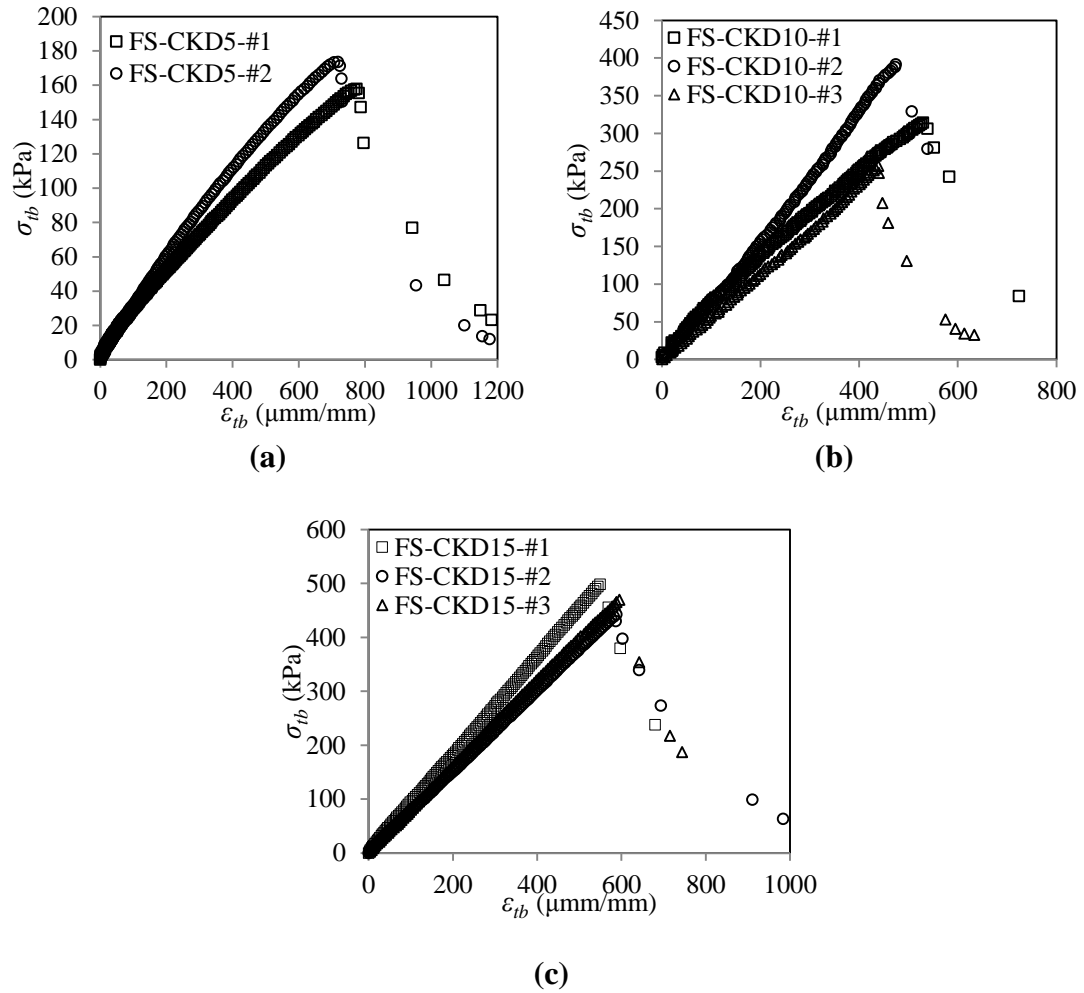
**Figure 4.10 Effect of Additive Content on the UCS and Axial Strain at Failure of (a) CKD-Stabilized, and (b) Lime-Stabilized Soil**



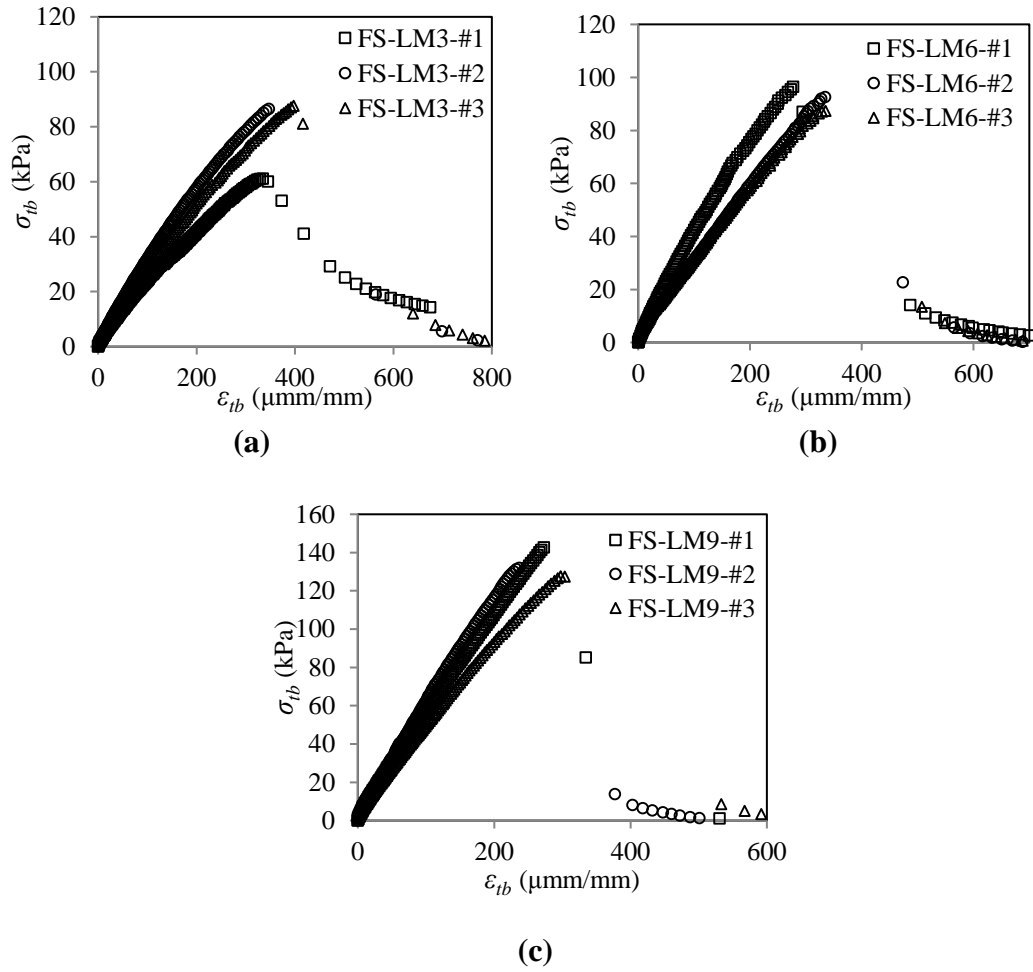
**Figure 4.11 Relationship between Resilient Modulus and UCS Values of All Soil-Additive Mixtures**



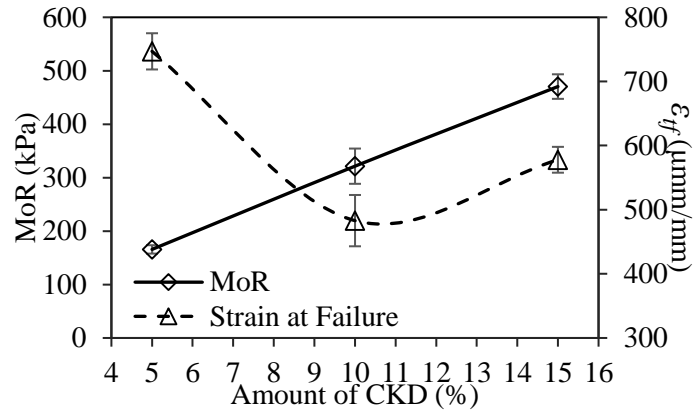
**Figure 4.12 The Cracked Beam at the End of the MoR Test**



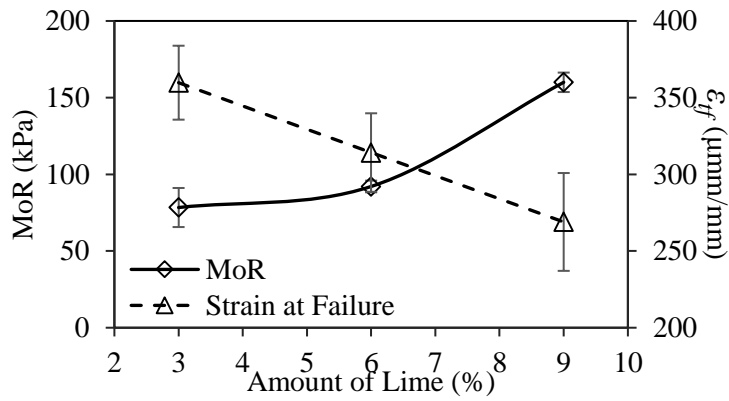
**Figure 4.13 Tensile Stress versus Tensile Strain at the Bottom of the CKD-Stabilized Beams during MoR Test (a) CKD5, (b) CKD10, and (c) CKD15 Specimens**



**Figure 4.14 Tensile Stress versus Tensile Strain at the Bottom of the Lime-Stabilized Beams during MoR Test (a) LM3, (b) LM6, and (c) LM9 Specimens**

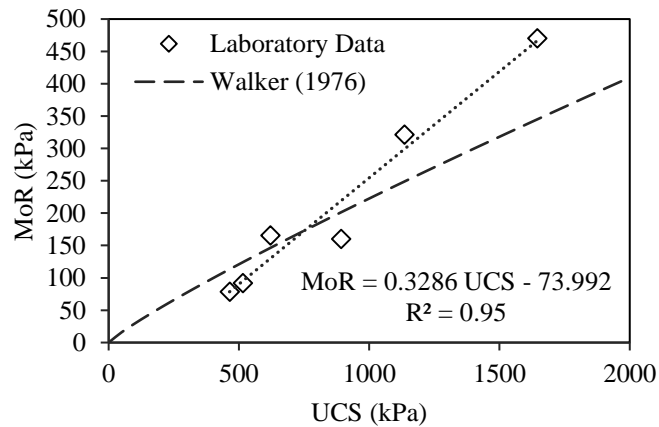


(a)

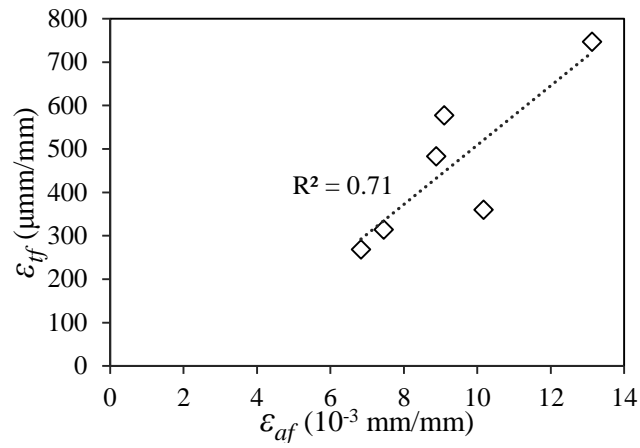


(b)

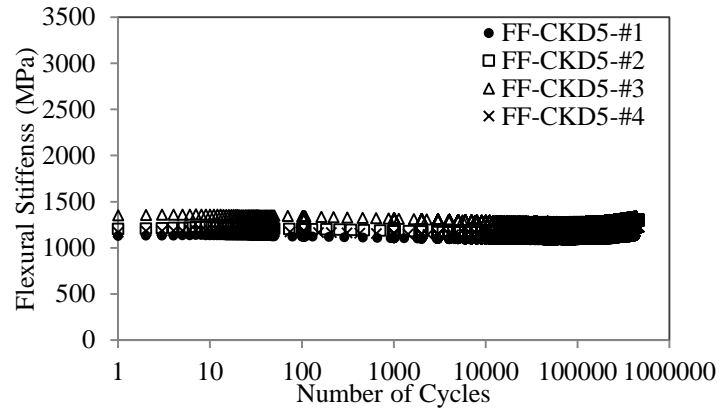
**Figure 4.15 Effect of Additive Content on the MoR and Tensile Strain at Failure of (a) CKD-Stabilized, and (b) Lime-Stabilized Soil**



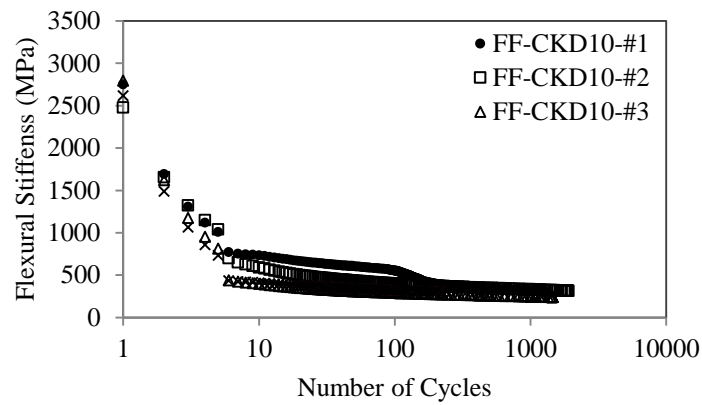
**Figure 4.16 Relationship between MoR and UCS Values of All Soil-Additive Mixtures**



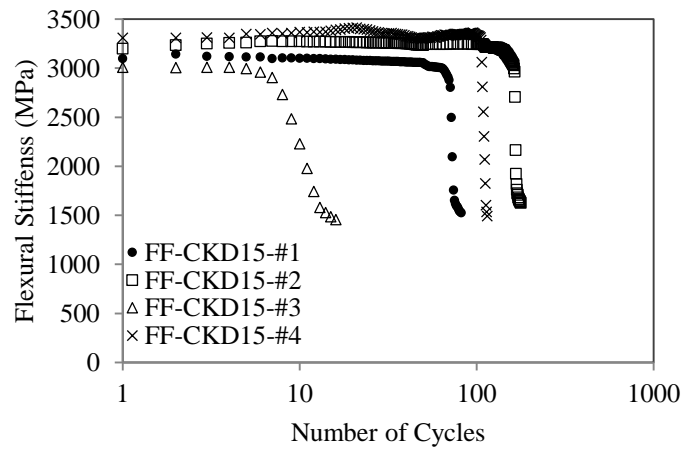
**Figure 4.17 Relationship between  $\epsilon_{tf}$  (from MoR Test) and  $\epsilon_{af}$ (from UCS Test) for All Soil-Additive Mixtures**



(a)

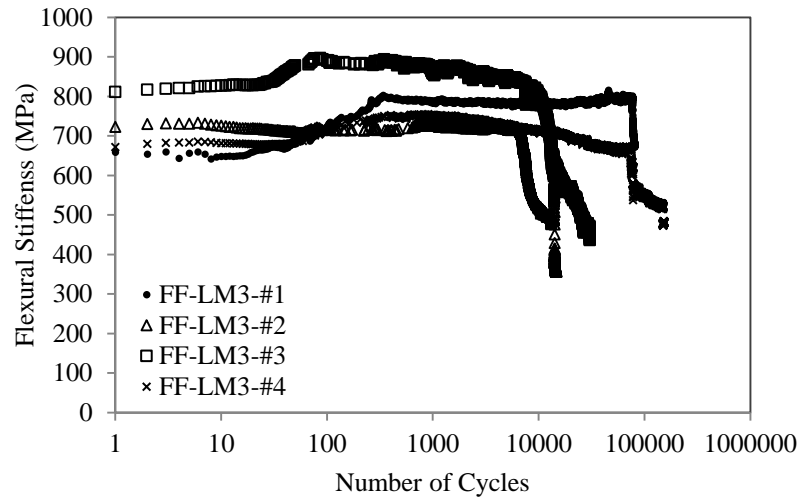


(b)

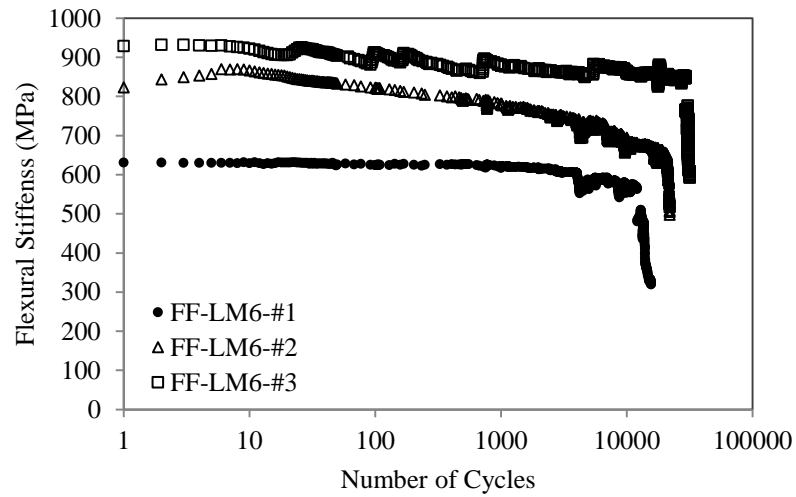


(c)

**Figure 4.18 Flexural Stiffness versus Number of Load Cycles for (a) CKD5, (b) CKD10, and (c) CKD15 Specimens**



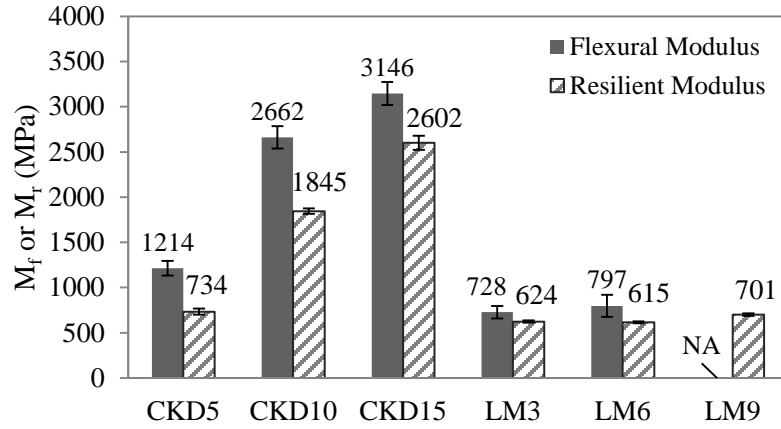
(a)



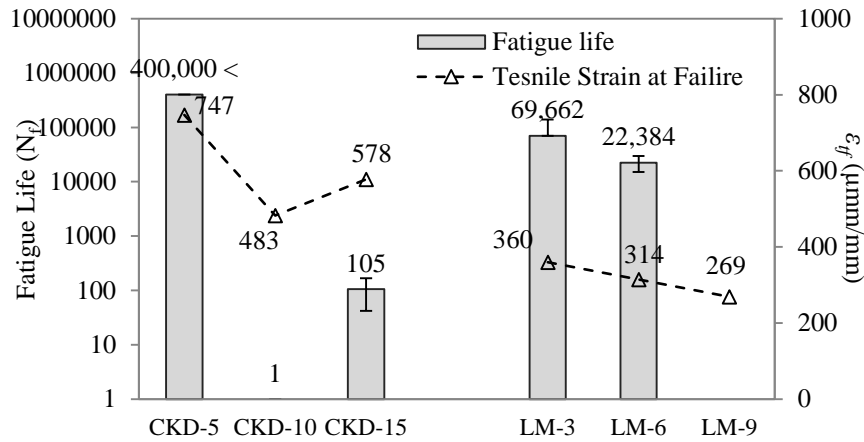
(b)

**Figure 4.19 Flexural Stiffness versus Number of Load Cycles for (a) LM3, and (b) LM6 Specimens**

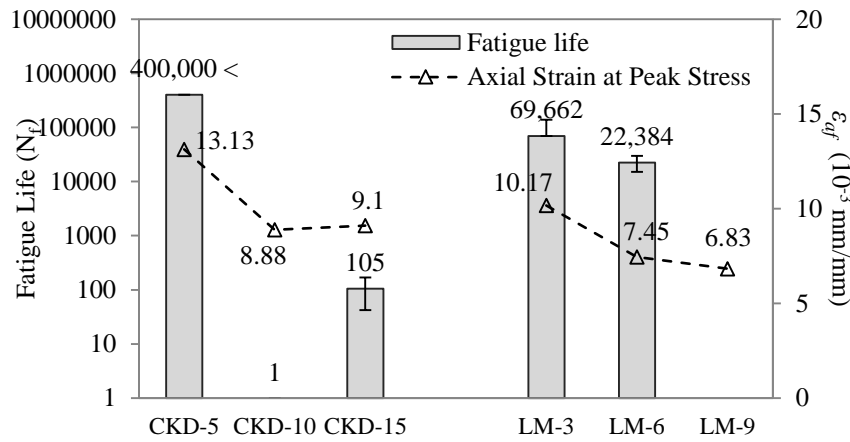




**Figure 4.20 Flexural Stiffness versus Number of Load Cycles for (a) LM3, and (b) LM6 Specimens**

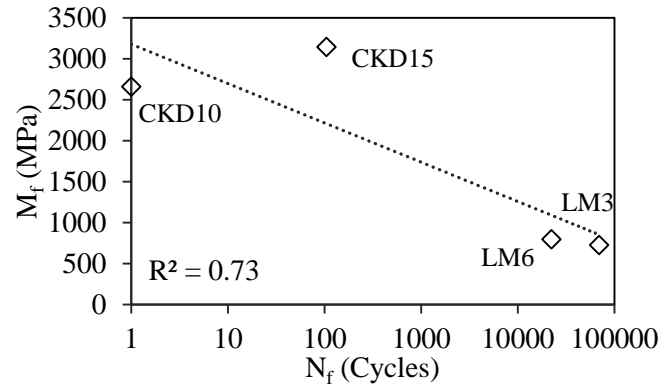


**(a)**

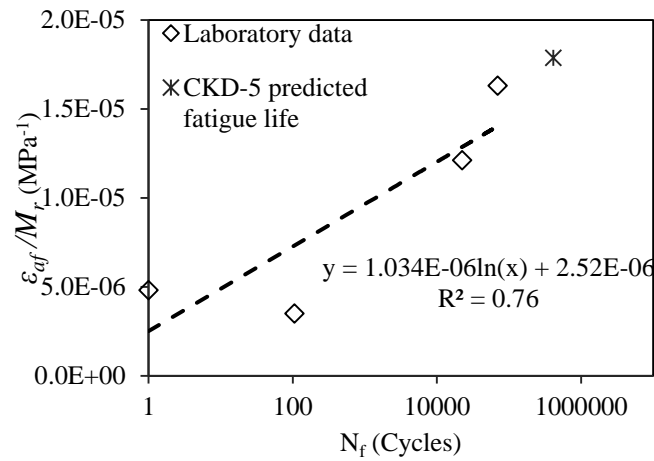


**(b)**

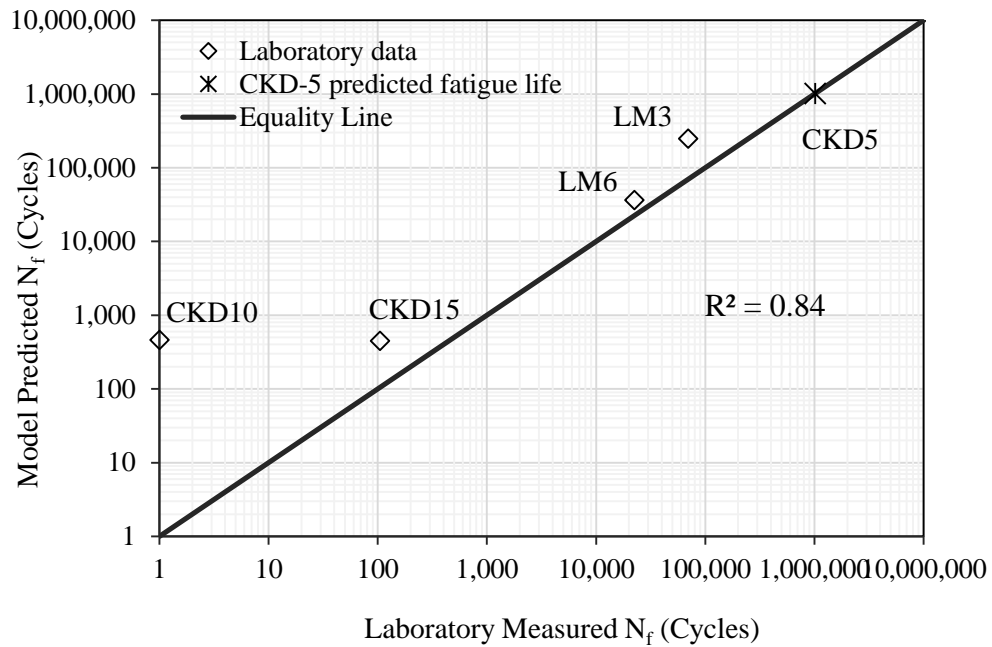
**Figure 4.21 Fatigue Life of Different Mixtures versus (a)  $\epsilon_{tf}$ , and (b)  $\epsilon_{af}$**



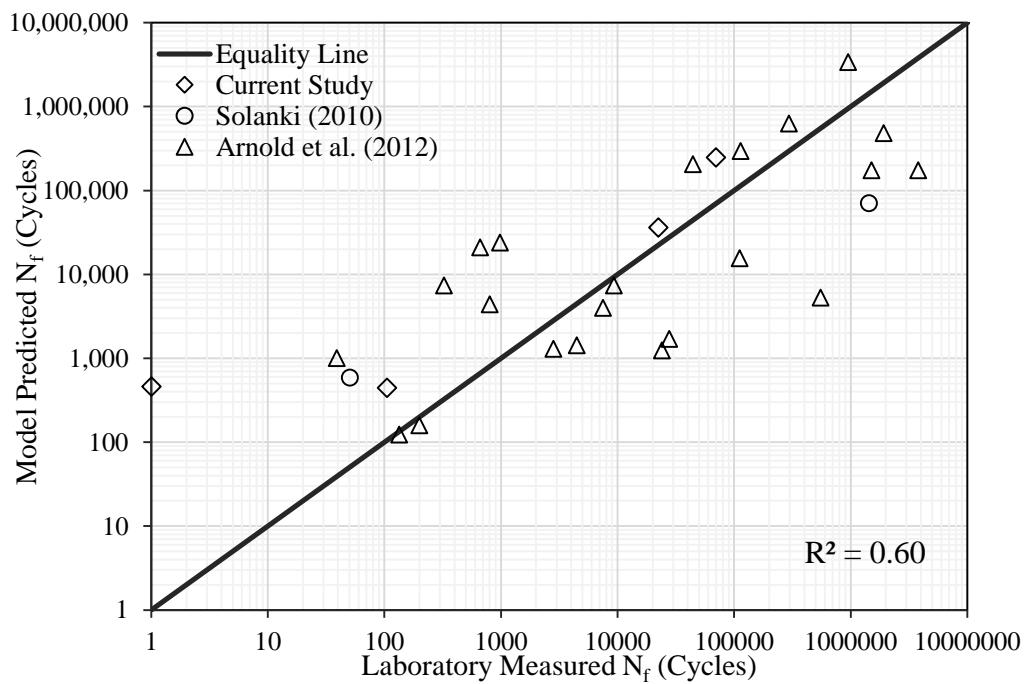
**Figure 4.22 Relationship between Flexural Modulus and Fatigue Life**



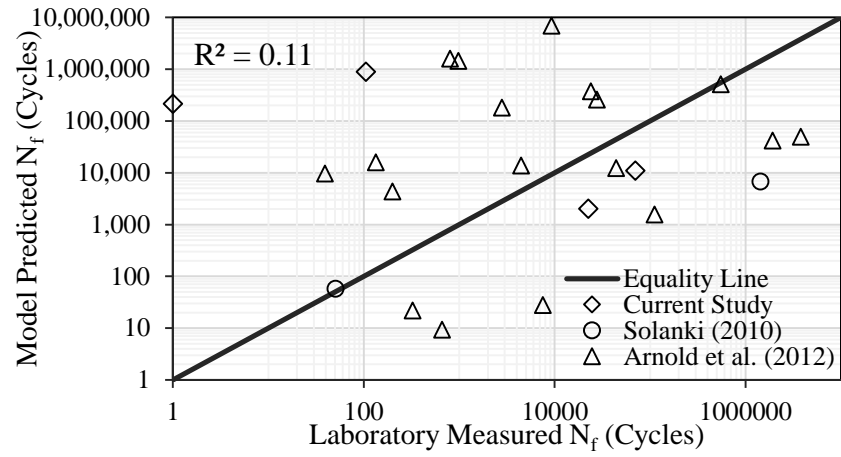
**Figure 4.23 Relationship between Fatigue Life and  $\epsilon_{af}/M_r$  of Tested Specimens**



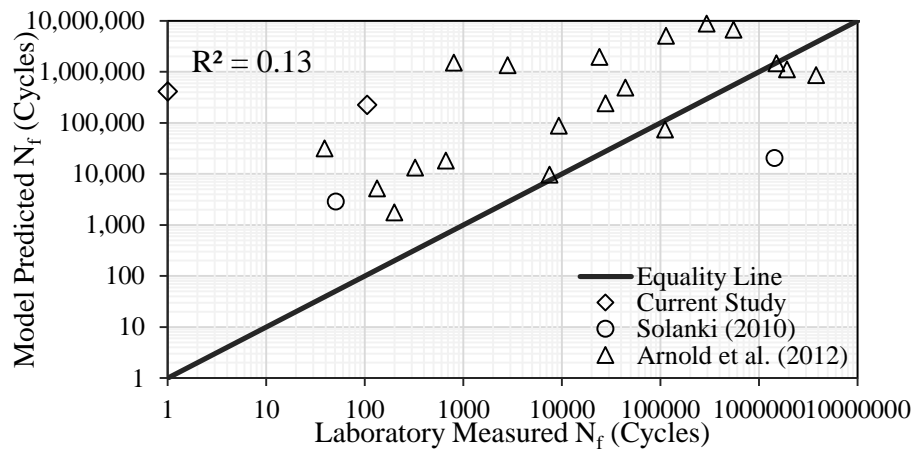
**Figure 4.24 Comparison between Laboratory Measured and Predicted (using Equation 4.20) Fatigue Life of Different Soil-Additive Mixtures**



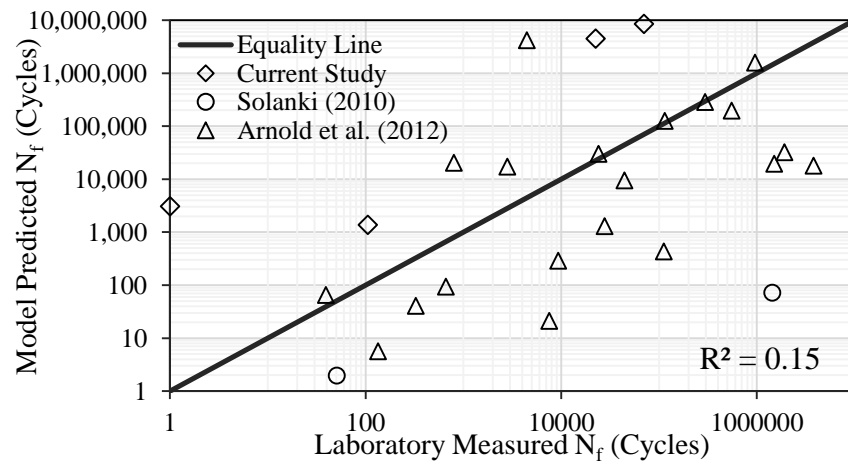
**Figure 4.25 Predictability of Fatigue Life Prediction Model (Equation 4.20) for Different Soil-Additive Mixtures Including Data from Solanki (2010) and Arnold et al. (2012)**



(a)



(b)



(c)

**Figure 4.26 Predicted versus Measured Fatigue Life using Models Proposed by (a) Freeme et al. (1982) (b) Jameson et al. (1992), and (c) Austroads (2004)**

## CHAPTER 5

### EVALUATING THE APPLICABILITY OF EULER-BERNOULLI BEAM THEORY IN DETERMINING FLEXURAL PROPERTIES OF CHEMICALLY-STABILIZED SOIL

#### 5.1 Introduction

The Euler-Bernoulli beam theory has been used widely to study the stress-strain behavior of chemically-stabilized soils in flexure (Raad, 1985; Laguros and Keshawarz, 1987; Mandal, 2013; Solanki and Zaman, 2014; and Jitsangiam et al., 2016). However, the accuracy of this theory relies on different parameters such as material type, deformation shape, and geometry of the beam (Supekar, 2007). Thus, it is important to verify the applicability of this theory for individual test configurations and material properties (Reddy et al., 1997).

Finite Element (FE) modeling of quasi-brittle materials and/ or subgrade materials has been used successfully for replicating/verifying laboratory test results and conducting parametric studies (Kuo and Huang, 2006; Zaman et al., 2009; Braton, 2010; Wu et al., 2011; and Mbaraga et al., 2014). Attempts have also been made to model the flexural behavior of chemically-stabilized soil under flexural loads using the FE method. For example, Peng and He (2009) used the Drucker-Prager criterion for modeling a chemically-stabilized subgrade (CSS) layer, as part of a multi-layered pavement system and studied the deflections due to the wheel load. Sargand et al. (2014) used a linear-elastic material model for CSS layer in order to simplify the simulation of a two-layered pavement structure under truck loads during construction.

Failure of chemically-stabilized geo-materials usually has a quasi-brittle behavior (Sture et al., 1999; Charbit, 2009; and Peng et al., 2012). The elastic-plastic damage

model is mostly used for modeling of the quasi-brittle fracture of materials such as rock, concrete and cemented geo-materials (de Borst, 2002; Murakami, 2012; and Parisio et al., 2014). The elastic-plastic damage model for simulating the degradation of stabilized soils has been applied successfully by Yu et al. (2007) and Peng et al. (2012).

In this study a general-purpose FE program, Abaqus Version 6.13 (Simulia, 2013), was used to simulate the laboratory UCS, MoR and FPF tests on six different soil-additive mixtures (CKD5, CKD10, CKD15, LM3, LM 6 and LM9). A widely used elastic-plastic damage model, namely concrete damage plasticity (CDP) approach, was employed to model the plastic damage of the material under UCS and MoR tests. The results of the FE analyses on each soil-additive mixture were compared with the experimental results (from Chapter 4) to investigate the applicability of the Euler-Bernoulli beam theory for MoR and FPF tests.

## 5.2 Concrete Damaged Plasticity Model in Abaqus

The concrete damage plasticity (CDP) model is capable of predicting the behavior of concrete and other quasi-brittle materials subjected to static, quasi-static and dynamic loading. The model was developed by Lubliner et al. (1989) based on the continuum damage mechanics. The CDP model assumes tensile cracking and compressive crushing of the quasi-brittle material as the two main failure mechanisms (Simulia, 2013). Figures 5.1-a and 5.1-b show the behavior of the model in compression and tension, respectively.

In this model the stress-strain relationships under uniaxial compression and uniaxial tension are expressed as follows:

$$\sigma_c = (1 - d_c)E_0(\varepsilon_c - \tilde{\varepsilon}_c^{pl}) \quad (5.1)$$

$$\sigma_t = (1 - d_t)E_0(\varepsilon_t - \tilde{\varepsilon}_t^{pl}) \quad (5.2)$$

where,  $\sigma_c$  = compressive stress,  $\sigma_t$  = tensile stress,  $d_c$  = degradation of the elastic stiffness in uniaxial compression,  $d_t$  = degradation of the elastic stiffness in uniaxial tension,  $E_0$  = initial (undamaged) elastic stiffness of the material,  $\varepsilon_c$  = total compressive strain,  $\varepsilon_t$  = total tensile strain,  $\tilde{\varepsilon}_c^{pl}$  = the equivalent plastic compressive strain, and  $\tilde{\varepsilon}_t^{pl}$  = the equivalent plastic tensile strain.

The compressive and tensile effective stresses ( $\bar{\sigma}_c$  and  $\bar{\sigma}_t$ , respectively) are defined as follows:

$$\bar{\sigma}_c = E_0(\varepsilon_c - \tilde{\varepsilon}_c^{pl}) \quad (5.3)$$

$$\bar{\sigma}_t = E_0(\varepsilon_t - \tilde{\varepsilon}_t^{pl}) \quad (5.4)$$

Accordingly, the stress tensor can be related to the effective stress tensor and the damage parameter using the following equations:

$$\sigma_c = (1 - d_c)\bar{\sigma}_c \quad (5.5)$$

$$\sigma_t = (1 - d_t)\bar{\sigma}_t \quad (5.6)$$

The tensile cracking and compressive crushing of the material are governed by the hardening/softening variables (Jankowiak and Lodygowski, 2005). In Abaqus, hardening data are given in terms of compressive and tensile inelastic strains ( $\tilde{\varepsilon}_c^{in}$  and  $\tilde{\varepsilon}_t^{in}$ , respectively). As it can be seen in Figure 5.1, the inelastic strain is calculated by subtracting the undamaged elastic strain ( $\varepsilon_{0c}^{el}$  or  $\varepsilon_{0t}^{el}$ ) from the total strain. The plastic strains are extracted from inelastic strains using the following equations:

$$\tilde{\varepsilon}_c^{pl} = \tilde{\varepsilon}_c^{in} \frac{d_c}{(1 - d_c)} \frac{\sigma_c}{E_0} \quad (5.7)$$

$$\tilde{\varepsilon}_t^{pl} = \tilde{\varepsilon}_t^{in} \frac{d_t}{(1 - d_t)} \frac{\sigma_t}{E_0} \quad (5.8)$$

In this study, the CDP parameters of the material in compression were determined from the stress-strain curves obtained from the laboratory UCS tests on the chemically-stabilized soil specimens. Also, the CDP parameters in tension are defined using the tensile stress-strain curves at the bottom of the chemically-stabilized beams during laboratory MoR tests. A detailed description of the CDP approach is available in the User's Manual of the Abaqus software (Simulia, 2013). The constitutive parameters describing the shape of the plastic flow and yield function were selected according to the suggested parameter values for cemented soils in the literature (Peng et al., 2013). A dilation angle of the  $\bar{p} - \bar{q}$  plane of  $36^\circ$  and the ratio of the biaxial compressive strength and uniaxial compressive strength ( $\sigma_{b0}/\sigma_{c0}$ ) of 1.16 were used based on previous studies (Peng et al., 2013).

### 5.3 Creating the Finite Element Models

#### 5.3.1 FE Model of UCS Test

The UCS test was simulated by creating a 3-D FE model of the chemically-stabilized cylindrical specimen under monotonic loading. Similar to the UCS cylindrical specimens, the FE model was 102 mm in diameter and 203 mm in height. The model was constrained against translation and rotation in all three directions at the bottom. Similar to the UCS test, the load was applied in the form of a uniform downward displacement at



the top surface of the model with a constant velocity of 0.02 mm/sec. The mesh size was selected through a mesh convergence study according to the average vertical stress at the top surface of the cylinder. The mesh consisted of 1920 eight-noded linear hexahedral elements of type C3D8R, and 2373 nodes. The dimensions and the mesh of the model are shown in Figure 5.2.

The analyses were conducted for six different soil-additive mixtures, namely CKD5, CKD10, CKD15, LM3, LM6, and LM9 (the same materials used in Chapter 4). For each soil-additive mixture, UCS stress-strain curve (see Figure 4.8) of one specimen was considered to define the CDP properties of the material in compression. The material was assumed to have a linear-elastic behavior at low strains (linear segment of the stress-strain curve), and after that, a compressive CDP model was defined in accordance with the corresponding UCS stress-strain curve. The Poisson's ratio was kept unchanged at 0.3 for all mixtures (Peng et al., 2013). Table 5.1 shows the compressive CDP model properties defined for each soil-additive mixture.

### ***5.3.2 FE Model of MoR Test***

To evaluate the applicability of the Euler-Bernoulli theory for determining the flexural properties of the chemically-stabilized soil, a FE model of the beam specimen subjected to MoR test was developed. A 3-D model of a simply-supported beam having a length of 381 mm, a height of 93.1 mm and a width of 63.5 mm was created in the Abaqus software (Figure 5.3). Considering the symmetry of the model about the x-y plane in Figure 5.3, and to reduce the computation time, only half of the beam's width was modeled. For the elements on the plane of symmetry, the displacements normal to the plane and rotations about the beam's longitudinal axis (x-axis) were constrained as the

boundary conditions. Also, the bottom of the beam at the supports (see Figure 5.3) were constrained against translations through y- and z- axes and rotation through x-axis. To simulate the loading, a uniform downward (through y-axis) displacement with a constant velocity of 0.02 mm/sec was applied on two lines located on one-third and two-third of the beam's length (Figure 5.3).

The 3-D model was composed of eight-noded linear hexahedral elements of type C3D8R. The mesh size was selected using a mesh convergence study according to the calculated displacement at the bottom of the beam. The final mesh configuration consisted of 1,200 elements and 1,804 nodes. The dimensions and mesh configuration of the finite element model are shown in Figure 5.3. A Poisson's ratio of 0.3 was used for all mixtures, as in the case of UCS test. The CDP model characteristics in tension for each soil-additive mixture are presented in Table 5.2. These values were defined in accordance with the tensile stress-strain curves at the bottom of the beam obtained from the MoR tests.

### ***5.3.3 FE Model of FPFF Test***

For all of the soil-additive mixtures in this study, the induced tensile strain at the bottom of the beam in FPFF test (200  $\mu\text{mm/mm}$ ) is lower than tensile strain at failure (see Table 4.8). Also, the stress-strain curves of the MoR tests show a linear behavior for the material before cracking of the beam. Hence, it could be assumed that the soil-additive specimens had a linear-elastic behavior at the beginning (first 50 load cycles) of the FPFF tests.

A 3-D finite element model of the FPFF test on a beam having a length of 381 mm, a height of 50.8 mm and a width of 63.5 mm was created. The model was developed

to replicate the FPFF test fixture configurations and the specimen clamping mechanism. Figure 5.4 shows the clamping mechanism of the FPFF fixture used in this study (Hartman and Gilchrist, 2004). The fixture consisted of two loading and two reaction clamps. Both loading (inner) and reaction (outer) clamps were allowed to freely rotate about z-axis and translate through x-axis. The movement of the loading clamps in y-axis was controlled by the applied displacement enforced by the load cell. The other rotations and translations were set to zero. To simulate the mentioned clamping mechanism, the clamps were modeled as rigid bodies. For each clamp a reference point (RP) was defined at the center point of the clamp's opening (i.e., the center point of the beam's cross section). The boundary conditions for each clamp were assigned to its corresponding reference point. The movements of the clamps were constrained to their attributed reference points. Due to symmetry, one-fourth of the test set-up, including one-fourth of the chemically-stabilized beam, one-half of one reaction clamp and one-half of one loading clamp, was modeled (Figure 5.5). The translation in z-axis, and rotations about x- and y- axes on the symmetry plane perpendicular to z-axis were fixed to zero. For the other surface of symmetry (symmetry plane normal to x- axis), translation in x- axis and rotations about y- and z- axes were set to zero. A hard normal contact was defined between the beam and clamps' surfaces. Separation was not allowed at the contacts. The model was developed using eight-noded linear hexahedral elements of type C3D8R. A convergence study was conducted in accordance with the vertical displacement at the bottom of the beam to select the mesh size. The final mesh was consisted of 2,600 elements and 3,276 nodes. The dimensions and mesh configuration of the finite element model are presented in Figure 5.5.

The beam was loaded by application of a downward displacement at the RP associated with the loading clamp. The magnitude of enforced displacement was selected high enough to induce a tensile strain of 200  $\mu\text{mm}/\text{mm}$  at the bottom of the beam. A stress insensitive linear-elastic material with a Poisson's ratio of 0.3 was assigned to the beam. The model was analyzed for five different soil-additive mixtures, namely CKD5, CKD10, CKD15, LM3 and LM6. The FPF test on LM9 specimen was not modeled due to the absence of the laboratory data. The elastic modulus for each mixture was equal to the corresponding  $M_f$  value achieved from the FPF test (Table 4.9).

## **5.4 FE Analysis Results and Discussion**

### **5.4.1 UCS Test**

After completion of the FE analysis, the nodal displacements of the center point on the top surface of the specimen was recorded for all loading steps. The displacements were divided by the initial height of the specimen (203 mm) to obtain the axial strain at each loading step. The compressive stress at each loading step was obtained from the average vertical component of the nodal stresses on the top surface of the model. Using these data, the axial stress-strain curve of the FE model was plotted for each soil-additive mixture.

Figure 5.6 shows the stress-strain curves of the FE models along with the laboratory stress-strain curves. It is evident from Figure 5.6 that the finite element results are in a very good agreement with the experimental results. For all of the soil-additive mixtures, the maximum compressive stress (peak stress) and axial strain at peak stress of the FE model are well matched with the experimental values. Also, the 3-D models

provide a good approximation of the post-peak (degradation) behavior of the material. Overall, it can be said that the UCS test of chemically-stabilized soil could be successfully simulated by using CDP material model.

#### **5.4.2 MoR Test**

In this study, FE models of the MoR tests conducted on the chemically-stabilized beam specimens were developed to verify the applicability of the Euler-Bernoulli beam theory. Figure 5.7 shows the deformed shape of the CKD15 beam specimen at the last step of loading. The deformations are magnified by a scale factor of 50 for presentation purpose. Figure 5.7 also shows the stress distribution along x-axis (longitudinal direction of the beam) in terms of MPa, through which the maximum tensile stresses were developed at the bottom of the beam. The positive and negative values are indicators of tensile and compressive stresses, respectively. The concentration of compressive stress at the zones close to loading points is evident in Figure 5.7. As expected, the maximum tensile stress, and consequently the maximum tensile strain, was observed in the mid-span at the bottom of the beam. Also, the tensile stresses of all nodes located at the bottom surface of the middle-third span of the beam were compared with each other. It was observed that the difference between maximum and minimum nodal stresses was less than 8.5%. This indicates that the MoR test setup could provide a reasonably constant bending moment, and consequently, a constant tensile stress/ strain at the bottom, through the middle-third span of the beam.

As mentioned earlier, the main material parameters used in the FE model were determined from the tensile stress-strain curves of the MoR tests. Hence, the stress-strain curves at the bottom of the FE model beam were close to those observed in the laboratory

and/or calculated. Figure 5.8 presents a comparison between the laboratory test results and those from the FE model. For all six soil-additive mixtures (CKD5, CKD10, CKD15, LM3, LM6, and LM9), the FE model resulted in stress-strain curves congruent with those found from the laboratory tests. This shows the capability of the CDP model in simulating the chemically-stabilized soil behavior in flexure.

As mentioned in Section 4.4.2.2, the vertical displacements of the beam's mid-height ( $\Delta U$ ) in MoR tests were measured by LVDTs, and  $\varepsilon_{tb}$  values were calculated using the Euler-Bernoulli beam theory (Equation 4.3). The  $\varepsilon_{tb}-\Delta U$  diagrams resulted from MoR tests and FE models were plotted for the comparison purpose. Figure 5.9 presents a comparison of the  $\varepsilon_{tb}-\Delta U$  curves from the two aforementioned methods. However, the calculated  $\varepsilon_{tb}$  and tensile stress values were used as material properties and  $\Delta U$  values were obtained from the FE model output. According to Equation 4.3,  $\varepsilon_{tb}$  and  $\Delta U$  had a linear relationship. Hence, as it can be seen from Figure 5.9, all of the laboratory-measured and calculated tensile strains showed a linear relationship with the measured vertical displacement. This was the case for brittle materials (CKD10, CKD15 and LM9 specimens). On the other hand, the specimens with lower additive contents (CKD5, LM3 and LM6) had a relatively nonlinear behavior. Therefore, in this case it was more likely to observe the highest difference of  $\Delta U$  prior to failure obtained from the FE model compared to that measured in the laboratory, as observed in Figures 5.9-a, 5.9-d and 5.9-e (16.7%, 18.8% and 14.2% difference for CKD5, LM3 and LM6, respectively). The differences in values for CKD10, CKD15 and LM9 materials were 11.3%, 7.2% and 13.5%, respectively (Figures 5.9-b, 5.9-c and 5.9-f, respectively). The relatively low values of the differences indicate that the Euler-Bernoulli beam theory can estimate the

induced tensile strain at the bottom of the chemically-stabilized beam in a MoR test setup within a reasonable range of accuracy.

#### **5.4.3 FPFF Test**

Figure 5.10 shows the deformed shape (by a scale factor of 150) of CKD5 beam's FE model when the maximum tensile strain at the bottom of the beam is 200  $\mu\text{mm/mm}$ . Also, distribution of the strains along the x-axis of the model (longitudinal direction of the beam) in terms of MPa is shown in Figure 5.10. The magnitude of induced strains at the bottom of the beam was very close to the strains at the top surface of the beam. From Figure 5.10 it can be seen that the strain contours are relatively parallel to the beam's neutral plane, on the left side of the loading clamp (the span between loading clamps). In other words, the nodes with the same distance from the neutral plane possess similar levels of strain, through the middle-third span of beam. By taking a note of the nodal  $\varepsilon_t$  values at the bottom of the middle-third of the beam, it was observed that the difference between maximum and minimum nodal  $\varepsilon_t$  was less than 4%. Hence, it can be said that the clamping mechanism in the FPFF fixture could successfully provide a constant flexural moment, and consequently, a constant  $\varepsilon_t$  at the bottom, through the middle-third span of the beam.

For each soil-additive mixture, the vertical displacement of the beam's mid-height at the tensile strain level of 200  $\mu\text{mm/mm}$  ( $\Delta U_{200}$ ) was extracted from the analyzed model. The FE model  $\Delta U_{200}$  values were compared with the LVDT measured  $\Delta U_{200}$  values of the laboratory FPFF test. For all of the mixtures, the LVDT measured vertical displacement at maximum tensile strain of 200  $\mu\text{mm/mm}$  was equal to  $106.9 \times 10^{-3}$  mm. A comparison between the FE model and laboratory measured  $\Delta U_{200}$  values is shown in

Figure 5.11. As it can be seen, the difference between  $\Delta U_{200}$  of FE analysis and experimental results ranges between 1.2% and 5.2%. Similar to the MoR test model, the minimum difference values were observed for the CKD10 and CKD15 specimens (1.9% and 1.2%, respectively), which had the highest flexural moduli. On the other hand, the other three specimens showed the highest difference between FE model and LVDT measured  $\Delta U_{200}$  (3.9%, 5.2% and 5.1% for CKD5, LM3 and LM6 materials, respectively). The range of percent difference between FE analysis and experimental results for FPF test is considerably lower than those of the MoR test. This can be attributed to the effective clamping mechanism provided by the FPF test fixture which allows friction free translations and rotations at the supports. This mechanism results in minimizing the stress concentration at the loading and reaction surfaces.

## 5.5 Conclusions

Finite element models of UCS, MoR and FPF laboratory tests on different soil-additive mixtures were developed using a general-purpose FE program, Abaqus Version 6.13. The results of the FE analysis on each soil-additive mixture were compared with the experimental results. Based on the study the following conclusions were made:

1. The stress-strain curves produced by the finite element models were consistent with those of the experimental results for UCS and MoR tests. Consequently, the UCS and MoR tests for different chemically-stabilized soils could successfully simulated by using concrete damage plasticity material model.
2. According to the FE model, the Euler-Bernoulli beam theory was found to have a reasonable accuracy in calculation of the strain at the bottom of the chemically-



stabilized beams in MoR test. The vertical displacements of the beam's mid-height achieved from FE analyses and experimental MoR tests had an difference between 7.2% and 18.8%.

3. The stress-strain curves of the MoR tests showed a linear behavior for the material before cracking of the beam. Hence, a linear-elastic behavior could be assumed for the beginning (first 50 load cycles) of the FPFF tests which have a relatively small induced strain level at the bottom of the beam (200  $\mu\text{mm/mm}$ ).
4. The vertical displacements of the beam's mid-height achieved from FE analyses and experimental FPFF tests had an insignificant difference (1.2% to 5.2%). Hence, the Euler-Bernoulli beam theory was found to have a higher accuracy in estimating the tensile strains at the bottom of the beam when a FPFF test fixture was used.

**Table 5.1 Material Parameters for CDP Model in Compression**

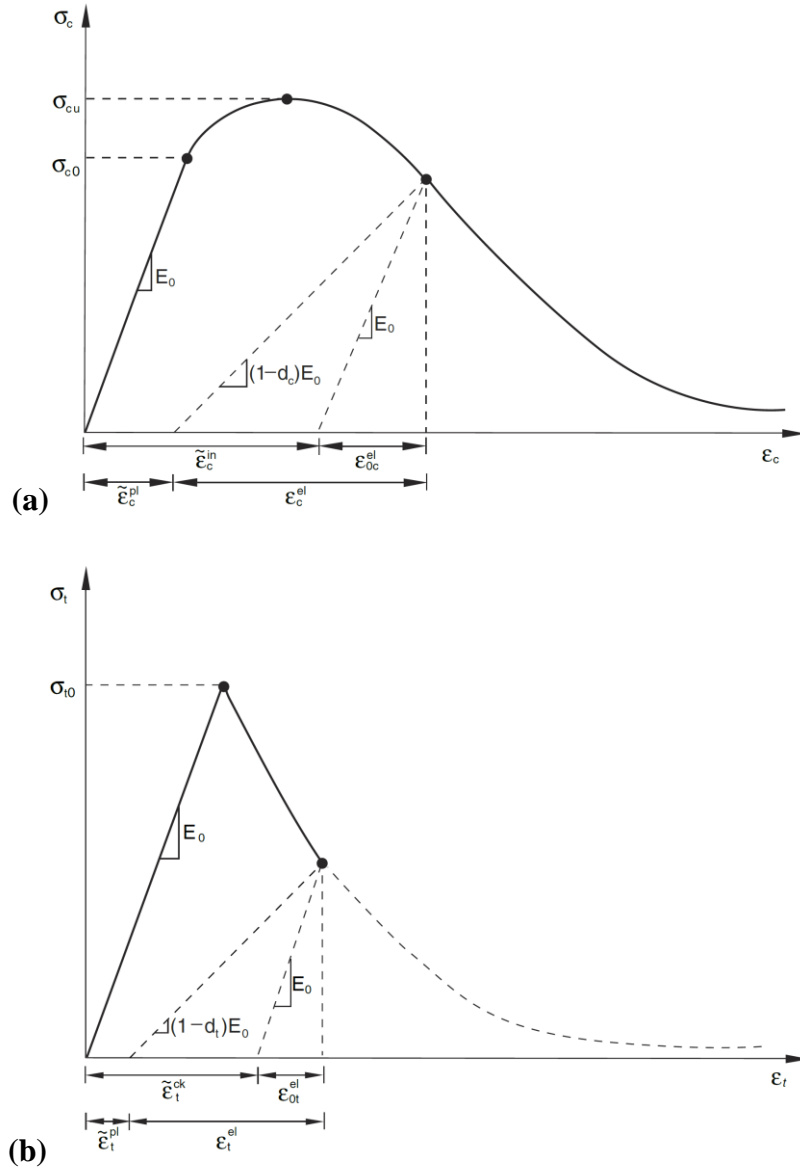
CKD5			CKD10			CKD15		
E = 220 MPa			E = 301 MPa			E = 461 MPa		
Inelastic Strains ( $10^{-3}$ mm/mm)	Yeild Stress (kPa)	Damage Parameter	Inelastic Strains ( $10^{-3}$ mm/mm)	Yeild Stress (kPa)	Damage Parameter	Inelastic Strains ( $10^{-3}$ mm/mm)	Yeild Stress (kPa)	Damage Parameter
0	159.2	0	0	640.5	0	0	923.6	0
1.03	319.9	0	0.31	809.6	0	0.38	1204.7	0
1.59	363.4	0	0.53	870.5	0	0.76	1348.8	0
2.20	395.0	0	0.78	924.9	0	0.99	1405.6	0
2.84	420.7	0	1.37	1007.8	0	1.71	1546.8	0
4.13	469.7	0	1.69	1042.1	0	2.25	1616.4	0
4.80	490.6	0	2.02	1072.1	0	2.52	1649.3	0
5.45	512.6	0	2.69	1129.9	0	3.40	1723.0	0
6.13	531.0	0	3.04	1154.7	0	4.00	1764.9	0
7.47	568.6	0	3.39	1179.3	0	4.31	1779.6	0
8.15	585.7	0	4.12	1218.7	0	4.98	1788.8	0
8.84	601.1	0	4.50	1234.4	0	5.33	1787.3	0.0008
9.54	613.5	0	5.32	1246.4	0	5.74	1773.0	0.0088
10.98	631.0	0	5.58	1239.7	0.0054	6.19	1748.2	0.0227
11.41	630.7	0.0005	5.87	1229.9	0.0133	6.78	1693.2	0.0535
12.26	620.4	0.0168	6.51	1198.5	0.0385	7.68	1564.0	0.1257
12.53	615.4	0.0247	6.84	1181.3	0.0523			
13.34	600.5	0.0483						
13.87	590.6	0.0641						

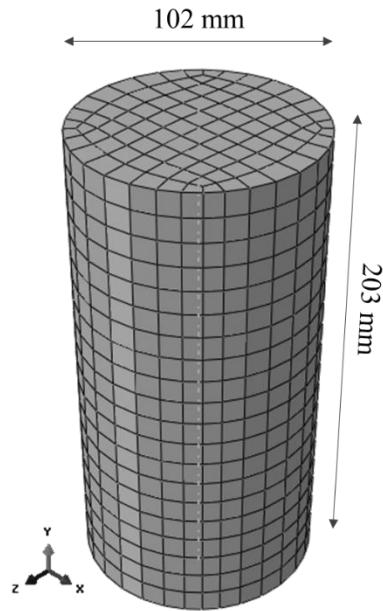
LM3			LM6			LM9		
E = 59 MPa			E = 125 MPa			E = 459 MPa		
Inelastic Strains ( $10^{-3}$ mm/mm)	Yeild Stress (kPa)	Damage Parameter	Inelastic Strains ( $10^{-3}$ mm/mm)	Yeild Stress (kPa)	Damage Parameter	Inelastic Strains ( $10^{-3}$ mm/mm)	Yeild Stress (kPa)	Damage Parameter
0	338.0	0	0	226.6	0	0	362.0	0
0.77	378.4	0	0.15	303.9	0	0.13	484.2	0
0.98	383.7	0	0.34	331.2	0	0.46	619.3	0
1.20	388.2	0	0.70	383.2	0	0.63	678.3	0
1.66	395.4	0	0.92	402.7	0	1.04	775.2	0
1.90	399.0	0	1.46	430.9	0	1.26	816.0	0
3.02	402.4	0	1.77	441.9	0	1.49	852.2	0
3.60	402.9	0	2.41	458.1	0	1.99	907.8	0
3.93	401.7	0.0029	2.76	462.6	0	2.25	929.7	0
4.61	399.0	0.0096	3.48	469.9	0	2.52	947.3	0
5.74	391.8	0.0276	3.85	470.7	0	3.09	968.8	0
6.93	382.8	0.0499	4.27	469.2	0.0031	3.42	963.7	0.0052
			5.19	459.5	0.0236	3.82	943.5	0.0261
			5.64	455.5	0.0322	4.28	907.4	0.0633
			6.82	429.7	0.0869	4.75	871.4	0.1005
			7.40	417.4	0.1132	5.22	835.3	0.1377

**Table 5.2 Material Parameters for CDP Model in Tension**

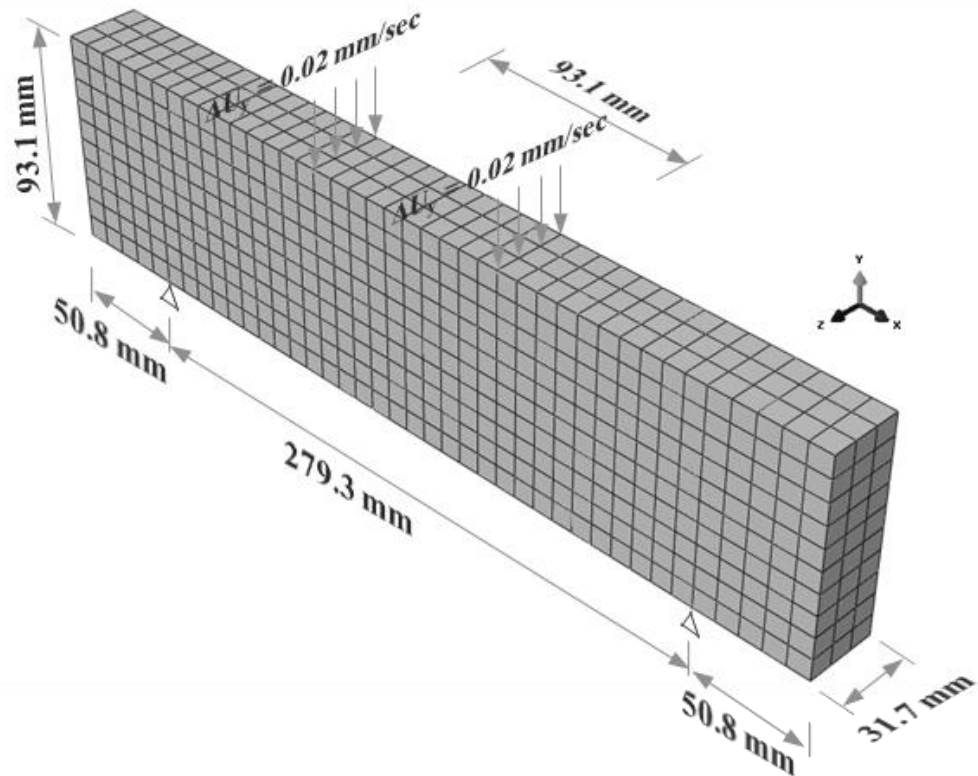
CKD5			CKD10			CKD15		
E = 245 MPa			E = 662 MPa			E = 790 MPa		
Cracking Strains ( $10^{-3}$ mm/mm)	Yeild Stress (kPa)	Damage Parameter	Cracking Strains ( $10^{-3}$ mm/mm)	Yeild Stress (kPa)	Damage Parameter	Cracking Strains ( $10^{-3}$ mm/mm)	Yeild Stress (kPa)	Damage Parameter
0	19.4	0	0	256.0	0	0	434.0	0
69.25	62.7	0	1.39	256.5	0	4.26	457.8	0
157.03	106.7	0	18.53	251.9	0.0178571	7.54	468.7	0
310.00	157.9	0	53.89	241.8	0.0571429	29.50	461.7	0.0148274
332.66	155.8	0.0134752	315.47	166.7	0.35	98.79	435.9	0.0698745
374.15	149.4	0.05385				282.18	366.5	0.2180717
523.31	125.7	0.2038042						
LM3			LM6			LM9		
E = 253 MPa			E = 398 MPa			E = 535 MPa		
Cracking Strains ( $10^{-3}$ mm/mm)	Yeild Stress (kPa)	Damage Parameter	Cracking Strains ( $10^{-3}$ mm/mm)	Yeild Stress (kPa)	Damage Parameter	Cracking Strains ( $10^{-3}$ mm/mm)	Yeild Stress (kPa)	Damage Parameter
0	19.2	0	0	59.8	0	0	116.7	0
0.04	42.9	0	0.02	83.2	0	0.00	126.3	0
0.07	57.1	0	0.03	95.4	0	0.00	138.7	0
0.08	59.3	0	0.04	96.4	0	0.01	142.6	0
0.09	61.0	0	0.10	87.0	0.0977786	0.28	85.2	0.4025893
0.11	60.0	0.0178383	0.70	9.4	0.892074	0.79	1.0	0.9928147
0.54	25.1	0.5889511	0.81	4.9	0.9434994			
0.67	18.6	0.6946819	0.90	2.5	0.9706835			
0.80	14.3	0.7660						



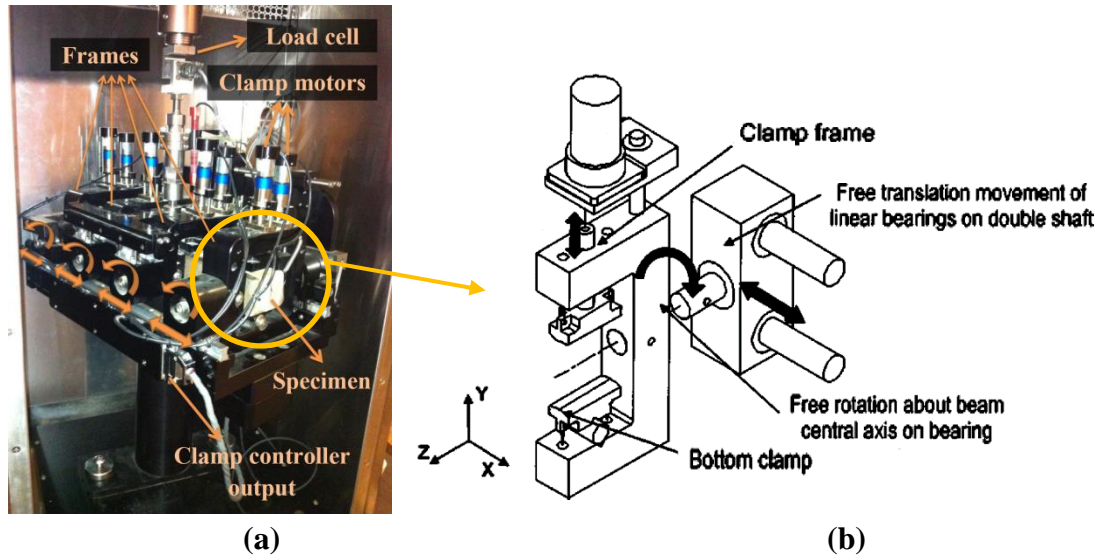
**Figure 5.1 Stress-Strain Terms of CDP Model in (a) Compression, and (b) Tension (Simulia, 2013)**



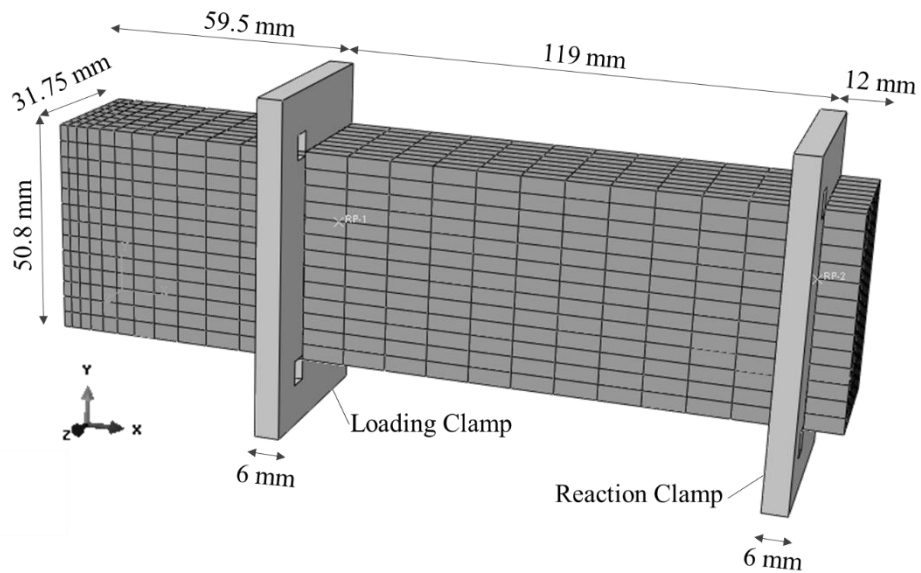
**Figure 5.2 Geometry and Mesh Configuration of FE Model of UCS Test**



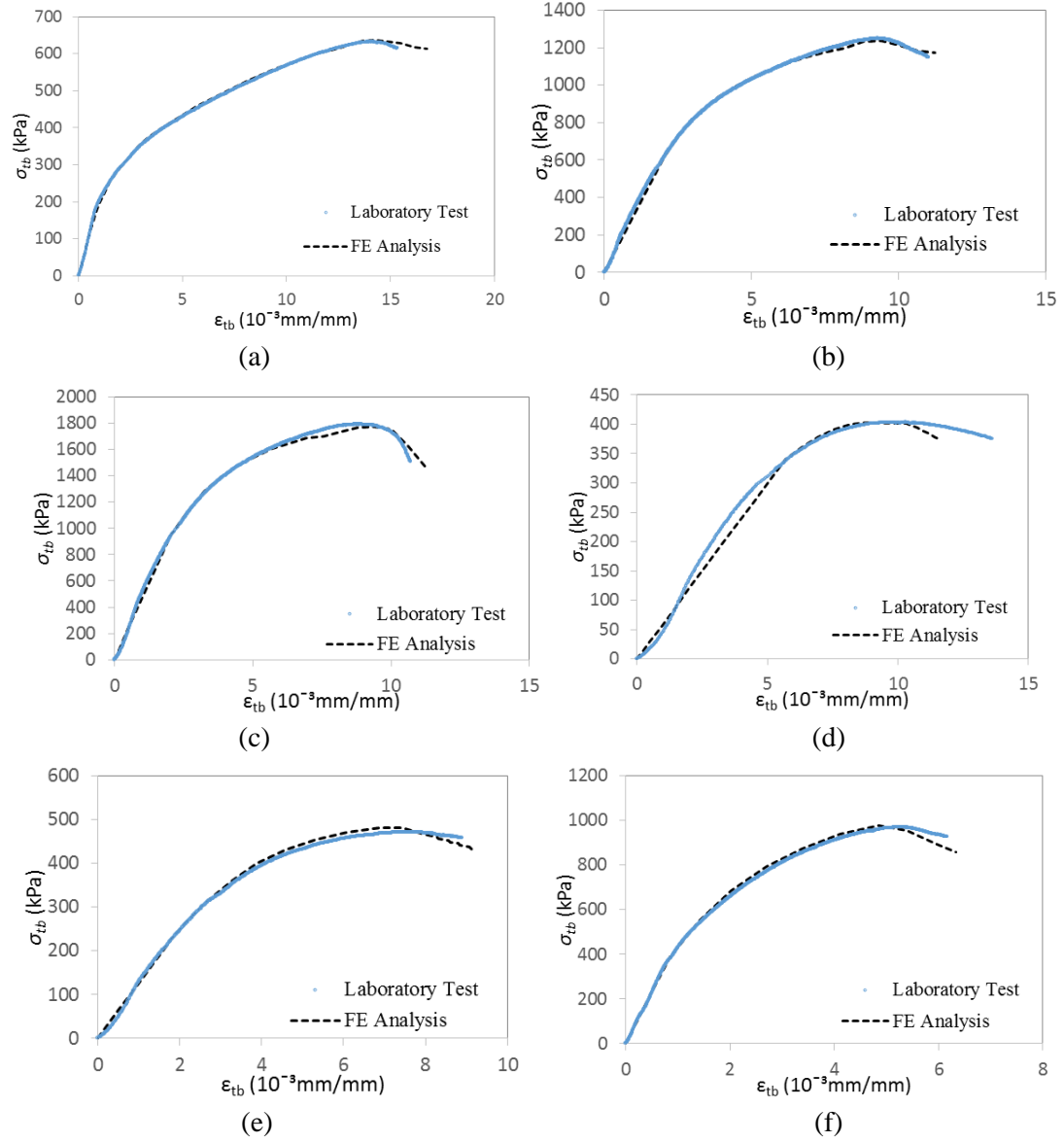
**Figure 5.3 Geometry and Mesh Configuration of FE Model of MoR Test**



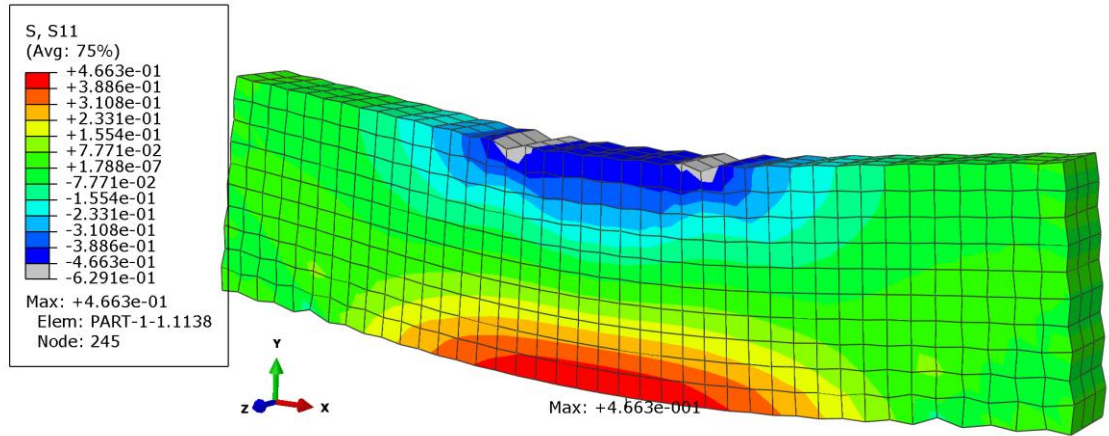
**Figure 5.4 (a) FPF Test Fixture, and (b) Detail of Specimen Clamping Mechanism in FPF Test Fixture (Hartman and Gilchrist, 2004)**



**Figure 5.5 Geometry and Mesh Configuration of FE Model of UCS Test**

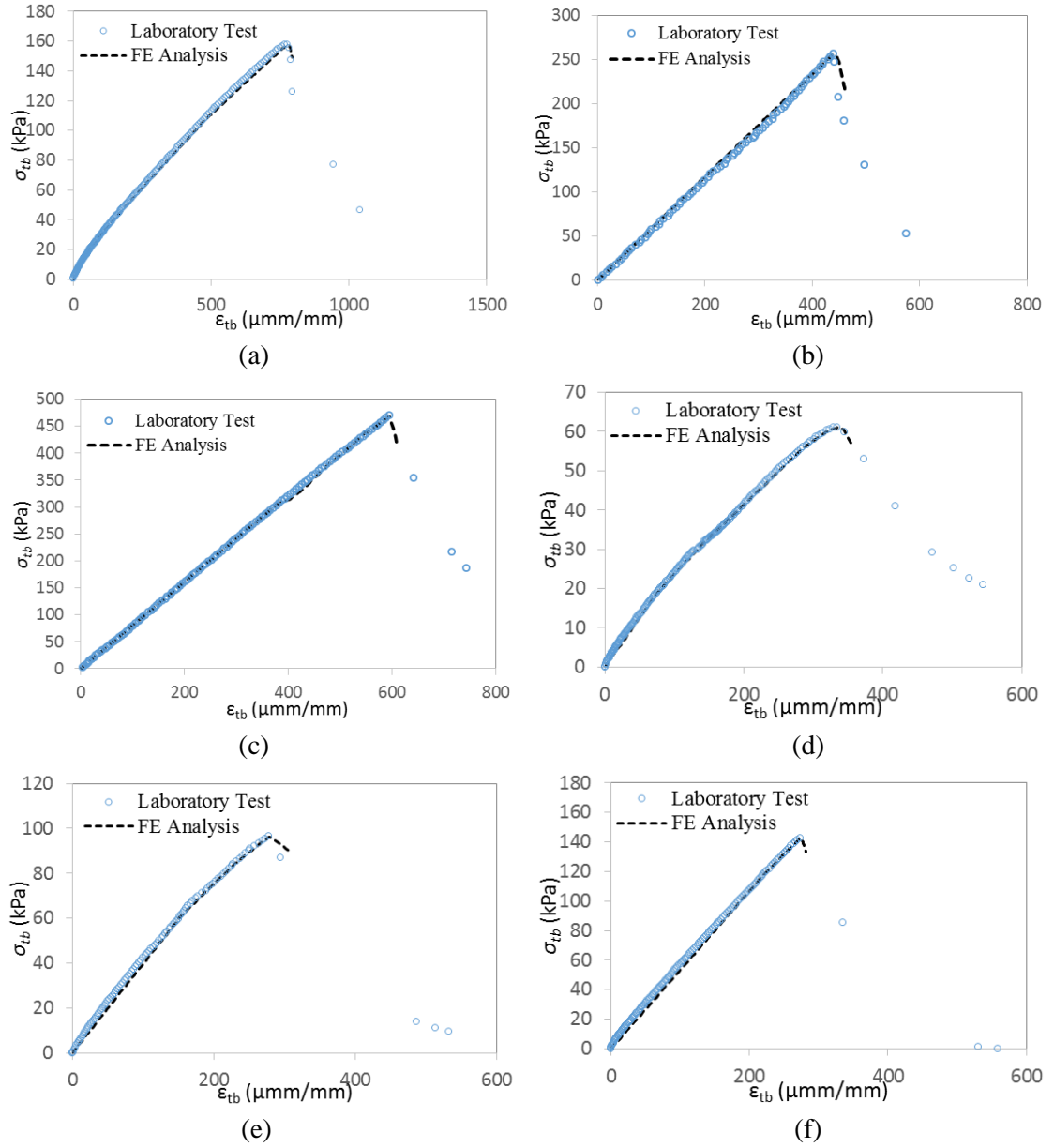


**Figure 5.6 Comparison between UCS Stress-Strain Curves of FE Models and Experimental Results for (a) CKD5, (b) CKD10, (c) CKD15, (d) LM3, (e) LM6, and (f) LM9**

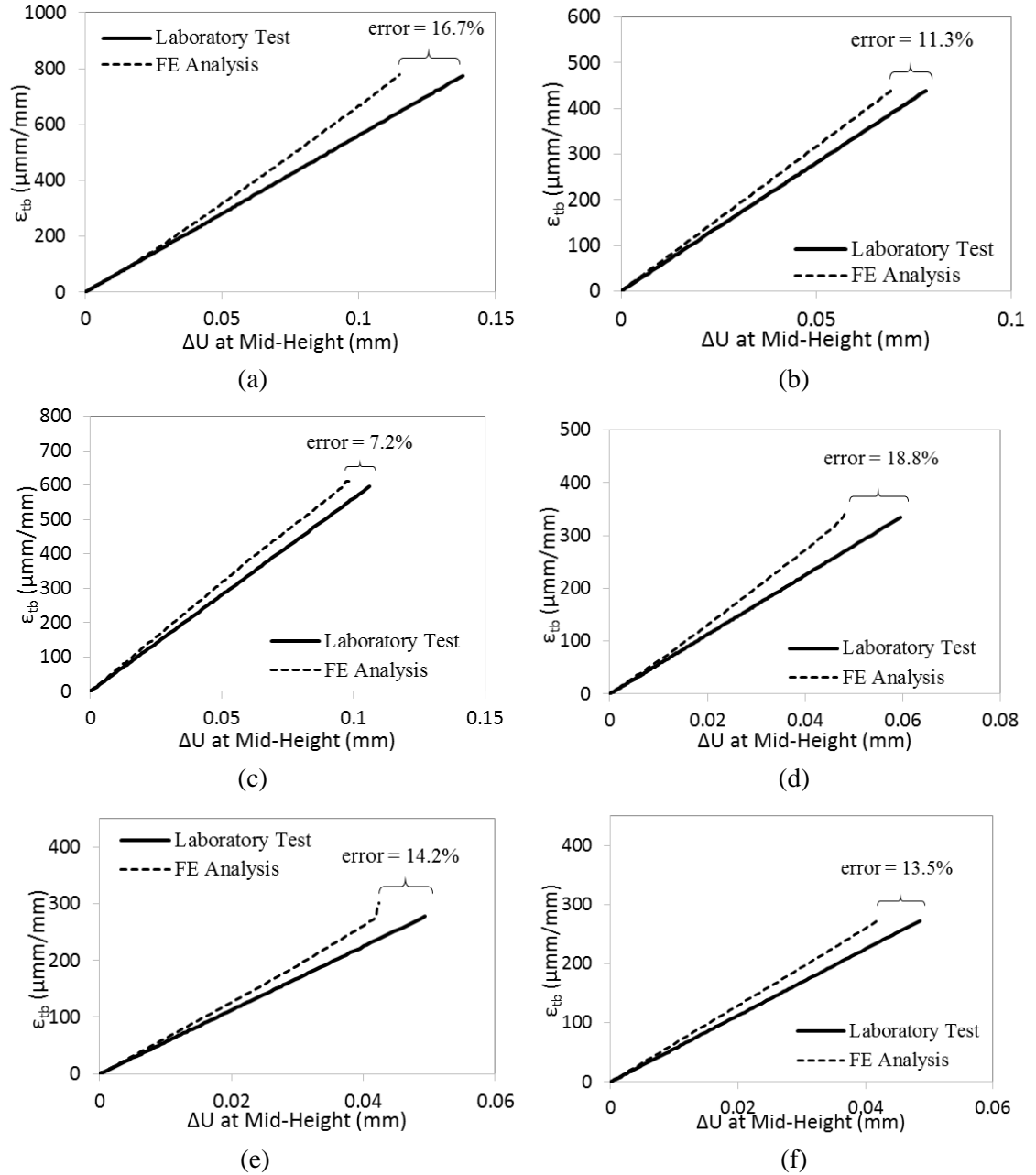


**Figure 5.7 Stress Distribution and Maximum Tensile Stress at x-direction of the FE Model of MoR Test for CKD15 Material**

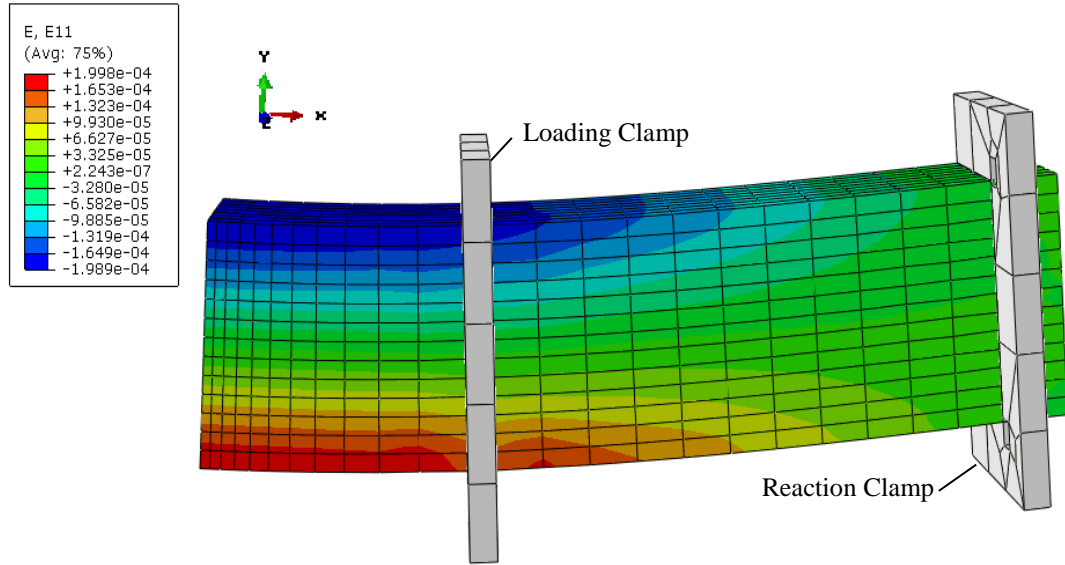




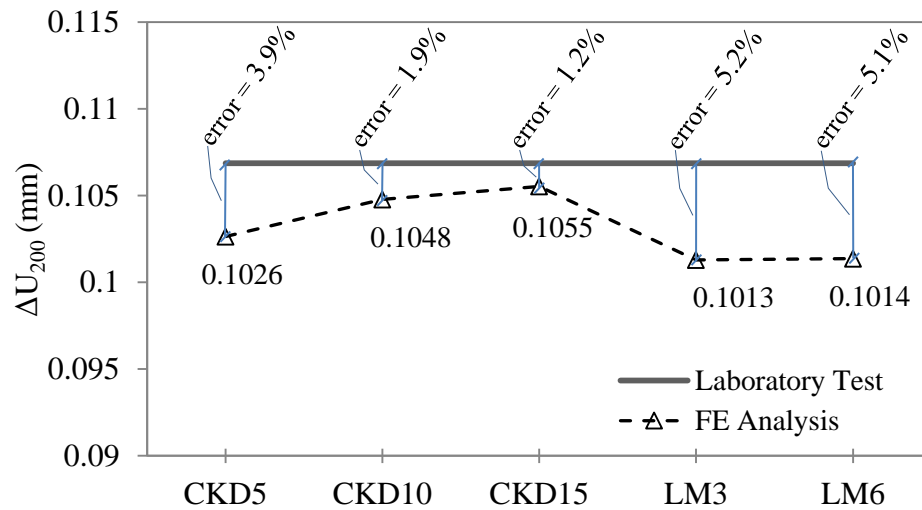
**Figure 5.8 Comparison between MoR Stress-Strain Curves of FE Models and Experimental Results for (a) CKD5, (b) CKD10, (c) CKD15, (d) LM3, (e) LM6, and (f) LM9**



**Figure 5.9 Comparison between  $\epsilon_{tb}$ – $\Delta U$  Curves from FE Models and Experimental Results for (a) CKD5, (b) CKD10, (c) CKD15, (d) LM3, (e) LM6, and (f) LM9**



**Figure 5.10 Strain Distribution in x-direction of the FE Model of FPF Test for CKD5 Material**



**Figure 5.11 Comparison between  $\Delta U_{200}$  Values Achieved from FE Model and LVDT Measurement for Different Materials**

## CHAPTER 6

### CONSIDERATION OF FLEXURAL PROPERTIES OF CHEMICALLY-STABILIZED SUBGRADE IN MECHANISTIC-EMPIRICAL DESIGN OF SEMI-RIGID PAVEMENTS

#### 6.1 Introduction

Semi-rigid pavements is a type of pavement in which the Hot Mix Asphalt (HMA) layer is placed over a chemically-treated layer (AASHTO, 2004). A major advantage of semi-rigid pavements is the reduction of transferred stresses to its subgrade layer. This leads to a decrease in the design thickness of HMA layer and, consequently, a reduction in construction costs (Little, 2000; TMR, 2012).

Due to soil stabilization with chemical additives, such as cement kiln dust (CKD), lime, cement and fly-ash (CFA), it gains tensile strength (Little, 2000). Therefore, the flexural characteristics of the chemically-stabilized subgrade (CSS) layer are more dominant compared to untreated subgrades (Zhang et al., 2010). Thus, it is important to consider the flexural behavior of a CSS layer in pavement design. The significance of determining the flexural modulus of the CSS layer in evaluating the overall performance of the pavement structure has been highlighted by several researchers (Pretorius and Monismith, 1972; Jameson et al., 1992; Austroads, 2004; Yeo, 2008; Siripun et al., 2012; and Arnold et al., 2012). Also, previous studies show that if the flexural modulus is measured at the strain levels and load/strain application rates close to those occurring in the field, the flexural modulus values could be higher than the resilient modulus of the CSS material (Solanki, 2010; Mandal, 2013; and Nazari et al., 2016).

Flexural fatigue cracking of CSS layers is a major distress in semi-rigid pavements (De Beer, 1990; Sebesta et al., 2004; Balbo, 2007; Yeo, 2008; and Saxena et

al., 2010). However, the fatigue model of the CSS layer has not been calibrated in the Mechanistic-Empirical Pavement Design Guide (M-EPDG) due to difficulties in conducting the required field investigations. According to Freeme et al. (1982), the failure of a CSS layer occurs in three stages: (1) shrinkage cracking; (2) fatigue crack initiation; and (3) crack propagation. Shrinkage cracks occur due to drying and thermal distresses in the early life of the pavement. Some researchers have proposed to multiply the stresses/strains by a factor greater than one to take the stress/strain concentration due to shrinkage cracking into account (Mitchell and Monismith, 1977; Freeme et al., 1982). Initiation of a fatigue crack at the bottom of a CSS layer usually takes place over the course of design life of the pavement as a result of repetitive cyclic loads due to the traffic. After initiation, the rate of bottom-up crack propagation depends on the thickness of the CSS layer and the fatigue endurance of the material (Otte et al., 1992; Theyse et al., 1996; and Austroads, 2004).

A useful tool for determining the level of induced tensile strain at the bottom of the CSS layer is Finite Element (FE) modeling of the pavement structure (AASHTO, 2004). In this study, the influence of different parameters on the induced tensile strains at the bottom of CSS layer in a semi-rigid pavement was investigated by conducting a parametric FE modeling and analyses. The minimum required HMA layer thickness to avoid fatigue failure in CSS layer was determined for different pavement structure configurations, using the FE model and laboratory test results. Then, the semi-rigid pavement structure was designed for different CSS configurations with the minimum required thickness of HMA layer in accordance with the M-EPDG (AASHTO, 2004).

## **6.2 Background of M-EPDG**

One of the first attempts for developing a method for designing pavement structures was made by California Highway Department in 1929. This effort resulted in introduction of the California Bearing Ratio (CBR) used for calculating the required thicknesses of the pavement layers (Porter, 1950). A series of experimental pavement tracks, known as AASHO Road Test, conducted between 1958 and 1960 in Ottawa, IL, formed the basis of developing the AASHTO guides for designing pavements in 1962, 1972, 1986 and 1993 (HRB, 1962; AASHTO, 1972; 1986; 1993). The 1993 AASHTO Guide for pavement design is the latest version of the pavement design guides based on the AASHO Road Test. The method used regression models to relate traffic, pavement structure and pavement performance. The abovementioned empirical design methods are based on laboratory experiments and field observations and measurements. Although these design guides have been upgraded over the years by conducting additional field experiments their scope is limited to the conditions in which the field experiments were conducted (Schwartz and Carvalho, 2007) and lack mechanistic basis in many cases.

The need for considering mechanistic approach in the design procedure was first highlighted in 1986 AASHTO design guide (AASHTO, 1986). Based on this need, a project for developing a mechanistic-empirical (M-E) pavement design procedure was initiated in 1996. That project aimed to reflect the influences of traffic loads, material properties and design features, and direct effects of the climate conditions on the performance of the pavements (AASHTO, 2004). Subsequently, the M-EPDG was developed under two projects funded by the National Cooperative Highway Research Program (NCHRP), namely NCHRP 1-37A (ARA Inc., 2004) and NCHRP 1-40

(AASHTO, 2010). The M-EPDG provides a novel pavement analysis and design tool which utilizes mechanistic structural response models to evaluate the pavement distresses, and employs nationally calibrated empirical distress transfer functions to predict pavement performance (Ceylan et al., 2015).

To implement the M-EPDG pavement analysis and design, the M-EPDG software was commercially released in 2011 as DARWin-ME version 1.0. The software has recently been rebranded as AASHTOWare Pavement ME Design. Contrary to 1993 AASHTO guide in which thicknesses of the pavement layers were calculated directly from the empirical equations, in the M-EPDG the design thicknesses are obtained through an iterative process. As mentioned previously, a set of nationally calibrated transfer functions are used to predict typical distress levels and pavement roughness from pavement response to traffic, climate and material input. The predicted distresses and roughness allow the designer to judge if the desired performance criteria are met over the design period (Diefenderfer, 2010). According to the predicted distresses and roughness obtained from M-EPDG analysis, the designer is required to optimize the designed pavement structure by changing the structural variables. For a flexible pavement, distresses such as rutting, bottom-up (alligator) cracking, top-down (longitudinal) cracking, and transverse (thermal) cracking are predicted along with the roughness, which is measured by International Roughness Index (IRI).

The number of axle loads leading to fatigue cracking in a HMA layer is determined by using the following equation for both bottom-up and top-down fatigue cracking:

$$N_{f-HMA} = k_{f1}(C)(C_H)\beta_{f1}(\epsilon_t)^{k_{f2}\beta_{f2}}(E_{HMA})^{k_{f3}\beta_{f3}} \quad (6.1)$$

where,  $N_{f-HMA}$  = number of axle loads leading to fatigue cracking in the HMA layer,  $\varepsilon_t$  = tensile strain at critical locations (mm/mm),  $E_{HMA}$  = dynamic modulus of HMA layer (MPa),  $k_{f1,f2,f3}$  = global field calibration parameters,  $\beta_{f1,f2,f3}$  = local or mixture-specific field calibration constants, and  $C$  is calculated from Equations 6.2 and 6.3.

$$C = 10^M \quad (6.2)$$

$$M = 4.84 \left( \frac{V_{be}}{V_a + V_{be}} - 0.69 \right) \quad (6.3)$$

where,  $V_{be}$  = effective binder content of the HMA by volume (%), and  $V_a$  = percent air voids in the HMA layer. Depending on the type of fatigue cracking,  $C_H$ , which is the thickness correction term, is calculated by Equations 6.4 and 6.5.

For bottom-up (alligator) cracking:

$$C_H = \frac{1}{0.000398 + \frac{0.003602}{1 + e^{(11.02 - 3.49 \times H_{HMA})}}} \quad (6.4)$$

For top-down (longitudinal) cracking:

$$C_H = \frac{1}{0.01 + \frac{12}{1 + e^{(15.676 - 2.8186 \times H_{HMA})}}} \quad (6.5)$$

where,  $H_{HMA}$  = total HMA thickness (mm/25.4)

The fatigue cracking area at the end of design life is calculated using the cumulative fatigue damages over time. According to Miner's hypothesis (Miner, 1945) the cumulative damage index (DI) is calculated as follows:

$$DI = \sum \left( \frac{n}{N_{f-HMA}} \right)_{j,m,l,p,T} \quad (6.6)$$

where,  $n$  = actual number of axle load applications within a specific time period,  $j$  = axle load interval,  $m$  = axle load type,  $l$  = truck type,  $p$  = month (accounts for effective



dynamic modulus and change in base and subgrade reaction),  $T$  = median temperature for the five temperature intervals or quintiles used to subdivide each month.

Also, the M-EPDG recommends the use of following equation for determining the fatigue life of the CSS layer in semi-rigid pavements:

$$\text{Log } (N_{f-\text{css}}) = \left( \frac{k_1 \beta_{c1} - \left( \frac{\sigma_t}{\text{MoR}} \right)}{k_2 \beta_{c2}} \right) \quad (6.7)$$

where, MoR = modulus of rupture of the CSS layer,  $k_1$  and  $k_2$  = regression coefficients, and  $\beta_{c1}$  and  $\beta_{c2}$  = field calibration factors. Due to the complexity of carrying out required field investigations, the fatigue cracking model was not field calibrated (ARA Inc., 2004). Hence, currently, the fatigue crack of the CSS layer is not taken into account in the designing process.

The roughness of the pavement at the end of the design period is measured in terms of terminal IRI. The terminal IRI is calculated by considering different distresses of pavement layers. The following equation is used in the M-E design method for calculating the IRI of new flexible pavements:

$$\text{IRI} = \text{IRI}_0 + C_1 \times \text{RD} + C_2 \times \text{FC}_{\text{Total}} + C_3 \times \text{TC} + C_4 \times \text{SF} \quad (6.8)$$

where,  $\text{IRI}_0$  = initial IRI (m/km),  $\text{RD}$  = average total rut depth (mm),  $\text{FC}_{\text{Total}}$  = area of fatigue cracking (percent of total lane area) for both top-down and bottom-up, including alligator, longitudinal, and reflection cracking in the wheel path,  $\text{TC}$  = length of HMA thermal cracking (m/km),  $\text{SF}$  = the site factor which is a function of climate, natural subgrade soil and age of the pavement, and  $C_{1,2,3,\text{and } 4}$  = calibration coefficients. The current national calibration coefficients are equal to 40, 0.4, 0.008, and 0.015 for  $C_1$  to  $C_4$ , respectively. The initial IRI shows the roughness of the pavement surface when the

pavement is opened to the traffic. At the beginning of the pavement's life all of the distresses are assumed to be equal to zero. However, the initial roughness of the pavement is a non-zero value because of the construction imperfections.

Due to the uncertainties involved in predicting the pavement performance, the M-EPDG evaluates pavement distress according to its corresponding reliability factor. The reliability shows the probability of occurrence of a specific distress/roughness, while it does not exceed its designated thresholds at the end of the pavement's design life (Mallela et al., 2014).

The newest version of AASHTOWare Pavement ME Design software (version 2.2) has the capability of calculating pavement responses such as stresses, strains, and deflections under different axle loads and climatic conditions. The software determines the accumulative damage at the end of the analysis period and evaluates the pavement's performance according to user-defined reliability levels. For conducting the M-E analysis on a pavement section, the software requires the design input parameters as follows:

- General pavement information, including design life, construction and traffic opening dates, type of the pavement (new, reconstructed, or rehabilitated flexible/rigid pavement), and site and project identifications.
- Performance criteria, such as IRI and other distresses as described before.
- Traffic parameters, namely average annual daily truck traffic (AADTT, for trucks of FHWA Class 4 or higher), number of lanes in design direction, percent trucks in design direction, percent trucks in design lane, truck class distribution, axle configuration, and operational speed.

- Climate data, which defines the area's environmental conditions, such as temperature, precipitation and freeze-thaw cycles that can significantly affect the pavement performance. The AASHTOWare provides a climate database collected from different weather stations. The user can extract the data from a specific weather station or create a virtual weather station using the climate data of multiple stations.
- Pavement structure and material properties, namely the thickness of the pavement layers and material properties.

In the M-EPDG, the aforementioned input parameters can be defined in three levels: Level 1 input data possess the most accuracy and require direct laboratory tests for each material property. Level 2 input data are less comprehensive and usually use some empirical equations for estimating the material properties. Level 3 input data yield the lowest accuracy and the inputs include default values from national or statewide databases.

In the present study, the M-E design of a semi-rigid pavement for different thicknesses and material properties of the CSS layer was conducted using the AASHTOWare pavement design software. Also, the influence of using flexural modulus of the CSS layer rather than using its resilient modulus on the designed pavement section was investigated.

### **6.3 Determining the Minimum Required Thickness of HMA Layer**

A parametric study was conducted on a semi-rigid pavement section to predict the fatigue cracking of the CSS layer. First, the traffic-induced tensile strains at the bottom

of the CSS layer ( $\varepsilon_{t-CSS}$ ) were determined using FE modeling of the pavement structure. Then, using the developed strain-based fatigue model from Chapter 4, the maximum allowed  $\varepsilon_{t-CSS}$  to avoid fatigue failure was determined.

### ***6.3.1 Finite Element Model of Semi-Rigid Pavement Structure***

A 3-dimensional (3-D) full-scale FE model of a three-layered pavement was developed using a general-purpose FE program, Abaqus 6.13 (Simulia, 2013). The pavement structure consisted of a HMA layer directly placed over a CSS layer, underlain by an untreated subgrade layer.

#### ***6.3.1.1 Geometry of the Model***

The dimensions of the model were selected large enough in order to minimize the boundary and edge effects using a trial and error process. Accordingly, the final model had dimensions of 2,915 mm in x- direction by 2,000 mm in z- direction, as shown in Figure 6.1. The depth of the model (dimension in y-direction) varied depending on the thicknesses of HMA and CSS layers.

A standard 80 kN single axle load with dual tires was applied over four tires, each having a load of 20 kN. The static load was applied on top of the HMA layer as a uniform pressure of 825 kPa distributed on rectangular contact areas (tire imprint on the pavement) with the dimensions shown in Figure 6.2. The dimensions of the rectangular tire imprints were selected according to the configurations suggested by Huang (2004) for a tire pressure of 827 kPa (default value suggested by the M-EPDG). Taking advantage of symmetry, only one-fourth of the pavement structure and the tire contact area was modeled to reduce the required time for the analysis (see Figure 6.2).

#### 6.3.1.2 Layer Thicknesses

The model comprised of three layers of a semi-rigid pavement structure: A HMA layer at the top, a CSS layer beneath the HMA layer, and an untreated subgrade layer at the bottom. A hard normal contact that prevented surface separation was defined as the bond between interfaces of pavement layers.

A thickness of 3,600 mm was assigned to the subgrade layer, which was assumed to be infinite implicitly. By selecting this thickness, the maximum value of stress change at the bottom of the untreated subgrade layer was observed to be less than 0.5% of the applied pressure at the surface of the model. The parametric finite element analyses were conducted on the models with different thicknesses of the HMA and CSS layers, and different material properties for the CSS layer. Table 6.1 shows the selected thicknesses of different layers. From Table 6.1 it is evident that the HMA layer thicknesses used in the model varied from 76 to 280 mm, while the CSS layer's thickness values ranged between 102 and 356 mm selected according to the values used in typical semi-rigid pavements (Balbo and Cintra, 1996; Hernando and del Val, 2016). It should be noted that according to the maximum mixing depth of typical rotary mixers (510 mm or less), the maximum thickness after compaction achieved in the field usually does not exceed 356 mm (Peterfalvi et al., 2015).

#### 6.3.1.3 Material Properties

The same soil-additive mixtures used in Chapter 4, namely CKD5, CKD10, CKD15, LM3, LM6 and LM9, were considered for the CSS layer. Since the principle purpose of the FE modeling was to determine the induced tensile strains at the bottom of the CSS layer, the  $M_f$  value of each soil-additive mixture was assigned as the elastic

modulus of the material in the model. The HMA material was assumed to be a S3 type asphalt mix with a Nominal Maximum Aggregate Size (NMAS) of 19.0 mm and a PG 64-22 binder. Accordingly, the modulus of the HMA layer was assumed to be 3,445 MPa (at 21.1 °C) in all models (Solanki, 2010). Also, the elastic modulus of the untreated subgrade layer was set to 82 MPa for all of the models (Solanki, 2010). The materials were assumed to be stress insensitive linear elastic. The selected material properties for different layers of the model are presented in Table 6.2.

#### *6.3.1.4 The FE Mesh and Boundary Conditions*

As stated earlier, being symmetric with respect to the x- and z-axes (Figure 6.2), only one-fourth of the problem was modeled and analyzed. The boundary conditions at the bottom of the untreated subgrade were considered fixed. Also, the horizontal displacement perpendicular to boundaries along the model sides was constrained. For the elements on the plane of symmetry, the displacements normal to the plane and rotations about the horizontal axis in the plane were limited to zero.

The zones beneath the tire contact area had the finest mesh size to capture the steep stress/strain gradients. The mesh size increased as the depth and the distance from the tire contact area increased. Linear hexahedral elements of type C3D8R (8-noded brick elements) were used for 3-D modeling of the pavement structure. Figure 6.1 shows the FE mesh for the model with 178 mm and 254 mm thicknesses for the HMA and CSS layers, respectively. Depending on the thicknesses of the HMA and CSS layers, the FE mesh consisted of 11,968 to 19,040 elements, and 14,875 to 22,610 nodes.

#### 6.3.1.5 Model Verification

In order to assure the accuracy of the developed FE model, a comparison was made between the  $\varepsilon_{t-CSS}$  values reported by Solanki (2010) using the KENLAYER program (Huang, 2004) and the FE results obtained in this study. The KENLAYER software considers the pavement as an axisymmetric multilayer elastic system (Huang, 2004). To compare the  $\varepsilon_{t-CSS}$  values reported from two studies, the same material properties and layer thicknesses as used by Solanki (2010) were used in the FE model developed in this study. For all the models, the HMA layer was assumed to have a thickness of 101.6 mm with a resilient modulus of 3,445 MPa and a Poisson's ratio of 0.35. The CSS layer was placed on an untreated subgrade soil with a modulus of 82 MPa and a Poisson's ratio of 0.4, and below the HMA layer. Solanki (2010) modeled the traffic load using a standard 80 kN single axle load. Hence, the loading configurations of the FE model was kept unchanged.

Table 6.3 shows the  $\varepsilon_{t-CSS}$  values achieved from the two studies (Solanki, 2010 and the FE model used in the current study) for different CSS layer materials and thicknesses. From Table 6.3, it can be observed that the differences between the calculated  $\varepsilon_{t-CSS}$  values in two studies ranged between 3% and 18%. Overall, considering the differences between the two models (axisymmetric vs 3-D) these agreements were considered reasonable. It must be mentioned that since the pavement modeled in the KENLAYER is axisymmetric, the tire load should be applied on a circular area, while in the 3-D FE model the tire imprint was simulated according to the axle configuration, which is more realistic.

### **6.3.2 Traffic Induced Tensile Strain at the Bottom of CSS Layer**

Based on the FE analyses, the maximum tensile strain values at the bottom of the CSS layer ( $\varepsilon_{t-CSS}$ ) were reported for the modeled pavement structures. Figure 6.3 shows the deformed shape and distribution of the horizontal strains along z- axis for the model with CKD5 material for the CSS layer. In Figure 6.3, the thicknesses for the HMA and CSS layers are 178 mm and 254 mm, respectively. For all cases, the maximum tensile strain was observed under the middle of tire imprints and in the direction of traffic (z-axis in the model). Figure 6.4 shows the changes in  $\varepsilon_{t-CSS}$  due to changes in thicknesses of the HMA and CSS layers for different CSS materials.

It is evident from Figure 6.4 that the  $\varepsilon_{t-CSS}$  values decreased due to an increase in thickness of the HMA layer. The increase in the CSS thickness, on the other hand, had a twofold effect on the  $\varepsilon_{t-CSS}$ . For sections with thinner HMA layers, the increase in CSS thickness resulted in lower  $\varepsilon_{t-CSS}$  values. For HMA layers thicker than 178 mm, however,  $\varepsilon_{t-CSS}$  increased in most cases by an increase in the CSS layer thickness. For example, for the CKD5 material and HMA layer thickness of 76 mm, the section with 102 mm thickness for the CSS layer showed the highest  $\varepsilon_{t-CSS}$  (311.9  $\mu\text{mm/mm}$ ), among other sections with thicker CSS layers. While, increasing the HMA layer thickness to 178 mm, the same section showed the lowest  $\varepsilon_{t-CSS}$  value (95.2  $\mu\text{mm/mm}$ ), compared to other sections. This was because of an increase in the distributed flexural stresses/strains in the CSS layer due to an increase in the layer's second moment of area and, consequently, increase in induced stresses/strains to the bottom of the CSS layer. Also, it was observed that the influence of the CSS layer thickness on the  $\varepsilon_{t-CSS}$  was reduced by increasing the HMA layer's thickness.



From Figure 6.4 it was observed that the maximum  $\varepsilon_{t-CSS}$  value of 359.6  $\mu\text{mm/mm}$  occurred for the pavement section with the smallest thickness of the HMA and CSS layers (76 and 102 mm, respectively) and the lowest CSS layer modulus (728 MPa). It was also found that the modulus of the CSS layer affected the  $\varepsilon_{t-CSS}$  values: an increase in the CSS modulus resulted in a reduction in  $\varepsilon_{t-CSS}$  values. For example, for HMA and CSS layer thicknesses of 178 and 254 mm, respectively, the  $\varepsilon_{t-CSS}$  values got reduced from 130.8  $\mu\text{mm/mm}$  to 76  $\mu\text{mm/mm}$  (42% reduction) by increasing the CSS layer modulus from 728 MPa (for LM3 material) to 3146 MPa (for CKD15 material). The minimum value of  $\varepsilon_{t-CSS}$  (30.7  $\mu\text{mm/mm}$ ) was obtained from the FE model for the pavement structure with CKD15 material for the CSS layer and 280 mm and 102 mm thicknesses for HMA and CSS layers, respectively.

### ***6.3.3 Minimum Required Thickness of HMA Layer***

The CSS layer of the pavement structure must endure the cyclic vehicular loads during the design life of the pavement. According to traffic configurations and anticipated design life, described in Section 6.4.1, the cumulative number of standard 80 kN equivalent single axle loads (ESALs) traversing the designed section after 20 years was equal to 9,011,450. Therefore, the minimum required fatigue life of the CSS layer must be equal or higher than 9,011,450 cycles (see Section 6.4.1).

Using the strain-based model developed in Chapter 4 (Equation 4.20), the maximum allowed  $\varepsilon_{t-CSS}$  was determined for a given fatigue life (9,011,450 cycles). It must be noted that Equation 4.20 was developed and validated using test results in a laboratory-scale condition. To modify the regression model for field conditions, crack propagation and shrinkage cracking of the CSS layer should be taken into consideration.

To consider the crack propagation, a shift factor for CSS material was introduced by Theyse et al. (1996), allowing thicker layers to have an extended effective fatigue life (after crack initiation), compared with thinner layers subjected to the same strain (Figure 6.5). Using Figure 6.5, the shift factors for different thicknesses of the CSS layer were determined and are presented in Table 6.4.

The shrinkage cracking of the CSS layer was taken into account by multiplying the induced strain at the bottom of the CSS layer by a modification factor,  $d$  (Mitchell and Monismith, 1977; Freeme et al., 1982). For the natural earth materials stabilized with lime and cement, Freeme et al. (1982) suggested a  $d$  factor of 1.1 for thicknesses less than 200 mm and 1.2 for layers thicker than 200 mm, respectively (see Table 6.4). By considering both crack propagation and shrinkage cracking, the following equation was developed based on Equation 4.20 to estimate the maximum allowed  $\varepsilon_{t-CSS}$ :

$$\varepsilon_{t-a} = \frac{4127.44 \varepsilon_{tf}}{(d)(M_f^{1.145}) \left( \log \left( \frac{9,011,450}{SF} \right) - 1.47 \right)} \quad (6.9)$$

where,  $\varepsilon_{t-a}$  = maximum allowed tensile strain at the bottom of the CSS layer,  $d$  = modification factor for shrinkage cracking,  $SF$  = shift factor for field crack propagation. The  $\varepsilon_{t-a}$  values, determined for different thicknesses of the CSS layer, are presented in Table 6.4 and are plotted in Figure 6.4.

The minimum required HMA layer thickness ( $H_{HMA-min}$ ) for different thicknesses of the CSS layer and materials (CKD5, CKD10, CKD15, LM3, LM6 and LM9) were determined by linear interpolation of the HMA thicknesses in Figure 6.4. These values are presented in Table 6.5. It was observed that for both CKD- and lime-stabilized soils, the  $H_{HMA-min}$  increased due to an increase in the additive content. This

was because the CSS layer becomes more susceptible to both fatigue and shrinkage cracking due to an increase in the additive content (Jameson et al.,1992; Van Blerk and Scullion 1995; and Sebesta, 2005). For sections with CKD10 and CKD15 materials and moderate thicknesses of the CSS layer, fatigue failure was inevitable for HMA thicknesses less than 300 mm. The thickness of the CSS layer did not have a consistent influence on the  $H_{HMA-min}$ . The  $H_{HMA-min}$  value increased by increasing the CSS thickness to a certain level (from 203 to 254 mm) and after that, it decreased for thicker CSS layers. Both the  $\epsilon_{t-CSS}$  value and the fatigue susceptibility of the material affected the  $H_{HMA-min}$ . For example, CKD5 material exhibited the highest fatigue life among the other materials in FPF tests (Figure 4.20). Also, the sections with CKD5 material and 356 mm thickness of CSS layer exhibited relatively low  $\epsilon_{t-CSS}$  values (Figure 6.4-a) compared to other CSS thicknesses. Consequently, the section with CKD5 material and 356 mm thickness of the CSS layer possessed the lowest value of  $H_{HMA-min}$ , among the pavement sections studied here. A majority of sections with CKD10 and CKD15 materials showed low resistance to fatigue failure due to low fatigue life of these materials in the FPF test (see Figure 4.20). These sections showed the highest values of  $H_{HMA-min}$  compared to others.

A high value for the  $H_{HMA-min}$  shows that the fatigue cracking is the most critical distress to be considered in designing asphalt pavements. For cases in which the  $H_{HMA-min}$  was relatively low, other pavement distresses such as rutting, bottom-up and top-down cracking, transverse cracking and IRI (analyzed using the M-EPDG method) become important design criteria as well.

## **6.4 Design of Semi-Rigid Pavement Using AASHTOWare**

### ***6.4.1 Selecting the Design Parameters***

#### ***6.4.1.1 General Information, and Performance Criteria Inputs***

Design of a new flexible pavement with a design life of 20 years was considered herein using the AASHTOWare Pavement ME Design software. The pavement was assumed to function as a state highway. The performance criteria for roughness and distresses were selected based on the suggested values by the M-EPDG for freeways (AASHTO, 2008). Along with IRI, distresses such as HMA top-down and bottom-up fatigue cracking, HMA thermal cracking, permanent deformation for total pavement, and permanent deformation (rutting) for the HMA layer were taken into consideration for evaluation of the pavement performance. A limiting value and a reliability value were assigned for each performance criterion, as listed in Table 6.6. The M-EPDG recommends a reliability level of 95% for freeways. Also, the M-EPDG recommends a range of 0.9 to 1.6 m/km for initial IRI as an indicator of the construction quality. The default value of 1 m/km was used as the initial IRI value. For all types of distresses, the national calibration coefficients (default values in the AASHTOWare design software) were used.

#### ***6.4.1.2 Traffic Input***

The traffic data were extracted from the average annual daily traffic (AADT) map of Cleveland County for CY2015 (Oklahoma AADT Maps, 2016). The AADT value was selected in accordance with the AADT of a section of Highway 9 passing through south of Norman, Oklahoma. The AADT at this section was around 30,000 vehicles for

CY2015. Hence, a value of 30,000 was selected for the expected AADT over the base year in both travel directions. Using the available traffic data for Oklahoma in the literature (Refai et al., 2014), a value of 8% was selected for the percent of heavy trucks (FHWA class 4 and above) in the average daily traffic (ADT). Accordingly, the average annual daily truck traffic (AADTT) over the base year in both directions was found to be 2,400. To make the results comparable with the FE analyses, it was assumed that all of the heavy trucks were of Class 9 with an ESAL value equal to one. Table 6.7 lists the design traffic configuration used for this purpose. A review of the previous studies show that the annual traffic growth rate generally ranges between 1.5% and 5% (Allen et al., 2001; Lu et al. 2007). By assuming a truck linear growth rate of 3% per year, the cumulative number of ESALs over the design period was determined as 9,011,450.

#### *6.4.1.3 Climate Input*

The predefined climate data from Oklahoma City weather station for CY1996 to CY2006 were downloaded from AASHTOWare's climate data archive (AASHTOWare-Climatic Data, 2016), and used as the climate data for design example herein. The station had a mean annual air temperature and precipitation of 15.9 °C and 803 mm, respectively. The average annual number of freeze-thaw cycles was 44.3.

#### *6.4.1.4 Pavement Structural Configuration and Material Properties*

The design section consisted of a HMA layer over a CSS layer, placed on top of an untreated subgrade layer. The same material properties used in the FE analyses were considered for designing the pavement. Table 6.8 shows the different design sections and the CSS material properties for each section. Similar to the FE model, five different thicknesses, namely 102, 152, 203, 254, 305, and 356 mm, for the CSS layer were

considered in this design. For each section the pavement was designed using two different modulus values of the CSS layer:  $M_r$ , obtained from resilient modulus tests, and  $M_f$ , obtained from FPF tests. The material properties of the HMA and untreated subgrade layers were kept constant for all of the test sections. Similar to the FE model, the HMA layer was assumed as a S3 mix having a NMA = 19 mm and binder type of PG 64-22. The mix was assumed to have a resilient modulus of 3,445 MPa at 21.1 °C. The material properties of the HMA layer are summarized in Table 6.9. The material properties of the HMA layer were defined through Level 3 input in the software. Hence, the software indirectly calculated the dynamic modulus of the HMA using the mix gradation and the binder properties, using its built-in regression equation (Bari and Witczak, 2006). The thickness of the HMA layer was to be designed using the M-E technique. The underlying subgrade was a semi-infinite layer of untreated soil of type A-4 (the same soil used for the study in Chapter 4) according to AASHTO classification system (AASHTO M145, 2000), with a resilient modulus of 82 MPa for all of the sections (see Table 6.2).

#### ***6.4.2 Designed Thicknesses of HMA Layer***

The M-EPDG analyses were conducted on all pavement sections (Sec-1 to Sec-36 in Table 6.8) for two types of CSS modulus ( $M_r$  and  $M_f$ ). The design of the sections was conducted through a trial and error process. For each section, the initial thickness of the HMA layer was selected in accordance with the corresponding  $H_{HMA-min}$  value from Table 6.5 in order to avoid fatigue cracking in the CSS layer. If all of the performance criteria were successfully met in the first trial of the M-E analysis, the  $H_{HMA-min}$  value was taken as the optimal thickness. In cases where one or more criteria were not met, the HMA thickness in the M-E model was increased by 25.4 mm increments, until all of the

performance criteria were met. As mentioned earlier, for each section (i.e. each CSS thickness and material) the model was run with two moduli values for the CSS layer, one reflecting the resilient modulus value and another one reflecting the flexural modulus. Using different moduli, the influence of modulus type on the designed thickness could be identified.

Table 6.10 and Figure 6.6 show the designed HMA thicknesses for different sections. For all of the sections designed with a CKD10 or CKD15 material for the CSS layer, the fatigue failure of the CSS layer was found to be the critical distress and the  $H_{HMA-min}$  was assigned as the designed HMA thickness. In other words, for these sections, the HMA thickness obtained through M-EPDG analysis, without considering fatigue performance of the CSS layer, was lower than the  $H_{HMA-min}$ . Therefore,  $H_{HMA-min}$  was selected as the final designed HMA thickness to prevent fatigue failure in the CSS layer. These sections are marked with \* symbol in Table 6.10. The sections with corresponding  $H_{HMA-min}$  thicknesses of higher than 300 mm are not presented in Figure 6.6, since HMA thicknesses higher than 300 mm usually are not cost-effective, and are rarely used in practice (NAPA, 2001; McDonald and Madanat, 2011). Therefore, considering the fatigue susceptibility of CSS layers with CKD10 and CKD15 materials, stabilization of the subgrade soil with 10% or higher amounts of CKD is not recommended for the soil used in this study. For the other materials (CKD5, LM3, LM6 and LM9, except for LM9 with a CSS thickness of 254 mm) other distresses evaluated by AASHTOWare M-E analysis, mostly HMA bottom-up and top-down fatigue cracking, were critical in selecting the design HMA thickness.

It was found that increasing the lime content from 3% (LM3) to 9% (LM9) did not affect the designed HMA thickness. However, for CKD-stabilized soil, increasing the additive amount from 5% (CKD5) to 10% (CKD10) and 15% (CKD15) resulted in fatigue failure of the CSS layer to become the most critical distress, and it led to an increase in the designed HMA thicknesses. It should be noted that although CKD10 and CKD15 had the highest  $M_r$  and  $M_f$  values among the studied materials, the designed HMA thicknesses attributed to them were the highest also. This was because of the fatigue susceptibility of those two materials under traffic loads (see Figure 4.20). Hence, it is important to evaluate the fatigue performance of the CSS material through flexural laboratory tests, particularly when using a large amount of additive (CKD10 and CKD15 in this study). These results support the observations by Yeo (2008) concerning the effect of additive amount on the fatigue life of the material. It is worth noting that, since the M-EPDG is not calibrated for the fatigue failure mechanisms pertaining to the CSS layer, it is not feasible to account for the fatigue cracking of the CSS layer. Consequently, for semi-rigid pavements with a CSS material prone to fatigue failure (such as CKD10 and CKD15), the M-EPDG results will overestimate the pavement performance. Formation of premature reflective cracks due to the fatigue failure of the CSS layer, is expected to reduce the design life of the pavement. This is an important finding of this combined experimental and modeling study.

For sections where fatigue failure of the CSS layer was not the most critical distress, the design HMA layer thickness was reduced by an increase in thickness of the CSS layer. From Figure 6.6 it can be seen that for CKD5 material, influence of changes in CSS layer's thickness from 102 mm (Sec-1) to 356 mm (Sec-6) is more significant



compared to lime-stabilized soils (Sec-19 to Sec-36). Accordingly, the lowest design HMA layer thicknesses were achieved for Sec-6 with 356 mm thick layer of CKD5 material. The designed HMA thicknesses for this section were found to be 216 and 178 mm by using  $M_r$  and  $M_f$  as the CSS moduli, respectively. Nowadays, manufacture of modern rotary mixers have made it is possible to construct CSS layers up to 356 mm thick (Peterfalvi et al., 2015).

It can be seen from Figure 6.6 that, for a majority of the sections, using  $M_f$  rather than  $M_r$  resulted in a more economic design (i.e., thinner designed HMA layer). Figure 6.7 gives a better illustration of differences between HMA layers' thicknesses designed based on the  $M_r$  ( $M_r$ -designed) and  $M_f$  ( $M_f$ -designed). A 38 mm reduction in designed HMA thickness was observed for CKD5 material with CSS layer thicknesses of 254, 305 and 356 mm (Sec-4, Sec-5 and Sec 6, respectively). It should be noted that a 38 mm reduction in the HMA layer thickness can significantly reduce the construction cost of the pavement (McDonald and Madanat, 2011). Also, the  $M_f$ -designed HMA thicknesses for Sec-1, Sec-2 and Sec-3 (sections with CKD5 material) showed 13, 25 and 25 mm reductions compared to the  $M_r$ -designed HMA thicknesses, respectively. The reduction in designed HMA thickness for these sections can be attributed to the considerable difference between  $M_r$  and  $M_f$  of the CKD5 material (734 and 1,214 MPa, respectively). For the sections with LM3, LM6 and LM9 materials (Sec-19 to Sec-36) the difference between  $M_r$ -designed and  $M_f$ -designed HMA thicknesses ranged between 0 to 13 mm. The difference between  $M_r$  and  $M_f$  of the CSS material for these sections was less significant compared to that of CKD5 (see Table 6.10).

From Figure 6.7, it is evident that for the sections with CKD5 material, the difference between  $M_r$ -designed and  $M_f$ -designed HMA thicknesses increased when the CSS layer thickness was increased. For the CSS layers stabilized with lime (LM3, LM6 and LM9) the changes in CSS layer thickness had not a clear effect on the difference between  $M_r$ -designed and  $M_f$ -designed HMA thicknesses (0 to 13 mm difference). This is because of the small differences between modulus values (both  $M_r$  and  $M_f$ ) of different soil-lime mixtures (see Table 6.10).

Overall, it is concluded that when chemical stabilization of the subgrade is considered, the short-term ( $M_f$ ) and long term flexural properties (fatigue life) of the CSS layer should be evaluated properly. By characterization of these flexural properties and selecting the appropriate soil-additive mixture, the premature fatigue failure and reflective cracking in the asphalt layers could be avoided. Additionally, by substituting the CSS resilient modulus with the properly determined flexural modulus in the M-E design procedure, the design HMA thickness, and consequently, the construction cost could significantly decrease.

## 6.5 Conclusions

In this study the influence of different parameters on the traffic induced tensile strains at the bottom of CSS layer in a semi-rigid pavement structure was investigated by conducting parametric finite element analyses. Using the finite element model analyses and laboratory test results, the minimum required HMA thickness to avoid fatigue failure in CSS layer was determined for different pavement sections. Then, the thickness of the HMA layer was designed for different sections by conducting M-EPDG analyses using

two different types of modulus ( $M_r$  and  $M_f$ ) for the CSS layer. Finally, a comparison was made between the  $M_r$ -designed and  $M_f$ -designed HMA thicknesses. The following conclusions were drawn:

1. The fatigue susceptibility of the CSS layer reduced by an increase in the HMA thickness. This is due to the fact that the traffic-induced tensile strain at the bottom of the CSS layer ( $\varepsilon_{t-CSS}$ ) reduces by an increase in the thickness of the HMA layer. Also, for the sections with thinner HMA layers an increase in CSS thickness resulted in a lower  $\varepsilon_{t-CSS}$  value.
2. The tensile strain at the bottom of the CSS layer was found to decrease with an increase in the flexural modulus of the CSS layer. The highest strain (359.6  $\mu\text{mm/mm}$ ) was observed for the pavement section with the thinnest HMA and CSS layers (76 and 102 mm, respectively) and the lowest CSS layer modulus (728 MPa).
3. For the CSS materials with relatively low fatigue lives (CKD10 and CKD15), the fatigue cracking of the CSS layer was the most critical distress to be considered in designing the pavement. Consequently, using these mixtures as the CSS layer of the semi-rigid pavements is not recommended, since it was found to result in a very high, and not economically feasible, values for  $H_{HMA-min}$ .
4. For the CSS materials that exhibited higher fatigue lives in the laboratory (CKD5, LM3 and LM6), other pavement distresses, such as rutting, bottom-up and top-down cracking, transverse cracking and IRI (analyzed using M-EPDG method), were critical for the pavement design. The sections with these materials were less prone to CSS fatigue failure and had relatively low  $H_{HMA-min}$  values.

5. It was found that increasing the lime content from 3% (LM3) to 9% (LM9) did not affect the designed HMA layer's thickness. While, for CKD-stabilized soil, increasing the additive from 5% (CKD5) to 10% (CKD10) and 15% (CKD15) resulted in dominance of CSS fatigue failure in design and an increase in the designed HMA thickness.
6. By substituting the CSS resilient modulus with the properly determined flexural modulus in the M-E design procedure, the designed HMA thickness, and consequently, the construction cost could significantly decrease. The difference between  $M_r$ -designed and  $M_f$ -designed HMA thicknesses was more significant when difference between  $M_r$  and  $M_f$  of the CSS material was larger.
7. Effect of environmental conditions (e.g., wet-dry and freeze-thaw cycles, and seasonal variations of moisture) on the fatigue life of the CSS was not considered in this study. Consideration of durability on  $M_r$  and  $M_f$  is important in designing pavements, to account for field conditions.

**Table 6.1 The Selected Layers Thicknesses for the Parametric Analyses**

HMA Layer Thicknesses	CSS Layer Thicknesses	Untreated Subgrade Thickness
(mm)	(mm)	(mm)
76	102	3600
127	152	
178	203	
229	254	
280	305	
	356	

**Table 6.2 Material Properties of the Finite Element Model**

Pavement Layer	Material Name	Unit Weight (kN/m <sup>3</sup> )	Elastic Modulus (MPa)	$\nu$
HMA	HMA	21	3445	0.35
CSS	CKD5	20	1214	0.3
	CKD10	20	2662	0.3
	CKD15	20	3146	0.3
	LM3	20	728	0.3
	LM6	20	797	0.3
	LM9	20	871	0.3
Subgrade	Subgrade	18	82	0.35

**Table 6.3 Comparison between  $\epsilon_{t-CSS}$  ( $\mu\text{mm/mm}$ ) Achieved from KENLAYER (Solanki, 2010) and FE Analyses (Current Study)**

CSS Thickness (mm)	V-soil + 6% Lime E = 715 MPa			V-soil + 10% CFA E = 951 MPa			V-soil + 10% CKD E = 1575 MPa		
	Solanki (2010)	Current Study	Difference	Solanki (2010)	Current Study	% Difference	Solanki (2010)	Current Study	% Difference
152	303	249	18%	270	232	14%	212	197	7%
203	233	239	-3%	205	215	-5%	158	171	-8%
254	183	199	-9%	159	172	-8%	121	136	-12%

E: Modulus of the CSS layer

**Table 6.4 Maximum Allowed  $\epsilon_{t-CSS}$  after Considering Shift Factor and Shrinkage**

			Material	CKD5	CKD10	CKD15	LM3	LM6	LM9
			Name						
			$M_f$ (MPa)	1214	2662	3146	728	797	871
			$\epsilon_{ff}$ ( $\mu\text{mm/mm}$ )	747	483	578	360	314	269
CSS	Thickness SF	$d$	Maximum Allowed $\epsilon_{t-CSS}$ ( $\mu\text{mm/mm}$ )						
(mm)									
102	1	1.1		150.3	39.5	39.1	130.0	102.3	79.1
152	1.4	1.1		154.2	40.6	40.1	133.4	105.0	81.2
203	1.9	1.2		145.3	38.2	37.8	125.7	99.0	76.5
254	2.7	1.2		149.5	39.3	38.9	129.3	101.8	78.7
305	3.8	1.2		153.9	40.5	40.0	133.1	104.8	81.1
356	5.3	1.2		158.6	41.7	41.2	137.2	108.0	83.5

**Table 6.5 Minimum Required HMA Layer Thickness to Avoid CSS Fatigue Failure**

CSS Thickness (mm)	$H_{HMA-min}$ (mm)					
	CKD5	CKD10	CKD15	LM3	LM6	LM9
102	126.7	250	249.1	142.6	163.9	186.9
152	136.6	281.3	280.3	161.0	184.3	212.2
203	147	> 300	> 300	179.7	206.9	239.1
254	133.6	> 300	> 300	179.5	209.7	245.1
305	93.5	> 300	> 300	166.5	200	238.2
356	46	> 300	273.7	149.2	187.2	226.9

**Table 6.6 Selected Performance Criteria for Pavement Design**

Performance Criteria	Limit	Reliability
Terminal IRI (m/km)	2.53	95%
HMA top-down fatigue cracking (m/km)	378.8	95%
HMA bottom-up fatigue cracking (%)	20	95%
HMA thermal cracking (m/km)	189.4	95%
Permanent deformation- total pavement (mm)	19	95%
Rutting- HMA only (mm)	10.2	95%

**Table 6.7 Design Traffic Configuration**

Parameter	Value
Two-way AADT	30,000
Number of lanes in design direction	2
Percent heavy trucks (FHWA Class 4 or higher), (%)	8
Initial two-way AADTT	2,400
Percent trucks in design direction	50
Percent trucks in design lane	80
Operational speed (km/h)	96
Average axle width, (m)	2.59
Dual tire spacing, (mm)	305
Tire pressure, (kPa)	827
Mean wheel location, (mm)	457.2
Traffic wander standard deviation, (mm)	254
Design lane width, (m)	3.65
Class 9 vehicle distribution, (%)	100
Class 9 vehicle growth rate (%)	3
Other vehicle classes distribution	0
Standard 80 kN axle load distribution factor (Class 9), (%)	100
Cumulative Class 9 traffic (ESALs)	9,011,450

**Table 6.8 CSS Material Properties and Thickness Layer for Different Design**

<b>Sections</b>							
Section Code	Material Name	$w_{opt}$	$\gamma_{dmax}$	Poisson's Ratio	$M_r$	$M_f$	CSS Layer Thickness
		(%)	(kN/m <sup>3</sup> )		(MPa)	(MPa)	(mm)
Sec-1	CKD5	13.7	17.79	0.3	734	1214	102
Sec-2							152
Sec-3							203
Sec-4							254
Sec-5							305
Sec-6							356
Sec-7	CKD10	14.6	17.48	0.3	1845	2662	102
Sec-8							152
Sec-9							203
Sec-10							254
Sec-11							305
Sec-12							356
Sec-13	CKD15	15.3	17.25	0.3	2602	3146	102
Sec-14							152
Sec-15							203
Sec-16							254
Sec-17							305
Sec-18							356
Sec-19	LM3	13	17.52	0.3	624	728	102
Sec-20							152
Sec-21							203
Sec-22							254
Sec-23							305
Sec-24							356
Sec-25	LM6	13.7	17.17	0.3	615	797	102
Sec-26							152
Sec-27							203
Sec-28							254
Sec-29							305
Sec-30							356
Sec-31	LM9	15.1	16.72	0.3	701	824	102
Sec-32							152
Sec-33							203
Sec-34							254
Sec-35							305
Sec-36							356



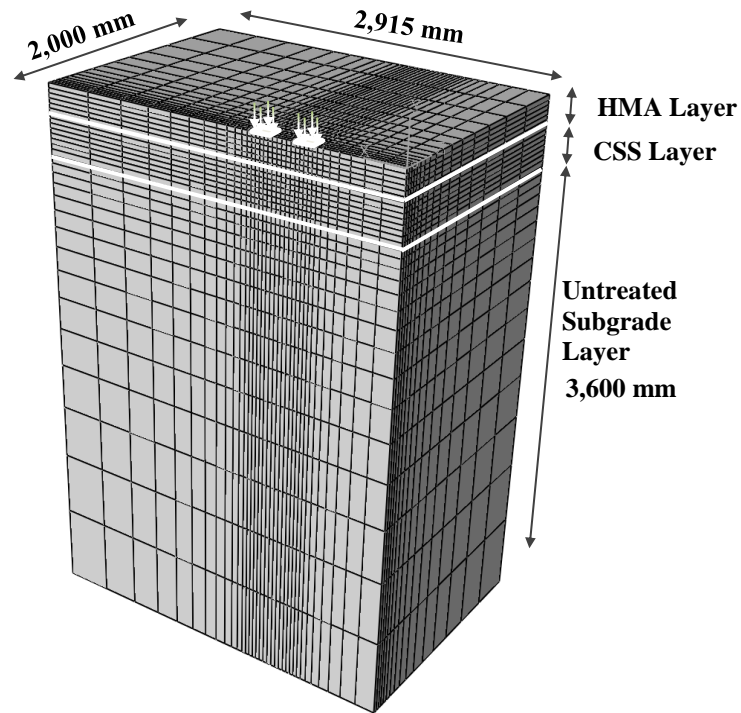
**Table 6.9 HMA Material Properties for Pavement Design**

Parameter	Value
Mix Type	S3
Binder Type	PG 64-22
Binder Content, (%)	4.1
Air voids, (%)	7
Percent finer than 25.4 mm, (%)	100
Percent finer than 19 mm, (%)	98
Percent finer than 9.51 mm, (%)	80
Percent finer than 0.075 mm (No. 200 sieve), (%)	58
Total unit weight, (kN/m <sup>3</sup> )	20.91
Poisson's ratio	0.35
Reference temperature, (°C)	21.1
Indirect tensile strength at -10 °C, (kPa)	7,090
Resilient modulus at the reference temperature, (MPa)	3,345

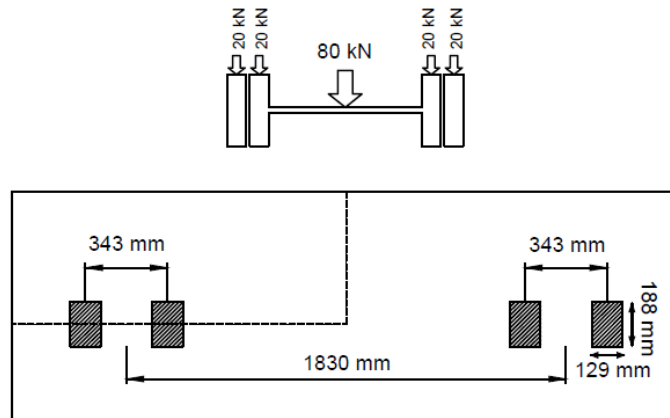
**Table 6.10 HMA Designed Thicknesses for Different Pavement Sections**

Section Code	CSS Material Name	CSS $M_r$ (MPa)	CSS $M_f$ (MPa)	CSS Layer Thickness (mm)	Designed HMA Thickness Using $M_r$ (mm)	Designed HMA Thickness Using $M_f$ (mm)
Sec-1	CKD5	734	1214	102	267	254
Sec-2				152	254	229
Sec-3				203	241	216
Sec-4				254	229	191
Sec-5				305	216	178
Sec-6				356	216	178
Sec-7	CKD10	1845	2662	102	254 *	254 *
Sec-8				152	> 300 *	> 300 *
Sec-9				203	> 300 *	> 300 *
Sec-10				254	> 300 *	> 300 *
Sec-11				305	> 300 *	> 300 *
Sec-12				356	> 300 *	> 300 *
Sec-13	CKD15	2602	3146	102	254 *	254 *
Sec-14				152	279 *	279 *
Sec-15				203	> 300 *	> 300 *
Sec-16				254	> 300 *	> 300 *
Sec-17				305	> 300 *	> 300 *
Sec-18				356	279 *	279 *
Sec-19	LM3	624	728	102	267	267
Sec-20				152	254	254
Sec-21				203	254	241
Sec-22				254	241	241
Sec-23				305	241	229
Sec-24				356	229	229
Sec-25	LM6	615	797	102	267	267
Sec-26				152	267	254
Sec-27				203	254	254
Sec-28				254	254	241
Sec-29				305	241	229
Sec-30				356	241	229
Sec-31	LM9	701	824	102	267	267
Sec-32				152	267	254
Sec-33				203	254	254
Sec-34				254	254	247 *
Sec-35				305	241	241
Sec-36				356	241	229

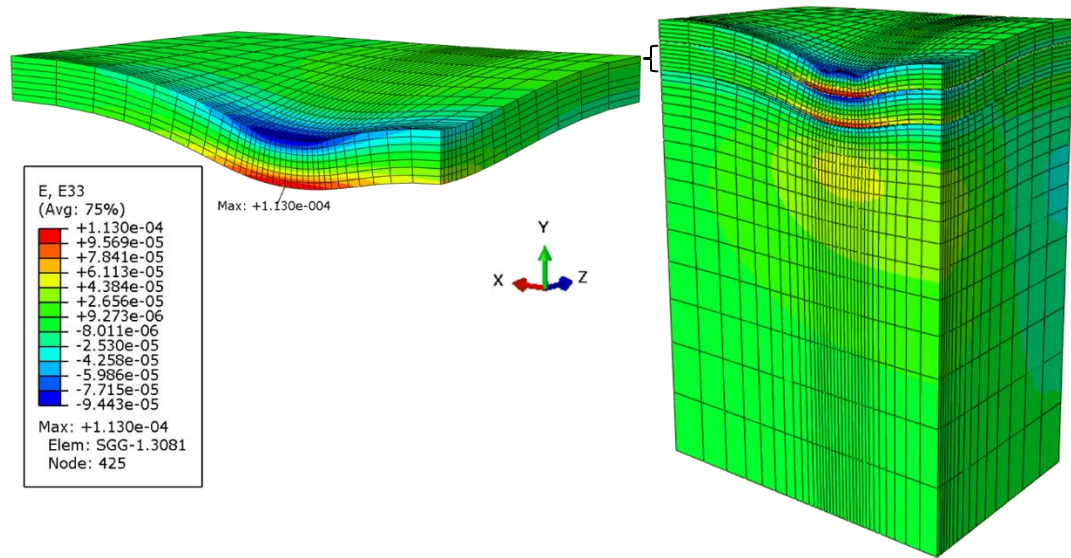
\* Fatigue Failure of the CSS Layer is Critical



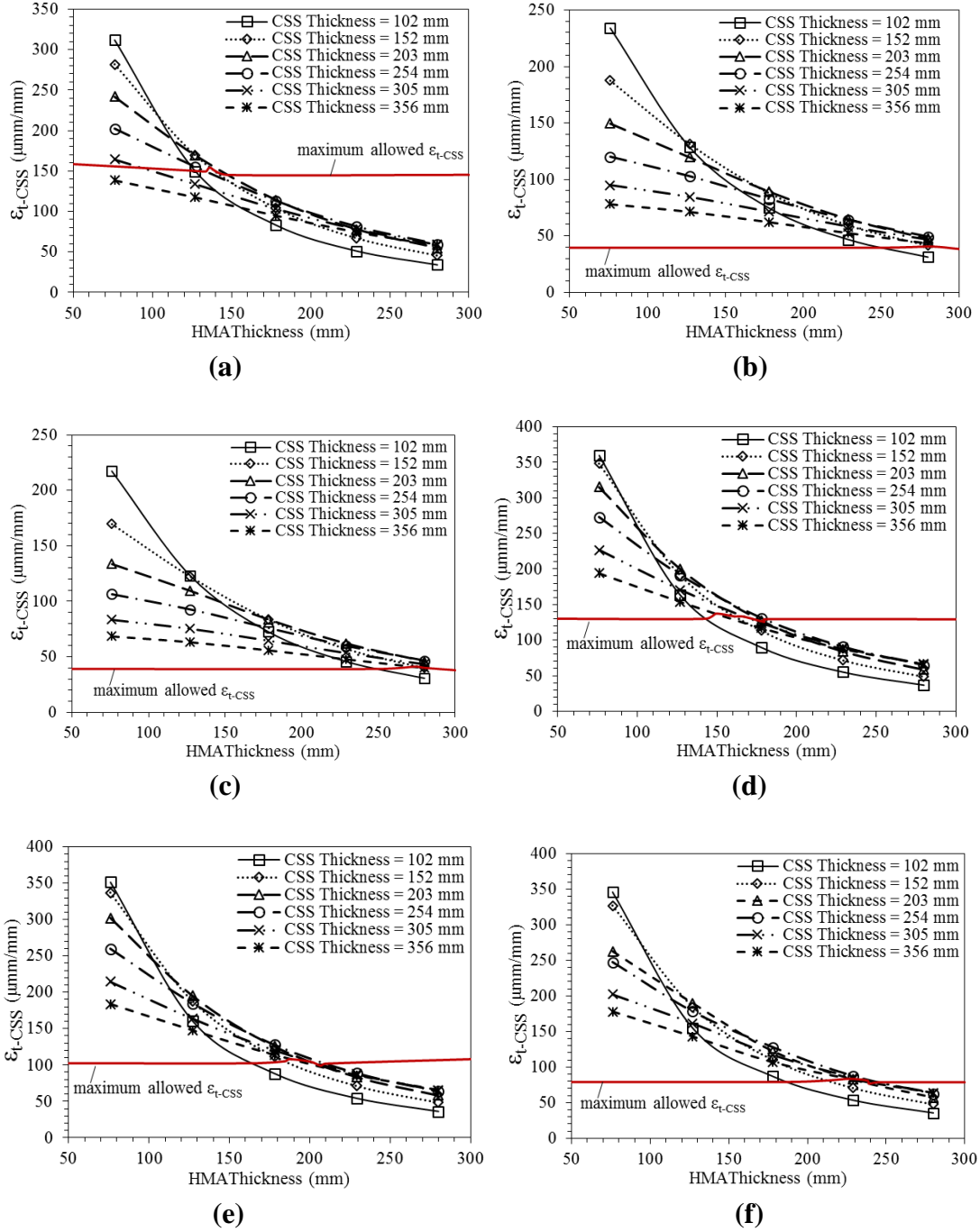
**Figure 6.1 Dimensions and Mesh of the 3-D Finite Element Model of Semi Rigid Pavement Structure**



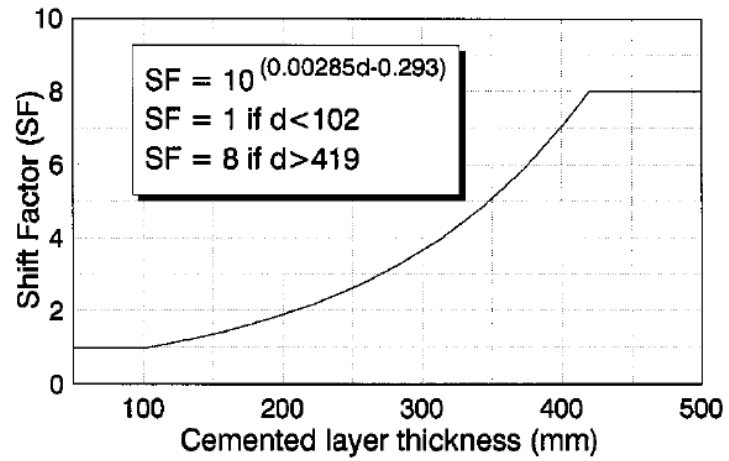
**Figure 6.2 Standard Axle Load Application and Configuration of the Tire Contact Area**



**Figure 6.3 Deformed Shape of the Pavement Structure and the CSS Layer**



**Figure 6.4 Variation of  $\epsilon_{t-CSS}$  for Different Thicknesses for HMA and CSS Layers with (a) CKD5, (b) CKD10, (c) CKD15, (d) LM3, (e) LM6, and (f) LM9 Material for CSS**



**Figure 6.5 Fatigue Crack Propagation Shift Factor for CSS Layer (Theyse et al., 1996)**

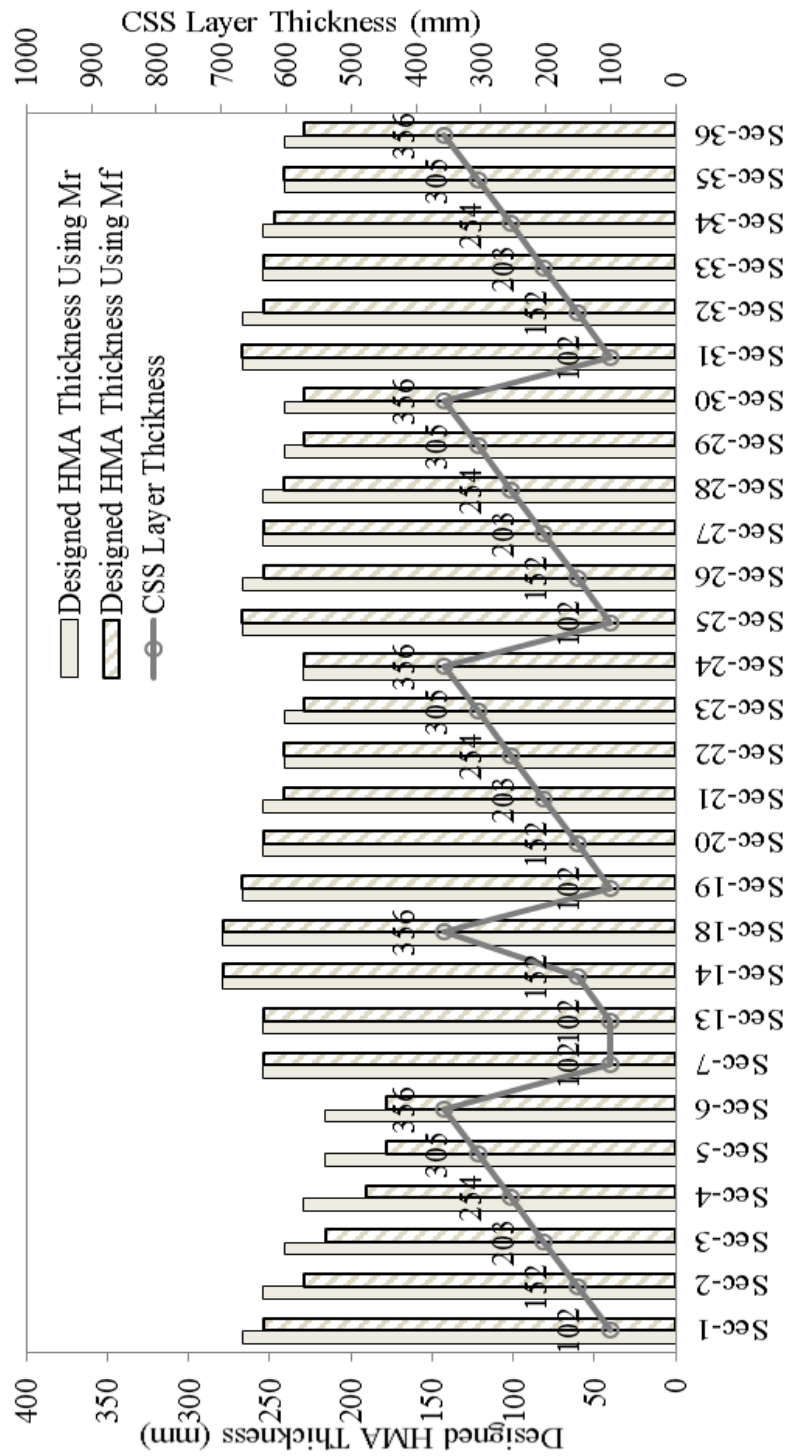
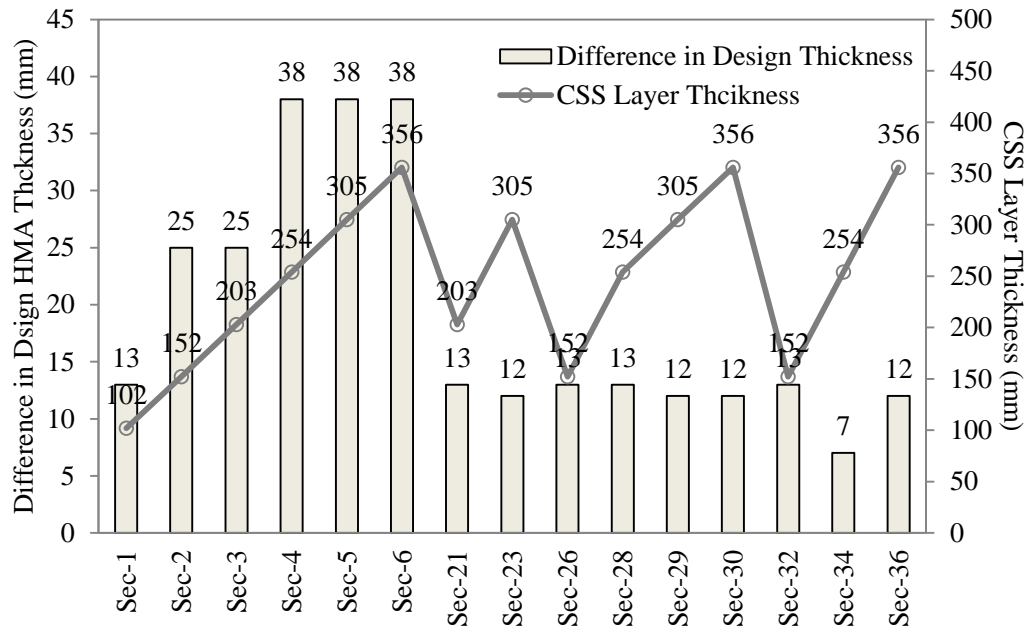


Figure 6.6 Designed HMA Layer Thicknesses for Different Pavement Sections



**Figure 6.7 Influence of Using  $M_f$  on Reduction of the Designed HMA Layer Thickness**



## CHAPTER 7

### SUMMARY, CONCLUSIONS, AND RECOMMENDATIONS

#### 7.1 Summary

During the construction of the pavement layers, the last occasion of increasing the chemically-stabilized subgrade quality (specifically, the modulus) is roller compaction. The Intelligent Compaction technologies are able to monitor the quality of compaction during the construction of the subgrade and assess the quality of the entire compacted area. One of the objectives of this study was to investigate the ability of the Intelligent Compaction Analyzer (ICA), developed at the University of Oklahoma, in quality control and quality improvement of CSS layers supporting asphalt pavements. The investigation consisted of four case studies associated with four different pavement construction projects in Oklahoma involving compaction of stabilized subgrades. The soils and additives, i.e. cement kiln dust (CKD) and lime were collected from the construction sites and laboratory  $M_r$  tests at different curing periods were conducted on the soil-additive mixtures. Using the test results regression models were developed to estimate the  $M_r$  of each soil-additive mixture based on moisture content and dry unit weight. The developed regression models for calibrating and/or validating ICA-estimated moduli could predict the  $M_r$  of the stabilized subgrade with an error ranged between  $\pm 15\%$  and  $\pm 25\%$  for different case studies.

The developed regression models for resilient modulus were used to calibrate and validate the ICA-estimated modulus during compaction of the CSS in the field. For this reason, field investigations such as nuclear density gauge (NDG), Dynamic Cone

Penetrometer (DCP) and Falling Weight Deflectometer (FWD) measurements, were conducted on the four construction projects. Also, for each construction project, the stabilized subgrade was compacted using ICA-equipped smooth drum roller, and the ICA-estimated moduli through the construction stretch were recorded. The validity of the ICA-estimated moduli was evaluated in accordance with the laboratory developed regression models and/or other in-situ tests (i.e., DCP and FWD tests). Results from these case studies show that the ICA could detect changes in stiffness in real-time, during the compaction of the CSS. The ICA was able to estimate the modulus of the stabilized subgrade with accuracy suitable for the control of compaction quality. Additionally, the ICA could be used to identify and remedy under-compacted regions during the construction of pavements. It was also found that the average subgrade modulus and overall uniformity of compaction could be improved with the use of the ICA.

Another objective of this study was to evaluate the important flexural properties, such as flexural modulus and fatigue life, of the chemically-stabilized soil. Also, the influence of considering these flexural properties on the overall design of the semi-rigid pavements using M-EPDG method was aimed to be studied. Despite various advantages of chemical stabilization, it can negatively affect the long-term performance of the pavement, in an overall sense. Without a good understanding of the flexural behavior of chemically-stabilized subgrade under vehicular traffic loading, it may result in a premature fatigue failure of the CSS layer and reflective cracking in the asphalt layers. To address these concerns, specimens of a lean clay soil mixed with different types and amounts of additive (5%, 10% and 15% CKD, and 3%, 6% and 9% lime), were prepared. Unconfined compressive strength (UCS) and resilient modulus tests on cylindrical specimens, and

modulus of rupture (MoR), flexural modulus and four point flexural fatigue (FPFF) tests on beam specimens were conducted. For flexural tests, the Euler-Bernoulli beam theory was used to determine the stress-strain behavior of the beams. The tested mixtures found to have relatively higher flexural moduli than their corresponding resilient moduli. Increasing additive amounts had a negative effect on fatigue performance of the stabilized subgrade soil, in general. Lightly-stabilized specimens showed the highest fatigue life among different mixtures.

In addition, the applicability of the Euler-Bernoulli beam theory in estimating the flexural characteristics of the chemically-stabilized beams was evaluated by creating three-dimensional finite element models of MoR and FPFF tests. The Euler-Bernoulli beam theory was found to have an acceptable accuracy in estimating the tensile strains at the bottom of the beam during these two tests.

Another important aspect of this study was to study the effect of considering the flexural properties and fatigue life of CSS layer on the designed hot mix asphalt (HMA) layer thickness in a semi-rigid pavement using M-EPDG method. Three-dimensional finite element models of different pavement sections under a standard 80 kN single axle load were developed. The thicknesses of hot mix asphalt (HMA) and CSS layers, and the material used for CSS layer were varied for different sections. The minimum required thickness of HMA layer to avoid fatigue failure of the CSS layer was determined for different sections using the finite element analyses and the developed fatigue life prediction model. The final thickness of the HMA layer was designed using M-EPDG software, namely AASHTOWare Pavement M-E Design. For each section, the M-EPDG analyses were conducted using both resilient modulus and flexural modulus for the CSS

layer. The results showed that for the CSS materials with relatively low fatigue lives, the fatigue cracking of the CSS layer was the most critical distress to be considered in designing of the pavement's structure. One of the most significant findings of this study was that by substituting the CSS resilient modulus with the properly determined flexural modulus in the mechanistic-empirical design procedure, the designed HMA thickness, and consequently, the construction cost could significantly decrease. It is important to note that the results discussed in this study are based on flexural laboratory tests on one soil type (lean clay soil) stabilized with chemical additives. Hence, different results can be obtained for other types of soil and additives. Also, effect of environmental conditions (e.g., wet-dry and freeze-thaw cycles, and seasonal variations of moisture) on the fatigue life of the CSS was not considered in this study. Consideration of durability on  $M_r$  and  $M_f$  is important in designing pavements, to account for field conditions.

## **7.2 Conclusions**

The major findings of this study and recommendations for future works are summarized in this chapter. Specific conclusions pertaining to a given topic covered in a given chapter were presented in that chapter. Based on the observations from this study, the following conclusions were made:

### ***7.2.1 Regression Models for $M_r$***

1. The specimens with higher degree of saturation (higher than 83%), i.e., specimens with high moisture content and high degree of compaction, showed lower  $M_{r-0}$  compared to other specimens. This could be attributed to build-up of

pore water pressure in the specimen testing and reduction in effective stress during  $M_{r-0}$ .

2. The increase in resilient modulus after 28 days of curing period was significant for the specimens with higher degree of saturation (higher than 83%). A  $r_{28}$  ratio of 38 was observed for the specimens with a degree of saturation of 87% for CS3. This could be attributed to the low  $M_{r-0}$  values due to creation of pore water pressure during  $M_{r-0}$  tests, and thixotropic effect during 28 days of curing.
3. The developed regression models for calibrating and/or validating ICA-estimated moduli could predict the  $M_{r-0}$  of the stabilized subgrade with an error ranged between  $\pm 15\%$  and  $\pm 25\%$  for different case studies. Also, the  $M_{r-28}$  values could be predicted within  $\pm 15\%$  of error range for all of the case studies. The developed regression models for resilient modulus were used to calibrate and validate the ICA-estimated modulus during compaction of the CSS in the field.
4. The  $M_{r-0}$  to  $M_{r-28}$  conversion relationships (using  $r_{28}$  ratio) could successfully convert  $M_{r-28}$  to  $M_{r-0}$  with an error ranged between  $\pm 12\%$ , and  $\pm 20\%$  for different case studies. Also, the conversion model for  $M_{r-7}$  to  $M_{r-0}$  predicted the  $M_{r-0}$  with and less than  $\pm 20\%$  error. These conversion relationships were aimed to be used for converting the ICA-estimated moduli to  $M_{r-28}$  and FWD moduli, and vice versa.
5. The resilient modulus of soil-CKD specimens using basic properties of the soil-CKD mixture could be predicted by developing a generic regression model. Majority of the estimated data points were within  $\pm 25\%$  error lines ( $R^2 = 0.72$ ).

Using this model the resilient modulus of fine grained soil stabilized with different amounts of CKD could be predicted for different moisture contents and dry unit weights.

### ***7.2.2 Calibration and Validation of ICA***

1. The ICA could detect changes in stiffness in real-time, during the compaction of the chemically-stabilized subgrade. Also, the variation in the degree of compaction between different test stations captured by ICA and NDG were in agreement in most of the test stations.
2. ICA was able to estimate the modulus of the stabilized subgrade with accuracy suitable for the control of compaction quality. The ICA could estimate the moduli of the subgrade with an error less than  $\pm 25\%$  compared to laboratory results, and with a coefficient of determination ranged between 0.55 and 0.67 for different case studies.
3. The ICA could be validated with the DCP and FWD measurements. It was observed that for CS1, the ICA-estimated subgrade modulus and FWD modulus have a good correlation ( $R^2 = 0.63$ ). Also, for CS4, the linear correlation between  $M_{ICA}$  and inverse of DPI had a  $R^2$  of 0.63.
4. The ICA could be used to identify and remedy under-compacted regions during the construction of pavements. In CS3 and CS4, it was shown that the average modulus of the entire subgrade could be improved. The level of compaction in the entire project stretch was also more uniform when the ICA compaction procedure was followed. For CS3 the coefficient of variation in modulus reduced from 7.4% to 4.6% due to remedial compaction.

5. For the regions at which more remedial VSDR passes were conducted the improvement in ICA-estimated moduli was more significant. For the sections where four additional VSDR passes were conducted the range of degree of compaction was significantly improved from 82.5%-93.1% to 87.0%-98.1%.

### ***7.2.3 Flexural Properties of Chemically-Stabilized Soil***

1. The flexural strength and flexural modulus of the chemically-stabilized soil increased due to an increase in the amount of additive. The increase was more significant for CKD-stabilized soil compared to lime-stabilized soil. The increase in flexural strength was around 94% by increasing the CKD content from 5% to 10%.
2. Generally, the strain at failure reduced by adding more additives with an exception for specimens stabilized with 10% CKD, which had the lowest strain at failure among the CKD-stabilized mixtures. The CKD5 specimens showed the highest tensile strain at failure among CKD-stabilized specimens. For the lime-stabilized specimens the tensile strain at failure decreased almost linearly by increasing the lime content from 3% to 9%.
3. All soil-additive mixtures found to have relatively higher flexural moduli (at a strain level of 200  $\mu\text{mm/mm}$ ) than their corresponding resilient moduli (at  $\sigma_d = 68.9 \text{ kPa}$  and  $\sigma_3 = 13.8 \text{ kPa}$ ). The flexural modulus values were aimed to be used as a substitute for resilient modulus of CSS layer in a semi-rigid pavement for designing using the M-EPDG method.

4. Increasing additive amounts had a negative effect on fatigue performance of the stabilized subgrade soil, in general. Lightly-stabilized specimens showed the highest fatigue life among different mixtures.
5. Strain in failure played a key role in the fatigue performance of the stabilized soil. For a specific additive type, mixtures with the highest strain at failure (CKD5 and LM3) possess the highest fatigue life. On the other hand, specimens with the lowest strain at failure in UCS and MoR tests (CKD10 and LM9 mixtures) failed at the beginning of the FPF test, due to increased brittleness.
6. The developed fatigue life prediction model could predict the fatigue life of the mixtures reported in the literature with a good accuracy ( $R^2 = 0.60$ ), compared to the proposed models in the previous studies. The developed model was aimed to be used for considering the fatigue life of CSS layer in designing a semi-rigid pavement using M-EPDG method.

#### ***7.2.4 Finite Element Model of Laboratory Tests***

1. The stress-strain curves produced by the finite element models were consistent with those of the experimental results for UCS and MoR tests. Consequently, the UCS and MoR tests for different chemically-stabilized soils could successfully simulated by using concrete damage plasticity material model.
2. According to the FE model, the Euler-Bernoulli beam theory was found to have a reasonable accuracy in calculation of the strain at the bottom of the chemically-stabilized beams in MoR test. The vertical displacements of the beam's mid-height achieved from FE analyses and experimental MoR tests had an difference between 7.2% and 18.8%.



3. The stress-strain curves of the MoR tests showed a linear behavior for the material before cracking of the beam. Hence, a linear-elastic behavior could be assumed for the beginning (first 50 load cycles) of the FPFF tests which have a relatively small induced strain level at the bottom of the beam (200  $\mu\text{mm/mm}$ ).
4. The vertical displacements of the beam's mid-height achieved from FE analyses and experimental FPFF tests had an insignificant difference (1.2% to 5.2%). Hence, the Euler-Bernoulli beam theory was found to have a higher accuracy in estimating the tensile strains at the bottom of the beam when a FPFF test fixture was used.

#### ***7.2.5 M-EPDG Analysis of Semi-Rigid Pavement***

1. The fatigue susceptibility of the CSS layer reduced by an increase in the HMA thickness. This is due to the fact that the traffic-induced tensile strain at the bottom of the CSS layer ( $\epsilon_{t-CSS}$ ) reduces by an increase in the thickness of the HMA layer. Also, for the sections with thinner HMA layers an increase in CSS thickness resulted in a lower  $\epsilon_{t-CSS}$  value.
2. The tensile strain at the bottom of the CSS layer was found to decrease with an increase in the flexural modulus of the CSS layer. The highest strain (359.6  $\mu\text{mm/mm}$ ) was observed for the pavement section with the thinnest HMA and CSS layers (76 and 102 mm, respectively) and the lowest CSS layer modulus (728 MPa).
3. For the CSS materials with relatively low fatigue lives (CKD10 and CKD15), the fatigue cracking of the CSS layer was the most critical distress to be considered in designing of the pavement's structure. Consequently, using these

mixtures as the CSS layer of the semi-rigid pavements is not recommended, since it was found to result in a very high, and not economically feasible, values for  $H_{HMA-min}$ .

4. For the CSS materials that exhibited higher fatigue lives in the laboratory (CKD5, LM3 and LM6), other pavement distresses, such as rutting, bottom-up and top-down cracking, transverse cracking and IRI (analyzed using M-EPDG method), were critical for the pavement design. The sections with these materials were less prone to CSS fatigue failure and had relatively low  $H_{HMA-min}$  values.
5. By substituting the CSS resilient modulus with the properly determined flexural modulus in the M-E design procedure, the designed HMA thickness, and consequently, the construction cost could significantly decrease. The difference between  $M_r$ -designed and  $M_f$ -designed HMA thicknesses was more significant when difference between  $M_r$  and  $M_f$  of the CSS material was larger.

### 7.3 Recommendations

Based on the observations from this study, the following recommendations are made for future studies:

1. As it was indicated in this study, the ICA-estimated moduli could be validated with in-situ tests such as FWD and DCP. However, due to field conditions and limitations each of these two tests could be conducted properly for only one project. Further studies may be undertaken to compare the ICA-estimated moduli with results of FWD and DCP tests for chemically-stabilized subgrades.

2. ICA technology shall be demonstrated on more construction sites varying with soil type, additive type and additive percentage to study the influence of these parameters on the ICA-estimated moduli.
3. Research studies shall be carried out to study the long-term benefits of the Intelligent Compaction.
4. The influence of wet-dry and freeze-thaw cycles as well as seasonal variations of moisture on the flexural performance of chemically-stabilized soil may be studied in the laboratory. Specifically, the influence of these environmental conditions on the flexural modulus and fatigue life of the beam specimens shall be investigated.
5. Further M-EPDG analyses for other types of soil and additive need to be conducted on semi-rigid pavement sections using laboratory evaluated flexural modulus and by considering CSS fatigue life. For these materials the influence of selecting flexural modulus rather than resilient modulus for the CSS layer on the overall design thicknesses and construction costs must be investigated.
6. Although the flexural modulus values for the soil-CKD and soil-lime mixtures considered here were found to be higher than the corresponding resilient modulus values, it may not be the case for other soil types mixed with chemical additives. It is recommended that similar comparisons be made between resilient modulus and flexural modulus of other soil types mixed with chemical additives.

7. In this study a generic model for estimating the resilient modulus of the CKD-stabilized soil based on physical properties of the mixture was developed. It is recommended that similar models be developed for soils stabilized with other types of stabilizing agent, such as lime, cement and CFA.
8. The influence of applied strain rate on the flexural modulus of chemically-stabilized beam may be evaluated by conducting FPF tests with different loading frequencies.
9. In this study the developed strain-based model for predicting the flexural fatigue of soil-additive mixture was achieved using a constant tensile strain of  $200 \mu\text{m}/\text{mm}$  for all of the mixtures. It is recommended that the accuracy of the model be modified by conducting FPF tests with other values for the induced tensile strain.
10. Due to limitations of CDP model in simulating high cycle fatigue, this model could not be applied for finite element simulation of fatigue cracking of the chemically-stabilized beams. It is recommended that the fatigue cracking of the stabilized beam be modeled using damage mechanics.
11. It is recommended to investigate the influence of specimen geometry on the propagation of stresses/strains in the specimen using parametric finite element analyses of MoR and FPF tests on beams with different geometries.
12. It is recommended that the induced shear stresses in the CSS layer of an actual pavement structure under traffic loads be evaluated. Also, the influence of these shear stresses on the flexural performance of the CSS layer be studied using Timoshenko beam theory.

## REFERENCES

1. AASHTO (1972). "Interim Guide for Design of Pavement Structures." American Association of State Highway and Transportation Officials, Washington, D.C.
2. AASHTO (1986). "Guide for Design of Pavement Structures." American Association of State Highway and Transportation Officials, Washington, D.C.
3. AASHTO (1993). "Guide for Design of Pavement Structures." Transportation Research Board, National Research Council, Washington, D.C.
4. AASHTO (2002). Guide for the Design of New and Rehabilitated Pavement Structures. National Cooperative Highway Research Program, AASHTO NCHRP Project 1-37A. American Association of State Highway and Transportation Officials (AASHTO), Washington, D.C.
5. AASHTO (2004). "Distribution of the Recommended Mechanistic-Empirical Pavement Design Guide (NCHRP Project 1-37A)." Memo to Interested Reviewers.
6. AASHTO (2004). "Guide for Mechanistic-Empirical Design of New and Rehabilitated Pavement Structures." Final Report prepared for National Cooperative Highway Research Program (NCHRP), Transportation Research Board, National Research Council, Washington D.C.
7. AASHTO (2008). "Mechanistic-Empirical Pavement Design Guide: A Manual of Practice." AASHTO Designation: MEPDG. Washington, D.C.
8. AASHTO M145 (2000). "Classification of Soils and Soil-Aggregate Mixtures for Highway Construction Purposes." American Association of State Highway and Transportation Officials, Washington D.C.
9. AASHTOWare Climatic Data (2016). "AASHTOWare Pavement ME Design - Climatic Data.", August 24, 2016, <http://www.me-design.com/MEDesign/ClimaticData.html>
10. Achampong, F., Usmen, M., and Kagawat, T. (1997). "Evaluation of Resilient Modulus for Lime and Cement-Stabilized Synthetic Cohesive Soils." Transportation Research Record: Journal of the Transportation Research Board, Vol. 1589, pp. 70 – 75.
11. Adedimila, A. S., and Kennedy, T. W. (1974). "Fatigue and Resilient Characteristics of Asphalt Mixtures by Repeated-Load Indirect Tensile Test." Research Report 183-5, Texas State Department of Highways and Public Transportation, Texas.

12. Ahnberg, H. (2006). "Strength of Stabilised Soil- A Laboratory Study on Clays and Organic Soils Stabilised with different Types of Binder" Doctoral dissertation, Lund University, Sweden.
13. Allen, D. L., Barrett, M. L., Graves, R. C., Pigman, J. G., Abu-Lebdeh, G., Aultman-Hall, L. and Bowling, S. T. (2001). "Analysis of Traffic Growth Rates." Report No. KTC-01-15/SPR213-00-1F.
14. Amber, Y., and Quintus, H. (2002). "Study of LTPP Laboratory Resilient Modulus Test Data and Response Characteristics." Final Report. FHWA-RD-02-051), USDOT, FHWA.
15. Amarsinh, L. and Shrinivas, P.P., Soil Stabilization Using Soil ISOMORPHISM.
16. AMMANN. "Ammann Compaction Expert." AMMANN, Switzerland. <<http://www.ammann-group.com/en/home/technology/intelligent-ground-compaction/>> (Jul. 21, 2013).
17. Andrei, D., Witczak, M. W., Schwartz, C. W., and Uzan, J. (2004). "Harmonized Resilient Modulus Test Method for Unbound Pavement Materials." Transportation Research Record: Journal of the Transportation Research Board, Vol. 1874, pp. 29-37.
18. Ansari, M. A., Noor, M. A., and Islam, M. (2007). "Effect of Fly Ash Stabilization on Geotechnical Properties of Chittagong Coastal Soil." Modeling and Analysis Solid Mechanics and Its Applications, Vol. 146, pp. 443-454.
19. Ansary, M. A., and Hasan, K. A. (2011). "Lime Stabilization on Soil of a Selected Reclaimed Site of Dhaka City." Journal of Geotechnical Engineering, 1(1), pp. 1-6.
20. ARA Inc. (2004). "Guide for Mechanistic-Empirical Design of New and Rehabilitated Pavement Structures." NCHRP Project 1-37A, prepared for National Cooperative Highway Research Program, Washington D.C.
21. Arnold, G., Morkel, C. and van der Weshuizen, G. (2012). "Development of Tensile Fatigue Criteria for Bound Materials." (No. 463), Vancouver.
22. Arellano, D., and Thompson, M. R. (1998). "Stabilized Base Properties (Strength, Modulus, Fatigue) for Mechanistic-Based Airport Pavement Design." Final Report, COE Report No. 4, Center of Excellence for Airport Pavement Research, University of Illinois, Urbana, Illinois.
23. ASTM (1963). "A Guide for Fatigue Testing and the Statistical Analysis of Fatigue Data." STP No. 91-A, Philadelphia.
24. ASTM Standard D1635 (2012). "Standard Test Method for Flexural Strength of Soil-Cement Using Simple Beam with Third-Point Loading." ASTM International, West Conshohocken, PA, DOI: 10.1520/D1635\_D1635M-12, [www.astm.org](http://www.astm.org).

25. ASTM D2487. (2011) "Standard Practice for Classification of Soils for Engineering Purposes (Unified Soil Classification System)." West Conshohocken, PA.
26. ASTM D422. (2007). "Standard Test Method for Particle-Size Analysis of Soils." West Conshohocken, PA.
27. ASTM D4318. (2010). "Standard Test Methods for Liquid Limit, Plastic Limit, and Plasticity Index of Soils." West Conshohocken, PA.
28. ASTM Standard D4609 (2008). "Standard Guide for Evaluating Effectiveness of Admixtures for Soil Stabilization." ASTM International, West Conshohocken, PA, DOI: 10.1520/D4609-08, [www.astm.org](http://www.astm.org).
29. ASTM Standard D6276 (2006). "Standard Test Method for Using pH to Estimate the Soil-Lime Proportion Requirement for Soil Stabilization." ASTM International, West Conshohocken, PA, DOI: 10.1520/D6276-99AR06E01, [www.astm.org](http://www.astm.org).
30. ASTM D698. (2012) "Standard Test Methods for Laboratory Compaction Characteristics of Soil Using Standard Effort." West Conshohocken, PA.
31. ASTM D854. (2010). "Standard Test Methods for Specific Gravity of Soil Solids by Water Pycnometer." West Conshohocken, PA.
32. Austroads (2004). "Pavement design", A Guide to the Structural Design of Road Pavements. Austroads, Australia.
33. Balbo, J. T., and Cintra, J. P. (1996). "Fatigue Verification Criteria for Semi-Rigid Pavements." In 2nd National Conference on Asphalt Mixtures and Pavements, Thessaloniki, Greece.
34. Bari, J., and Witczak, M. (2006). "Development of a New Revised Version of the Witczak E\* Predictive Model for Hot Mix Asphalt Mixtures (with discussion)." Journal of the Association of Asphalt Paving Technologists, 75, pp. 381–417.
35. Barksdale, R. D. (1991). "Fabrics in Asphalt Overlays and Pavement Maintenance." NCHRP Synthesis of Highway Practice, No. 171, Transportation Research Board, Washington D.C.
36. Barman, M., Imran, S. A., Nazari, M., Commuri, S. and Zaman, M. (2015). "Intelligent Compaction of Stabilized Subgrade of Flexible Pavement." In IFCEE 2015.
37. Barman, M., Nazari, M., Imran, S. A., Commuri, S. and Zaman, M. (2016). "Quality Improvement of Subgrade through Intelligent Compaction. In Transportation." Research Board 95th Annual Meeting No. 16-4340.
38. Barman, M., Nazari, M., Imran, S. A., Commuri, S., Zaman, M., Beainy, F. and Singh, D. (2014). "Application of Intelligent Compaction Technique in Real-Time

Evaluation of Compaction Level during Construction of Subgrade.” In Transportation Research Board 93rd Annual Meeting (No. 14-5183).

39. Barman, M., Nazari, M., Imran, S.A., Commuri, S., Zaman, M., Beainy, F. and Singh, D. (2016). “Quality Control of Subgrade Soil Using Intelligent Compaction.” Innovative Infrastructure Solutions, Vol. 1, No. 1, p.23.
40. Baus, R. L., and Stires, N. R. (2010). “Mechanistic-Empirical Pavement Design Guide Implementation.” Report No. GT06-10, Department of Civil and Environmental Engineering, University of South Carolina, South Carolina.
41. Bhattacharya, P. G., and Pandey, B. B. (1986). “Flexural Fatigue Strength of Lime-Laterite Soil Mixtures.” Transportation Research Record: Journal of the Transportation Research Board, Vol. 1089, pp. 86-92.
42. BOMAG. “Systems for soil and asphalt compaction- Variocontrol.” BOMAG, Boppard, Germany. <<http://www.bomag.com/world/en/variocontrol.htm>> (Jul. 21, 2013).
43. Burnham, T. R. (1997). "Application of Dynamic Cone Penetrometer to Minnesota Department of Transportation Pavement Assessment Procedures." No. MN/RC-97/19.
44. Butalia, T. S., Huang, J., Kim, D. G., and Croft, F. (2003). “Effect of Moisture Content and Pore Water Pressure Build on Resilient Modulus of Cohesive Soils.” Resilient Modulus Testing for Pavement Components, ASTM STP 1437.
45. Camargo, F., Larsen, B., Chadbourn, B., Roberson, R., and Siekmeier, J. (2006). “Intelligent Compaction: A Minnesota Case History.” Proc., 54th Annual University of Minnesota Geotechnical Conf., St. Paul, Minnesota.
46. Carmichael, R. F., and Stuart, E. (1985). “Predicting Resilient Modulus: A Study To Determine The Mechanical Properties of Subgrade Soils (Abridgment).” Transportation Research Record, (1043).
47. Casmer, J. D. (2011). “Fatigue Cracking of Cementitiously Stabilized Pavement Layers Through Large-Scale Model Experiments.” MS Thesis, Geological Engineering, University of Wisconsin, Madison, Wisconsin.
48. Cebon, D. (1999). “Handbook of Vehicle-Road Interaction.” Swets and Zeilinger Publishers, Lisse, The Netherlands
49. Ceylan, H., Gopalakrishnan, K. and Kim, S. (2015). “Smart Airport Pavement Health Monitoring.” International Airport Review, Vol. 19, No. 3.
50. Charbit, B. (2009). “Numerical analysis of laterally loaded lime/cement columns”. Proceedings of 20th European Young Geotechnical Engineers Conference. 2010.



51. Chang, G., Xu, Q., Rutledge, J., and Garber, S. (2014). "A Study on Intelligent Compaction and In-Place Asphalt Density." Report No. FHWA-HIF-14-017.
52. Chang, G., Xu, Q., Rutledge, J., Horan, R., Michael, L., White, D., and Vennapusa, P. (2011). "Accelerated Implementation of Intelligent Compaction Technology for Embankment Subgrade Soils, Aggregate Base, and Asphalt Pavement Materials." FHWA-IF-12-002. Federal Highway Administration, Washington D.C.
53. Cleveland, G. S., Button, J. W., and Lytton, R. L. (2002). "Geosynthetics in Flexible and Rigid Pavement Overlay Systems to Reduce Reflection Cracking." No. FHWA/TX-02/1777-1, Texas Transportation Institute, Texas A & M University System, Chicago.
54. Commuri, S., Imran, S., Zaman, M., Barman, P. M. and Nazari, M. (2014). "Evaluation of Performance of Asphalt Pavements Constructed Using Intelligent Compaction Techniques." Final Report No. FHWA-OK-14-15.
55. Commuri, S., Mai, A. and Zaman, M. (2009). "Calibration Procedures for the Intelligent Asphalt Compaction Analyzer." Journal of Testing and Evaluation, Vol. 37, No. 5, pp.1-9.
56. Commuri, S., and Zaman, M. (2008). "A Novel Neural Network-Based Asphalt Compaction Analyzer." International Journal of Pavement Engineering, Vol. 9, No. 3, pp. 177-188.
57. Commuri, S., Zaman, M., Beainy, P.F., Singh, D., Nazari, M., Imran, S. and Barman, M. (2012). "Pavement Evaluation Using a Portable Lightweight Deflectometer." No. OTCREOS11. 1-14-F.
58. Das, B. M. (2008). "Advanced soil mechanics." 3<sup>rd</sup> Edition, CRC Press, Boca Raton, Florida.
59. Davis, H. E. (1964). "The Testing and Inspection of Engineering Materials." 3rd ed., 167592, McGraw-Hill, New York.
60. De Beer, M. (1986). "Behaviour of Cementitious Subbase Layers In Bitumen Base Road Structures." MS Thesis, University of Pretoria, South Africa.
61. De Borst, R. (2002). Fracture in Quasi-Brittle Materials: a Review of Continuum Damage-Based Approaches." Engineering Fracture Mechanics, 69(2), pp. 95-112.
62. Diefenderfer, S. D. (2010). "Analysis of the Mechanistic-Empirical Pavement Design Guide Performance Predictions: Influence of Asphalt Material Input Properties." Report No. FHWA/VTRC 11-R3.
63. Drumm, E. C., Reeves, J. S., Madgett, M. R. and Trolinger, W. D. (1999). "Subgrade Resilient Modulus Correction for Saturation Effects-Closure".

64. Dynapac. "Dynapac Compaction Analyzer." Dynapac, Wardenburg, Germany. <[http://www.intelligentcompaction.com/downloads/presentation/Akesson\\_Dynapac%20I.pdf](http://www.intelligentcompaction.com/downloads/presentation/Akesson_Dynapac%20I.pdf)> (Jul. 21, 2013).
65. Ebrahimi, A., Kootstra, B. R., Edil, T. B. and Benson, C. H. (2012). "Practical Approach for Designing Flexible Pavements Using Recycled Roadway Materials as Base Course." *Road Materials and Pavement Design*, 13(4), pp.731-748.
66. Elliot RP, Thornton SI (1988). Resilient modulus and AASHTO pavement design. *Trans. Res. Record*.1192: 1-7.
67. Farrar, Michael J., and Turner J. P. (1991). "Resilient Modulus of Wyoming Subgrade Soils." Report No. MPC Report No. 91-1.
68. Foley, G., and Australian Stabilization Expert Group (2001). "Mechanistic Design Issues for Stabilized Pavement Materials." Contract report, AUSTROADS, Rc91022-3.
69. Francken, L., Beuving, E. and Molenaar, A. A. A. (1996), "Reflective Cracking in Pavements: Design and Performance of Overlay Systems." Proceedings of the third international RILEM conference, Maastricht, Netherlands.
70. Freeme C. R., Maree, J. H., and Viljoen A. W. (1982). "Mechanistic Design of Asphalt Pavements and Verification Using the Heavy Vehicle Simulator." Proceedings of 5th Int. Conf. Structural Design of Asphalt Pavements, Ann Arbor, Vol. 1, pp. 156-73.
71. Ganju, E., Prezzi, M., Salgado, R., Siddiki, N. Z., and Sommer, K. (2015). "QA/QC of Subgrade and Embankment Construction: Technology Replacement and Updated Procedures." Report No.: FHWA/IN/JTRP-2015/01.
72. Gillespie, T.D. (1993). "Effects of Heavy-Vehicle Characteristics on Pavement Response and Performance." (No. 353). Transportation Research Board.
73. Gnanendran, C. T., and Piratheepan, J. (2008). "Characterization of a Lightly Stabilized Granular Material by Indirect Diametrical Tensile Testing." *International Journal of Pavement Engineering*, Vol. 9, No. 6, pp. 445-456.
74. Gomez, J. D. P. (2009). "Influence of Curing Time on the Resilient Modulus of Chemically Stabilized Soils." MS Thesis, University of Oklahoma, Norman, Oklahoma.
75. Hanley, H. J., Masad, E. A., Iyengar, S. R., Rodriguez, A. K., and Bazi, H. S. (2013). "Co-Polymer Soil Subgrade Binders." The Texas A&M University System, U.S. Patent Application 14/102,071.

76. Heersink, D. K., Furrer, R. and Mooney, M. A. (2013). "Intelligent Compaction and Quality Assurance of Roller Measurement Values utilizing Backfitting and Multiresolution Scale Space Analysis." arXiv preprint arXiv:1302.4631.
77. Hernando, D. and del Val, M. A. (2016). "Guidelines for the Design of Semi-Rigid Long-Life Pavements." *International Journal of Pavement Research and Technology*, Vol. 9, No. 2, pp.121-127.
78. Hicks, R. G., and Monismith, C. L. (1971). "Factors Influencing the Resilient Modulus of Granular Materials." *Highway Research Record* 345, HRB, National Research Council, Washington, D.C., pp. 14-31.
79. Highway Research Board (HRB) (1962). *The AASHO road test-Report 5-Pavement Research*. Special Report No. 61E.
80. Hoffman, O., Guzina, B. and Drescher, A. (2004). "Stiffness Estimates Using Portable Deflectometers." *Transportation Research Record*, 1869, Transportation Research Board, National Research Council, Washington D. C., pp. 59-66.
81. Holewinski, J. M., Soon, S., Drescher, A. and Stolarski, H. K. (2003). "Investigation of Factors Related to Surface-initiated Cracks in Flexible Pavements (Final Report)." University of Minnesota Department of Civil Engineering, Minnesota Department of Transportation.
82. Hossain, Z., Zaman, M., and Doiron, C. (2011). "Development of Flexible Pavement Database for Local Calibration of MEPDG." Final Report, SPR No. 2209, Oklahoma Department of Transportation, Planning and Research Division, Oklahoma.
83. Hu, W., Huang, B., Shu, X. and Woods, M. (2016). "Utilizing Intelligent Compaction Meter Values to Evaluate Construction Quality of Asphalt Pavement Layers." *Road Materials and Pavement Design*, pp.1-12.
84. Huang, Y. (2004). "Pavement Analysis and Design." 2nd Ed., Prentice-Hall, Inc., Upper Saddle River, New Jersey.
85. Hudson, W. R., and Kennedy, T. W. (1968). "Evaluation of Tensile Properties of Subbases for Use in New Rigid Pavement Design- An Indirect Tensile Test for Stabilized Materials." Research Report Number 98-1, Center for Highway Research the University of Texas, Austin, Texas.
86. Imran, S. A. (2016). "Modeling and Analysis of the Interaction between Roller Drum and Pavement Material during Compaction." PhD Dissertation. School of Electrical and Computer Engineering, University of Oklahoma, Oklahoma.
87. Jameson, G. W., Sharp, K. G., Yeo, R. (1992). "Cement-Treated Crushed Rock Pavement Fatigue Under Accelerated Loading: the Mulgrave (Victoria) ALF Trial, 1989/1991." Australian Road Research Board Report ARR 229. ARRB, Australia.

88. Jameson, G., and Sharp, K. G. (2004). "Technical Basis of Austroads Pavement Design Guide." Austroads Publication No. AP-T33/04, Austroads, Sydney, New South Wales, Australia.
89. Jitsangiam, P., Nusit, K., Chummuneerat, S., Chindaprasirt, P., and Pichayapan, P. (2016). "Fatigue Assessment of Cement-Treated Base for Roads: An Examination of Beam-Fatigue Tests." *J. Mater. Civ. Eng.* 10.1061/(ASCE)MT.1943-5533.0001601 , 04016095.
90. Kaplan, M. F. (1963). Strains and Stresses of Concrete at Initiation of Cracking near Failure." *ACI Journal, Proceedings* Vol. 60, No. 7, pp. 857-879.
91. Khattak, M., and Alrashidi, M. (2006). "Durability and Mechanistic Characteristics of Fiber Reinforced Soil- cement Mixtures." *International Journal of Pavement Engineering*, Vol. 7, No. 1, pp. 53-62.
92. Khoury, N. N., and Zaman, M. (2004). "Correlation among Resilient Modulus, Moisture Variation, and Soil Suction for Subgrade Soils." *Transportation Research Record*. 1874, Transportation Research Board, Washington, D.C., 99-107.
93. Khoury, N., and Zaman, M. M. (2007). "Durability of Stabilized Base Courses Subjected to Wet-Dry Cycles." *International Journal of Pavement Engineering*, Vol. 8, No. 4, pp. 265-276
94. Khoury, N., Brooks, R., Boeni, S. Y., and Yada, D. (2013). "Variation of Resilient Modulus, Strength, and Modulus of Elasticity of Stabilized Soils with Postcompaction Moisture Contents." *Journal of Materials in Civil Engineering*, Vol. 25, No. 2, pp. 160-166.
95. Kim, D., Kweon, G., and Lee, K. (2001). "Alternative Method of Determining Resilient Modulus of Subgrade Soils Using A Static Triaxial Test", *Canadian Geotechnical Journal*, Vol. 38, No. 1, pp. 107-116.
96. Kim, M., Tutumluer, E., and Kwon, J. (2009). "Nonlinear Pavement Foundation Modeling for Three-Dimensional Finite-Element Analysis of Flexible Pavements." *International Journal of Geomechanics*, Vol. 9, No. 5, pp.195-208.
97. Kumar, S.A., Aldouri, R., Nazarian, S. and Si, J., 2016. Accelerated assessment of quality of compacted geomaterials with intelligent compaction technology. *Construction and Building Materials*, 113, pp.824-834.
98. Laguros, J. G. (1965). "Lime-Stabilized Soil Properties and the Beam Action Hypothesis." *Highway Research Record*, Vol. 92, pp. 12-20.
99. Laguros, J. G. and Keshwarz, M. S. (1987). "Construction and Performance of the Stabilized Base Course on U. S. 77 Ponca City, Kay County." Report No. FHWA/OK 87(7), Oklahoma DOT Item Number 2128, Oklahoma City, Oklahoma.

100. Lambe, T. W., and Whitman, R. V. (1969). "Soil Mechanics." John Wiley and Sons, New York.
101. Lav, A. H., Lave, M. A., and Goktepe, A. B. (2006). "Analysis and Design of a Stabilized Fly Ash as Pavement Base Material." *Fuel*, Vol. 85, pp. 2359-2370.
102. Lenke, L. R., McKeen, R. G., and Grush, M. (2001). "Evaluation of a Mechanical Stiffness Gauge for Compaction Control of Granular Media." Report No. NM99MSC-07.2, New Mexico State Highway and Transportation Department, Albuquerque, New Mexico.
103. Lin, S., Ashlock, J. C., Kim, H., Nash, J., Lee, H. D., and Williams, R. C. (2015). "Assessment of Nondestructive Testing Technologies for Quality Control/Quality Assurance of Asphalt Mixtures-Tech Transfer Summary." InTrans Project Report No. 13-446.
104. Little, D. N. (1995). "Handbook for Stabilization of Pavement Subgrades and Base Courses with Lime." Kendall/Hunt Publishing Company, Iowa.
105. Little, D. N. (1996). "Evaluation of Resilient and Strength Properties of Lime-Stabilized Soils for the Denver, Colorado Area." Report for the Chemical Lime Company.
106. Little, D. N. (2000). "Evaluation of Structural Properties of Lime Stabilized Soils and Aggregates." Mixture Design and Testing Protocol for Lime Stabilized Soils, National Lime Association Report Vol. 3.
107. Little, D. N., and Nair, S. (2009). "Recommended Practice for Stabilization of Subgrade Soils and Base Materials." Final Report, NCHRP Project 20-07, Transportation Research Board of the National Academies, Washington, D.C.
108. Little, D. N., Males, E. H., Prusinski, J. R., and Stewart, B. (2000). "Cementitious Stabilization." 79th Millenium Rep. Series, Transportation Research Board, Washington, D.C.
109. Lotfi, H. and Witczak, M. W. (1982), "Dynamic Characterization of Cement-Treated Base/Subbase Materials", Presentation at the 1982 Annual Transportation Research Board Meeting, 30 pp.
110. Loulizi, A., Al-Qadi, I., Lahouar, S. and Freeman, T. (2002). "Measurement of Vertical Compressive Stress Pulse in Flexible Pavements: Representation for Dynamic Loading Tests." *Transportation Research Record: Journal of the Transportation Research Board*, (1816), pp.125-136.
111. Lu, Q., Zhang, Y., and Harvey, J. T. (2007). "Analysis of Truck Traffic Growth for the Mechanistic Empirical Pavement Design Guide." In Proc. TRB 2007 Annual Meeting.

112. Mallela, J., Quintus, H. V., and Smith, K. L. (2004). "Consideration of Lime-Stabilized Layers in Mechanistic-Empirical Pavement Design." Final Report submitted to the National Lime Association, Arlington, Virginia.
113. Mallela, J., Titus-Glover, L., Bhattacharya, B., Darter, M. and Von Quintus, H. (2014). "Idaho AASHTOWare Pavement ME Design User's Guide, Version 1.1." Report No. FHWA-ID/14-211B.
114. Mandal, T. (2013). "Fatigue Behavior and Modulus Growth of Cementitiously Stabilized Pavement Layers." MS Thesis, University of Wisconsin, Madison, Wisconsin.
115. Maser, K. R. (2003). "Non-Destructive Measurement of Pavement Layer Thickness." Final Report No. 65A0074.
116. Maupin, G. W. (2007). "Preliminary field investigation of intelligent compaction of hot-mix asphalt." Final Rep. No. VTRC-08-R7, Virginia Transportation Research Council, Virginia DOT, Charlottesville, VA.
117. McDonald, M., and Madanat, S. (2011). "Life-Cycle Cost Minimization and Sensitivity Analysis for Mechanistic-Empirical Pavement Design." Journal of Transportation Engineering, Vol. 138, No. 6, pp.706-713.
118. McKenzie, N., Coughlan, K., and Cresswell, H. (2002). "Soil Physical Measurement and Interpretation for Land Evaluation" Vol. 5. CSIRO Publishing., Australia.
119. McLean, D. B., and Monismith, C. L. (1974). "Estimation of Permanent Deformation in Asphalt Concrete Layers Due To Repeated Traffic Loading." Transportation research record, (510).
120. Miller, G. A. and Azad, S. (2000). "Influence of Soil Type on Stabilization with Cement Kiln Dust." Construction and Building Materials, Vol. 14, pp. 89-97.
121. Miller, G. A., and Martha, L. J. (2012). "Mineral Industry Surveys– Directory of Lime Plants in the United States in 2011." U.S. Geological Survey, U.S. Department of the Interior, Washington, D.C.
122. Miner, M. A. (1945). "Cumulative Damage in Fatigue." Journal of Applied Mechanics, Vol. 12, No. 3, pp. 159-164.
123. Mitchell, J. M., 1960. "Fundamental Aspects of Thixotropy in Soils." journal of the soil mechanics and foundations division, Vol. 86, No. 3, pp.19-52.
124. Mitchell, J. K., and Monismith, C. L. (1977). "A Thickness Design Procedure for Pavements with Cement Stabilized Bases and Thin Asphalt Surfacing." Volume I of proceedings of 4th International Conference on Structural Design of Asphalt Pavements, Ann Arbor, Michigan.

125. Mitchell, J. K., and Shen, C. K. (1967). "Soil-Cement Properties Determined by Repeated Loading in Relation to Bases for Flexible Pavements", Second International Conference on the Structural Design of Asphalt Pavements Proceedings, Ann Arbor, Michigan, pp. 427-452.
126. Mohammad, L., Huang, B., Puppala, A., and Allen, A. (1999). "Regression Model for Resilient Modulus of Subgrade Soils." Transportation Research Record: Journal of the Transportation Research Board, (1687), pp.47-54.
127. Molenaar, A. A. A. (1984). "Fatigue and Reflection Cracking Due to Traffic Loads." In Proceedings of Association of Asphalt Paving Technologists, Vol. 53-84, p. 440.
128. Molenaar, A. A. A. (2005). "Cohesive and Non-Cohesive Soils and Unbound Granular Material for Bases and Sub-Bases in Roads." Lecture notes CT4850, Part I. Delft University of Technology. Delft.
129. Molenaar, A. A. A., and Pu, B. (2008). "Prediction of Fatigue Cracking in Cement Treated Base Courses." Proceedings of 6th RILEM International Conference on Cracking in Pavements, pp. 191-199.
130. Mooney, M. A. and Rinehart, R. V. (2007). "Field Monitoring of Roller Vibration during Compaction of Subgrade Soil." Journal of Geotechnical and Geoenvironmental Engineering, Vol. 133, No. 3, pp. 257-265.
131. Mooney, M. A., Rinehart, R. V., Facas, N. W., Musimbi, O. M., White, D. J., and Vennapusa, P. K. (2011). "National Cooperative Highway Research Program (NCHRP) report 676: Intelligent Soil Compaction System." Final Report NCHRP 21-09 Intelligent Soil Compaction System (2006 to 2010).
132. Muhunthan, B., and Sariosseiri, F. (2008) "Interpretation of Geotechnical Properties of Cement Treated Soils", Research Report FHWA-DTFH61-05-C-00008, Compaction Control of Marginal Soils in Fills, Washington State Transportation Center (TRAC), Washington State University, USA.
133. Murakami, S. (2012). "Continuum Damage Mechanics. A Continuum Mechanics Approach to the Analysis of Damage and Fracture." Springer, Dordrecht.
134. Naik, R. T., Canpolat, F., and Chun, Y. (2003). "Uses of CKD Other than for Flue Gas Desulfurization." Report No. CBU-2003-35, A CBU Report for Holcim (US), the University Of Wisconsin, Milwaukee, Wisconsin.
135. NAPA (2001). "HMA Pavement Mix Type Selection Guide." Information Series 128. National Asphalt Pavement Association and FHWA.
136. Nazari, M., Ghabchi, R., Zaman, M., and Commuri, S. (2016). "Influence of Tensile Strain at Failure on Flexural Properties of a Cementitiously Stabilized Subgrade Soil." International Journal of Geomechanics, p. 04016057.

137. Nazarian, S., Yuan, D., and Williams, R. B. (2003). "A Simple Method for Determining Modulus of Base and Subgrade Materials." Proceedings of Symposium on Resilient Modulus Testing for Pavement Components, Salt Lake City, Utah, pp. 152-164.
138. NCHRP (1997). "Laboratory Determination of Resilient Modulus for Flexible Pavement Design." NCHRP Web Document 14 for Project 1-28, Transportation Research Board, Washington, DC.
139. ODOT (2009a). "Oklahoma DOT Materials Approved Products List– Cement Kiln Dust (CKD)." Materials and Testing e-Guide (702.03), <http://www.okladot.state.ok.us/materials/htm-smap/11062p-CKD.htm>. Last Accessed: September, 2013
140. ODOT (2009b). "OHD L-50: Soil Stabilization Mix Design Procedure." Oklahoma Highway Department Procedure, Oklahoma DOT, Last Accessed: December, 2013.
141. Oklahoma AADT Maps (2016). "Maps AADT - Annual Average Daily Traffic." August 03, 2016, <http://www.okladot.state.ok.us/Maps/aadt/index.htm>
142. Otte, E. (1972). "The Stress- Strain Properties of Cement- Treated Materials." MS Thesis, University of Pretoria, South Africa.
143. Otte, E. (1978). "A Structural Design Procedure for Cement- Treated Layers in Pavements." DSc Thesis, University of Pretoria, South Africa.
144. Otte, E., Savage, P. F., and Monismith, C. L. (1992). "Structural Design of Cemented Pavement Layers." Transportation Engineering Journal of ASCE, Vol. 108, TE4, pp.428-446.
145. Ozel, M. R. and Mohajerani, A. (2011). "Prediction of Subgrade Resilient Modulus for Flexible Pavement Design." Scientific Research and Essays, 6(21), pp.4567-4576.
146. Parisio, F., Samat, S., and Laloui, L. (2014). "An Elasto-Plastic-Damage Model for Quasi-Brittle Shales." In Proceedings of the 48th US Rock Mechanics/Geomechanics Symposium, No. EPFL-CONF-199463.
147. Parker, S. P. (1989), "McGraw-Hill Dictionary of Scientific and Technical Terms." The McGraw-Hill Companies, Inc., New York.
148. Parsons, R. L., Kneebone, E. and Milburn, J. P. (2004). "Use of Cement Kiln Dust for Subgrade Stabilization." Report No. KS-04-3, Kansas Department of Transportation.



149. Peng C., Decheng F., Ruxin J., and Yin Z. (2013). "Plastic Damage Model to Evaluate the Fracture Size of Semi-Rigid Base Pavement." *Research Journal of Applied Sciences, Engineering and Technology*, pp. 596-601.
150. Peng, Y., and He, Y. (2009). "Structural Characteristics of Cement-Stabilized Soil Bases with 3D Finite Element Method." *Frontiers of Architecture and Civil Engineering in China*, Vol. 3(4), pp. 428-434.
151. Peterfalvi, J., Primusz, P., Marko, G., Kisfaludi, B., and Kosztka, M. (2015). "Evaluation of the Effect of Lime-Stabilized Subgrade on the Performance of an Experimental Road Pavement." *Croatian journal of forest engineering*, Vol. 36, No. 2, pp. 269-282.
152. Peterson, P. L. (2005). "Continuous Compaction Control MnRoad Demonstration." Minnesota Department of Transportation, MN/RC – 2005-07.
153. Petry, T. M. and Little, D. N. (2002). "Review of Stabilization of Clays and Expansive Soils in Pavements and Lightly Loaded Structures– History, Practice, and Future." *Journal of Materials in Civil Engineering*, Vol. 14, No. 6, pp. 447-460.
154. Ping, W. V. and Ling, C. C. (2007). "Enhancement of Resilient Modulus Data for The Design of Pavement Structures in Florida." Report No. FL/DOT/RMC/BD-543-4.
155. Preteseille, M. and Lenoir, T. (2015). Mechanical fatigue behavior in treated/stabilized soils subjected to a uniaxial flexural test. *International Journal of Fatigue*, 77, pp.41-49.
156. Pretorius, P.C., and Monismith, C.L., 1972. Fatigue Crack Formation and Propagation in Pavements Containing Soil-Cement Bases. *Highway Research Record*, (407).
157. Porter, O. J. (1950). "Development of the Original Methods for Highway Design: Symposium on Development of CBR Flexible Pavement Design Method for Airfields." *Transactions, ASCE*, pp.461-467.
158. Proctor, R. R. (1933). "Fundamental principles of soil compaction." *Engineering News Record*, Vol. 111, No. 9, pp. 245-248.
159. Prusinski, J. R., and Bhattacharia, S. (1999). "Effectiveness of Portland Cement and Lime in Stabilizing Clay Soils." *Transportation Research Record: Journal of the Transportation Research Board*, Vol. 1632, pp. 215-227.
160. Pu, B. (2007). "Analysis of the Performance of Pavements with a Cement Treated Base." Master of Science Thesis Report, Delft University of Technology, Delft, Netherlands.

161. Puppala, A., Ramakrishna, A. and Hoyos, L. (2003). "Resilient Moduli of Treated Clays from Repeated Load Triaxial Test." *Transportation Research Record: Journal of the Transportation Research Board*, (1821), pp.68-74.
162. Qubain, B. S., Seksinsky, E. J., and Li, J. (2000). "Incorporating Subgrade Lime Stabilization into Pavement Design." *Transportation Research Record: Journal of the Transportation Research Board*, Vol. 1721, pp. 3-8.
163. Raad, L. (1985). "Behavior of Stabilized Layers Under Repeated Loads." *Transportation Research Record: Journal of the Transportation Research Board*, Vol. 1022, pp. 72-79.
164. Rada, C., Witczak, W. M. (1981). "Comprehensive Evaluation of Laboratory Resilient Moduli Results for Granular Material." *Transportation Research Record: Journal of the Transportation Research Board*, Vol. 810, pp. 23-33.
165. Rahim, A. M. and George, K. P. (2004). "Subgrade Soil Index Properties to Estimate Resilient Modulus." In *Proceedings 83th Annual Meeting of the Transportation Research Board*, CDROM.
166. Ramakrishna, A. M. (2002). "Evaluation of Resilient Moduli Characteristics of Chemically Treated Soil from North Texas." MS Thesis, University of Texas, Arlington, TX.
167. Refai, H., Bitar, N., Schettler, J., and Al Kalaa, O. (2014). "The Study of Vehicle Classification Equipment with Solutions to Improve Accuracy in Oklahoma" Report No. FHWA-OK-14-17.
168. ReliaSoft Corporation (2007). *Accelerated Life Testing Reference*, ReliaSoft Publishing, Tucson, Arizona.
169. Rodd, A. V., MacLeod, J. A., Warman, P. R., and McRae, K. B. (2004). "Surface Application of Cement Kiln Dust and Lime to Forages: Effect On Soil pH." *Canadian journal of soil science*, Vol. 84, No. 3, pp. 317-322.
170. Rodriguez, R. (2008). Engineering Behavior of Soft Clays Treated with Circulating Fluidized Bed Combustion Fly Ash." In *Masters Abstracts International*, Vol. 46, No. 04.
171. Sakai. "Compaction Information System."  
<<http://www.sakaiaamerica.com/technology/intelligent-compaction/>> (Jul. 21, 2013).
172. Sargand, S., Khoury, I., Gray, J., and Al-Jhayyish, A. (2014). "Incorporating Chemical Stabilization of the Subgrade in Pavement Design and Construction Practices." Final Report, Federal Highway Administration, No. FHWA/OH-2014/12, Washington D.C.

173. Santha, B. (1994). "Resilient Modulus of Subgrade Soils: Comparison of Two Constitutive Equations." *Transportation Research Record*, (1462).
174. Sarkar, G., Islam, M. R., Alamgir, M., and Rokonuzzaman, M. (2012). "Study on the Geotechnical Properties of Cement based Composite Fine-grained Soil." *International Journal of Advanced Structures and Geotechnical Engineering*, Vol. 1(2), pp.42-49.
175. Saxena, P., Tompkins, D., Khazanovich, L., and Balbo, J. (2010). "Evaluation of Characterization and Performance Modeling of Cementitiously Stabilized Layers in the Mechanistic-Empirical Pavement Design Guide." *Transportation Research Record: Journal of the Transportation Research Board*, (2186), pp.111-119.
176. Schwartz, C. W., and Carvalho, R. L. (2007). "The Complex Guiding the Simple: Enhancement of Mechanistic-Empirical Pavement Rutting Models Using Nonlinear Finite Element Analysis." In *Proceedings of the Advanced Characterization of Pavement and Soil Engineering Materials Conference*, pp. 441-449.
177. Sebesta, S., Scullion, T. and Estakhri, C.K. (2004). "Selection of Maintenance Repair Methods on Expansive Subgrades." Texas Transportation Institute, Texas A & M University System.
178. Seed, H. B., Mitchell, J. K. and Chan, C. K. (1962). "Studies of Swell and Swell Pressure Characteristics of Compacted Clays." *Highway Research Board Bulletin*, (313).
179. Selezneva, O. I., and Hallenbeck, M. (2013). "Long-Term Pavement Performance Pavement Loading User Guide (LTPP PLUG)." Federal Highway Administration, FHWA-HRT-13-089, Washington D.C.
180. Seng, S., and Tanaka, H. (2012). "Properties of Very Soft Clays: A Study of Thixotropic Hardening and Behavior under Low Consolidation Pressure." *Soils and Foundations*, Vol. 52, No. 2, pp.335-345.
181. Schaefer, V. R., White, D. J., Ceylan, H., and Stevens, L. J. (2008). "Design Guide for Improved Quality of Roadway Subgrades and Subbases." Iowa Highway Research Board (IHRB) Project TR-525.
182. Shalaby, A. and Fréchet, L. (2000). "Reflective Cracking on C-SHRP Long Term Pavement Performance Sites." *Proceedings of the RILEM fourth international conference on reflective cracking in pavements*, RILEM Publications, Ottawa, Canada, pp. 241–250.
183. Shook, J. F., Finn, F. N., Witczak, M. W., and Monismith, C. L. (1982). "Thickness Design of Asphalt Pavement the Asphalt Institute Method." 5th International Conference on the Structural Design of Asphalt Pavements, Delft, Netherlands.

184. Siekmeier, J. A., Young, D. and Beberg, D. (2000). "Comparison of the Dynamic Cone Penetrometer with other Tests during Subgrade and Granular Base Characterization in Minnesota." ASTM STP 1375, 3, West Conshohocken, Pennsylvania.
185. Simulia, D. S. (2013). "Abaqus 6.12 Documentation." Providence, Rhode Island, USA.
186. Singh, D., Commuri, S., and Zaman, M. (2011). "Evaluation of Predictive Models for Estimating Dynamic Modulus of HMA Mixes Used in Oklahoma." *Journal of the Transportation Research Board*, Vol. 2210, No. 1, pp. 57-72.
187. Sobhan, K., and Das, B. M. (2007). "Durability of Soil-Cements against Fatigue Fracture." *ASCE Journal of Materials in Civil Engineering*, Vol. 19, No. 1, pp. 26-32.
188. Sobhan, K., and Mashnad, M., (2003). "Fatigue Behavior of a Pavement Foundation with Recycled Aggregate and Waste HDPE Strips." *ASCE Journal of Geotechnical and Geoenvironmental Engineering*, Vol. 129, No. 7, pp. 630-638.
189. Solanki, P. (2010), "Characterization of Cementitiously Stabilized Subgrades for Mechanistic-Empirical Pavement Design". PhD Dissertation. School of Civil engineering and Environmental Science, University of Oklahoma, Oklahoma.
190. Solanki, P., Khoury, N. N., Zaman, M., Dean, J., and Seiter, S. (2009). "Engineering Properties of Stabilized Subgrade Soils for Implementation of the AASHTO 2002 Pavement Design Guide (No. FHWA-OK-08-10)." School of Civil Engineering and Environmental Science, University of Oklahoma, Oklahoma.
191. Solanki, P., and Zaman, M. (2014). "Behavior of Stabilized Subgrade Soils under Indirect Tension and Flexure." *Journal of Materials in Civil Engineering*, Vol. 26.
192. Solanki, P., and Zaman, M. (2016). "Design of Semi-Rigid Type of Flexible Pavements." *International Journal of Pavement Research and Technology*, In Press.
193. Solanki, P., Zaman, M. M., and Dean, J. (2010). "Resilient Modulus of Clay Subgrades Stabilized with Lime, Class C Fly Ash, and Cement Kiln Dust for Pavement Design." *Transportation Research Record: Journal of the Transportation Research Board*, Vol. 2186, No. 1, pp. 101-110.
194. Siripun, K., Jitsangiam, P., and Nikraz, H., and Leek, C. (2012). "Fatigue Cracking Behaviours on Cement Treated Crushed Rock." *The Proceedings of the ISAP 2012 International Symposium on Heavy Duty Asphalt Pavements and Bridge Deck Pavements*, Nanjing, China.
195. Sture, S., Alqasabi, A., and Ayari, M. (1999). "Fracture and Size Effect Characters of Cemented Sand." *International journal of fracture*, Vol. 95 No. 1-4, pp. 405-433.

196. Supekar, A. H. (2007). "Design, Analysis and Development of A Morphable Wing Structure for Unmanned Aerial Vehicle Performance Augmentation." ProQuest.
197. Swanson, T. E., and Thompson, M. R. (1967). "Flexural fatigue strength of lime-soil mixtures." Highway Research Record, Vol. 198, pp. 9-18.
198. Theyse, H. L., De Beer, M., and Rust, F. C. (1996). "Overview of South African Mechanistic Pavement Design Method." Transportation Research Record, No 1539. Transportation Research Board, Washington D.C.
199. Thompson, M. R. (1966) "The Split-Tensile Strength of Lime-Stabilized Soils." Lime Stabilization, Highway Research Record, No 92, Highway Research Board, pp. 69-79.
200. Thompson, M. R. (1986). "Mechanistic Design Concepts for Stabilized Base Pavements." Civil Engineering Studies, Transportation Engineering Series No. 46, Illinois Cooperative Highway and Transportation Series No. 214, University of Illinois, Urbana, Illinois.
201. Thompson, M. R. (1994). "High-Strength Stabilized Base Thickness Design Procedure." Transportation Research Record: Journal of the Transportation Research Board, Vol. 1440, pp. 1-7.
202. Thompson, M. R., Robnett, Q. L. (1976). "Resilient Properties of Subgrade Soils." Final Report FHWA-IL-UI-160, University of Illinois, Urbana, Illinois.
203. Titi, H. H., Elias, M. B. and Helwany, S. (2006). "Determination of Typical Resilient Modulus Values for Selected Soils in Wisconsin." Report No. WHRP 06-06).
204. TMR (2012). "Structural Design Procedure of Pavements on Lime Stabilized Subgrades." Technical Note 74, Department of Transport and Main Roads, Brisbane.
205. TRB (2009). "Development of an In-Situ Test That Will Measure Performance Properties of Sub-Grade Soils Stabilized with Cementitious Materials." TRB Research Needs Statements, <http://rns.trb.org/dproject.asp?n=12637>, Last Accessed: October, 2012.
206. Toohey, N.M., Mooney, M.A. and Bearce, R.G., 2013. Relationship between Resilient Modulus and Unconfined Compressive Strength for Lime-Stabilized Soils. Journal of Geotechnical and Geoenvironmental Engineering, Vol. 139, No. 11, pp.1982-1985.
207. Tuncer, E. R. and Basma, A. A. (1991). "Strength and Stress-Strain Characteristics of A Lime-Treated Cohesive Soil." Transportation Research Record, (1295).
208. Van Niekerk, A. A., Molenaar, A. A. A., and Houben, L. J. M. (2002). "Effect of Material Quality and Compaction on the Mechanical Behavior of Base Course

- Materials and Pavement Performance.” In 6th International Conference Bearing Capacity of Roads, Railways and Airfields, pp. 1071-1081.
209. Von Quintus, H. L., Bush, A. J., and Baladi, G. Y. (1994). “Nondestructive Testing of Pavements and Backcalculation of Moduli.” Second Volume. ASTM, STP 1198.
  210. Walker, R.N., Paterson, W.D.O., Freeme, C.R., and Marais, C.P. (1977). “The South African Mechanistic Pavement Design Procedure.” Proc. 4th Int. Conf. on Structural Design of Asphalt Pavements, Vol. 2.
  211. Wen, H., Balasingam, M., Edil, T., Tinjum, J., Gokce, A., Wang, J., Casmer, J., and Su, Z. (2011). “Characterization of Cementitiously Stabilized Layers for Use in Pavement Design and Analysis.” Project 04-36 Test Procedure Evaluation Report, prepared for National Cooperative Highway Research Program, Washington D.C.
  212. Wen, H., Muhunthan, B., Wang, J., Li, X., Edil, T. and Tinjum, J.M. (2014). Characterization of cementitiously stabilized layers for use in pavement design and analysis (No. Project 4-36).
  213. White, D. J., Vennapusa, P., Gieselman, H., Zhang, J., Goldsmith, R., Johanson, L. and Quist, S. (2010). “Accelerated Implementation of Intelligent Compaction Technology for Embankment Subgrade Soils, Aggregate Base, and Asphalt Pavement Materials.” Final Report ER10-08 US12, ND Field Project August, 9.
  214. Witczak, M. W., (2000). "Harmonized Test Methods for Laboratory Determination of Resilient Modulus of Flexible Pavement Designs.". NCHRP 1-28A, Draft Report, Vol. 1.
  215. Witczak, M. W., and Uzan, J. (1988). “The Universal Airport Design System.” Report 1 of 4: Granular Material Characterization. Department of Civil Engineering, University of Maryland, College Park, Maryland.
  216. Yeo, R. (2008). “The Development and Evaluation of Protocols for the Laboratory Characterisation of Cemented Materials.” Austroads Publication No. AP-T101/08, Austroads, Sydney, New South Wales, Australia.
  217. Yoder, E. J., Witczak, M. W. (1975). Principles of pavement design, A Wiley Interscience Publication, New York, USA.
  218. Young, C., and Oetken, N. “AccuGrade.” Caterpillar, Illinois, USA. <[http://www.intelligentcompaction.com/downloads/TPF/MSIC\\_OpenHouse\\_CAT.pdf](http://www.intelligentcompaction.com/downloads/TPF/MSIC_OpenHouse_CAT.pdf)> (Jul. 21, 2013).
  219. Yu, X. J., Fang, Z., Wang, S. Y., Yan, Y., and Yin, J. H. (2007). “A Simple Plastic-Damage Model for the Cement-Soil Admixture.” Key Engineering Materials, 353, pp. 1145-1148.

220. Zambrano, C., Drnevich, V., Bourdeau, P. (2006). "Advanced Compaction Quality Control." Indiana DOT Final Report FHWA/IN/JTRP - 2006/10, Purdue University.
221. Zhang, P., Li, Q., and Wei, H. (2010). "Investigation of Flexural Properties of Cement-Stabilized Macadam Reinforced with Polypropylene Fiber." *Journal of Materials in Civil Engineering*, Vol. 22, No. 12.
222. Zhu, J. (1998). "Characterization of Cement-Kiln-Dust Stabilized Base/ Subbase Aggregate." PhD Dissertation, School of Civil Engineering and Environmental Science, the University of Oklahoma, Norman, Oklahoma.